

DOCTORAL THESIS

Milling of Gamma titanium aluminides

ABHISHEK VIVEK HUKKERIKAR

Project partners



Supervised by

- Dr Pedro J. Arrazola
- Dr Patxi Aristimuño

For achieving Doctoral Degree in
APPLIED ENGINEERING

High Speed Machining Research Group,
Mechanical and Industrial Production department,
Mondragon Unibertsitatea,
Arrasate – Mondragon.
March 2022.

Intellectual property rights and reproduction authorisation



Recognition – Non-Commercial –(by-nc-nd): it does not allow commercial use of the original work or the generation of derivative works.

Statement of originality

I, Abhishek Vivek Hukkerikar, declare that this thesis is the result of my personal endeavour and, that it has not been previously submitted to obtain another degree or professional qualification.

I declare that the work presented in the document is my original work. All sources, references, and literature used or excerpted during the elaboration of this work are properly cited to the best of my knowledge and are listed in complete reference to the due sources.

Arrasate-Mondragon, March 2022

Acknowledgments

Every project can be equated to a movie winning an Oscar award where the lead actor collects it for acting. Nevertheless, the award is not only the recognition of an actor's work but of an entire team that puts together the movie. Similarly, we (I, Akshara, and little Mytri) would like to take this opportunity to name the team which played an instrumental role in helping us reach this goal.

To begin with, we dedicate this work to Guru Raghavendrararu, Guru Satyatmateertharu, Mukhya Pranadevaru, and to the Absolute, Shri Hari. We humbly salute our teacher Pranesh Achar for instilling the spirit of hard work, patience, and focus even during adversities.

Mom, Dad, and Aditi have always been and will always be the constant source of inspiration and support in all activities of our lives. Many more to go. Papa and mummy, too, have been supportive throughout in all aspects. Thank you, grandparents, elders, and the little ones in the family for their blessings and warm regards.

We want to pay our earnest respects to the University for making available all the infrastructure for the proper completion of this work.

This project and the learning derived out of it would nearly be impossible without the principal architects / the teachers – Pedro Arrazola and Patxi Aristimuño. Frankly, it is difficult to articulate their interventions, support, teaching, and a constant source of compelling to achieve better for a time spanning more than four years. We are indebted for orienting and structuring our thinking. It has been an invaluable, unique, and an enriching gift.

We would thank Xabier Arrasate for his co-ordination and support on all formal aspects of the entire project.

Working with the high-performance machining research group colleagues has been a great experience. A special mention to the colleagues (Andres, Harry, Faruk, Gorka, Iñigo, Julen and Xabier Lazkano). A special thanks to Denis for helping with all the samples on short notice!

It was indeed a good fortune to have such good industrial partners who have swiftly and promptly helped us out during the entire project. We profusely thank Pär Lindberg

and Adnan Mahmood for immaculately co-ordinating the entire project, helping us with our scenic stay, and imparting qualitative training at Sandviken. It was a wonderful time. The experience would be incomplete without the kind and knowledgeable course training from Dr Susanne Norgren. We truly appreciate her co-ordination of milling experiments and inputs on tribology even during the pandemic time. We express our sincere gratitude to Dr David Blurtsyan for providing qualitative inputs and course corrections to the research work. We wish to thank Dr Sinuhé Hernández for his help in tribology and great discussions during *fika*.

A special vote of thanks to Dr Todor Stoyanov, Tobias Mathys, Dr Niklaus Rüttimann, Dr Michael Eglin, and Dr Martin Manikowski for their support during the thesis.

We thank Dr Ainhara Garay Araico for her support during SI analyses. We also thank Larraitz and Erika for their help in all the work related to material characterization.

We are obliged for the support given by Antoine Morandea, Damian Joly and the entire CEROC team for the work relating to tribological characterization. It was an enriching experience.

We would like to express our sincere gratitude to the warm and qualitative inputs of Ms. Sharon Baker for helping us with structuring the document.

Finally, thanks to all the people directly or indirectly related to the research work for their contributions.

ABSTRACT

Gamma Titanium Aluminide (γ – TiAl) alloys are intermetallics with approximately half the density of nickel based superalloys. Their low density, high specific strength, and good structural integrity at high temperatures make them potential candidates for aeroengine components.

However, characteristics such as poor ductility at room temperature, high hardness, and substantial surface damage during machining have earned these alloys the reputation of “difficult to cut”. Therefore, the present study aims to assess the machinability and surface integrity of second generation Ti-48Al-2Cr-2Nb γ – TiAl alloys through end bull milling.

First, a tribological characterisation of the tool coating (TiAlSiN) under dry, flood and Minimum Quantity Lubrication (MQL) was carried out. The effectiveness of tool coatings in reducing tribological properties was evaluated by conducting experiments with uncoated pins. The tribological characteristics of the γ – TiAl alloys were subsequently benchmarked against one of the most used titanium alloys, Ti-6Al-4V. The effect of contact parameters such as contact pressure and sliding velocity on the evolution of tribological phenomena was determined.

Secondly, a comprehensive sensitivity analysis of the milling input parameters to the output parameters during the bull end milling of Ti-48Al-2Cr-2Nb was conducted. The influence of microstructures (Near lamellar and Duplex) was analysed together with three types of lubrications (dry, flood and MQL), two bull end mill tools, and milling process parameter (cutting speed).

The assessment of output parameters of cutting forces, tool wear, and surface integrity in the form of surface roughness, sub-surface microstructural alterations, and sub-surface microhardness demonstrated the relevance of all the input parameters in affecting the output ones. As a result, a process window with long tool life and high surface integrity was established in accordance with industrial requirements.

LABURPENA

Titanio aluminuroaren aleazioak (γ – TiAl) konposatu intermetalikoak dira eta nikel oinarriko superaleazioen dentsitate erdia dute gutxi gorabehera. Daukaten dentsitate baxuagatik, erresistentzia espezifiko altuagatik eta tenperatura altuetan duten egiturazko osotasun onagatik hegazkingintzako aplikazioetan erabiltzeko hautagai potentzialak dira.

Hala ere, giro-tenperaturan duten harikortasun eskasak, gogortasun handiak eta mekanizazioan sortzen diren gainazaleko kalte handiek bezalako ezaugarriek, aleazio hauei "mekanizatzen zailak" izatearen ospea eman diete. Hori dela eta, ikerketa honek Ti-48Al-2Cr-2Nb γ – TiAl aleazioen bigarren belaunaldiko mekanizagarritasuna eta gainazaleko osotasuna ebaluatu nahi ditu fresatze bidez mekanizatzean.

Lehenik eta behin, erremintaren estalduraren (TiAlSiN) karakterizazio tribologikoa egin zen lubrifikazio gabe, hozkarri txorrotada bidezko lubrifikazioarekin eta kantitate minimoko lubrifikazioarekin (MQL). Estaldurek propietate tribologikoak murrizteko duten eraginkortasuna estali gabeko tresnekin egindako esperimentuekin alderatuz ebaluatu da. Ondoren γ – TiAl aleazioen ezaugarri tribologikoak titanio-aleaziorik erabilienetako batekin alderatu ziren, Ti-6Al-4V-rekin. kontaktu parametroek, hala nola kontaktu presioak eta irristatze-abiadurak, fenomeno tribologikoetan duten eragina zehaztu zen.

Bigarrenik, fresatzeko erreminta torikoa erabiliz Ti-48Al-2Cr-2Nb-ren fresatze eragiketaren sarrera eta irteera parametroen sentsibilitate analisi integrala egin zen. Bi mikroegituren eragina, ia-laminarra eta duplexa, hiru lubrifikazio-mota (lehorra, hozkarri txorrotada eta MQL), fresatzeko erreminta torikoak eta fresatze eragiketako ebaketa parametro bat (ebaketa-abiadura) aztertu ziren.

Parametro zientifikoen (ebaketa-indarrak) eta industria-parametroen ebaluazioak (erreminten higadura eta gainazaleko osotasuna [gainazaleko zimurtasuna, gainazaleko mikroegituraren alterazioak eta gainazaleko mikrogogortasuna]) frogatu zuen sarrera parametro guztien eragin garrantzitsua irteerako parametroetan. Ondorioz, erremintaren bizitza luzea eta gainazaleko osotasun handiko prozesu-leiho bat ezarri zen.

RESUMEN

Las aleaciones de aluminuro de titanio gamma (γ -TiAl) son intermetálicas con aproximadamente la mitad de densidad que las superaleaciones basadas en el níquel. Su baja densidad, su alta resistencia específica y su buena integridad estructural a altas temperaturas las convierten en candidatas potenciales para componentes de motores de avión.

Sin embargo, características como la escasa ductilidad a temperatura ambiente, la elevada dureza y los importantes daños en la superficie durante el mecanizado han hecho que estas aleaciones tengan la reputación de ser "difíciles de mecanizar". Por lo tanto, el presente estudio tiene como objetivo evaluar la maquinabilidad y la integridad superficial en el fresado de una aleación γ -TiAl de segunda generación, la Ti-48Al-2Cr-2Nb.

En primer lugar, se llevó a cabo una caracterización tribológica del recubrimiento de la herramienta (TiAlSiN) en seco, lubricación convencional y con mínima cantidad de lubricación (MQL). La eficacia de los recubrimientos de las herramientas en la reducción de las propiedades tribológicas se evaluó mediante la comparación con experimentos realizados con pines sin recubrimiento. Las características tribológicas de la aleación Ti-48Al-2Cr-2Nb se compararon posteriormente con una de las aleaciones de titanio más utilizadas, la aleación Ti-6Al-4V. Se determinó el efecto de los parámetros de contacto, como la presión de contacto y la velocidad de deslizamiento, en la evolución de los fenómenos tribológicos.

En segundo lugar, se llevó a cabo un análisis exhaustivo de la sensibilidad de los parámetros de entrada y salida durante el fresado con herramienta tórica de Ti-48Al-2Cr-2Nb. Se analizó la influencia de dos microestructuras, la casi laminar y la dúplex, junto con tres tipos de lubricación (en seco, lubricación convencional y MQL), dos herramientas tóricas de fresado y un parámetro de corte (velocidad de corte).

La evaluación de los parámetros científicos (fuerzas de corte) e industriales (desgaste de la herramienta e integridad de la superficie [rugosidad de la superficie, alteraciones microestructurales de la sub-superficie y microdureza de la sub-superficie]) demostró la relevancia de todos los parámetros de entrada sobre los de salida. Como resultado,

se estableció una ventana de proceso con una vida útil de la herramienta y requerimientos de integridad superficial válida para aplicaciones industriales.

CONTENTS

1 Introduction.....	1
2 Literature review	8
2.1 State of the art: Gamma titanium aluminide alloys.....	8
2.2 State of the art: Machinability of Gamma Titanium Aluminide alloys	22
2.3 State of the art: Tribology in metal cutting	44
2.4 Summary of the literature review.....	56
3 Material characterisation	59
3.1 Centrifugal casting	59
3.2 Optical metallography	64
3.3 Thermal characterisation and material hardness	70
3.4 Conclusion of material characterisation.....	74
4 Tribological characterisation	76
4.1 Experimental setup and methodology	77
4.1.1 Pin-on-Cylinder (POC) tests	77
4.1.2 Adhesion and wear assessment.....	82
4.2 Design of experiments	85
4.3 Results.....	89
4.3.1 Friction characterisation	89
4.3.2 Adhesion and coating wear assessment	101
4.3.3 Heat partitioning between tool and workpiece	124
4.4 Conclusion of tribological characterisation	129
5 Bull end milling tests.....	133
5.1 Experimental setup: Methodology and validation	133
5.1.1 Methodology: Cutting forces	139
5.1.2 Methodology: Tool wear	140
5.1.3 Methodology: Surface Integrity	141
5.2 Design of experiments	146
5.2.1 Experimental plan	150
5.3 Results	151
5.4 Conclusion of the bull end milling tests.....	179
6 Conclusions and future outlook	182
6.1 Conclusions	182
6.2 Future prospects	185

LIST OF FIGURES

Figure 1 ICAO plan to reduce carbon emissions [3]	1
Figure 2 Distribution of alloys in aero-engine applications [7]	2
Figure 3 The process flow chart of the PhD and the interconnectivity of workpackages	4
Figure 4 Manufacturing and processing routes for gamma - TiAl alloys-based components.	9
Figure 5 A schematic of spark plasma sintering [22]	10
Figure 6 Scheme of centrifugal casting of gamma – TiAl alloy components	11
Figure 7 Misruns/casting defects during the casting of gamma -TiAl alloys [24]	12
Figure 8 Additively manufactured GE blades in service [28]	13
Figure 9 The binary titanium aluminium phase diagram [29]	14
Figure 10 The heat treatment temperatures and corresponding microstructures of dual phase gamma titanium aluminides [37], [39], [40].....	17
Figure 11 Tensile properties of microstructures of Ti-47Al-1Cr-1V-2.5Nb [39]	18
Figure 12 Better performance of 3 rd generation TiAl vis-à-vis 2 nd generation TiAl, titanium and nickel alloys [45]	20
Figure 13 Cross sectional view of jet turbine engine and placement of LPT blade (A) fan section (B) compressor section (C) combustion section (D) low, intermediate and high-pressure section [52]	21
Figure 14 Tool wear and cutting time for different generations of γ -TiAl alloys as shown by [59]	28
Figure 15 Standard referred for tool wear analysis.....	33
Figure 16 Tool wear types [87].....	36
Figure 17 Schematic representation of surface integrity characteristics [95].....	38
Figure 18 An illustration of important roughness parameters [98].....	39
Figure 19 Deformation of lamellae during turning of 3rd generation the Ti-45Al- 8Nb-0.2C-B (TNB-V3) gamma-TiAl alloys [10].....	40
Figure 20 Comparison of lubrication strategies by [61]	42
Figure 21 Tool wear curves observed at 50 m/min and $f = 0.08$ mm/tooth by [90] ..	43
Figure 22 (A) Three basic components in sliding friction (B) corresponding cutting zone (c) three zone model[104]	45
Figure 23 Possible superposition of wear mechanisms on the surface of a material...	46

Figure 24 Stress distribution on the tool as proposed by [117]	47
Figure 25 The pin-on-cylinder configuration as proposed by [134].....	51
Figure 26 The decomposition of apparent friction coefficient into adhesive and deformation components [136]	51
Figure 27 Hertzian contact condition with assumption of sphere on an infinitely long flat plate	52
Figure 28 Pictorial representation of quantification of heat between pin and workpiece during POC tests	53
Figure 29 Vacuum arc remelting of to obtain Ti-48Al-2Cr-2Nb feed material for castings (Image courtesy: Inductotherm Pvt. Ltd.) (b) ISM and Centrifugal casting process to achieve bars for machining.....	59
Figure 30 (a) Bar dimensions after cleaning and turning of cast ingots. (b) Ingots after waterjet cutting.....	60
Figure 31 X ray tomography of cast ingots to check for porosities and other defects	60
Figure 32 Furnace for Hot Isostatic Pressing of the bars (Image Courtesy: MTI Corporation, Richmond)	61
Figure 33 The EDX profile of cast Ti-48Al-2Cr-2Nb bars indicating the near ideal elemental composition	62
Figure 34 The EDX profile of Ti-48Al-2Cr-2Nb cast + HIP + HT bars indicating a near ideal phase composition	63
Figure 35 Scheme of optical metallography (a) along the axis (b) across the axis	64
Figure 36 Optical micrographs of cast Ti-48Al-2Cr-2Nb ingots revealing the near lamellar microstructure (a) along the axis (b) across the axis	65
Figure 37 Optical micrographs of cast + HIP + HT Ti-48Al-2Cr-2Nb ingots revealing the Duplex - lamellar with interdendritic γ -grains microstructure (a) along the axis (b) Across the axis	66
Figure 38 A band of small α_2 and gamma grains observed on the periphery of cast + HIP + HT ingots (duplex microstructure).....	67
Figure 39 Grain diameter distribution of near lamellar and duplex microstructure between 50 – 250 μm	68
Figure 40 The phase quantification of the phases carried out via LAS suite software for Ti-48Al-2Cr-2Nb cast alloy	69
Figure 41 Thermal characterization of NL and Duplex bars represented by (a) density (b) specific heat (c) thermal diffusivity (d) thermal conductivity.....	71

Figure 42 Optical metallographs of (a) near lamellar before heating (b) near lamellar after heating (c) duplex bars before heating (d) duplex bars after heating upto 1673.15 K.....	72
Figure 43 Pin-on-cylinder testing employing customized tribometer and pins.....	78
Figure 44 The composition of pins	79
Figure 45 Special fixture to hold the MQL pipe in position.....	81
Figure 46 Representational image of Keyence VHX 5000 (McSwain Engineering Inc.).....	82
Figure 47 The quantification of adhesion (a) Accumulated particles above the sticking area (b) Sticking area after cleaning accumulated particles.....	83
Figure 48 Cross-sectioning procedure for selected pins (a) pin dimensions (b) sticking area of the pins (c) optical measurement of sticking area (d) cross sectioning of the pins (e) measurement of coating wear.....	84
Figure 49 Variation of apparent friction coefficient of Ti-6Al-4V alloy with dry, EML, MQLSE1 and MQLVP.....	94
Figure 50 Track analysis of Ti-6Al-4V with dry lubrications showing a crack free surface.....	95
Figure 51 Variation of apparent friction coefficient of Ti-48Al-2Cr-2Nb (NL) alloy with dry, EML, MQLSE1 and MQLVP	97
Figure 52 Track analysis of Ti-48Al-2Cr-2Nb (NL) with dry lubrications showing a crack free but damaged surface.....	98
Figure 53 Variation of apparent friction coefficient of Ti-48Al-2Cr-2Nb (D) alloy with dry, EML, MQLSE1 and MQLVP19004	100
Figure 54 Track analysis of Ti-48Al-2Cr-2Nb (D) with dry lubrications showing wear track surface w with cracks.....	101
Figure 55 Increase in adhesion area with increase in contact pressure and sliding velocity for Ti-6Al-4V observed with dry, EML, MQLSE1 and MQLVP lubricants.....	105
Figure 56 Coating intact at (a)1.31 GPa and a possible coating erosion at (b) 3.27 GPa with EML for Ti-6Al-4V alloy	108
Figure 57 Coating intact at (a)1.31 GPa and coating erosion at (b) 3.27 GPa with EML for Ti-6Al-4V alloy	109
Figure 58 No damage to coating with MQLSE1 at (a)1.31 GPa and (b) 3.27 for Ti-6Al-4V alloy	110

Figure 59 Marginal increase in adhesion area with increase in contact pressure and sliding velocity for Ti-48Al-2Cr-2Nb (NL) across all the contact conditions observed with dry, EML, MQLSE1 and MQLVP lubricants	112
Figure 60 Marginal increase in adhesion area with increase in contact pressure and sliding velocity for Ti-48Al-2Cr-2Nb (D) across all the contact conditions observed with dry, EML, MQLSE1 and MQLVP lubricants	113
Figure 61 No damage to coating wear observed in dry conditions at (a) 1.31 GPa and (b) 3.27 GPa for Ti-48Al-2Cr-2Nb (NL) alloy	117
Figure 62 No damage to coating wear observed with EML at (a) 1.31 GPa and (b) 3.27 GPa for Ti-48Al-2Cr-2Nb (NL) alloy.....	118
Figure 63 No damage to coating wear observed with MQLSE1 at (a) 1.31 GPa and (b) 3.27 GPa for Ti-48Al-2Cr-2Nb (NL) alloy.....	119
Figure 64 Coating intact at (a)1.31 GPa and coating erosion at (b) 3.27 GPa in dry conditions for Ti-48Al-2Cr-2Nb (D) alloy	120
Figure 65 No damage to coating wear observed with EML at (a) 1.31 GPa and (b) 3.27 GPa for Ti-48Al-2Cr-2Nb (D) alloy	121
Figure 66 Coating intact at (a)1.31 GPa and coating completely worn at (b) 3.27 GPa in MQLSE1 conditions for Ti-48Al-2Cr-2Nb (D) alloy.....	122
Figure 67 The difference in the temperature recorded by the thermocouples during the temperature measurements of Ti-6Al-4V alloy with dry lubricant	124
Figure 68 The statistical relationship of each alloy with input (sliding velocity, contact parameter) and output (apparent friction coefficient, adhesion area) based on Pearson correlation.....	128
Figure 69 Milling machine used to carry out tests.....	133
Figure 70 Dimensions of (a) Setup1 for tool wear measurement (b) Setup 2 for cutting forces and SI analysis.....	134
Figure 71 The process flow diagram of bull end milling test	135
Figure 72 Setup validation of Ti-48Al-2Cr-2Nb (NL) with EML and $v_c = 100$ m/min compared to previous research.....	137
Figure 73 The methodology of measuring cutting forces	139
Figure 74 Methodology followed for tool wear measurement	140
Figure 75 Surface roughness measurements of the Rectangle block to obtain R_a , R_t and R_z profiles	141

Figure 76 Assessment of sub-surface microstructure alteration of a Rectangle block	142
Figure 77 Analysis of surface drags.....	143
Figure 78 The bending length of surface drag	143
Figure 79 The microhardness profile of longitudinal surface at 115 m/min and MQLSE1	145
Figure 80 Comparative bull end mill tests between TSS and Hardlox coating at various contact conditions with (a) and (e)Dry, (b) and (f) EML, (c) and (g) MQLSE1 and (d) and (h) MQLVP lubricants	148
Figure 81 Higher tool livers observed for (a) Ti-48Al-2Cr-2Nb (NL)and (b) Ti-48Al- 2Cr-2Nb (D) with EML at $v_c = 125$ m/min.....	154
Figure 82 Output parameters of Ti-48Al-2Cr-2Nb (NL) and Ti-48Al-2Cr-2Nb (D) observed with EML at $v_c = 100, 115$ and 125 m/min	155
Figure 83 Surface pits observed for Ti-48Al-2Cr-2Nb (D) with EML at $v_c = 125$ m/min	156
Figure 84 Output parameters of Ti-48Al-2Cr-2Nb (NL) and Ti-48Al-2Cr-2Nb (D) observed with MQLSE1 at $v_c = 100$ and 115 m/min	162
Figure 85 Cracks observed for Ti-48Al-2Cr-2Nb (D) at $v_c = 115$ m/min with MQLSE1	163
Figure 86 The output parameters of Ti-48Al-2Cr-2Nb (NL) and Ti-48Al-2Cr-2Nb (D) observed with MQLVP19004 at $v_c = 100$ and 115 m/min.....	168
Figure 87 The lamellar colonies embedded between alpha 2 and gamma grains in Ti- 48Al-2Cr-2Nb (NL) microstructure.....	171
Figure 88 Duplex microstructure showing the absence of lamellar colonies in some cases	178

LIST OF TABLES

Table 1 Sensitivity analysis carried out in this research project.....	3
Table 2 The mechanical properties of phases of titanium aluminides [5][30]	13
Table 3 Mechanical and thermal properties of prominent superalloys and gamma titanium aluminides [32], [34], [35], [36]	15
Table 4 Microstructure of dual phase gamma titanium aluminides and their respective mechanical influences [32], [42]–[44]	19
Table 5 Different generation of gamma – TiAl alloys [50]	21
Table 6 Various machining operations reported for different generations of gamma – TiAl alloys	29
Table 7 Machining parameters for milling of gamma -TiAl alloys.....	32
Table 8 Tool wear and subsequent mechanisms observed during machining of gamma – TiAl alloys	37
Table 9 Defects observed during surface integrity analyses of gamma – TiAl alloys	41
Table 10 Critical assessment of tribology characterization in published literature	55
Table 11 Process parameters of hot isostatic pressing of cast Ti-48Al-2Cr-2Nb ingots	61
Table 12 The heat treatment conditions employed for cast ingots to achieve duplex microstructure	61
Table 13 Phase composition of cast and cast + HIP + HT microstructures.....	69
Table 14 Nomenclature of the alloys and lubricants in the chapter 4.....	77
Table 15 Material properties obtained from ultrasound analysis and the literature	80
Table 16 Physical-Chemical data of all lubricants	81
Table 17 The total test carried out for Ti-6Al-4V, Ti-48Al-2Cr-2Nb NL and D alloys with different lubricants	87
Table 18 Design of experiments for Ti-48Al-2Cr-2Nb (NL and D) and Ti-6Al-4V, phase 1 and phase 2.....	88
Table 19 Absolute uncertainty observed during the friction characterisation of NL, D and Ti64 alloys with dry, EML, MQLSE1 and MQLVP lubricants.....	89
Table 20 Apparent friction coefficients of Ti-6Al-4V and Ti-48Al-2Cr-2Nb (NL and D) with dry, EML, MQLSE1 and MQLVP lubricants	91
Table 21 Dependency of sliding velocity on contact pressures in evolution of μ_{app} for all lubricants and Ti-6Al-4V alloy	92

Table 22 Relationship between sliding velocity and contact pressures in terms of evolution of μ_{app} for all lubricants seen in Ti-48Al-2Cr-2Nb (NL) alloy	96
Table 23 Relationship between sliding velocity and contact pressures in terms of evolution of μ_{app} for all lubricants seen in Ti-48Al-2Cr-2Nb (D) alloy	99
Table 24 Absolute uncertainty from adhesion measurements of the NL, D and Ti64 alloys with dry, EML, MQLSE1 and MQLVP lubricants	102
Table 25 Quantification of adhesion area of Ti-48Al-2Cr-2Nb (NL) and Ti-48Al-2Cr-2Nb (D) with dry, EML, MQLSE1 and MQLVP 19004 lubricants	103
Table 26 Adhesion profiles of Ti-6Al-4V at varying contact pressures with coated and uncoated pins under dry, emulsion, MQLSE1 and MQLVP oils	106
Table 27 Adhesion profiles of Ti-48Al-2Cr-2Nb (NL) at varying contact pressures with coated and uncoated pins dry, emulsion, MQLSE1 and MQLVP oils	115
Table 28 Adhesion profiles of Ti-48Al-2Cr-2Nb (D) at varying contact pressures with coated and uncoated pins dry, emulsion, MQLSE1 and MQLVP oils	116
Table 29 Coating wear analysis of Ti-6Al-4V, Ti-48Al-2Cr-2Nb (NL), and Ti-6Al-4V, Ti-48Al-2Cr-2Nb (D) in dry, EML and MQLSE1 lubricant at 1.31 and 3.27 GPa.....	123
Table 30 The Heat partition coefficients of all alloys under all lubrications calculated at 2.3 GPa and 80 m/min.....	125
Table 31 The test matrix of setup validation tests	136
Table 32 Input parameters used in the study	138
Table 33 Tool wear measurement data for T1745 with EML at 100 m/min	140
Table 34 An example of SD measurements on specimen machined with MQLSE1 oil at $v_c = 115$ m/min	144
Table 35 Experimental plan of preliminary tests	146
Table 36 Experimental plan of milling tests	150
Table 37 The tool wear profiles of three time intervals before tool failure of Ti-48Al-2Cr-2Nb (NL) with EML at cutting speeds of 100, 115 and 125 m/min.....	152
Table 38 The tool wear profiles of three time intervals before tool failure of Ti-48Al-2Cr-2Nb (D) with EML at cutting speeds of 100, 115 and 125 m/min.....	153
Table 39 The minimum SI data sheet of Ti-48Al-2Cr-2Nb (NL) and Ti-48Al-2Cr-2Nb (D) observed with EML at $v_c = 100, 115$ and 125 m/min.....	158

Table 40 The tool wear profiles of three time intervals at 100 m/min and with last time interval at 115 m/min, before tool failure for Ti-48Al-2Cr-2Nb (NL) with MQLSE1	160
Table 41 The tool wear profiles of three time intervals at 100 m/min and with last time interval at 115 m/min, before tool failure for Ti-48Al-2Cr-2Nb (D) with MQLSE1	161
Table 42 The minimum SI data sheet of Ti-48Al-2Cr-2Nb (NL) and Ti-48Al-2Cr-2Nb (D) observed with MQLSE1 at $v_c = 100$ and 115 m/min.....	164
Table 43 The tool wear profiles of last three time intervals at 100 m/min and with last time interval at 115 m/min, before tool failure for Ti-48Al-2Cr-2Nb (NL) with MQLVP.....	166
Table 44 The tool wear profiles of last three time intervals at 100 m/min and with last time interval at 115 m/min, before tool failure for Ti-48Al-2Cr-2Nb (D) with MQLVP.....	167
Table 45 The minimum SI data sheet of Ti-48Al-2Cr-2Nb (NL) and Ti-48Al-2Cr-2Nb (D) observed with MQLVP19004 at $v_c = 100$ and 115 m/min	170
Table 46 The longitudinal face subsurface micrographs of three time intervals before tool failure of Ti-48Al-2Cr-2Nb (NL) with EML at cutting speeds of 100, 115 and 125 m/min	172
Table 47 The longitudinal face subsurface micrographs of three time intervals before tool failure of Ti-48Al-2Cr-2Nb (D) with EML at cutting speeds of 100, 115 and 125 m/min	173
Table 48 The longitudinal face subsurface micrographs of three time intervals before tool failure of Ti-48Al-2Cr-2Nb (NL) with MQLSE1 at cutting speeds of 100 m/min and last time interval at cutting speed 115 m/min.....	174
Table 49 The longitudinal face subsurface micrographs of three time intervals before tool failure of Ti-48Al-2Cr-2Nb (D) with MQLSE1 at cutting speeds of 100 m/min and last time interval at cutting speed 115 m/min.....	175
Table 50 The longitudinal face subsurface micrographs of three time intervals before tool failure of Ti-48Al-2Cr-2Nb (NL) with MQLVP at cutting speeds of 100 m/min and last time interval at cutting speed 115 m/min.....	176
Table 51 The longitudinal face subsurface micrographs of three time intervals before tool failure of Ti-48Al-2Cr-2Nb (NL) with MQLVP at cutting speeds of 100 m/min and last time interval at cutting speed 115 m/min.....	177

GLOSSARY

Symbol	Nomenclature	Units
μ_{adh}	Adhesive friction coefficient	-
α_2	Alpha 2 phase	-
a_p	Apparent contact area	mm ²
μ_{app}	Apparent friction coefficient	-
a_p	Axial depth of cut	mm
α	Clearance angle	0
α	Contact radius (Hertzian)	mm
P	Cooling pressure	bar
S_{pin}	Cross-sectional area of PoC pin	mm ²
v_c	Cutting speed	m/min
$\mu_{plastic\ def}$	Deformative friction coefficient	-
ρ	Density	kg/m ³
ΔT	Difference in temperature of thermocouples	K
dx	Distance between thermocouples	mm
E	Elastic moduli	GPa
e	Engineering strain	-
R	Engineering stress	MPa
K_r	Entering angle	0
f_n	Feed per revolution	mm/rev
V_b	Flank wear	mm
λ	Friction angle	°
μ	Friction coefficient	-
$\varphi_{friction-Wp}$	Friction heat flux incident on the pin	W
τ_f	Friction stress	MPa
$\varphi_{friction-Wp}$	Frictional heat flux incident on workpiece	W
γ	Gamma phase	-
P_g	Global power consumed during PoC tests	W
$\varphi_{friction}$	Heat flux consumed due to friction	W
β_{pin}	Heat transmitted to the pins	J

P_{avg}	Hertzian contact pressure	GPa
I_o	Initial length of the sample	mm
A_o	Initial section of sample	mm ²
F_{ins}	Instantaneous applied load	N
A_{ins}	Instantaneous measured area	mm ²
$v_{c\ max}$	Maximum cutting speed	m/min
σ_{cmax}	Maximum normal stress	MPa
P_{net}	Net power	W
F_n	Normal Force	N
σ_n	Normal stress	MPa
ν	Poisson's ratio	-
P_f	Power consumed due to friction	W
P_{pd}	Power consumed during plastic deformation	W
a_e	Radial depth of cut	mm
R_1	Radius of spherical pin	mm
R_2	Radius of workpiece	mm
α	Rake angle	°
a_r	Real contact area	mm ²
m	Shear friction factor	-
φ	Shear plane angle	°
τ_c	Shear stress	MPa
K_c	Specific cutting force	N/mm ²
C_p	Specific heat	J/(kg*K)
n	Spindle speed	rev/min
λ_{therm}	Thermal conductivity	W/ (m*K)
α_{therm}	Thermal diffusivity	m ² /s
F_t	Thrust Force	N
l_c	Tool – chip contact length	mm
r_ϵ	Tool tip radius	mm
ϵ	True strain	-
σ	True stress	MPa
$Vol_{\ sample}$	Volume of sample	mm ³

Acronym	Meaning
AM	Additive Manufacturing
CCD	Central Composite Design
CNC	Computer Numeric Control
DOE	Design Of Experiments
EBM	Electron Beam Melting
ECM	Electro Chemical Machining
EDM	Electro Discharge Machining
EDS	Energy Dispersive X-ray Spectroscopy
EML	Emulsion
FEM	Finite Elemental Modelling
GE	General Electric Corp.
HIP	Hot Isostatic Pressing
HT	Heat Treatment
ICAO	International Civil Aviation Organisation
ISO	International Standard Organization
LPT	Low Pressure Turbine
MAZ	Machining Affected Zone
MQCL	Minimum Quantity Cooling Lubrication
MQL	Minimum Quantity Lubrication
MWF	Metal Working Fluids
NNS	Near Net Shape
OM	Optical Microscopy
POC	Pin-on-Cylinder
RSM	Response Surface Modelling
SD	Surface Drag
SEBM	Selective Electron Beam Melting
SEM	Scanning Electron Microscope
SI	Surface Integrity
SPS	Spark Plasma Sintering
UN	United Nations
WEDM	Wire Electro Discharge Machining

Chapter 1

INTRODUCTION

1 INTRODUCTION

The global warming and climate change have compelled the United Nations (UN) to adopt strong measures to curtail carbon emissions. In this context, many industrial sectors have taken actions to reduce their carbon footprints. Data published by Hoser et al. [1] indicates that the airline industry contributes about 1.7 – 1.9 % of greenhouse gas emissions. A working paper [2] published by International Civil Aviation Organization (ICAO) highlights that aviation alone was responsible for 543 million tons of Carbon-dioxide (CO₂) emissions. This same paper sets out various steps to mitigate climate change by being carbon-neutral in emissions, while still achieving 2050 growth targets. The Figure 1 highlights the importance the ICAO plan attaches to known aircraft technologies.

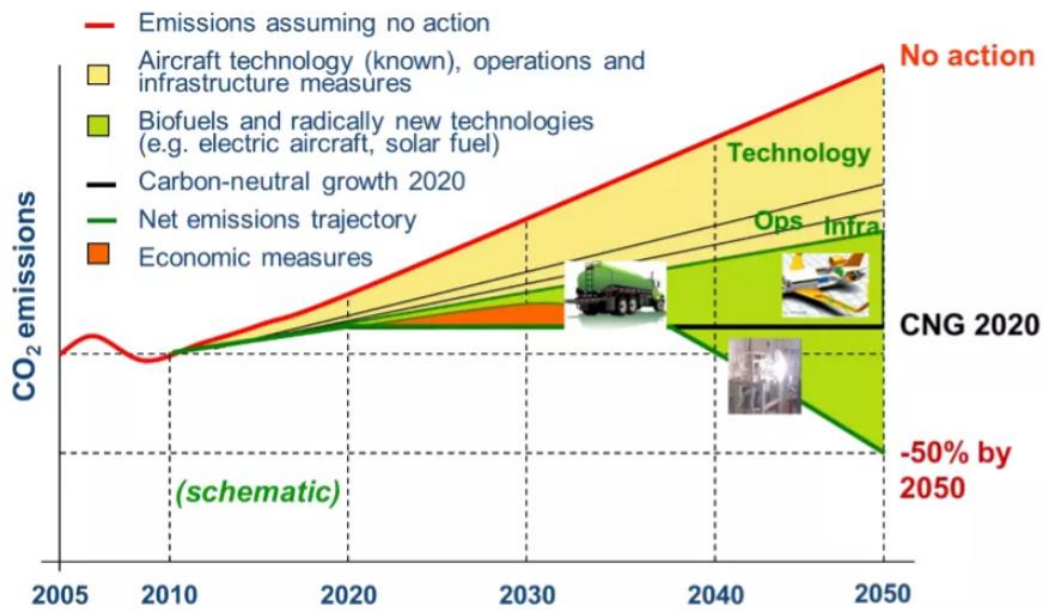


Figure 1 ICAO plan to reduce carbon emissions [3]

The aeroengine industry as a subset of aircraft manufacturing, is investigating strategies to comply with these requirements. One avenue of exploration is replacing heavier nickel based alloys with lightweight intermetallics to achieve fuel savings (Dimiduk [4]), and a potential candidate is Gamma Titanium Aluminide (γ – TiAl) family. These are intermetallic alloys composed of titanium and aluminium (45 – 47%) coupled with additional alloying elements such as chromium, niobium, and manganese to improve mechanical properties. They are considered an appropriate replacement option because they are 50% lighter than nickel based superalloys and present a combination

Introduction

of properties suited for high temperature applications namely high melting point, low density, high specific strength and moduli, low diffusivity, good structural stability, and good resistance to oxidation and high ignition (Appel et al. [5]). According to the data compiled by Bewlay et al. [6], 190,000 gamma – TiAl blades are in use as Low Pressure Turbine (LPT) blades in GE^{nx} engines.

Despite these obvious advantages, the use of gamma – TiAl alloy has not to date been extended to other aeroengine applications such as fans, compressors, and combustors. As Figure 2 illustrates, nickel based superalloys are preferred in the hotter regions (combustor chambers and turbines) and titanium alloys in colder sections (fans and compressors).

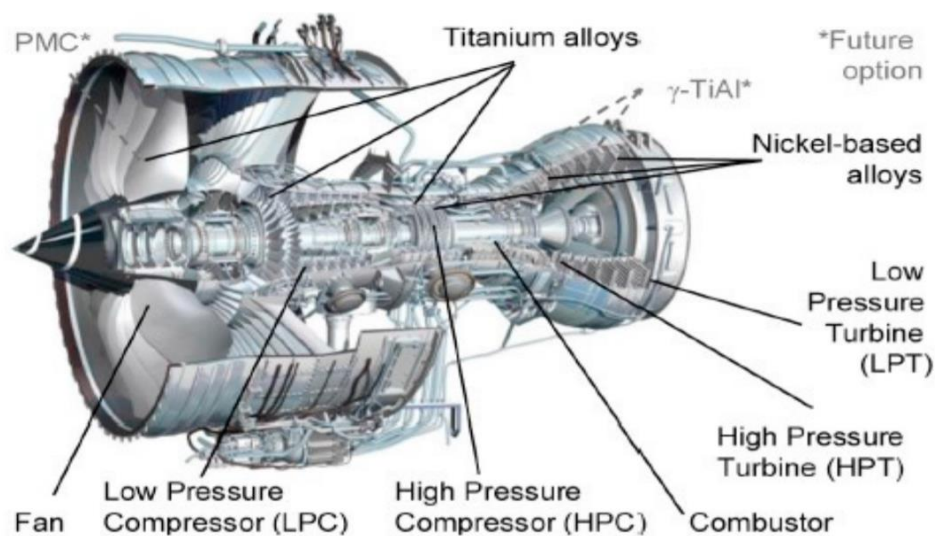


Figure 2 Distribution of alloys in aero-engine applications [7]

One of the reasons for this limited use of the gamma – TiAl alloys is their “*difficult to cut*” nature. As explained by Klocke et al. [8], the tendency of gamma – TiAl alloys is to rapidly wear the cutting edges of the tool during machining. This is corroborated by Aspinwall et al. [9] who reported cutting difficulties due to high hardness and brittleness at room temperature, low thermal conductivity, high elevated strength, low fracture toughness, and chemical reactivity with many tool materials. The interest in the machinability of gamma – TiAl is growing, however. In another study Klocke et al. [10] reported that although milling, turning, and drilling operations for gamma – TiAl

Introduction

alloys have been the subject of investigation, there remains a need to optimize machining strategies. This is particularly true in the case of aerospace sector, where efficient productivity and optimized surface integrity are indispensable. In view of these arguments, this research project presents a comprehensive machining study to assess the effect of microstructure, cutting tools, lubrication strategies, and process parameters on tool wear, cutting forces and the surface integrity of gamma – TiAl alloys.

To this end, this Ph.D. work *defines a process milling window for Ti-48Al-2Cr-2Nb gamma titanium aluminides consisting of workpiece alloy microstructures, lubricants, milling tools, and machining parameters while ensuring surface integrity and tool life required in the aerospace applications.*

This thesis work has been carried out in collaboration with three industrial partners:

- AB Sandvik Coromant (Sweden) supplied the cutting tools and imparted trainings related to machinability.
- Blaser Swisslube AG (Switzerland) supplied the lubricants used during the study.
- Access e.V. (Germany) supplied with Ti-48Al-2Cr-2Nb ingots used in the study.

All the research work, experimental tests, and academic activities were carried out at Mondragon Unibertsitatea. An experimental sensitivity analysis of input parameters (alloys, lubricants, tools, cutting machining parameters) on output parameters (cutting forces, tool wear and surface integrity) was carried out as set out in Table 1.

Table 1 Sensitivity analysis carried out in this research project.

Experimental sensitivity analysis of input and output parameters	
Input parameters	Output parameters
1. Alloys Ti-48Al-2Cr-2Nb (Near lamellar), Ti-48Al-2Cr-2Nb (Duplex)	1. Cutting forces (N)
2. Lubricants Dry, Emulsion (Vasco 7000), MQLSE1, MQLVP19004.	2. Tool wear (mm)
3. Tools T1745 (TIALSIN coating), TSPL (Hardlox coating)	3. Surface integrity Surface roughness (μm), Material damage, Sub-surface microhardness ($\text{HV}_{0.02}$)
4. Machining parameters Cutting speed (m/min):100,115,125,150	


 Bull end milling

The flow chart shown in Figure 3 maps the role taken to achieve the sensitivity analysis.

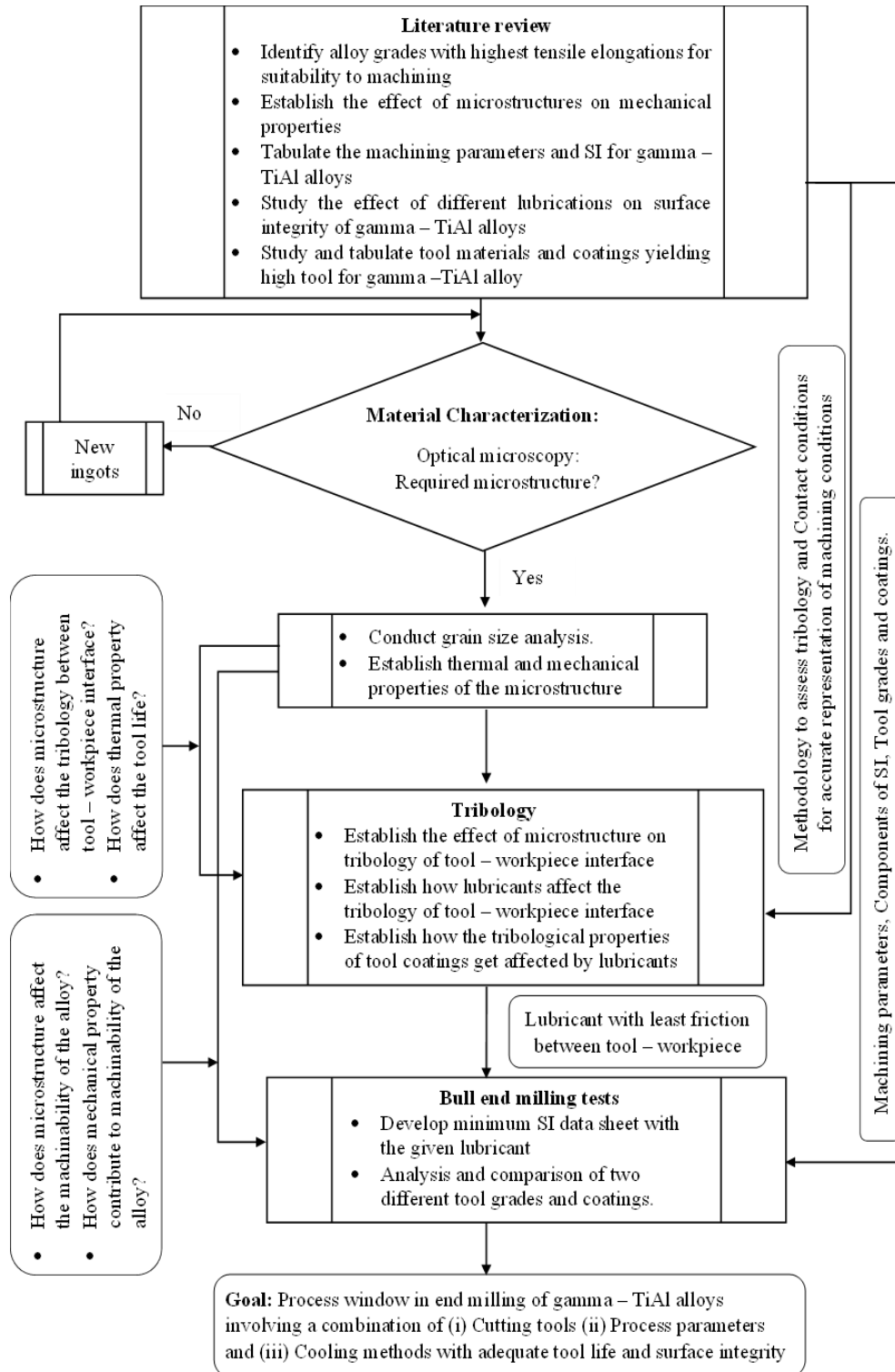


Figure 3 The process flow chart of the PhD and the interconnectivity of workpackages

Thus, there are two core aspects to the PhD (i) Tribological characterisation (ii) Bull end milling tests to derive SI data sheet. These aspects would lead to deliver the process

bull end milling window with a combination of input parameters as shown in the Figure 3. Thus, the two core aspects are formulated into objectives as:

Objective 1: To conduct tribological (friction, adhesion and coating wear, and heat partition) characterisation of Ti-48Al-2Cr-2Nb (Near lamellar), Ti-48Al-2Cr-2Nb (Duplex), and Ti-6Al-4V alloys using Pin-on-Cylinder (POC) tests with dry, emulsion (EML), MQLSE1 and MQLVP 19004 lubricants.

Objective 2: To conduct bull end milling tests on Ti-48Al-2Cr-2Nb (Near lamellar) and Ti-48Al-2Cr-2Nb (Duplex) using the lubricants specified in tribological characterisation. Extract tool wear data and generate '*Minimum Surface Integrity data sheet*' with each lubricant.

The thesis comprises of four chapters whose contents are detailed as follows:

Chapter 2: Literature review

The chapter describes the literature review of gamma titanium aluminide alloys, machinability and tribological aspects relating to machining.

Chapter 3: Material characterisation

This chapter describes the microstructure (Optical Metallography (OM)) and thermal characterisation of the Ti-48Al-2Cr-2Nb alloy. After OM, grain size analysis was carried out. Energy Dispersive X-Ray Spectroscopy (EDS) was used to confirm if the ingot composition matched the ideal stated composition. Subsequently, thermal characterisation in the form of density, specific heat, thermal diffusivity, and thermal conductivity was conducted. Vickers hardness tests were carried out to ascertain the hardness profiles of each microstructure.

Chapter 4: Tribological characterisation

This chapter outlines the Pin-on-Cylinder tests carried out on Ti-48Al-2Cr-2Nb (Near lamellar), Ti-48Al-2Cr-2Nb (Duplex), and Ti-6Al-4V alloys to characterise friction, adhesion and coating wear assessment, and heat partitioning between tool and workpiece with dry, EML, MQLSE1 and MQLVP 19004 lubricants.

Chapter 5: Bull end milling tests

This chapter describes the milling tests on Ti-48Al-2Cr-2Nb (Near lamellar) and Ti-48Al-2Cr-2Nb (Duplex) alloys with dry, emulsion, MQLSE1 and MQLVP 19004 lubricants, with TiAlSiN and Hardlox coated tools. A minimum surface integrity data sheet consisting of industrial parameters of surface roughness, sub-surface microstructural alterations, sub-surface microhardness along with scientific parameter of cutting forces is presented. The chapter concludes with a process milling window of the alloys.

Chapter 6: Conclusions and future outlook

This chapter presents the conclusions of the PhD work and proposes new work to improve the work carried out.

CHAPTER 2

LITERATURE REVIEW

2 LITERATURE REVIEW

This chapter is divided into three sections. The first section describes the state of the art of gamma – TiAl alloys. The second section presents the development in machinability of these alloys. The final section is focused on the tribological aspects during machining and their relevance and applicability for machining gamma – TiAl alloys.

2.1 STATE OF THE ART: GAMMA TITANIUM ALUMINIDE ALLOYS

Gamma – TiAl alloys are intermetallic alloys with a combination of properties such as low density, good high temperature creep and strength, oxidation resistance, and high melting point (Appel et al. [5], Dimiduk [4]). These properties make gamma – TiAl alloys ideal candidates for applications involving high cyclic mechanical and thermal loads (Bentley et al. [11]).

Bewlay et al. [6] have presented a review of the adoption of gamma – TiAl alloys in the automotive and aerospace sectors. The authors mention that in 2011 General Electric (GE) began to employ Low Pressure Turbine (LPT) blades of composition Ti-48Al-2Cr-2Nb (Trade name GE 48-2-2) and that by 2017 more than 1,600,000 lbs of TiAl alloys have been produced with 190,000 GE 48-2-2 blades in service in Boeing 787 and Boeing 747-8 airliners.

The interest in gamma – TiAl alloys is on the rise and other aeroengine manufacturers are implementing gamma – TiAl alloys in their products. SNECMA has introduced the Ti-48Al-2Cr-2Nb composition in their LEAPTM engines which power the Boeing 737, Airbus A320 and soon be introduced in Comac C919 (Bewlay et al. [6]). MTU has used a forgeable TiAl alloy Ti-44Al-4Nb-1Mo -0.1B as LPT blades in their products (Habel et al. [12]). Rolls Royce is working on using gamma – TiAl alloys in their upcoming iterations (Hood et al. [13]).

While the primary application of gamma – TiAl alloys is in the aerospace sector, they are also employed in other sectors. For example, Tetsui et al. [14] note that Mitsubishi motors have implemented turbo-chargers made of gamma – TiAl alloys in the Lancer car model. The production routes of gamma – TiAl alloy components are presented in Figure 4.

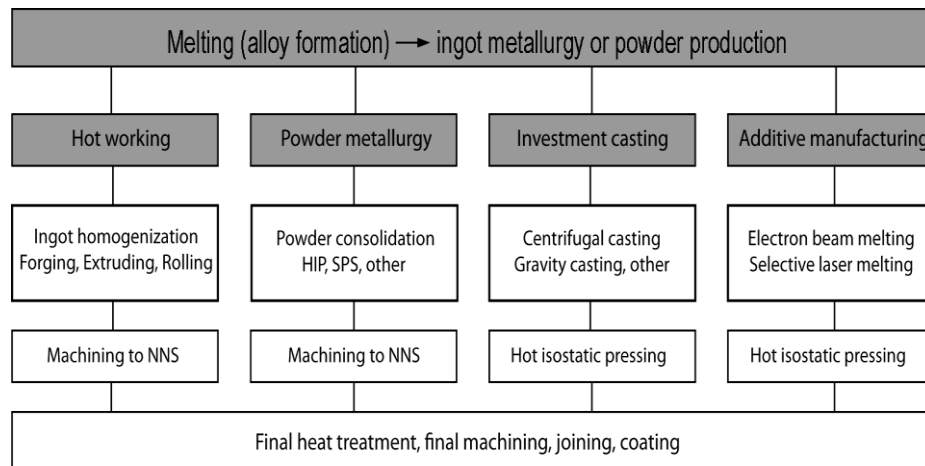


Figure 4 Manufacturing and processing routes for gamma - TiAl alloys-based components.

The hot working of gamma – TiAl alloys is challenging due to their high strength at elevated temperatures (Appel et al. [15]). Bewlay et al. [6] in their work mention that hot forging and extrusion are two hot working routes normally used. Pratt and Whitney (PW) and MTU have used forged LPT blades for the last stages of their new geared turbofan (GTFTM) aeroengines. Because of complex compositions, the gamma – TiAl alloys are normally subjected to isothermal forging operations and subsequent annealing processes. Clemens et al. [16] have reported that several wrought alloys developed in last decade have very narrow processing windows and if subjected to hot working, have to be forged in isothermal conditions and subjected to machining to obtain Near Net Shape (NNS) products, adding to the production complexities. Additionally, the high production cost related to dies, stringent process requirements, and the inability to produce complex shapes are limiting factors of hot working routes for gamma – TiAl alloys.

The powder metallurgy production route offers many advantages in comparison to hot working routes. Appel et al. [5] state that elemental powder technologies and prealloyed powder techniques are the most reported powder metallurgy approaches for gamma – TiAl alloys. However, the mechanical properties are compromised by porosity and high interstitial contamination in the case of elemental powder technologies. The examples of elemental powder technologies include reactive sintering or mechanical alloying.

The prealloyed powder techniques, in contrast, allow greater control over the mechanical properties and deliver homogenous microstructure (Appel et al. [5], Clemens et al.[17]). Processes like gas atomization, rotating electrode process, plasma

rotating electrode process and Spark Plasma Sintering (SPS) come under this domain. Liu et al. [18] state that the problems related to centre-line porosity, chemical inhomogeneity, and regions of varying densities and microstructures are can be avoided by powder metallurgical method. Couret et al. [19] while working with Ti-47Al-2Cr-2Nb and Ti-44Al-2Cr-2Nb-1B alloys were able to achieve fine refined microstructures with high yield strength, ultimate tensile strength and elastic modulus, representing an advantage with respect to conventional Hot Isostatic Processing (HIP). Molénat et al. [20] sintered Ti-44Al-2Nb-2Cr-1B billets and achieved a refined microstructure with good mechanical properties within a temperature range of 35°C. A study by Voisin et al. [21] sintered Ti-48Al-2Cr-2Nb and Ti-48Al-2W-0.08B alloys through SPS. The authors were able to achieve desired microstructure and subsequently a good balance of strength and ductility due to the capabilities of fast heating and cooling rate. The Figure 5 shows the schematic of SPS used for gamma – TiAl alloys.

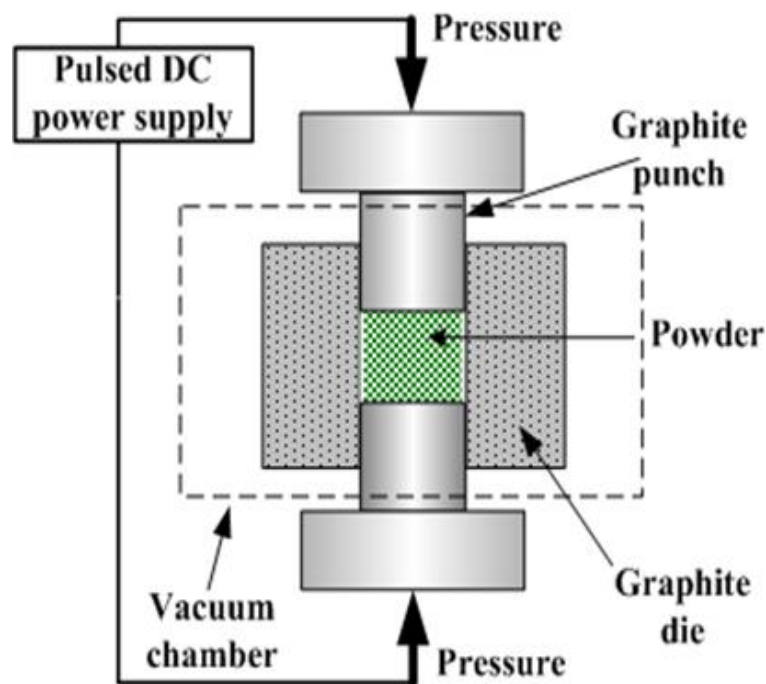


Figure 5 A schematic of spark plasma sintering [22]

Thus, a lot of work has been conducted in the domain of powder metallurgy particularly through SPS route. However, though SPS appears to be a promising route to produce the gamma – TiAl alloys, the ability to control specific microstructural composition is limited due to the short duration of the process (Couret et al. [19]). This has inhibited commercial production of gamma – TiAl via this route.

The investment casting is by far the most widely used process for the production of gamma – TiAl LPT blades. The centrifugal casting process is most suited for the manufacturing of gamma – TiAl alloys owing to the intricate geometry of the blades, high brittle-ductile transition temperature (750°C), narrow solidification range of the alloys and reactivity of the melt. Aguilar et al. [23] have written about the centrifugal casting process followed at Access e.V. Germany for the production of gamma – TiAl alloys blades. Figure 6 shows each process step followed during the centrifugal casting of gamma – TiAl alloy LPT blades.

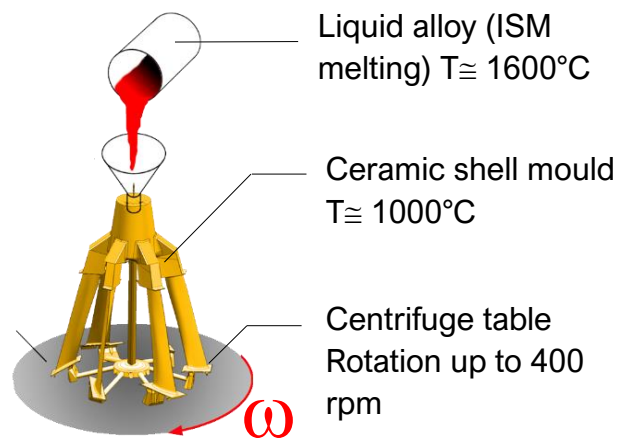


Figure 6 Scheme of centrifugal casting of gamma – TiAl alloy components

Aguilar et al. [23] state that aeroengine products like LPT blades are in lengths between 200 and 400 mm require demanding and sophisticated processes for manufacturing. The blades are often fraught with defects like middle line shrinkage porosity, misruns, and incomplete mould filling during centrifugal casting. Jana et al. [24] have highlighted that the LPT blades for aircraft engine applications widely differ in geometry with less than 1 mm thickness at the trailing edges. Due to such fine geometries, the melt cools faster in the thinner regions than in thicker regions, causing misruns, as shown in Figure 7. Optimisation studies have been focused on casting cluster design and process parameter optimization to achieve 100% mould filling.

Despite the defects in geometries of the components, the centrifugal casting is the most preferred process due to greater control over the heating and cooling rates of the melt. This enables better achievement of desired microstructures.

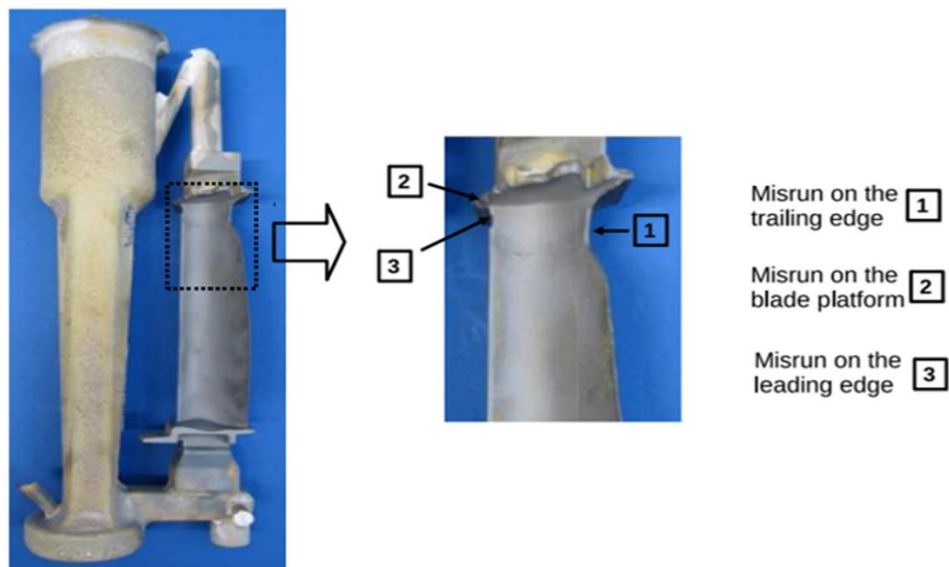


Figure 7 Misruns/casting defects during the casting of gamma -TiAl alloys [24]

Additive Manufacturing (AM) is a relatively new production route. Kim et al. [25] remark that compared to traditional production routes, AM delivers components with complex geometries with has minimum material wastage. The author mentions that on one hand where titanium alloys like Ti-6Al-4V have received the focus, the research regarding gamma – TiAl is limited.

Bewlay et al. [6] quote that Selective Laser Melting (SLM) and Electron Beam Melting (EBM) are the two most used AM methods on gamma – TiAl alloys. Schwerdfeger et al. [26] worked on optimization of process parameters during the Selective Electron Beam Melting (SEBM) of Ti-48Al-2Cr-2Nb alloy and reported aluminium losses from the composition during the process. Kim et al. [25] investigated the microstructural transformation and high temperature creep behaviour of EBM Ti-48Al-2Cr-2Nb alloy and reported massive transformation of microstructure owing to faster cooling rates. Additionally, the EBM sample was reported to have low strength than conventional samples and lower creep resistance. Mizuta et al. [27] investigated the tensile properties SLM and EBM manufactured Ti-48Al-2Cr-2Nb alloy and concluded that SLM with preheating increased the tensile properties drastically. Thus, AM still faces problems with depletion of alloy components, inability to deliver required microstructure and inconsistencies of material properties of alloys. Yet, AM is receiving increased attention from researchers. Apparently, some of the foregoing issues were mitigated

and GE began using AM LPT blades in the GE9x jet engine. The blades are shown in Figure 8.



Figure 8 Additively manufactured GE blades in service [28]

Appel et al. [5] mention that the phase diagram of titanium aluminides, as shown in Figure 9, is a matter of debate and that the proposal of Schuster et al. [29] is widely accepted.

The phase diagram of titanium aluminium displays three significant solid phases of $\alpha_2 - \text{Ti}_3\text{Al}$, $\gamma - \text{TiAl}$, and TiAl_3 . The crystal properties are substantiated in Table 2. Of the three phases, only the $\alpha_2 - \text{Ti}_3\text{Al}$ and $\gamma - \text{TiAl}$ are relevant to industrial and engineering applications as they are suited to aeronautical requirements. The TiAl_3 phase though having balanced mechanical properties and better oxidation resistance has received less attention due to its high brittleness (Appel et al. [5]). The advantages and disadvantages of each phase listed below explain why $\alpha_2 - \text{Ti}_3\text{Al}$ and $\gamma - \text{TiAl}$ are preferred phases.

Table 2 The mechanical properties of phases of titanium aluminides [5][30]

Phase	Melting point (°C)	Density (kg/m ³)	Elastic modulus (GPa)	Usable temperature (°C)	0.2 % YS MPa	Oxidation resistance
TiAl_3	1340	3400	200	-	-	-
$\alpha_2 - \text{Ti}_3\text{Al}$	1600	4300	145	700	700 – 900	Poor
$\gamma - \text{TiAl}$	1460	3900	175	900	400 – 650	Fair

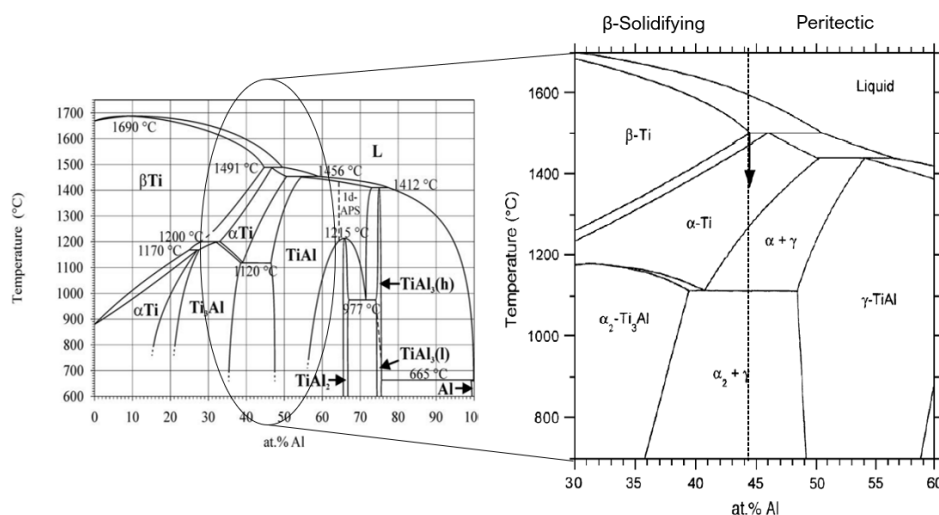


Figure 9 The binary titanium aluminium phase diagram [29]

The α_2 - Ti_3Al Phase: This phase has been extensively studied and it exists in the range of 22 – 39% (atomic) aluminium. Polmear [31] mentions that the most favourable point of this phase is outstanding strength to weight ratios, but their limitation is the low creep strength. Brookes [32] states that when alloyed with niobium, the ductility gets improved owing to the substitution of niobium atoms for titanium atoms in the crystal lattice.

The TiAl_3 phase: Appel et al., Gupta et al. and Polmear et al. ([15], [30], [31]) report that though the phase has better oxidation resistance and very good strength to weight ratio at high temperatures, due to the inherent brittleness at room temperature, it has eluded industrial applications. Appel et al. [15] mention that though attempts have been made to improve ductility by additions of Cu, Mn, Zn, Fe and Cr, the products have suffered cleavage fractures. Therefore, this phase is currently excluded from aeroengine applications.

The γ – TiAl phase: This phase exists between 49 – 66% (atomic) with $L1_0$ structure. Gupta et al. [33] mention that this phase remains ordered till melting point of 1440°C and hence is preferred for application with high mechanical and thermal stresses. Appel et al. [15] quote that the γ – TiAl phase alloys solidify either through β phase or peritectically depending on the processing conditions and alloy compositions as shown in Figure 9. The authors further mention that for engineering applications binary near γ – TiAl are preferred with 80 – 98% volume fraction of γ – TiAl and rest with α_2 - Ti_3Al phase. The Table 3 substantiates the thermal and mechanical properties of gamma –

TiAl (Ti-48Al-2Cr-2Nb) against nickel and titanium-based alloys used for aeronautic applications.

Table 3 Mechanical and thermal properties of prominent superalloys and gamma titanium aluminides [32], [34], [35], [36]

Property	Ni-based	Ti-based	Gamma-TiAl Ti-48Al-2Cr- 2Nb
Young's modulus (E) at RT, GPa	195 - 220	95 - 115	160 - 175
Young's modulus (E) at 800°C, GPa	150 - 160	60 - 70	132
Proof strength ($R_{p0.2}$) at RT, MPa	800 - 1200	345 - 1000	275 - 380
Ultimate Tensile strength (R_m) at RT, MPa	1250 - 1450	480 - 1200	360 - 500
Density (ρ), g/cm ³	7.9 - 8.5	4.5 - 4.6	3.9
Thermal expansion at RT, $\mu\text{m}/(\text{m.K})$	11.2 - 14.6	7.2 - 9.5	22
Ductility at RT, %	3 - 5	10 - 25	1 - 3
Melting point T_m , °C	1480	1668	1480
Poisson's Ratio (ν) at RT	0.31	0.34	0.23 - 0.27

Four prominent microstructures of TiAl alloys have been reported by Kothari [37]. While the fully lamellar, near lamellar and duplex microstructures are obtained via heat treatment at temperatures greater than 1125°C (Eutectoid point), the near gamma microstructure is obtained by heat treatment at temperatures near 1000°C. The explanation of each microstructure shows its grain size and phase composition:

The fully lamellar microstructure is obtained by the heat treatment in the pure alpha phase field at temperature T_1 as shown in Figure 10 (a). Upon cooling to the room temperature, the α -Ti phase precipitates into alternating plates of α_2 and γ plates forming a fully lamellar morphology. Thus microstructure is usually characterized with coarse grains in the range of 200 μm to 1000 μm as reported by Kothari [37]. Ramanujan [38] states that the lamellar microstructure at room temperature can increase ductility directly or in combination with fine recrystallised γ grains.

The near lamellar microstructure is obtained by heating below the α -transus temperature T2 and above the duplex temperature of 1250 – 1300°C as shown in Figure 10 (b). The heating leads to the coarsening of the alpha grains. The microstructure thus comprises of fine-grained lamellar colonies intermixed with newly coarsened alpha grains with an average grain size of 150 μm to 200 μm .

The duplex microstructure is a result of further coarsened alpha grains due to the decrease in the heat treatment temperature (near 1300°C). As the name suggest, duplex microstructure consists of alpha grains and lamellar colonies in equal proportions. It is obtained by heat treatment in region T3 as indicated in Figure 10 (c). Kothari [37] reports that the predominant gamma phase is gradually reduced in volume until the equilibrium volume fraction is reached and grain growth occurs. The microstructure is characterized by smaller grain sizes.

The near gamma is formed in the heat treatment in the $\alpha_2+\gamma$ phase field below the Eutectoid point (T_e) as shown in Figure 10 (d). The microstructure is characterized by equiaxed gamma grains with α_2 precipitates forming at grain boundaries. The average grain size for this microstructure ranges between 30 μm to 50 μm as reported by Kothari [37]. The gamma phase is the soft phase.

There has been a concerted effort in the past to understand the mechanical properties of different microstructures. Kim [39] has worked to investigate the evolution of microstructures and their effect on room temperature tensile properties and fracture toughness behaviour.

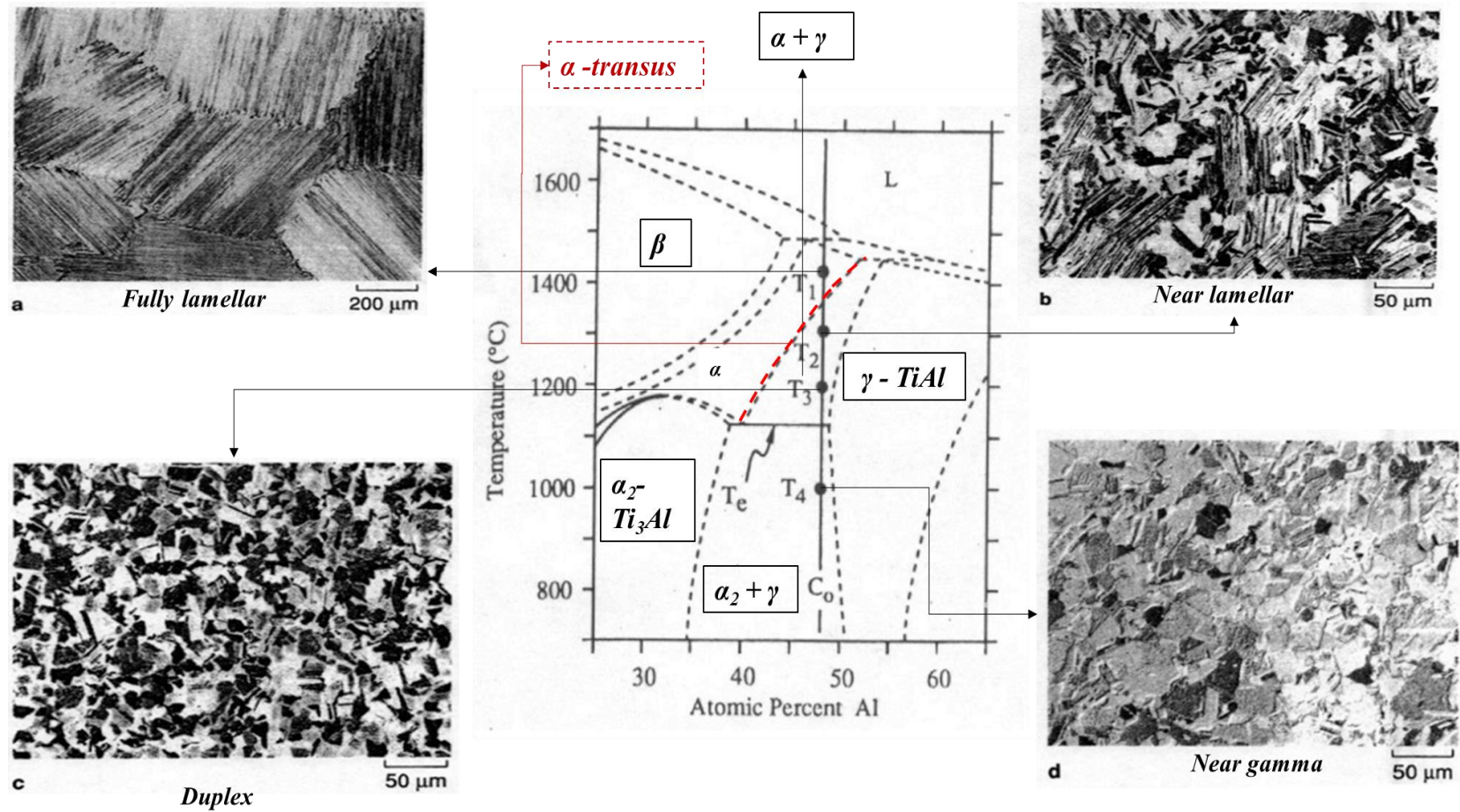


Figure 10 The heat treatment temperatures and corresponding microstructures of dual phase gamma titanium aluminides [37], [39], [40]

Shih et al. [41] in their work have made a comparative study between two microstructures – fully lamellar and the duplex microstructure and consequently noted that the duplex microstructure displays greater room temperature tensile yield strength (490 MPa) and ductility (3.1%) in comparison to the fully lamellar microstructure. Additionally, the authors mention that fully lamellar microstructure is better suited for high temperature (> 650°C) strength, creep, rupture resistance and high-cycle fatigue life. Kim et al. [39] have underscored the fact that the tensile properties and fracture toughness depend on microstructures and concluded that:

1. The duplex microstructure yields best ductility and reasonable strength but results in the lowest fracture toughness as depicted in Figure 11 (graph E and graph F).
2. The near lamellar microstructure results in the highest strength with reasonable ductility as seen in Figure 11 (graph D).
3. The full lamellar microstructures result in low strength and poor ductility, but excellent fracture toughness as illustrated in Figure 11 (graph A, graph B and graph C).

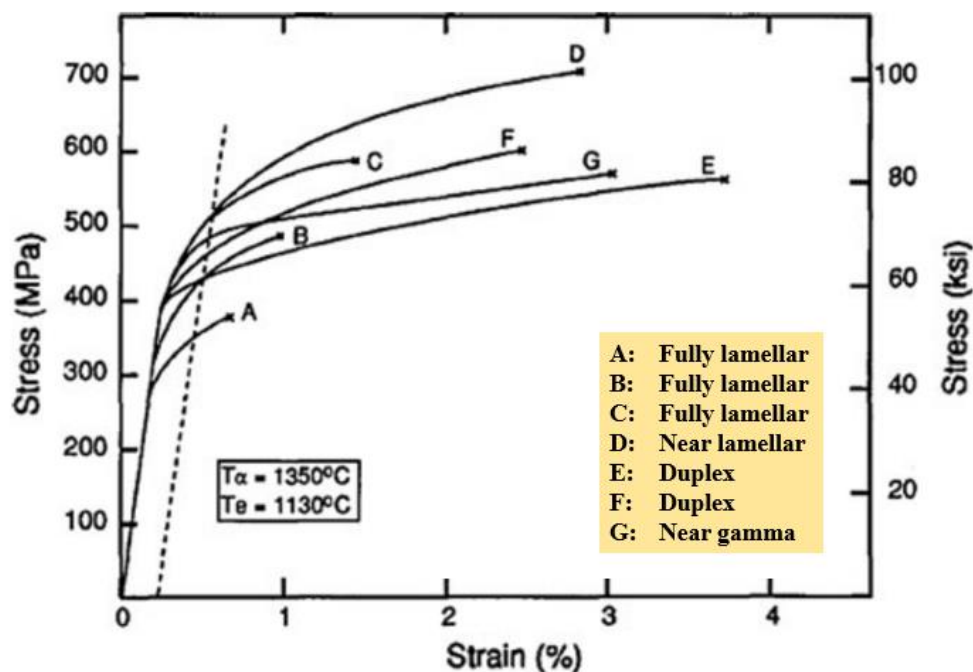


Figure 11 Tensile properties of microstructures of Ti-47Al-1Cr-1V-2.5Nb [39]

It is evident that there is a large scatter for the mechanical properties of fully lamellar and duplex in Figure 11. This scatter is because of the different cooling rates adopted to achieve the microstructures. The studies from Ramanujan et al. [38] and Gupta et al.

[30] corroborate the foregoing outcomes. A notable fact is that the state of the art indicates a lot of machining research of gamma – TiAl alloys has been carried out with fully lamellar and duplex microstructures. However, the near lamellar microstructure, with a good balance of mechanical properties has been rarely considered. The Table 4 presents the pros and cons of each microstructure of gamma – TiAl alloys.

Table 4 Microstructure of dual phase gamma titanium aluminides and their respective mechanical influences [32], [42]–[44]

Microstructure	Composition	Mechanical properties	
		Pros	Cons
Fully lamellar	Very large lamellar ($\alpha_2 + \gamma$) grains (in the order of 100 μm , sometimes mm in size)	Good fracture toughness and creep properties.	Poor tensile ductility
Duplex	Interspersed lamellar grains (alternating lathes of α_2 and γ) and equiaxed γ -TiAl grains, roughly equal in size.	High tensile strength and ductility	Poor fracture toughness and low creep strength
Near lamellar	Large volume fraction of lamellar ($\alpha_2+\gamma$) grains intermixed with some smaller grains of γ - TiAl.	Better fracture toughness and creep properties.	Average ductility
Near gamma	Relatively small α_2 -Ti ₃ Al grains which sandwiched between mostly equiaxed γ -TiAl grains.	Higher ductility at HT	Poor ductility at RT

There have been three generations of gamma – TiAl alloys designed hitherto. Bhibhanshu [45] mentions that all the iterations of the alloys are related to improving the fuel efficiency of jet engines by increasing the combustion temperature. As high combustion demands newer advanced material, new alloy chemistries are experimented with. Bewlay et al. [6] quote that the first formulations / first generation alloys were binary TiAl alloys with composition range of Ti-(42-48)Al suffered from low ductility and high temperature creep and oxidation problems. Therefore, the second generation alloys were developed with the formulation of Ti– (45–48) Al– (1–3) X– (2–5) Y– (<1) Z, where X = Cr, Mn, V; Y = Nb, Ta, W, Mo; Z = B, C, Si. Though the second-generation alloy had satisfactory room temperature ductility and displayed good fracture toughness values; they were found to have high room temperature strength as

mentioned by Appel et al. [46]. Takeyama et al. [47] have also noted that the elemental addition of V, Nb, Ta, Cr, Mo, W led to alteration of volume fraction and size of lamellar colonies. One of the prominent second-generation alloy compositions are the Ti-48Al-2Cr-2Nb alloy. With the improvement in the efficiency of the jet engine, newer compositions were formulated which were stable beyond the working temperature of second-generation alloys (beyond 700°C). This led to the development of third generation TiAl alloys rich in Nb and lean in Al. A comparison of all the three generations is given in Figure 12 as follows:

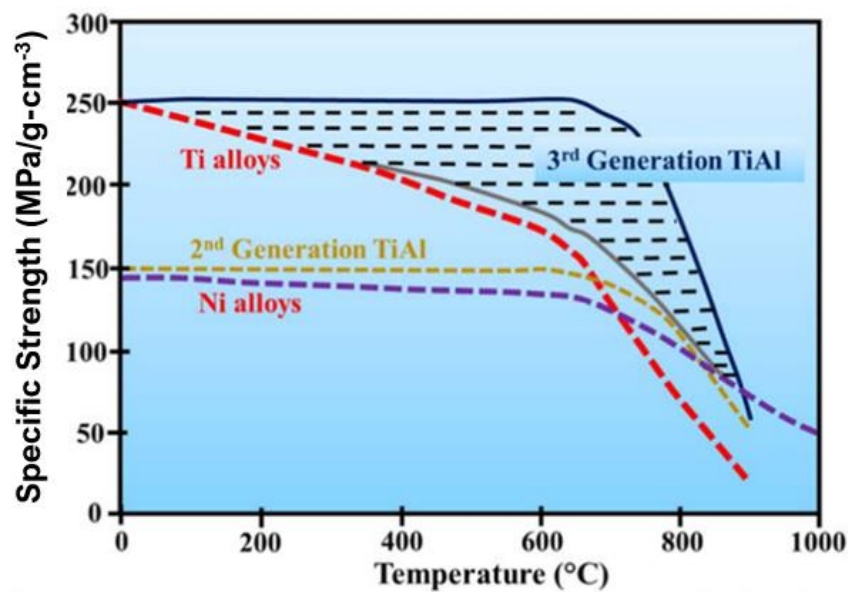


Figure 12 Better performance of 3rd generation TiAl vis-à-vis 2nd generation TiAl, titanium and nickel alloys [45]

The most prominent formulations of each generation are showed in Table 5. Bhibhanshu [45] quotes that the third generation alloys show improved tensile strength and improved hot workability than second-generation alloys. Tetsui et al. [48], [49] and Appel et al. [15] have reported on specific effect of each alloying element and which can be enlisted as follows:

- Al/Ni: Increases strength levels (Ni: β -stabilizing element; Al: α - stabilizing element)
- C, Si, N: Improves creep resistance and high temperature performance
- Nb, Ta, Mo, W: Improve oxidation resistance
- Cr, V, Mn, Si : Improve ductility but reduce oxidation resistance

Table 5 Different generation of gamma – TiAl alloys [50]

Composition in atomic %	Trade name	Year	Generation	Developer (Country)
Ti-48Al-IV-0.1C	-	1983	1	Pratt & Whitney (USA)
Ti-(46-50) Al-2Cr-2Nb	48-2-2	1989	2	General Electric (USA)
Ti-46.5Al-2Cr-3Nb-0.2W(+0.1C+0.2Si)	K5/K5SC	1994	2	US Air Force Lab. (USA)
Ti-45Al-(5-10) Nb-(0-0.4) C, B	TNB/ γ -Met	1995	3	Plansee (Austria)
Ti-(45-47) Al-2Nb 2Mn+0.8vol.%TiB ₂	45XD/47XD	1995	2	Howmet Corp. (USA)
Ti-47Al-2W-0.2Si	ABB-2	1996	-	Asea Brown Boveri (Switzerland-Sweden)
Ti-47Al-4Nb-4Zr-1B-0.2Si	-	1997	3	Rolls Royce plc (Britain)
Ti-35Al-1.5Cr-3Nb-0.7Mo-1Zr-0.2Si-0.1C (Wt. %)	VTI-3L	2001	3	VIAM (Russia)
Ti-42Al-5Mn	-	2002	3	Mitsubishi Heavy Industries (Japan)
Ti-43.7Al-3.2(Nb, Cr, Mo)-0.2B	TNB/TNM	2007	3	IPSM (Russia), GKSS (Germany)

Shih et al. [41] report that Ti-48Al-2Cr-2Nb composition displayed a balance of processability, ductility, oxidation resistance and strength. Importantly, the Ti-48Al-2Cr-2Nb alloy was the first gamma -TiAl alloy to be employed in an aeroengine (Bewlay et al. [51]). The Figure 13 shows the area of implementation of gamma – TiAl alloys as LPT blades.

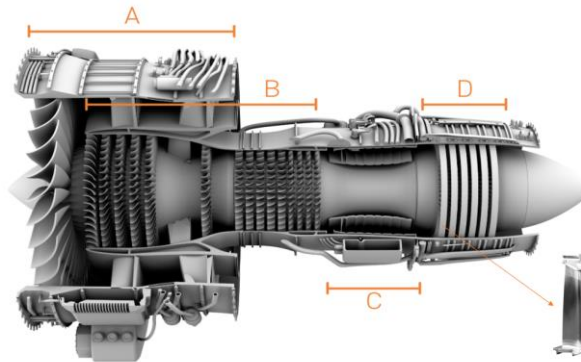


Figure 13 Cross sectional view of jet turbine engine and placement of LPT blade (A) fan section (B) compressor section (C) combustion section (D) low, intermediate and high-pressure section [52]

2.2 STATE OF THE ART: MACHINABILITY OF GAMMA TITANIUM ALUMINIDE ALLOYS

The selection of machining operation is dependent on dimensional requirements, type of geometry and the features required of the final components. The nature of the workpiece alloy, amount of the material removed, tool wear and time taken decide the costs of the operations. Hood et al. [34] have stipulated the assessment criteria for machinability as:

1. Tool life – The amount or rate of material removed by the tool, under standard conditions until the performance of the tool becomes unacceptable or the tool flank wear has reached a standard amount.
2. Cutting forces or power – Forces acting on the tool measured using dynamometer under specified conditions or the power consumption.
3. Surface finish, surface integrity and component accuracy – Surface finish produced under specified cutting conditions.
4. Chip shape – The chip shape as it influences the clearance of the chips from around the tool, under standardized conditions.

The materials exhibiting good machinability have long tool life, good surface finish and low cutting force and power requirements. Machining data are necessary to generate comprehensive machining solutions for materials and especially for the aerospace industry, which relies on intricate geometries and precision of components.

Studies published by Castellanos et al. [53], Priarone et al. [54] and Klocke et al. [8] state that the gamma – TiAl alloys are difficult to cut materials and are characterized by low tool life. The material properties of gamma – TiAl alloys like low thermal conductivity, strength retention at high temperatures, work hardening tendency and chemical affinity towards tool materials poses problems during machining.

Low thermal conductivity of the gamma – TiAl alloys is one of the reasons for accelerated tool wears. Priarone et al. [55] have worked with Ti-48Al-2Cr-2Nb alloy and quoted that while machining gamma – TiAl alloys, excessive generation of heat in cutting zone has controlling influence on tool wear rate. To reduce the heat, the authors while making a comparative study between dry, MQL and flood (water based) lubricants while turning propose to use flood as it has high heat extraction capacity in

comparison to other lubricants. This outcome underscores how the low thermal conductivity of gamma – TiAl alloy aids in quicker tool wear. Aspinwall et al. [56] in the work of measuring cutting temperatures when ball nose end milling of Ti–45Al–2Mn–2Nb + 0.8 vol% TiB₂XD and Ti–45Al–8Nb–0.2C gamma – TiAl alloys have supported the above mentioned observations by stating that low thermal conductivity of the alloy induces wear effects which adversely affect the workpiece integrity.

Klocke et al. [8] in their work of turning Ti–45Al–2Mn–2Nb + 0.8 vol% TiB₂XD gamma – TiAl alloy have explicitly remarked on the poor thermal conductivity of the alloy. The authors further mention that the hot hardness and resultant poor machinability of gamma – TiAl alloy is due to the high brittle – ductile transition temperature. Kolahdouz et al. [57] in support of the foregoing statement mention that the difficulty in machining of gamma – TiAl alloys is due to high strength and brittleness and low thermal conductivity among others.

The gamma – TiAl alloys are also known to pose problems during machining due to their tendency to work harden at room temperatures. Appel et al. [58] have observed that the work hardening is related to the brittleness of materials at ambient temperatures. The authors further mention that for most microstructures and compositions / generations of gamma – TiAl alloys the brittle micro-mechanisms of failure persists up to temperatures in excess of 700°C limiting the tensile ductility. Castellanos et al. [53] also support the above mentioned findings by stating the poor machinability of gamma – TiAl alloys is a result of the work hardening tendency of the alloys.

Settineri et al. [59] in their study of evaluation the machinability of three generations of gamma – TiAl alloys have identified that the reactivity of workpiece with the cutting tool material, low thermal conductivity, and work hardening effects to be detrimental to machining.

No publications with machinability of the first-generation gamma – TiAl alloys were found. Studies of machinability have been prominently focused on second and third generation gamma – TiAl alloys. Machining operations of turning, milling, grinding, drilling, and electro chemical machining have been carried out. The machinability with respect to each generation of gamma – TiAl alloys are described:

Most of the machining operations with second-generation gamma – TiAl alloys reported in literature involved milling and turning. Ge et al. [60] performed end milling assessment of second-generation Ti-48Al-2Mn-2Nb alloy using TiAlN coated carbide tools and showed that high cutting speed increases cutting forces and tool wear. Subsequently, while surface roughness showed to decrease with increased in cutting speed, the microhardness $HV_{0.1}$ decreased with the increasing depth from the machined surface.

Priarone et al. [61] investigated the influence of cutting parameters and cooling conditions on tool wear, surface finish and power consumption while milling of EBM built Ti-48Al-2Cr-2Nb alloy. The authors concluded that among wet, dry and MQL, the MQL is the best method to offer low tool wear though it consumed twice as much power as dry and flood cooling.

Kolahdouz et al. [57] subjected a second generation Ti-48Al-2Cr-2Nb-1B alloy to high speed end milling using TiAlN coated carbide tool. The authors concluded that MQL is a better lubrication option than dry conditions. The authors further quoted that MQL delivered better Machining Affected Zone (MAZ) properties (low residual stresses) and reduced power consumption.

Thus, from end milling, it was noticeable that among flood, dry and MQL, the MQL provided better tool life, better surface roughness and better sub-surface properties. However, there were contradictory results regarding the power consumption of the process.

In the case of turning some novel lubrication strategies were seen to be adopted in literature. Priarone et al. [62] conducted turning of Ti-48Al-2Cr-2Nb alloy using RCMT 1204 M0-SM S05F round inserts under nebulized cutting fluid (MQL with emulsion and water nebulized by compressed air) and concluded that emulsion mist gave better outcomes than pure water mist.

The drilling of second-generation gamma – TiAl alloys has been investigated in only few studies. A comparative study between low and high aspect ratio while drilling second generation Ti-48Al-2Cr-2Nb was carried out by Mathew et al. [63]. The authors evaluated machinability by assessing thrust force, torque, burr formation, surface

quality, tool condition and chip morphology and concluded that the dry environment was unsuitable for high aspect ratio drilling.

In another drilling study, Priarone et al. [64] worked on the drilling of EBM built Ti-48Al-2Cr-2Nb alloy and concluded that tool wear strongly affected the cylindricity and roundness error and proposed error minimization could be achieved by limiting cutting parameters or by replacing tools frequently at high cutting speeds.

Electro Discharge Machining (EDM) is one of the key non- traditional machining processes which is reported to be widely used in the aerospace industry due to high precision as reported by Gautier et al. [65]. The authors carried out Wire Electro Discharge Machining (WEDM) studies on Ti-48Al-2Cr-2Nb and studied the effect of process parameters like pulse on time, pulse off time, servo-reference voltage, and wire tension on surface roughness parameters. The authors concluded that combined optimization of roughness parameters is difficult owing to counteracting effect of input parameters.

The state of the art on machinability of second-generation alloys showed that though machining operations have been carried out, the focus was to assess the effect of machining parameters on tool wear and lubricants. The research works lacked the SI integrity post machining. In cases where SI was conducted (Kolahdouz et al. [57]), the machining parameters were found to be ($v_c = 300$ m/min and 600 m/min) out of the scope of machining. Additionally, the SI conducted was incomprehensive.

The machinability and SI assessment of third generation gamma – TiAl alloy is more widespread as compared to its predecessor. Mantle et al. [66] have worked on the ball nose end milling of Ti-45Al-2Mn-2Nb-0.8% TiB₂ (XDTM) and assessed the surface integrity of the alloy. The assessment of sub-surface microstructures showed the presence of cracks, pullouts, fracture, smear, and deformation of lamellae. This damage could be attributed to presence of borides.

Beranoagirre et al. [67] worked on the ball nose end milling of Ti-(44–45)Al-(5–10)Nb-(0,2-0,4) C TNB alloy with AlTiN coated tungsten carbide tools and compared the results with Ti-(43–46)Al-(1–2)Mo-(0 -2)Si-Cu (MoCuSi) formulation. The authors concluded that TNB was difficult to cut than the MoCuSi formulation. However, the

study only limited to the experimental sensitivity analysis of machining parameters and comparative analysis of the foregoing alloys. The SI of the alloys was absent.

Perez [68] has presented the wear mechanisms of coarse and fine WC grain inserts during face milling of Ti-45Al-2Mn-2Nb-0.8% TiB₂ (XDTM) alloy. Evaluating chip morphology and formation, cutting forces, tool wear and surface integrity, the author showed that insert geometries having large radius and sharp cutting edges proved to advantageous in machining gamma – TiAl alloys. However, the study presented only surface roughness and microhardness measurements. No assessment of sub-surface alterations or residual stress was done. Thus, no information was available regarding the changes occurring in the microstructure post machining.

Apart from milling, turning has been the most widely applied operation. Mantle et al. [69] worked on the turning of Ti-45Al-2Mn-2Nb-0.8% TiB₂ (XDTM) and conducted surface integrity analysis; wherein the authors highlighted the formation of hardened layer and mention that while using WC tools. The authors reported that was impossible to produce crack free surfaces with finish cutting parameters, indicating the detrimental effect of boride particles on SI of the alloy.

Similarly, Klocke et al. [8] conducted the finish turning of Ti-45Al-2Mn-2Nb-0.8% TiB₂ (XDTM) alloy under different lubrication like dry, flood, high pressure lubricant (wet), cryogenic cooling with liquid nitrogen and Minimum Quantity Lubrication (MQL). The authors concluded that cryogenic cooling had lower tool wear and limited surface and sub-surface defects.

Sharman et al. [70] conducted turning operations on Ti-45Al-2Mn-2Nb + 0.8% TiB₂ (XDTM) with uncoated WC (K10 ISO grade) indexable inserts under flood conditions. The authors identified the microstructure as near lamellar and from the SI analysis concluded that the sub-surface damage consisted of deformed lamellae, cracked TiB₂ particles and highly strained surface layer with cracks running into the workpiece body.

Ultrasonic assisted creep feed grinding of Ti-45Al-2Mn-2Nb-0.8% TiB₂ (XDTM) alloy using vitrified SiC and EP diamond wheels was reported by Bhaduri et al. [71]. The authors reported higher sub-surface defects in comparison to Creep feed grinding (CFG).

A CFG operation using a single layer electroplated diamond grinding wheel on Ti-45Al-2Mn-2Nb-0.8% TiB₂ (XDTM) was also reported by Hood et al. [72]. The authors reported G ratios of upto 100 with a grit size of D252. As observed in other machining operations, subsurface assessment showed cracks and fracture/pullout to a depth of 20 µm, while rough grinding. It is important to underscore those operations with Ti-45Al-2Mn-2Nb-0.8% TiB₂ (XDTM) alloy have resulted in sub-surface cracks. Researchers have attributed the cracks due to the presence of TiB₂ particles. Thus, the process windows provided by the researchers is not free of sub-surface cracks, regardless of the cutting parameters and lubrications.

Klocke et al. [73] compared the ECM of Ti-45Al-2Mn-2Nb-0.8% TiB₂ (XDTM), Ti-43.5Al-4Nb-1Mo-0.1B (TNM), Ti-48Al-2Cr-2Nb alloys. Assessing the material removal behaviour and rim zones, the authors concluded that the compared to traditional processes, the ECM did not lead to cracked lamellae structure.

Only a few studies were found where the alloy composition did not confirm to the formulations of convention gamma – TiAl alloys. Tetsui et al. [49] developed Ti-42Al-5Mn alloy from forging perspective and was subjected it to machining tests K10 cobalt matrix reinforced WC tools. The machinability was quoted to be superior to conventional/ established formulations of TiAl alloy though the machining was carried out speeds < 40 m/min. Beranoagirre et al. [74] in their work presented EDM of extruded MoCuSi and ingot MoCuSi gamma – TiAl alloys and concluded based on wear, surface hardness, roughness and SI analysis that extruded workpiece delivered better results than ingot counterparts.

One of the key studies published and relevant to the present work is by Settineri et al. [59], which compares the milling and turning performance of the two generations of gamma – TiAl alloys. The tool wear results for end milling are as presented in Figure 14. The results indicate that the end milling of second-generation Ti-48Al-2Cr-2Nb alloy yielded the highest tool life in comparison third-generation alloys of Ti-45Al-2Mn-2Nb-0.8% TiB₂ (XDTM), Ti-43.5Al-4Nb-1Mo-0.1B (TNM). As seen in previous studies, the of presence of TiB₂ ceramic particle in XDTM was highlighted to be the reason for high abrasive wear in third-generation alloy. Apart from the surface defects, the authors also found cracks or crack-like structures particularly for the alloys with boron additions.

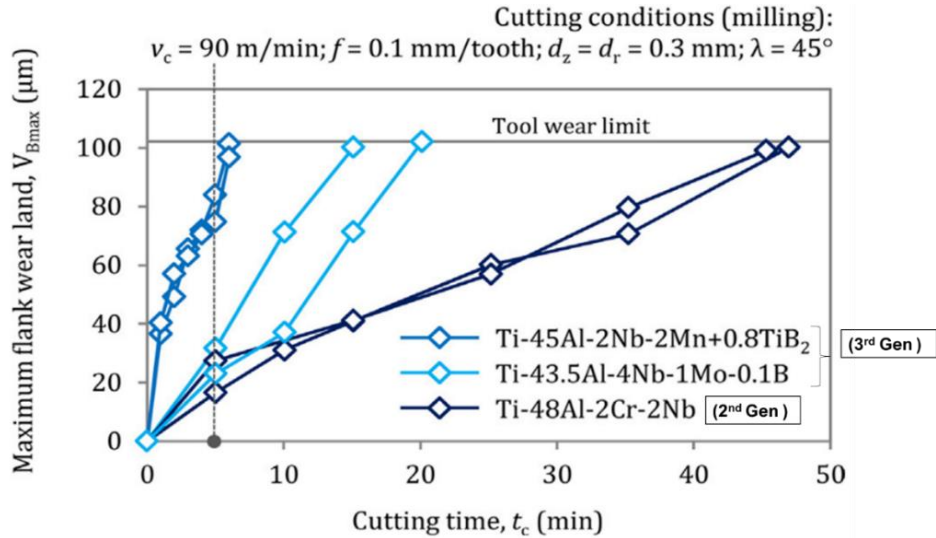


Figure 14 Tool wear and cutting time for different generations of γ -TiAl alloys as shown by [59]

From the machinability review of the second and third generations of gamma – TiAl alloys, it was found that assessments with milling and turning operations were more widespread than drilling and ECM operations. The SI profiles of both the generations was found to be different. Importantly, the third generation alloys Ti-45Al-2Nb-2Nb-0.8% TiB₂ (XDTM), Ti-43.5Al-4Nb-1Mo-0.1B (TNM) were found to be harder than second generation Ti-48Al-2Cr-2Nb alloy (Settineri [59]). Importantly, the sub-surface alterations indicated that the third-generation alloys were more prone to cracks, pits, fractures, and pullout due to the presence of boride particles.

The review also indicated a lack of comprehensive SI assessment for second-generation gamma – TiAl, particularly with the changes occurring in the sub-surface microstructure after machining. A list of machining parameters carried out with second and third generation gamma – TiAl alloys is presented in Table 6.

Table 6 Various machining operations reported for different generations of gamma – TiAl alloys

Machining operation		Generation of Gamma -TiAl alloy		
		2 nd Generation <ul style="list-style-type: none"> Ti-48Al-2Cr-2Nb Ti-48Al-2Mn-2Nb 	3 rd Generation <ul style="list-style-type: none"> Ti-45Al-2Mn-2Nb-0.8% TiB₂ (XDTM) Ti-43.5Al-4Nb-1Mo-0.1B (TNM) Ti-(44-45) Al-(5-10) Nb-(0.2-0.4) C (TNB) 	Other compositions <ul style="list-style-type: none"> Ti-(43-46) Al-(1-2) Mo-(0,2) Si-Cu (MoCuSi)
Milling	Ball nose end milling		Mantel et al. [66], Beranoagirre et al. [67], Aspinwall et al. [56]	Beranoagirre et al. [67]
	End milling	Ge et al. [60], Priarone et al. [75], Priarone et al. [61], Priarone et al. [55], Kolahdouz et al. [57], Settineri et al. [59]	Settineri et al. [59]	
	Face milling		Pérez [68]	
Turning		Mantle et al. [69], Settineri et al. [59], Priarone et al. [55], Priarone et al. [62], Finkeldei et al. [76]	Klocke et al. [8], Settineri et al. [59], Sharman et al. [70],	Tetsui et al. [49]
Creep feed grinding			Bhaduri et al. [71], Hood et al. [77]	
Drilling		Mathew et al. [78], Priarone et al. [64]		
EDM		Gautier et al. [65]		Beranoagirre et al. [74]
ECM		Klocke et al. [73]	Clifton et al. [79], Klocke et al. [73]	

Different cutting tool materials have been applied for machining of gamma – TiAl alloys. The literature review indicates the absence of dedicated tool concepts specifically for TiAl alloys.

The Tungsten Carbide – Cobalt (WC-Co) materials have been tried with a lot of coatings. The selection of grain size/binder content is also dependent on cutting conditions (roughing, finishing) and process (turning, milling, drilling).

M'Saoubi et al. [80] have stated that while using WC tools, particularly on the third - generation gamma – TiAl alloys, the sub-surface defects of fracture, cracks, pullouts etc. are very prominent owing to the presence of TiB₂ particles. However, the authors have not proposed ideal machining parameters for gamma – TiAl alloys.

Al-Ahmari et al. [81] have investigated end milling operation on Ti-47Al-2Nb-2Cr alloy to using WC end mills. The study investigated the optimal parameters for the minimal surface roughness (*Ra*) values. However, no tool wear patterns, or mechanisms have been provided.

The temperature in the cutting zone is also a critical parameter for the tool life as higher temperatures lead to accelerated tool wear. Aspinwall et al. [56] have reported temperatures of 450°C while using worn ball nose end mills for gamma – TiAl alloys. The authors state that thermal effects on surface integrity are minimum when machining at cutting speeds lower than 200 m/min.

Beranoagirre et al. [67] in their work conducted the milling of Ti-(44–45) Al-(5–10) Nb-(0,2-0,4) C TNB alloy and Ti-(43–46) Al-(1–2) Mo-(0,2) Si-Cu (MoCuSi, extruded and cast) alloy with 16 mm WC-Co end mills with AlTiN coating. While the authors have not described the tool wear mechanism and deliberated on type of tool failures, they have proposed that foregoing tool coatings are best suited for machining gamma – TiAl alloys with best tool life observed between 50 and 70 m/min with feed per tooth between 0.05 and 0.06 mm and axial and radial depths of cuts of 1 mm each.

There have been studies with very high cutting speed of up to 600 m/min. Kolahdouz et al. [57] conducted high-speed milling of EBM built Ti-48Al-2Cr-2Nb-1B alloy with cutting speeds between 300 and 600 m/min and a high radial depth of cut of 5 mm using TiAlN nanocoated WC end mill. They observed that the surface roughness values

decreased with increase in cutting speed. For the same cutting speed, the increase in axial depth of cut yielded higher R_a values.

The study by Pérez et al. [68] presents a new experimental investigation of the wear mechanisms of coarse and fine WC grain inserts during face milling of the 3rd generation gamma – TiAl alloy, Ti-47Al-2Nb-2Mn (at.%) + 0.8 vol% TiB₂ (XDTM). The authors observed that the inserts with fine grain WC grain size (< 1 µm) and 10 % Co content wore down at a lower rate than those with coarse (1-2 µm) WC grain size.

Ge et al. [60] have worked on the milling of Ti-48Al-2Mn-2Nb gamma – TiAl alloys with TiAlN coated WC end mills with cutting speeds in the range of 60-240 m/min. The authors mention that milling forces increased slowly with increasing cutting speed upto 240 m/min (R_a 0.176 µm vis-à-vis 0.245 at 60 m/min), but that the degree of rise was higher with the increase in flank wear value. The authors mention that with the increase in cutting speed, the surface integrity can be improved but it leads to the increase in milling forces and decrease of tool life.

From the survey, it could be concluded that for finishing operations of gamma – TiAl alloys, a cutting speed between 50 to 70 m/min appeared to be optimum to obtain an acceptable tool life and surface roughness. The suitable depth of cut appears to be between 0.5 to 1 mm (axial and radial) and the feed per tooth values between 0.05 to 0.12. A brief survey of cutting data collected from literature review is as shown in Table 7.

Table 7 Machining parameters for milling of gamma -TiAl alloys

Reference	Cutting data					
	Cutting speed (v_c) m/min	Feed per tooth (f_z) mm/tooth	Radial depth of cut (a_e) mm	Axial depth of cut (a_p) mm	Operation	Roughing /Finishing
Aspinwall et al. [56]	50, 70, 120, 135, 240, 345	0.12	0.2, 0.5	0.2, 0.5	High speed ball nose end milling	Finishing
Beranoagirre et al. [82]	50, 60	0.04, 0.05, 0.06	1	1	End Milling	Finishing
Beranoagirre et al. [67]	50, 60, 70	0.04, 0.05, 0.06	1	1	End Milling	Finishing
Ge et al. [60]	60, 120, 240	0.08	0.5	5	High speed ball nose end milling	Finishing
Hood et al. [13]	160, 250, 340	0.06	0.25	0.25	High speed ball nose end milling	Finishing
Hood et al. [83]	55, 88, 160	0.05, 0.1	0.2	0.025-1	High speed ball nose end milling	Finishing
Kolahdouz et al. [57]	300, 600	0.005	5	0.10, 0.20	High speed ball nose end milling	Finishing
Mantle et al. [66]	70, 120	0.06, 0.12	0.2, 0.5	0.2, 0.5	High speed ball nose end milling	Finishing
Priarone et al. [61]	35, 50, 71	0.06, 0.08, 0.1	0.3	0.3	End Milling	Finishing
Priarone et al. [75]	50	0.1	0.3	0.3	End Milling	Finishing
Priarone et al. [55]	25, 50, 100	0.08	0.3	0.3	End Milling	Finishing
Perez et al. [68]	20, 50, 80, 100, 300, 400	0.1, 0.5	30	1	Face Milling	Finishing

This sub-section mentions the output parameters of tool wear and surface integrity and displays the outcomes from the relevant studies. Different tool wear types are defined from the standard ISO – 8688 – 2 and the respective studies encountering specific wear type are mentioned accordingly.

The tool wear refers to loss of material caused by tribological phenomena. As such tool wear is one of the most complex aspects of machining operation and it depends on chemical, mechanical properties of tool and workpiece, tool geometry, cutting fluids properties and subsequently the machining operating parameters. The degree of the tool wear is dependent on the relative degree of the machining components. Kalpajian et al. [82] in their work state that there is difficulty encountered in analytic study of tool wear and therefore, the tool wear patterns are derived empirically. These tool wears are driven by inherent mechanisms of abrasion, adhesion, diffusion fatigue and plastic deformation respectively, which are explained in reference material of Sandvik Coromant [83].

The standard (ISO-8688-2) [84] as depicted in Figure 15 stipulates six main forms of tool wears.

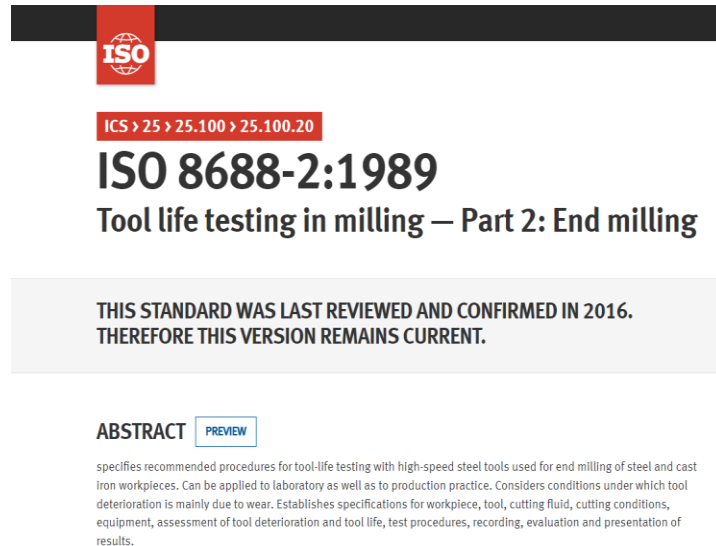


Figure 15 Standard referred for tool wear analysis

Flank wear is defined by Ng et al. [85] as the loss of tool material from the tool side or flank leading to the development of a land. The flank wear according to the standard (ISO-8688-2) [84] is further classified into uniform (VB1), non-uniform (VB2) and localized flank wear (VB3). Flank wear is the most reported wear in the literature for gamma – TiAl alloys. Hood et al. [13] have reported a progression of uniform VB1 to

non-uniform flank wear VB2 during milling of Ti-45Al-8Nb-0.2C and Ti-45Al-2Mn-2Nb-0.8% TiB₂ (XDTM) with AlTiN WC-Co tools. Authors quote that adhesion to be the main mechanisms.

Chipping wear is defined as the deterioration of the cutting edge in a sudden manner in accordance with ISO-8688-2 [84]. Hood et al. [34] in their work mention that chipping mainly occurs in the region of a pre-existing crack or defect and mechanical or thermal shocks are the main initiating factors. Chipping in machining of gamma – TiAl alloys is not as widespread as flank wear though it has been reported by Priarone et al. [58], Settineri et al. [62], Pérez et al. [73], and Priarone et al. [100].

It is important to note that literature review indicated chipping wear to be more prominent than other wears while machining third generation Ti-45Al-2Nb-2Mn (at %) + 0.8 vol % TiB₂ XD in comparison to third-generation gamma – TiAl, due to the boride particles which are relatively hard to machine. Nevertheless, chipping, and micro-chipping have been observed by Settineri et al. [59] while milling and turning the second generation Ti-48Al-2Cr-2Nb gamma – TiAl alloys which has relatively better machinability than other compositions.

The standard ISO-8688-2 [84] states that the gradual loss of the tool material from the tool rake face during cutting constitutes face wear. Abrasion and diffusion are the driving mechanism for this wear type. A crater could be caused by a hard particle being dislodged from the workpiece and make a grinding action against the tool or a diffusive mechanism between hot chip and tool material may also lead to the formation of the crater. The presence of the wear may potentially weaken the cutting edge causing it to fail catastrophically. The solution suggested by in reference material of Sandvik Coromant [83] is that tool hardness, hot hardness and minimum chemical affinity between materials minimizes the tendency for crater wear. The crater wear has not been reported exclusively for the machining of gamma – TiAl alloys as it difficult to discern the type of wear at high cutting speeds and high feed rates. This statement is supported by Hood et al. [34].

Cracks are normally resulted by exposure to thermal and mechanical loading in an interrupted manner where the respective loads are not large enough to cause fracture, like that in interrupted cutting processes like milling. Hood et al. [34] mention that the

occurrence of the cracks is perpendicular to cutting edge. Cracks have not been widely reported in machining of gamma – TiAl alloys as the carbide tools have better fatigue resistant properties. Priarone et al. [87] have reported the occurrence of micro-cracks with uncoated ISO K30/K40 end mills. The authors reported that corner wear was very prominent in the tools and that chipping of cutting-edge tip was observed along with micro-cracks revealed after Scanning Electron Microscopic (SEM) observation

Flaking is denoted by the loss of tool fragments in the form of flakes. This type of tool wear was not most widely observed in the literature review.

The ISO-8688-2 [98] and Ng et al. [99] state catastrophic failure as the rapid deterioration or complete failure of the cutting part of the tool. This marks the usefulness of the tool and is the end of path for the preceding tool wears. This type of tool wear is harmful and could lead to the undesired surface integrity characteristics of the component. As gamma – TiAl alloys are difficult to machine alloy, catastrophic failure have been observed and reported by Priarone et al. [64] for drilling operations. Zhang et al. [88] and Hood et al. [34] in their work have reported that catastrophic failure was observed particularly when the tests reached the end of test time of 90 min. The Figure 16 depicts the schematic of all tool wear types. The literature mostly indicated flank wear to be the most common wear type for gamma – TiAl alloys with adhesion being the dominant wear mechanism. The Table 8 presents the tool wear types and wear mechanism observed in the literature.



Figure 16 Tool wear types [84]

Table 8 Tool wear and subsequent mechanisms observed during machining of gamma – TiAl alloys

Reference	Material/Alloy	Operation	Tool wear					
			Tool wear limit (V_b) mm	Wear types			Wear mechanisms	
				Flank wear	Chipping wear	Corner wear	Adhesion	Other
Hood et al. [34]	Ti-45Al-8Nb-0.2C	End milling	0.2 mm	✓			✓	Failure of tool
Beranoagirre et al. [91]	Ti-(44-45) Al-(5-10) Nb-(0.2-0.4) C	Drilling	0.3 mm	✓			✓	
Hood et al. [13]	1. Ti-45Al-8Nb-0.2C (at. %) 2. Ti-45Al-2Nb-2Mn (at %) + 0.8 vol % TiB ₂ XD	End milling	0.3 mm	✓			✓	Face wear
Peréz et al. [68]	Ti-47Al-2Nb-2Mn (at %) + 0.8 vol % TiB ₂	Face milling	0.3 mm	✓	✓		✓	
Settineri et al. [59]	1. Ti-48Al-2Cr-2Nb 2. Ti-43.5Al-4Nb-1Mo-0.1B 3. Ti-45Al-2Nb-2Mn (at %) + 0.8 vol % TiB ₂ XD	Turning and milling	0.1 mm	✓	✓		✓	Abrasion wear
Priarone et al. [61]	Ti-48Al-2Cr-2Nb	Milling	0.1 mm	✓	✓	✓		Not mentioned
Priarone et al. [89]	Ti-48Al-2Cr-2Nb	Milling	0.1 mm	✓	✓	✓		Not mentioned
Priarone et al. [64]	Ti-48Al-2Cr-2Nb	Drilling	0.1 mm	✓	✓	✓		Not mentioned
Priarone et al. [55]	Ti-48Al-2Cr-2Nb	Milling and turning	0.1 mm	✓	✓	✓		Not mentioned

Field et al. [89] have defined workpiece surface integrity as “*The inherent or enhanced condition produced in a machining or surface generation operation*”. Liang et al. [90] have categorized the workpiece surface integrity into three broad components of *Surface topography*, *Microstructural alterations*, and *Mechanical properties*. The surface topography deals with the analysis of surface defects and surface roughness properties. The second component deals with the changes taking place in the microstructural aspects like plastic deformation, analysis of grain size and texture and occurrence of a white layer. The final component assesses the change in the mechanical properties before and after the process of machining by checking microhardness and residual stresses of the workpiece in study. The components are enlisted in Figure 17.

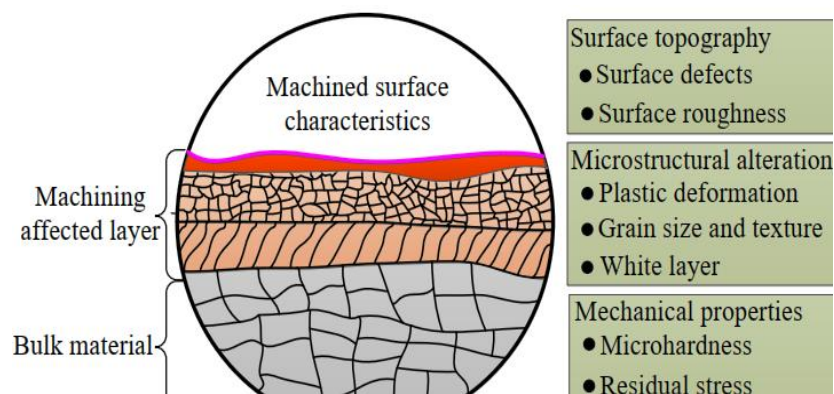


Figure 17 Schematic representation of surface integrity characteristics [91]

In most of the cases the surface texture and surface topography analysis, for detecting surface defects like macrocracks, microcracks, tears, lap and pits etc., is conducted by visually inspecting the workpiece material as stated by Kahles [92]. However, since these are not the most reliable methods, non-destructive methods like ultrasonic optical scanning, binocular inspection, magnetic particle testing, dye-penetrant test and eddy current tests have been commonly used. If the machined component can be subjected to destructive testing, then Optical Microscopy (OM) or SEM is the most reliable check for surface defects.

The ISO 4287: 1998 manual categorizes the roughness measurement into 7 parameters as follows:

- *Ra*: The arithmetic mean roughness value.
- *Rmr (c)*: Material component of the profile.
- *RSm*: Mean peak width of the profile.

- R_t : The total height of the roughness profile.
- Rz_i : Greatest height of the roughness profile.
- $Rz1Max$: Maximum roughness depth.
- Rz : Mean roughness depth.

A more comprehensive explanation of the roughness parameters can be found in Mitutoyo surface roughness manual [93]. The guide mentions that mean roughness depth Rz is the preferred parameter for the study of surface as it is more holistic indicator of the surface quality in comparison to the other parameters enlisted above. The illustrations of the roughness parameters are provided in Figure 18.

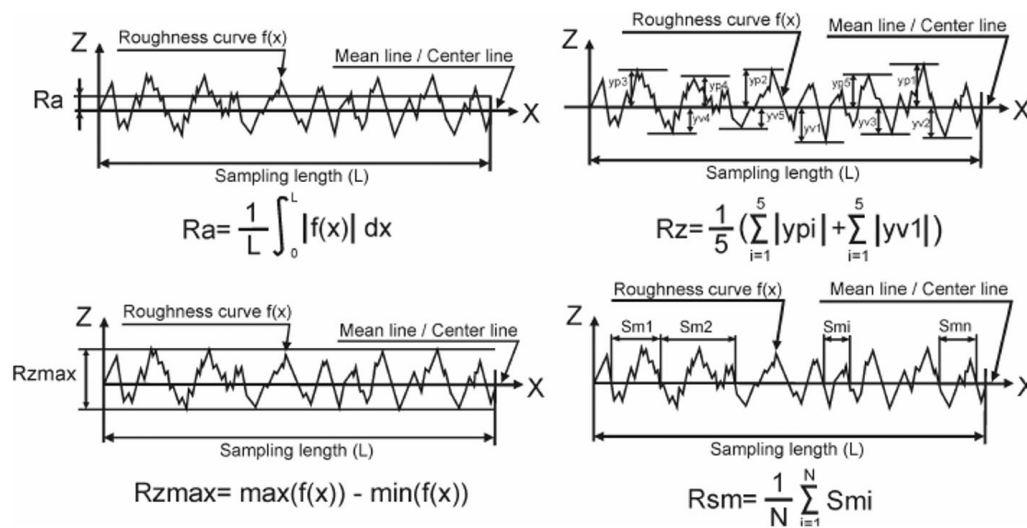


Figure 18 An illustration of important roughness parameters [94]

The sub-surface damage has been assessed in almost all the studies which have been reviewed for this study. Klocke et al. [10] have recorded the deformation of lamellae for third generation Ti-45Al-8Nb-0.2C-B (TNB-V3) alloy indicating high strains during turning exercises. This could be seen in Figure 19. It is important to remark the deformation of lamellae is dependent on the microstructure and phase composition of the alloy.

It is important to state that the surface integrity is a function of machining conditions under dry and metal working fluids. Priarone et al. [62] while turning Ti-48Al-2Cr-2Nb alloy with RCMT 1204 M0-SM S05F inserts have conducted the 3D surface roughness analysis under dry, emulsion and Minimum Quantity Lubrication (MQL) conditions.

The authors found that the 3D surface roughness parameter S_a and S_z indices for MQL were better than machining in dry and under flood cooling using emulsions.

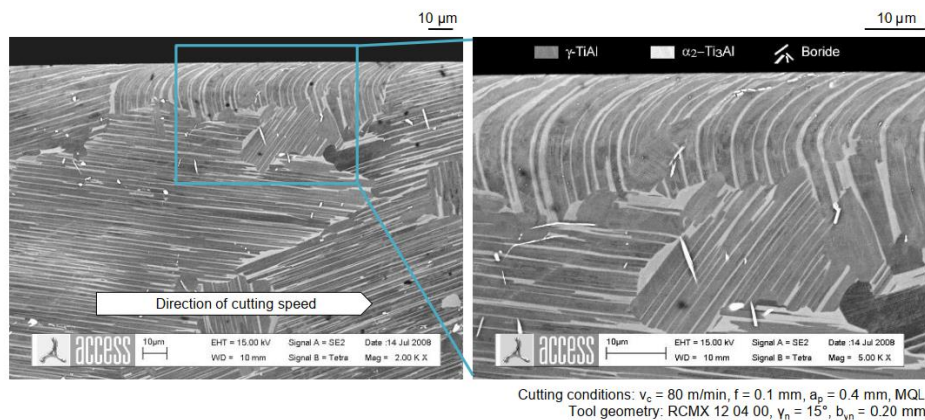


Figure 19 Deformation of lamellae during turning of 3rd generation the Ti-45Al-8Nb-0.2C-B (TNB-V3) gamma-TiAl alloys [10]

Settineri et al. [59] in their work have reported smearing, tears, and surface cracking during turning and that ‘crack-like’ structures were particularly found for gamma – TiAl alloys with boride composition while no cracks were reported for milling exercises. The Table 9 reports the different components of surface integrity reported in literature.

From the review of SI analyses of gamma – TiAl alloys, it could be concluded that less information exists on the profiles of second-generation alloys. Importantly, comparative SI studies of different microstructures of gamma – TiAl was not found. With the change in the microstructural composition, the deformation of sub-surface grains is likely to differ in different microstructures of gamma – TiAl alloys. However, this could not be conclusively established from the review.

Table 9 presents the defects observed during SI analyses of second and third generation gamma – TiAl alloys. It could be seen that most of the analyses focus on surface defects and only article has reported the sub-surface microstructural changes during milling and turning operations.

Table 9 A summary of Surface Integrity analyses of second and third generation gamma titanium aluminide alloys observed during turning and milling operations

Surface integrity defects during machining	Machining	Material	Causes attributed to defects	Reference
Lamellae deformation and cracks (length not measured)	Turning	Ti-45Al-2Mn-2Nb + 0.8 % vol. TiB ₂ (XD)	Strain at high temperatures during machining. Cracks are attributed to presence of borides	Klocke et al. [10]
Lamellae deformation in the direction of cutting and cracks (length not measured)	Turning	Ti-45Al-2Mn-2Nb + 0.8 % vol. TiB ₂ (XD)	High temperatures, strains, and strain rates.	Sharman et al. [70]
Fracture/ pull-out on the surface of the workpiece surface and decrease in yield strength, deformation of lamellae (length not measured)	Milling	Ti-45Al-8Nb-0.2C (TNB) & Ti-45Al-2Mn-2Nb + 0.8 % vol. TiB ₂ (XD)	Low plastic deformation / brittle nature at room temperature. Decrease in yield strength attributed to tensile residual stresses.	Hood et al. [34]
Surface crack	Milling	Ti-(43-46) Al-(1-2) Mo-(0.2) Si-Cu	Excessive cutting speed and brittleness of TiAl alloys	Beranoagirre et al. [67]
Surface cracks leading failure by crack propagation.	Milling	Ti-45Al-2Mn-2Nb + 0.8 % vol. TiB ₂ (XD)	Low ductility of work piece	Mantle et al. [99]
Fracture/ pullout, plastic deformation (< 10 – 20 μm below machine surface) Increase in subsurface hardness (upto 300 μm)	Milling	Ti-45Al-2Mn-2Nb + 0.8 % vol. TiB ₂ (XD)	Strain hardening and poor ductility at surface.	Mantle et al. [66]

The Metal Working Fluids (MWFs) have been classified based on different criteria like formulation (oil-based, water-based), manufacturing process (cutting fluid, grinding oil, cutting oil etc.) or quantity (flood, MQL) as stated by Brinksmeier et al. [96]. Armarego [97] states that MWF aids in the manufacturing of a component by increasing tool life, improving the surface finish, reducing the cutting forces and power consumption, reducing distortion due to temperature rise in the workpiece and facilitating the removal of chips. The prominent strategies to deliver the MWFs are flood, Minimum quantity lubrication (MQL) / Minimum quantity cooling (MQC), cryogenic cooling, simultaneous use of MQL and cryogenic cooling and, solid lubrication. From the literature, it could be gathered that with respect to gamma – TiAl alloys, dry machining has given bad results in terms of high tool wear and low tool life. This is due the low thermal conductivity of alloys and the inability of dissipation of heat during dry machining. Although few studies exist, there are publications detailing the comparison of different MWF strategies.

Priarone et al. [61] have made a comparative study of milling of gamma – TiAl alloys in dry, flood, and MQL lubrication and stated that MQL process had some of the benefits in terms of surface quality and tool life but the process is expensive with regard to power consumption. The authors quote that MQL delivered the best surface roughness and delivered a tool life 6 times that of dry machining and 24 times that of flood lubrication. The results of the comparison could be seen in Figure 20.

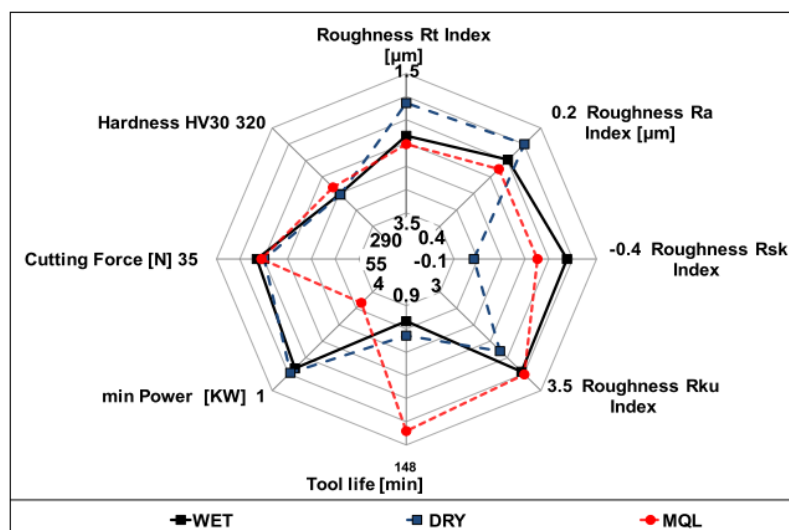


Figure 20 Comparison of machining output parameters for lubrication of wet, dry, and MQL by [61]

In yet another study conducted by Priarone et al. [87] (Figure 21), the milling performance of ISO K30/K40 end mills was assessed on gamma – TiAl alloys in flood, dry and MQL process conditions. The results showed the MQL delivered better tool life than flood and dry conditions.

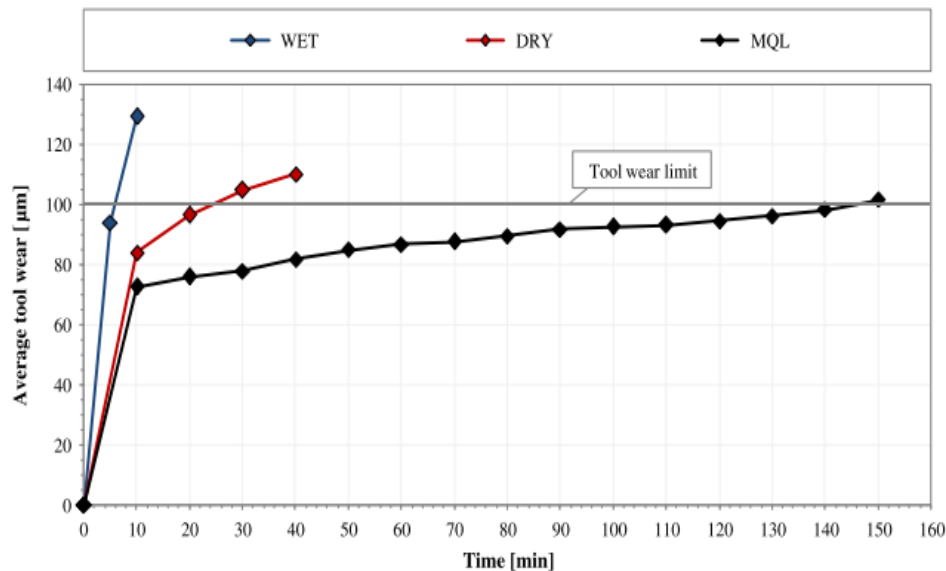


Figure 21 Tool wear curves observed at 50 m/min and $f = 0.08$ mm/tooth by [87]

Klocke et al. [10] have experimented with dry, flood, MQL and cryogenic machining of a third-generation gamma – TiAl alloy. The authors opine those high temperatures in shear zone leads to transitioning of alloys from brittle to ductile zone. However, the high temperatures are particularly disadvantageous for the tool as they exert thermal load on cutting edges and lead to accelerated tool wear. The authors reported that dry and MQL showed poor tool life particularly at higher cutting speed (80 -100 m/min) while cryogenic cooling using liquid nitrogen (boiling point of -196°C) yielded better surface roughness, lower force components and less tool wear vis-à-vis dry and MQL strategies.

The review of metal working fluid indicated that the dry cutting is particularly detrimental when working at high cutting speeds (>70 m/min). The heavy thermal load on cutting edges leads to accelerated tool wear. The flood cooling provided poor results while MQL delivered best tool life with pressured of 5.5 – 6 bars.

2.3 STATE OF THE ART: TRIBOLOGY IN METAL CUTTING

Tribology is defined by “*The science and technology of interactive surfaces moving in relation to each other*”. It is important to understand why tribology in metal is cutting an important aspect. Astakhov et al. [98] state that in metal cutting around 30 – 50% of the energy required by the cutting system is spent for the useful work and the rest of energy around 25 – 60% is simply wasted. The authors further state that a great part of the wasted energy is spent in tool - chip and tool – workpiece interfaces due to non-optimized tribological processes. From the foregoing statement one can understand that by proper selection of application – specific tool material (coating), an assured performance criterion of tool life, quality of machined surface, efficiency etc. could be obtained. In addition to it Trent et al. [99] state in their work that though components of cutting tool tribology have been studied from the early part of the 20th century, there lacked a systematic approach to study all the components in relation to each other for example, tool wear has been widely studied but the corresponding components like process efficiency were unconsidered as reported by Astakhov et al. [98].

Grzesik [100] mentions that tribological characterisation during metal cutting involves the assessment of three characteristics: friction, wear, and type of lubrication. Shaw [101] defines friction as “*The resisting force that a surface experiences when it slides over another and it always oppositely directed to the relative velocity vector for the two surfaces*”. Suh et al. [102] in their work have detailed the genesis of friction into three components or mechanisms namely: Asperity deformation component μ_d , Ploughing force component μ_p and Adhesion component μ_a respectively. The relative contribution of each component to the friction coefficient depends on condition of sliding interface, material properties, surface topography and the environment. These mechanism are supported by Grzesik [100] and represented in Figure 22 (A, B and C).

Trent [118], Grzesik [119] and Suh et al. [121] state the occurrences of each mechanism as follows:

1. Adhesive: The adhesive component involves the shearing junctions formed by contacted surface asperities at high pressure and temperatures. Intensive adhesion occurs when two asperities in contact weld together and due to the

tangential motion, the micro-welded junction breaks but its shear strength causes a resistance to motion.

2. Asperity deformation: The plastic deformation of asperities, causing material flow when a body slides over another, which is responsible for the static coefficient of friction.
3. Ploughing action: Holmberg et al. [103] state that the rounded cutting edges initiate a ploughing action when very small material layers are removed from the workpiece material. The ploughing effect is initiated when hard asperity or hard particle penetrates a softer material and forms a groove by plastic flow.

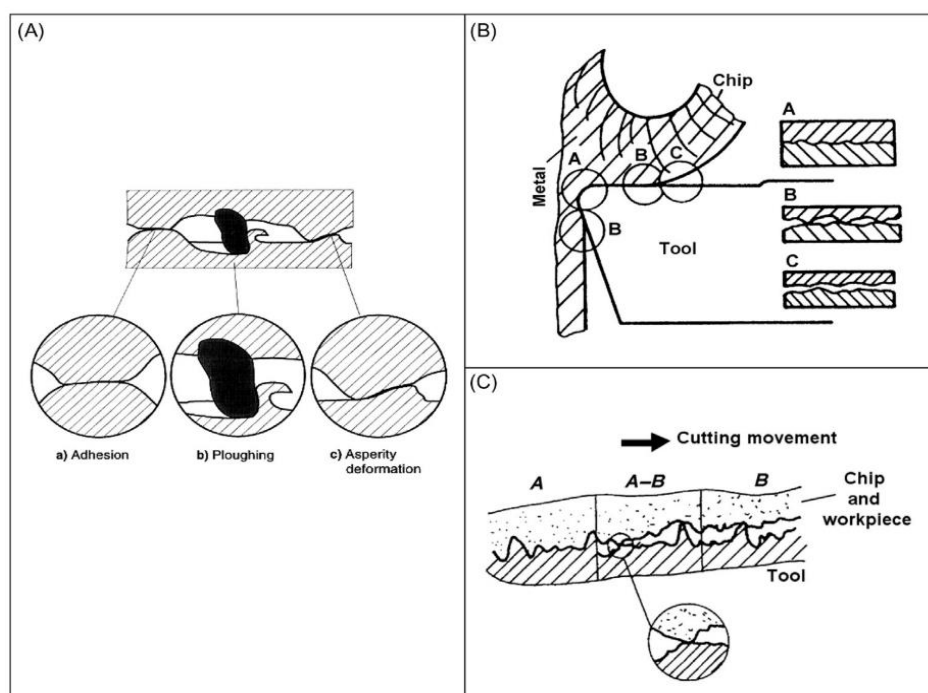


Figure 22 (A) Three basic components in sliding friction (B) corresponding cutting zone (c) three zone model[100]

Of the three components, the authors have postulated that the adhesion of the workpiece asperities on to the sliders are the main reason for the rise in friction coefficient. The wear particles entrapped between the sliding surfaces further lead to a steep rise in the value of friction coefficient as the sliding continues. The Figure 23 explains the possible ways in which material transfer takes place between two solids. This makes quantification of adhesion and wear to be an integral part of friction determination exercises. Adhesion could be defined as the accumulation or smearing of

workpiece particles on the tool surface, providing information of the interaction of tool coatings and workpiece.

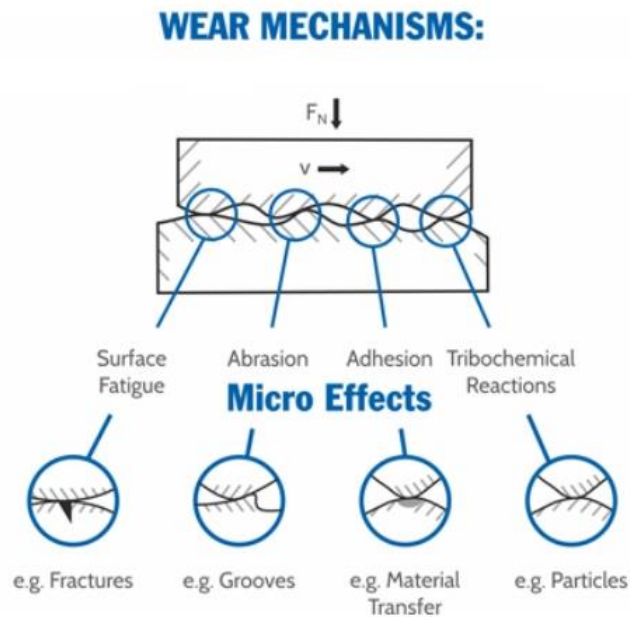


Figure 23 Possible superposition of wear mechanisms on the surface of a material [104]

Melkote et al. [105] in their work state that the dominant mechanism of sliding friction tends to be the adhesive interaction between surface asperities, especially for non-viscoelastic materials. The relative contribution of ploughing action of hard asperities and the tool wear chunks /particles to the friction is dependent on the tribological contact conditions. The low friction coating and the presence of lubricants is known to drastically reduce friction.

A lot of qualitative work has gone in modelling the evolution of friction and variance of its nature between tool-workpiece and tool-chip contact. In 1945, Merchant [106] identified that relationship between cutting forces and thrust forces on friction coefficient. Albrecht [107] proposed a revised model which accommodated for the ploughing force due to the action of cutting edge. However, the variation of friction and stresses along the rake face due to the change in contact conditions (sliding velocity, contact pressure and temperature) were out of the purview of the force measurements. Subsequently, split – tool approaches were proposed where the tool is divided into sections along the rake face (varying the distance from the cutting edge) and measuring the sections along each section of tool using two dynamometers. This approach has

been highlighted by Childs [108]. There exist some drawbacks like complexity in manufacturing tools, impracticality to use coated tools etc. to this approach.

The work from Ortiz-de-Zarate et al. [109] has improved this approach by the use of partially restricted contact length tools allowing for more robust and simpler way to map normal and shear stress distributions.

Hedenqvist and Olsson [110] proposed sliding tests to characterize tribological phenomena using tribometers. The tribometers were improved subsequently by Zemzemi et al. [111]. Puls et al. [112] have proposed new methodologies for characterizing friction. The first school of thought goes by the theory expressed by Zorev [113] who described the contact stress distribution as shown in the Figure 24.

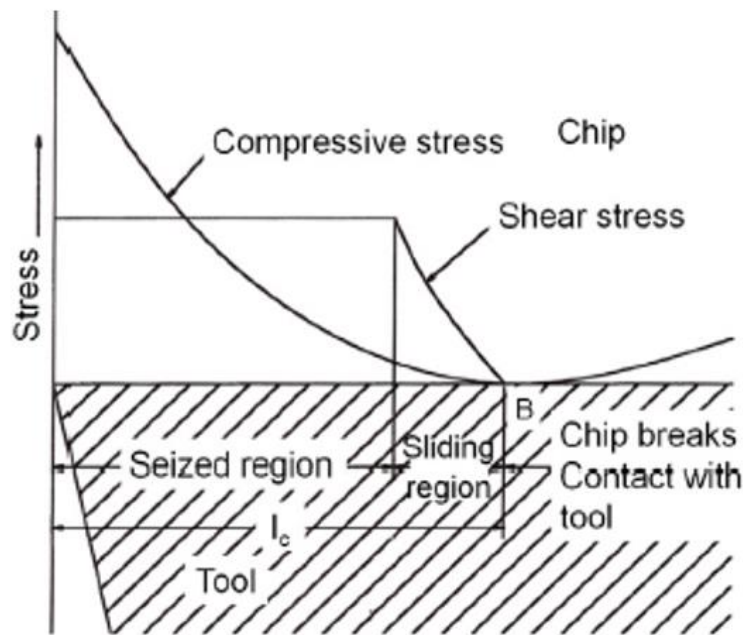


Figure 24 Stress distribution on the tool as proposed by [114]

Zorev [114] states that the highest stress is encountered by the tool tip and that the stress wanes gradually till the point where the chip breaks contact with the tool (Point B in Figure. 24). However, the shear stresses are held constant from the tool tip which then start waning from the sliding region. The model divides the tool contact area in to sticking zone (seizure or plastic zone) near the tool edge and sliding (elastic contact) beyond the sticking region. Melkote et al. [105] state the distribution of normal stress as shown in Equation 1 as:

$$\sigma_c = \sigma_{cmax} \left(\frac{x}{l_c} \right)^n \quad (1)$$

Where l_c is the tool-chip contact length, x is the distance from the chip separation point, and n is the exponent parameter. The stress distribution (σ_c) in the sliding zone satisfies the Coulomb's friction law as stated in Equation 2:

$$\tau_c = \mu \sigma_c \quad (2)$$

Where, the τ_c is the shear stress, and μ is the friction coefficient. Assuming constant shear friction along the entire tool-chip interface, the shear stress could be determined using shear friction factor m as shown in Equation 3 as:

$$\tau = mk \quad (3)$$

Where k is the shear flow strength of the material at the tool-chip interface. On the similar lines, Shirakashi et al. [115] derived the Equation 4:

$$\tau_f = k \left(1 - e^{-\frac{\mu \sigma_n}{k}} \right) \quad (4)$$

Where, τ_f and σ_n are the friction and normal stresses. Childs [108] has worked to model the variation of friction between chip and tool during continuous chip formation in turning at low, intermediate, and high speeds. The authors argue that there are limitations to the law proposed by Shirakashi et al. [115]. The author mentions as early experiments investigated the chip – tool friction and chip formation through observed values of λ (friction angle), Φ (shear plane angle), and the α (rake angle of the tool). The author further states that there are no unique relationships between Φ , λ and rather for a measured value of λ a range of (Φ - α) values be allowable depending on the value of α .

Subsequently, Childs [108] states that friction modelling assuming Coulomb's law being applicable to entire tool-chip contact area is inconsistent and that model proposed in equation 4 assumes fully plastic conditions when the degree of contact between A_r/A_p (A_r is the real contact area and A_p is the apparent contact area) to be close to 1. In such condition, the author mentions that friction stress is not expected to be proportional to normal stress.

Arrazola et al. [116] have characterized the Coulomb's friction coefficient at the tool – chip interface and compared the results with Finite Elemental Modelling (FEM). The authors contend that friction varies along the tool – chip interface and emphasize why the application of a variable friction coefficient brings good correlation between numerical and experimental studies.

Zhang et al. [117] in their work have presented a new friction model at the tool-chip interface in dry orthogonal cutting and state that along with the consideration of sliding zone and sticking zone, the model also considers the thickness of the stagnation layer and shear flow layer at sticking region and transition region respectively.

Rech et al. [118] have quoted that in most of the cases the Coulomb model with constant friction coefficient, irrespective of temperature and pressure is usually adopted to simulate friction phenomena at interfaces. This is a malpractice as cutting operations involve exceptional mechanical and thermal loadings. In the analysis of friction during experiments or in finite element modelling studies, it was a common practice to assume a constant friction coefficient during the entire process or neglect the effect of friction coefficient whatsoever.

A composite machining model would deliver values of mechanical-thermal properties of workpiece, tribological parameters of friction and adhesion of workpiece on tools, tool wear, assessment of heat generated and its respective partitioning between tool and workpiece, effects of lubricants in heat dissipation. Melkote et al. [105] have explained the different methodologies for characterization of tribological parameters during metal cutting and can be summarized into three types as follows:

1. Measurement of cutting forces.
2. Use of conventional tribometers.
3. Customized tribometers.

Arrazola et al. [119] have used the orthogonal turning tests for AISI 4340 steel using uncoated carbide (K313 grade) cutting tool inserts and compared the results with simulation tests. The authors quote that comparing forces between the Coulomb friction and sticking-sliding friction that the influence is larger over the thrust force than by cutting force.

Özel et al. [120] have conducted the analysis of orthogonal cutting process using FE simulations with friction inputs observed experimentally. San-Juan et al. [121] in their work have worked on friction characterization in orthogonal milling process by the analysis of cutting force and radial force and have studied the influence of cutting speed and feed per revolution on friction performance. From the explanation of Childs [108] and the statements by Melkote et al. [105], this approach is unable to distinguish between the sticking and sliding zone of contact and improvements like the split tool tests or use of analytical assessment of secondary deformation zone are necessary.

The second approach is to replicate the friction conditions in the machining process by using conventional tribometers independent of cutting process. The tribometers follow a close configuration where the commercial cutting tool/ pin made of tool material traces refreshed workpiece at sliding speeds and contact temperatures representative of cutting conditions. However, Melkote et al. [105] state the contact pressures are in the tune of 0 – 15 MPa, which are too low considering metal cutting processes.

Therefore, several modifications have been done to the tribometers and customized assemblies like the one proposed by Zemzemi et al. [111]. Such tribometers are more representative of the cutting process and many versions of tribometers have been developed. Claudin et al. [131] proposed a new configuration wherein a pin rubs the refreshed surface of the workpiece and large feed allows the pin a helical movement on the workpiece surface avoiding superposition of scratches on workpiece. A cylinder was used to simulate the workpiece and the tribometer assembly comprising of dynamometer could be installed on a lathe allowing for high sliding velocities which exist during machining. The mechanism is shown in Figure 25.

Zemzemi et al. [132] mention as the contact pressure and sliding velocity vary at the tool-workpiece contact, the friction coefficient and heat partition coefficient also vary subsequently. Thus, the macroscopic or apparent friction coefficient would be equivalent to the ratio of tangential and normal forces and can further be decomposed into adhesive and deformative friction coefficients as shown in Equation 5:

$$\mu_{app} = \frac{F_t}{F_n} = \mu_{adh} + \mu_{plast} \quad (5)$$

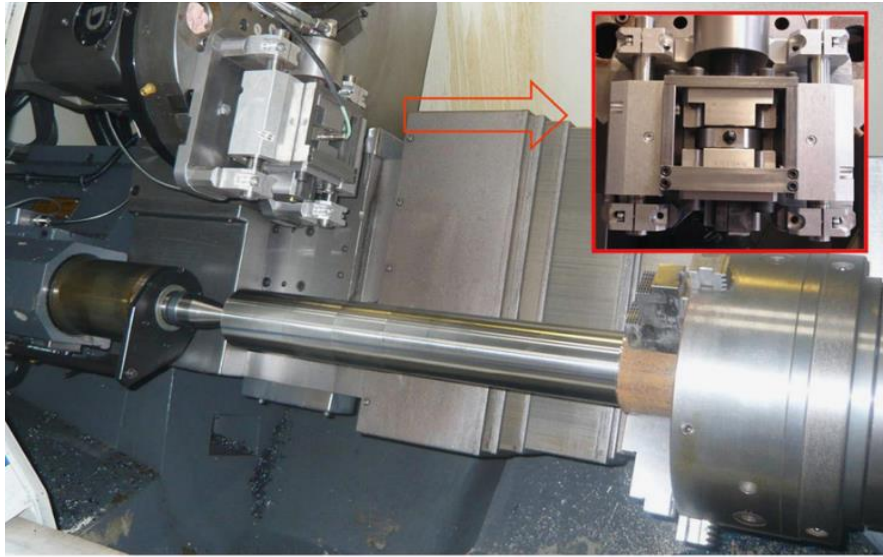


Figure 25 The pin-on-cylinder configuration as proposed by [131]

Where μ_{app} is the apparent friction coefficient, F_t and F_n represent thrust and normal forces, respectively, μ_{adh} is the adhesive friction component and μ_{def} is the deformative friction coefficient. This decomposition of apparent friction coefficient is represented in Figure 26.

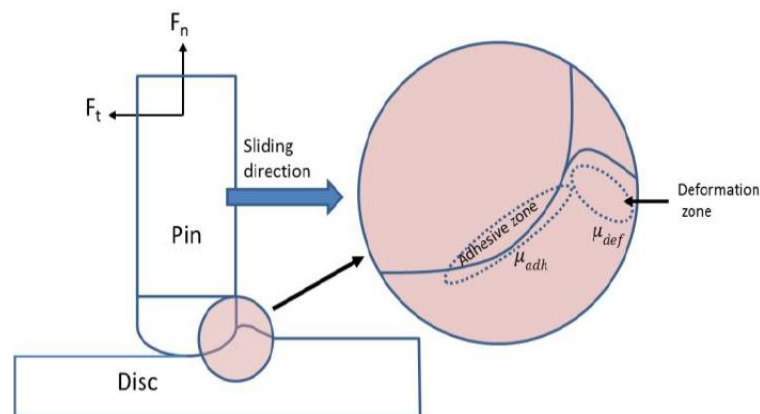


Figure 26 The decomposition of apparent friction coefficient into adhesive and deformation components [133]

The contact conditions are most important part of the study, and the accuracy of the results depends squarely on their assumptions. Rastakar et al. [122] in their work have characterized oxide layers formed on gamma – TiAl alloys using ball-on-disc tribometers, applying loads ranging from 20N to 100N and arrived at Hertzian contact pressures between 1.1 GPa to 2.3 GPa respectively. Milton et al. [133] in their work emphasize that during machining of Ti-6Al-4V alloys, the typical contact pressures

between the tool and work-material are in the range of 1.5 GPa to 2.5 GPa for titanium alloys.

The literature indicates that the normal forces have been calculated by simple formulation of forces acting of contact area. Grzesik et al. [134] in their work have indicated that for Pin-on-Cylinder (POC) tests involving Ti-6Al-4V, a normal force of 1000 N yields a contact pressure of 1.5 GPa. However, this approach does not consider the actual contact area between the pin and the workpiece which is based on the respective material properties.

The Hertzian contact theory encompasses the material properties –Young’s modulus, Poisson’s ratio and geometries of the material involved thereby giving more accurate values of the contact conditions between two materials. Shigley’s mechanical engineering design book [135] have explained different configurations on the Hertzian contact theory. The local conditions at the time of contact of the tool and the workpiece resemble a sphere in contact with plane. The contact radius a of the pin is calculated as shown in Equation 6 as:

$$a = \sqrt[3]{\frac{3 * F_n}{8} * \left[\frac{\frac{1-\nu_1^2}{E_1} + \frac{1-\nu_2^2}{E_2}}{\frac{1}{2 * R_1} + \frac{1}{2 * R_2}} \right]} \quad (6)$$

Where ν_1 and ν_2 are the Poisson’s ratios, E_1 and E_2 are the elastic moduli, and R_1 and R_2 are the radii, of the pin and the workpiece surface respectively. While R_1 has an established radius, R_2 is considered to be infinity for long cylinders in accordance with the Hertzian contact conditions. The contact condition is shown in Figure 27.

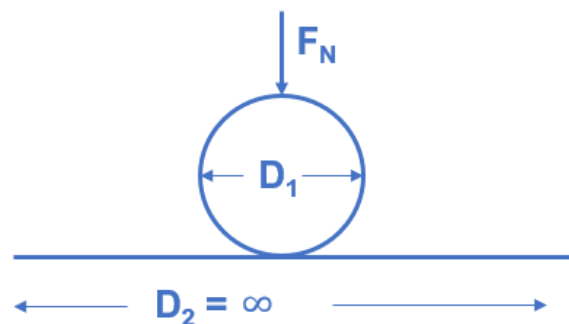


Figure 27 Hertzian contact condition with assumption of sphere on an infinitely long flat plate

The Elastic moduli could be achieved by an ultrasonic analysis of the material in velocity of sonic pulse in lateral direction (v_l) and transversal (v_t) directions respectively. ρ stand for density of the material. The relationship is shown in as Equation 7.

$$E = \frac{\rho v_t^2 (3v_l^2 - 4v_t^2)}{(v_l^2 - 2v_t^2)} \quad (7)$$

When all the components are generated, the subsequent normal forces required could thus be achieved by Equation 8 as follows:

$$F_n = \frac{P_n * 2 * \pi * a^2}{3} \quad (8)$$

It is important to quantify the heat generated during the POC tests as it reveals information on efficiency and performance of coatings, adhesion, and wear mechanisms etc. The heat generated and partitioned during the tests is illustrated in Figure 28.

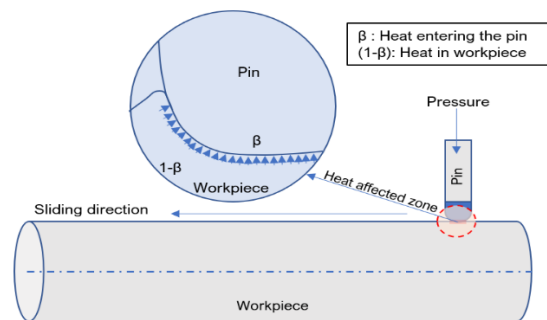


Figure 28 Pictorial representation of quantification of heat between pin and workpiece during POC tests

The global power consumed during the tests is expended as plastic deformation of softer material and friction between workpiece and pin. The breakdown is represented in Equation 9 as follows:

$$P_g = P_{pd} + P_f = F_t * v_s \quad (9)$$

Bonnet et al. [136] state that 90% of the power during the plastic deformation is converted to heat and 10% is devoted to strain hardening and that the quantification of heat is subject to scientific assessment and difficult to measure. The heat consumed during strain hardening is dependent on properties like density, specific heat

temperature gradients, tensor stress and strain rate of material during the process, requiring dedicated measurements. Therefore, in the current study the component of plastic deformation is omitted. Assuming that the entire power consumed by the frictional component is converted to heat, the remaining friction power can be enunciated as represented in Equation 10 as:

$$P_f = F_{t\ local} * V_{s\ local} = \varphi_{friction} \quad (10)$$

The heat dissipated during the friction tests can be sub-divided into the frictional heat entering the workpiece and frictional heat entering the pin, as shown in Equation 11:

$$\varphi_{friction} = \varphi_{friction-WM} + \varphi_{friction-pin} \quad (11)$$

In order to measure the instantaneous heat flow entering the pin ($\varphi_{friction-pin}$), special pins with holes for *K*-type thermocouple placement were used. The heat flux entering the pin is given by is dependent on material properties and the placement of thermocouples. The instantaneous heat is given by Equation 12:

$$\varphi_{friction-pin} = l * S_{pin} * \frac{\Delta T}{dx} \quad (12)$$

Where $\varphi_{friction-pin}$ is the flux entering the pin, λ is the thermal conductivity of pin, S_{pin} is the pin cross-sectional area, ΔT is the temperature difference measured in the pin and dx is the distance between the thermocouples. The heat transmitted to the pins (β) can be calculated as shown in Equation 13:

$$\beta_{pin} = \frac{\varphi_{friction-pin}}{\varphi_{friction}} \quad (13)$$

Where, β is the amount of the energy transmitted to the pins and conversely $(1 - \beta)\%$ would be the heat remaining in the workpiece. The relationship or the sensitivity of the input parameters on the output parameters could be studied by Pearson correlation as shown in Equation 14:

$$C = \frac{\sum_{i=1}^n (x_i - \bar{x})(y_i - \bar{y})}{\sqrt{\sum_{i=0}^n (x_i - \bar{x})} \sqrt{\sum_{i=0}^n (y_i - \bar{y})}} \quad (14)$$

Where C is correlation constant or index, and x and y are the input variables, which in the present case are the values of sliding velocity and contact pressure.

Table 10 Critical assessment of tribology characterization in published literature

Authors	Alloy	Machining/ Methodology	Tools	Model limitations w.r.t machining/coating/coolant performance assessment
Rastakar et al. [122]	Ti-45Al-2Nb-2Mn-1B (at%)	Ball on disc tribometer	Steel balls	(i) Bearing steel balls used as tool material (ii) Closed config. tribometer. Tool traces the same path.
Li et al. [123]	Ti-48Al-2Nb-2Cr-1B (at%)	Ball on disc tribometer	WC/Co, Si ₃ N ₄ and Al ₂ O ₃	(i) Single contact pressure for each tool considered. Variation of friction coefficient with contact conditions is absent. (ii) Closed config. tribometer. Tool traces the same path.
Chu et al. [124]	Ti-25Al (at%); Ti-40Al (at%); Ti-50Al (at%); Ti-53Al (at%)	Uni-directional friction tester	Alloy steel – JIS SKS 95	No industrial cutting tool materials.
Cheng et al. [125]	Ti-45Al-8.5Nb- (W, B, Y) (at%)	Ball on disc tribometer	WC-8Co, Si ₃ N ₄ and GCr ₁₅ steel	(i) Very low cutting speeds from machining point of view (ii) Very low contact pressure of 5N to 10N. Both the contact conditions are insignificant from machining.
Gialanella et al. [126]	Ti-48Al-2Cr-2Nb-1B (at%)	Disc on block slider	AISI M2 steel	(i) Only one sliding velocity of 37.68m/min has been used.
Özel et al. [127]	Ti-6Al-4V	Turning and FEM simulations.	Uncoated, TiAlN coated and TiAlN+cBN	Assumed to be constant for all speeds, $\mu = 0.7$ for WC/Co, $\mu = 0.5$ for TiAlN.
Wang et al. [128]	Ti-6Al-4V	High speed milling	Binderless cBN	No friction coefficient assumed.
Wyen et al. [129]	Ti-6Al-4V	Orthogonal turning	WC/Co	Constant $\mu = 0.32$ for all cutting speeds [10 – 110 m/min].
Cotterell et al. [130]	Ti-6Al-4V	Orthogonal turning	WC	Constant $\mu = 0.52$ for all cutting speeds [30 -120 m/min].

2.4 SUMMARY OF THE LITERATURE REVIEW

The gamma – TiAl alloys are intermetallics with unique properties like low density, high specific strength, oxidation resistance, high melting point and structural stability at elevated temperatures making them ideal candidates to be used in aeroengine components. However, due to their low thermal conductivity, strength retention at high temperatures, work hardening and chemical affinity, makes them difficult to process at room temperature.

Four production routes have been tried to produce components of gamma – TiAl alloys. The routes are hot working, powder metallurgy, casting, and additive manufacturing. The investment casting route was found to be more widely used as it gives higher freedom of melt composition.

Three generation of gamma – TiAl alloys with different compositions have been formulated. The most prominent alloy compositions are second - generation Ti-48Al-2Cr-2Nb and third - generation Ti-45Al-2Mn-2Nb-0.8% TiB₂ (XDTM), Ti-43.5Al-4Nb-1Mo-0.1B (TNM). The three generations are the most used compositions in aeroengines.

Four prominent microstructures for TiAl alloys have been reported. Fully lamellar, Near lamellar, Duplex and Near gamma. Lamellar and Duplex microstructures were found to be microstructures with superior strength and superior strength with good ductility respectively.

The machinability of the alloys was stated to be difficult due to the existence of brittle – ductile regime at temperatures near 760 – 770° C meaning that the material is brittle till high temperatures. Therefore, very high cutting speeds were rare occurrence with respect to good tool life. The consolidation of machining parameters as shown in Table 8 yields that most of the studies have used cutting speeds of 50 – 70 m/min with a feed per tooth in the range of 0.04 – 0.06 mm/tooth, axial depth of cut in the range of 0.1 – 0.3 mm, radial depth of cut in the range of 0.2 – 0.5 mm respectively. Flank wear was seen to be the most evident wear type and adhesion to be the most evident wear mechanism. Catastrophic tool failures were reported near the tool life of 90 min.

Different lubrications like dry, flood, MQL, MQCL, Cryogenic have been reported. For the gamma – TiAl alloys, heat extraction occupies higher prominence than lubrication

owing to low thermal conductivity of the alloys. Literature had indicated the MQL has delivered higher tool life but has proven to be expensive. The caveat being that effectivity of MQL was only up to cutting speeds upto 80 m/min. Seemingly, the MQL lubrication was found to deliver better surface finish than other lubrications.

The surface integrity analysis yielded that deformation of lamellar colonies was prominently displayed in the sub-surface analysis. The deformation of the lamellae was further dependent on the microstructure and composition. The occurrences of fractures, cracks, pull out were widely seen in the third-generation alloys due to the presence of TiB_2 particles. Hardened layers upto 300 μm have reported.

However, assessment of surface integrity as a function of entire tool life was not found leading to the absence of information on how the sub-surface defects change with increasing tool life. Importantly, any SI comparisons between different microstructures of the gamma – TiAl alloys is absent. No study was uncovered which made a comprehensive and comparative analysis of SI in different lubrication conditions. Also, literature mostly indicated the deformation lamellae without its measurement from the surface. No information was present on methodology adopted to measure the deformation of lamellae.

The low thermal conductivity gamma – TiAl is one of the reasons for excessive heat incidence on tool leading to accelerated tool wears. The literature indicated the absence of any study which made tribological characterization of friction, coating wear and adhesion of workpiece on coatings, heat generation and partitioning between tool and workpiece. Thus, no data exists on the effectivity of coatings while machining gamma – TiAl alloys.

Chapter 3

**MATERIAL
CHARACTERISATION**

3 MATERIAL CHARACTERISATION

This chapter is divided into three sections. The first section describes the production of Ti-48Al-2Cr-2Nb bars to obtain machinable workpieces. This is followed by material characterization through optical metallography. The final section enunciates the thermal characterization and hardness testing.

3.1 CENTRIFUGAL CASTING

The Ti-48Al-2Cr-2Nb ingots (feed material for casting) were produced via Vacuum Arc Remelting (VAR) process. This process was chosen since it allows greater control over alloy chemistry. Subsequently, this feed material was subjected Induction Skull Melting (ISM) and centrifugal casting at Access e.V. to deliver the bars for machining. In total, three separate heats comprising 6 pours delivered a total of 18 bars. The representational image of the equipment is as shown in Figure 29 (a).

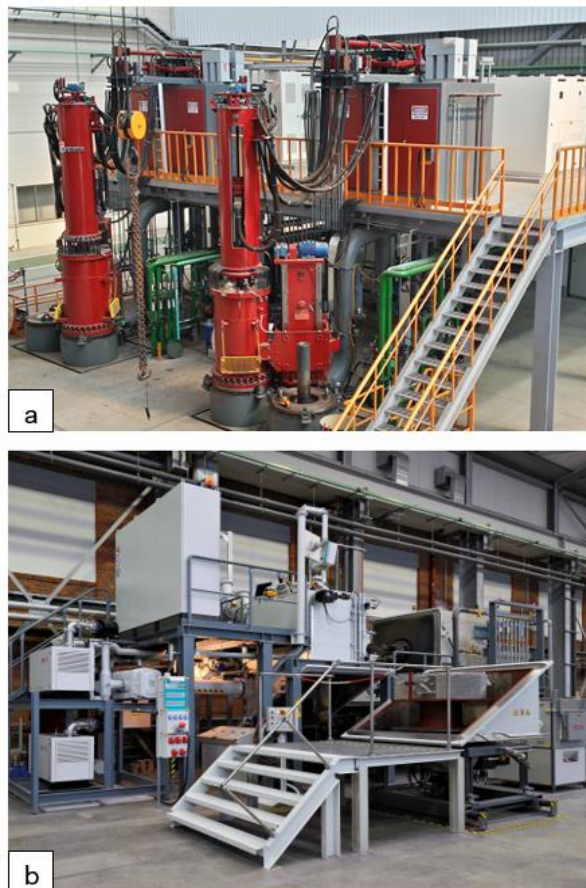


Figure 29 Vacuum arc remelting of to obtain Ti-48Al-2Cr-2Nb feed material for castings (Image courtesy: Inductotherm Pvt. Ltd.) (b) ISM and Centrifugal casting process to achieve bars for machining

The bars after the casting process comprise of the riser material at one end. This is extra material and is removed by waterjet cutting as shown in Figure 30 (a).

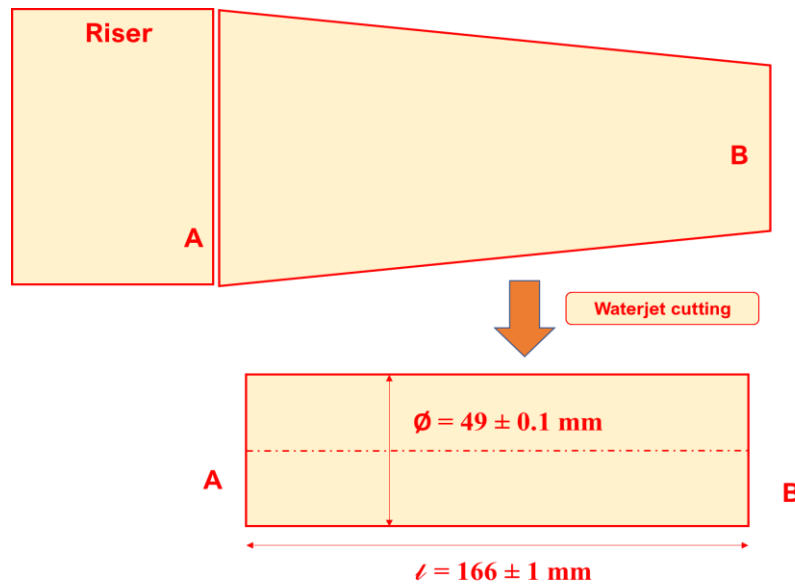


Figure 30 (a) Bar dimensions after cleaning and turning of cast ingots. (b) Ingots after waterjet cutting

The bars were subsequently turned at MU MGEP to achieve cylindrical bars of diameter $49 \pm 0.1 \text{ mm}$ with length of $166 \pm 1 \text{ mm}$ (Figure 30 (b)). Subsequently, the turned bars were returned back to Access e.V. to check for internal defects like porosity or shrinkages. This was done by X ray tomography (Figure 31). The X ray profiles of all the 18 bars was developed. All the bars confirmed the absence of internal defects.

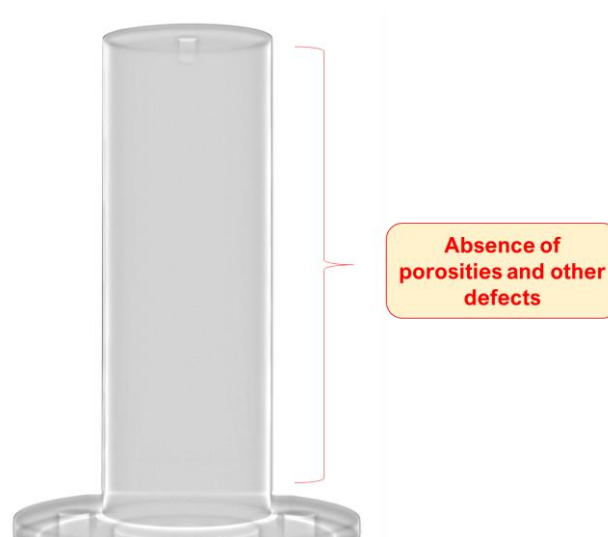


Figure 31 X ray tomography of cast ingots to check for porosities and other defects

Material characterisation

As the PhD entails to compare machining of two microstructures (i) Near lamellar (ii) Duplex, a sum of 4 bars were subjected to Hot Isostatic Pressing (HIP) and Heat Treatment (HT) in the ($\alpha + \gamma$) region to achieve the Duplex microstructure. The furnace for HIP processing is depicted in Figure 32.

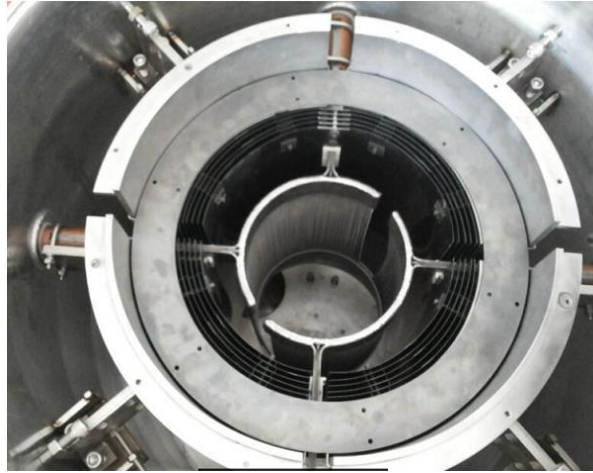


Figure 32 Furnace for Hot Isostatic Pressing of the bars (Image Courtesy: MTI Corporation, Richmond)

This operation was outsourced to Bodycote, a service provider for heat treatment services. The process parameters utilized during HIP are presented in Table 11. The heat treatment parameters are shown in Table 12.

Table 11 Process parameters of hot isostatic pressing of cast Ti-48Al-2Cr-2Nb ingots

Process parameters employed during Hot Isostatic Pressing (HIP)	
Parameters	Value
Temperature (K)	1423.15
Atmosphere	Argon (99.98%)
Pressure (MPa)	175 ± 10
Dwell time (min)	360 ± 30
Heating rate (K/min)	< 10
Cooling rate (K/min)	< 10

Table 12 The heat treatment conditions employed for cast ingots to achieve duplex microstructure

Heat treatment conditions for cast ingots	
Parameters	Value
Temperature (K)	1473
Dwell time (min)	120

Material characterisation

Of the 18 bars, 2 bars each from cast and cast + HIP + HT processes were utilised for optical microscopy process as detailed in section 3.2. The remaining 14 bars (cast) and 2 bars (cast + HIP + HT) were used for machining.

Additionally, to check if the elemental composition of each of the bar microstructures, Energy dispersive X-ray spectroscopy (EDX) was carried out. The results showed that no dissolution of alloy components was observed and that the results matched with the nominal chemistry of the alloy. Figures 33 and 34 present the results cast and cast + HIP + HT alloys.

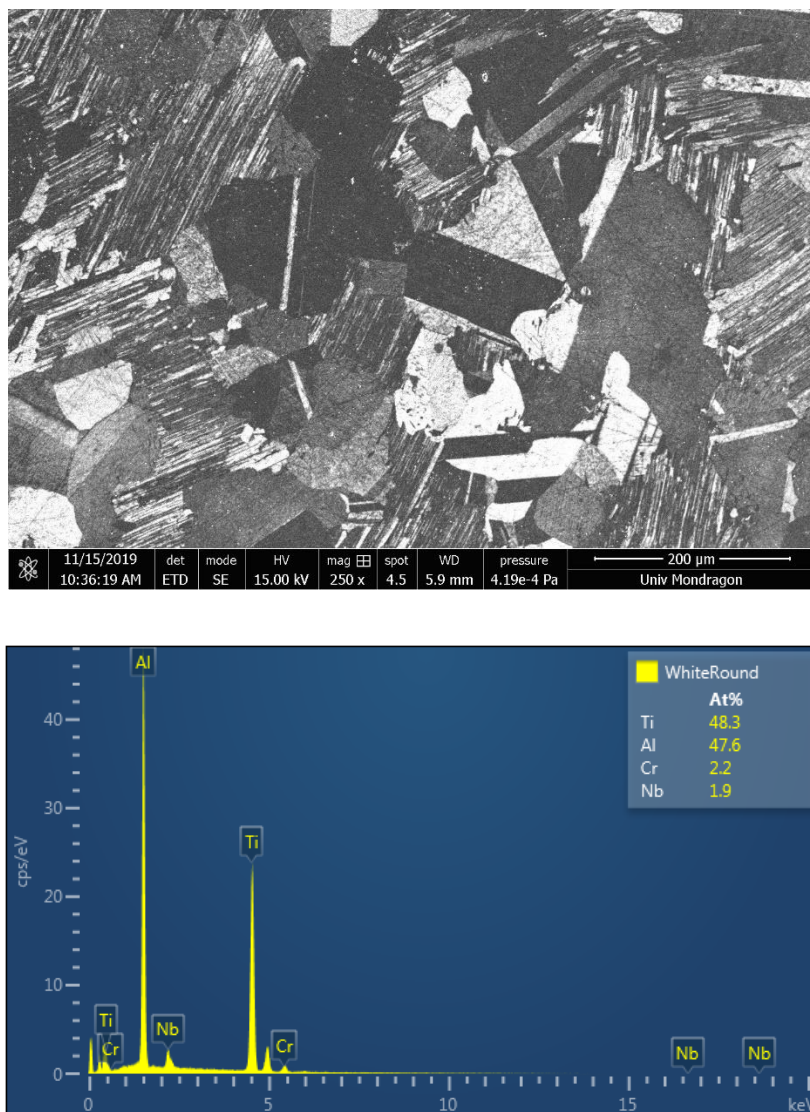


Figure 33 The EDX profile of cast Ti-48Al-2Cr-2Nb bars indicating the near ideal elemental composition

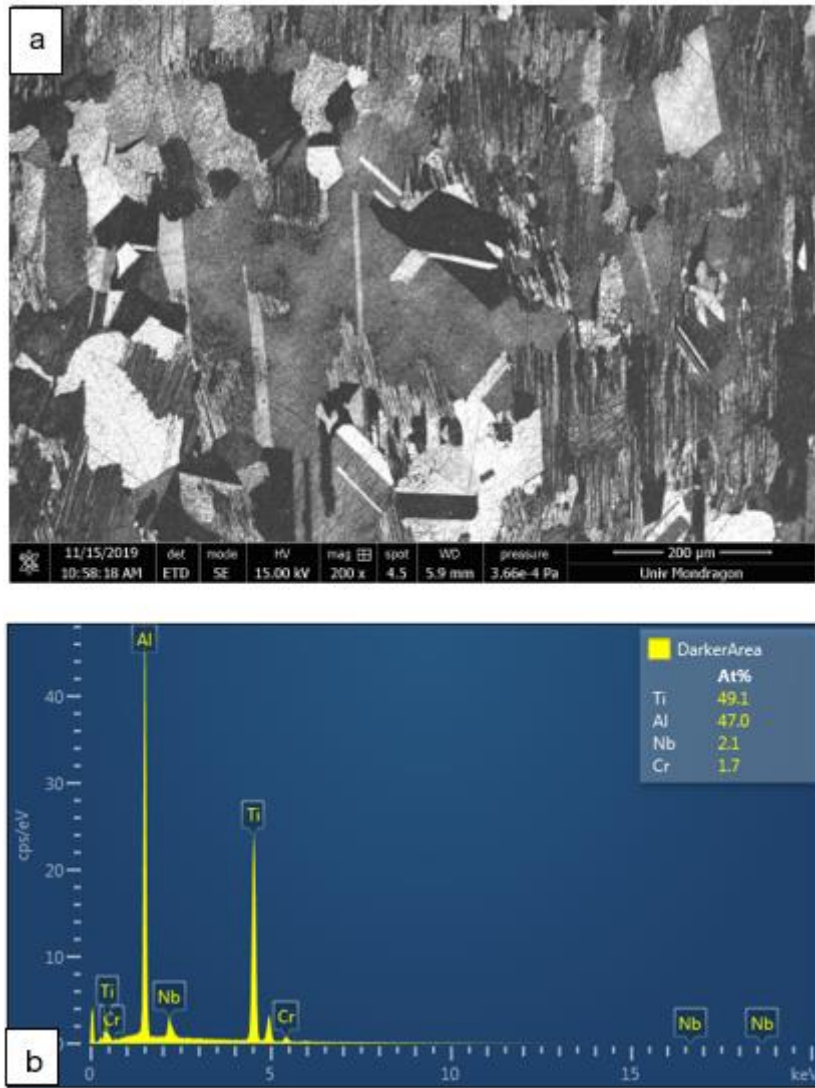


Figure 34 The EDX profile of Ti-48Al-2Cr-2Nb cast + HIP + HT bars indicating a near ideal phase composition

The results indicate that the difference in the composition of titanium for both the ingots is $\pm 2.5\%$. The ratio of Al / (Al + Ti) is 50.36% for cast and 51.09 % for cast + HIP + HT. This means that the balance of properties between the high temperature oxidation and fracture toughness are maintained for applications in aeroengines in accordance with the proposition of Brotzu et al. [137].

3.2 OPTICAL METALLOGRAPHY

The aim of the optical metallography was to determine the microstructure in the cast and cast + HIP + HT bars respectively. The exercise also envisaged to check if the microstructure was distributed uniformly in the bars. Thus, samples were extracted from the bars along and across the axis. The exercise was repeated three times with different bar specimens. The scheme of evaluation is presented in Figure 35.

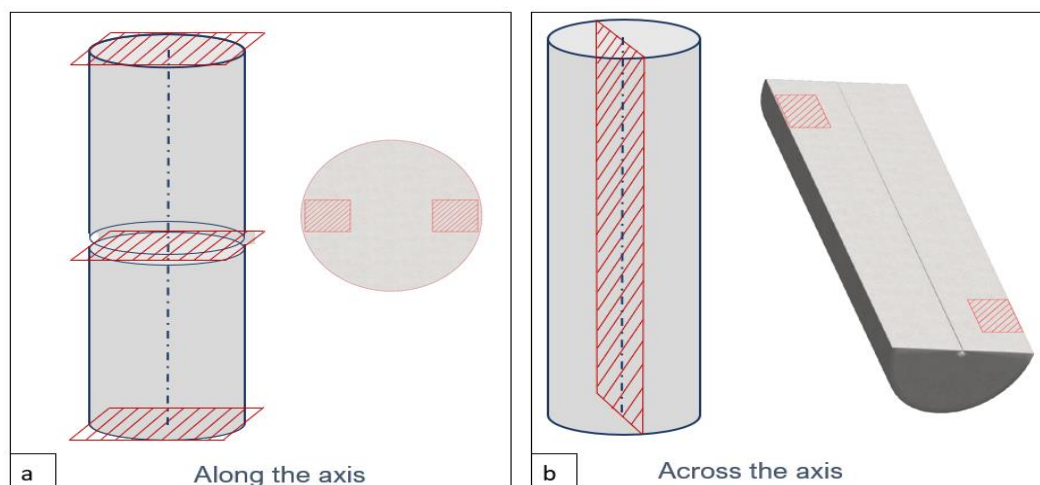


Figure 35 Scheme of optical metallography (a) along the axis (b) across the axis

The optical metallography samples were obtained by Wire Electro Discharge Machining (WEDM) and standard sample preparation procedure was carried out in the form of moulding, grinding and polishing and etching with Kroll's reagent (97 mL H₂O, 2 mL HNO₃, 1mL HF). The Figure 36 shows the optical metallograph of the cast bars. It could be identified as near lamellar structure with interspersed alpha (α_2 upon solidification) and gamma grains. The microstructure was found to be homogenous along and across the axis of the ingot. However, the periphery of the bars comprises of α_2 and γ grains embedded between lamellar colonies.

The Figure 37 displays the optical metallograph of cast + HIP + HT bars. This could be characterized as duplex – lamellar with interdendritic γ -grains. The presence of lamellar colonies indicates inconsistencies during heat treatment where the grain growth was impeded. The duplex-lamellar microstructure was homogeneously distributed along the axis. However, the examinations across the axis revealed that the periphery of the ingots consisted of a band of $120 \pm 7 \mu\text{m}$ with very small α_2 and γ grains (Figure 38). Thus, the grain size is found to increase from the surface to the centre of the bars.

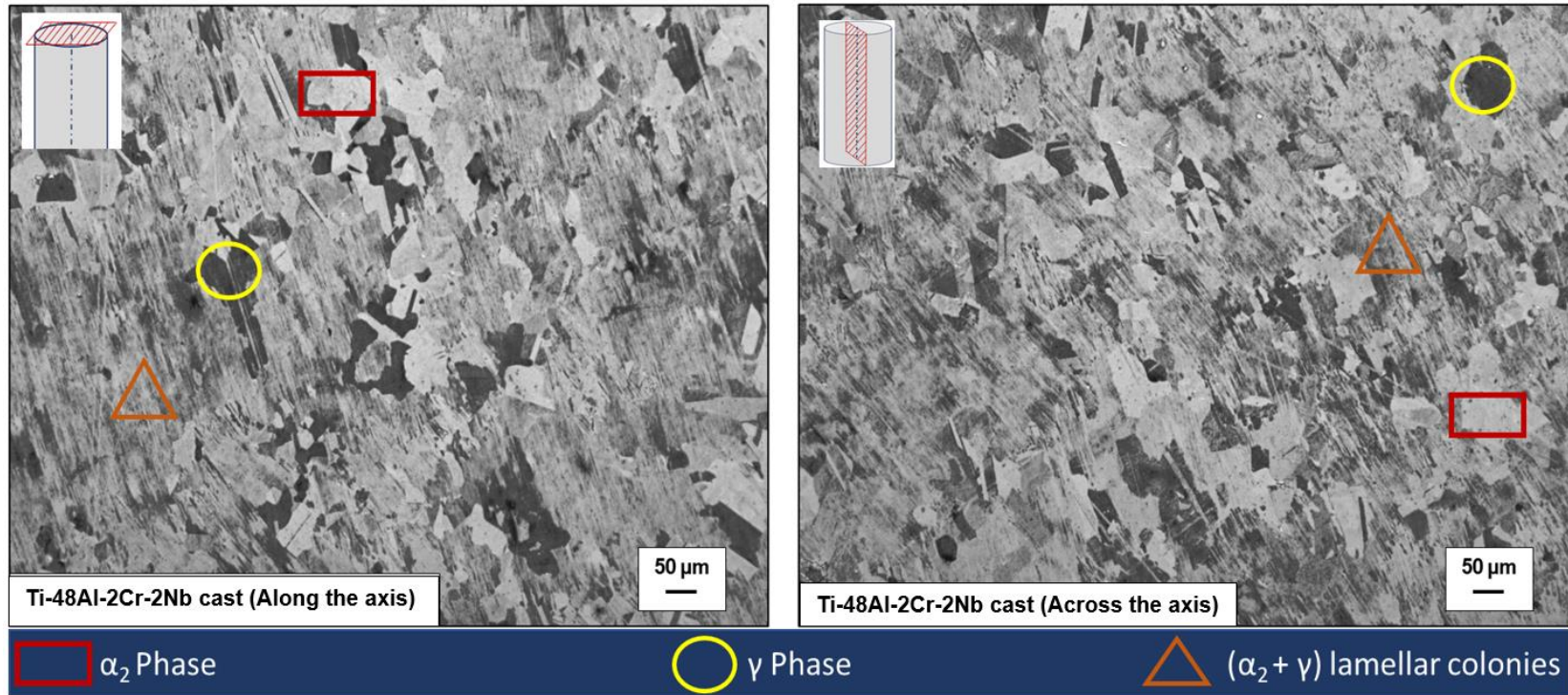


Figure 36 Optical micrographs of cast Ti-48Al-2Cr-2Nb ingots revealing the near lamellar microstructure (a) along the axis (b) across the axis

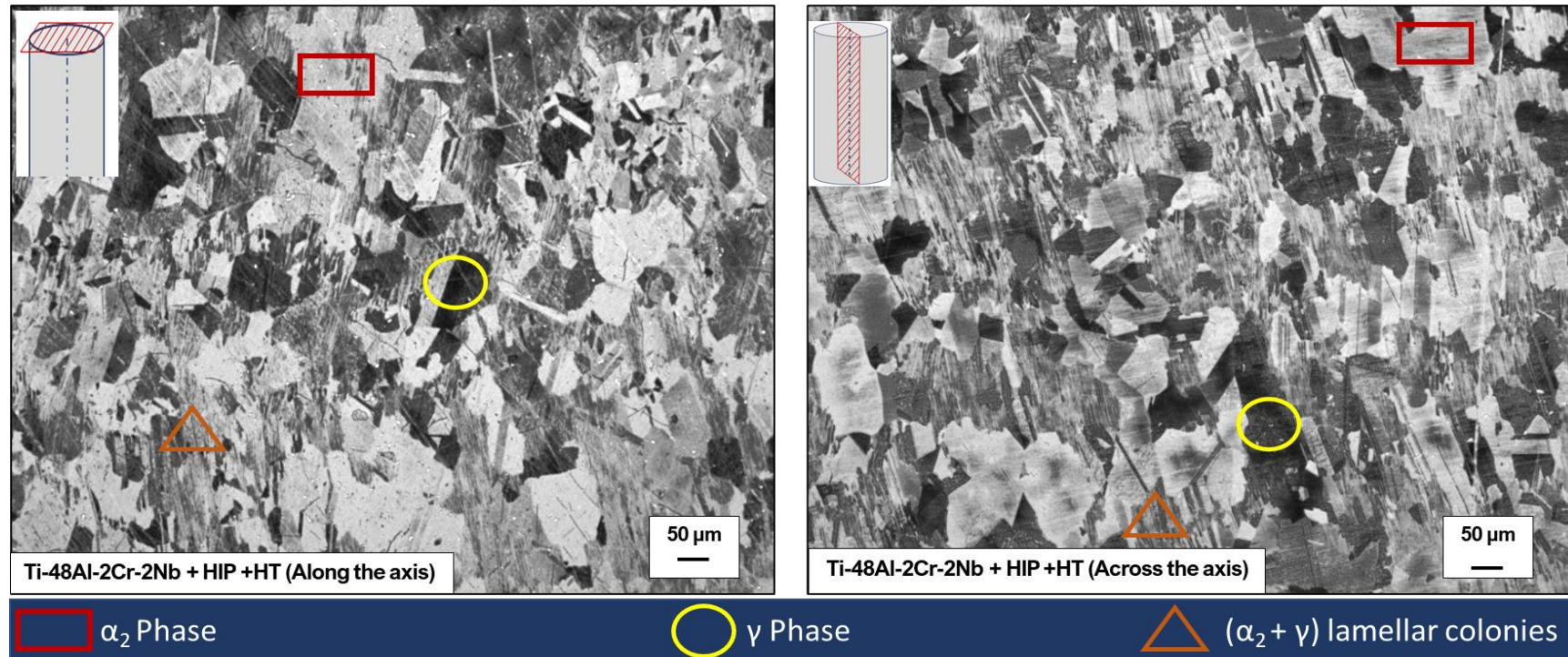


Figure 37 Optical micrographs of cast + HIP + HT Ti-48Al-2Cr-2Nb ingots revealing the Duplex - lamellar with interdendritic γ -grains microstructure (a) along the axis (b) Across the axis

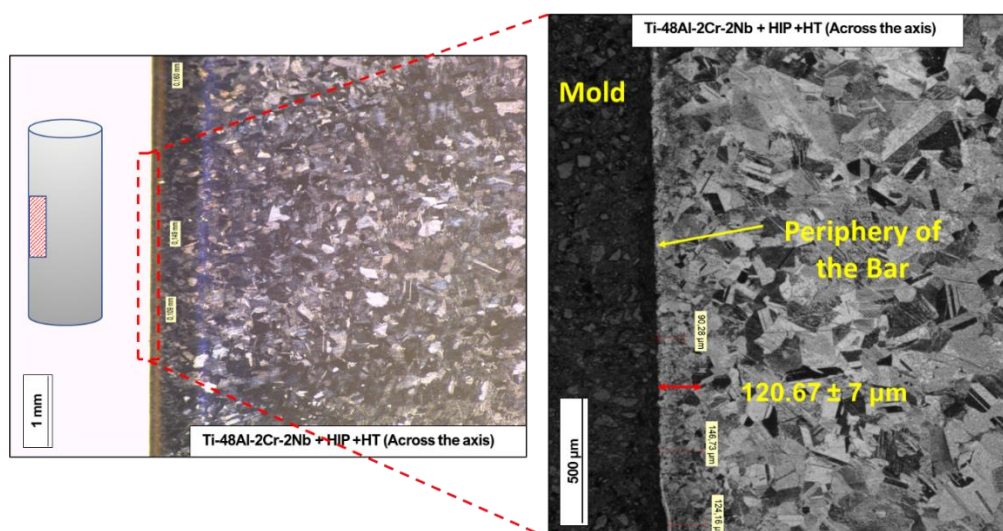


Figure 38 A band of small α_2 and γ grains observed on the periphery of cast + HIP + HT ingots (duplex microstructure)

The subsequent grain diameter distributions (histogram) of both the microstructures are as shown in Figure 39. It is important to remark that the microstructure for both near lamellar and duplex comprises of elongated (lamellar colonies), spherical (α) and irregular shapes (γ). Thus, the length and the width of the grains were measured and subsequently the area of a specific grain was calculated. The grain diameter was calculated in accordance with the procedure reported by Gottstein [138] as shown in Equation 15:

$$d = \sqrt{\frac{4 \cdot a}{\pi}} \quad (15)$$

Where a is the area and d the diameter of the grain. In the case of near lamellar microstructure, the histogram shows almost equal statistical frequencies for grain diameters between 50 – 100 μm and for 100 – 150 μm . As small α_2 and γ grains are embedded between the lamellar colonies, the result indicates the presence of small grain sizes for the α_2 and γ grains (0 – 50 μm) and large grain size for lamellar colonies (150 – 200 μm).

For duplex, the statistical frequency of grain diameters between 50 – 100 μm was found to be the highest. This was followed by grain diameters between 100 – 150 μm .

The frequency of grain diameters between 50 – 100 μm show the presence of lamellar structures. The presence of grain diameters between 0 – 50 μm and 150 μm and above shows the presence of α_2 and γ grains and lamellar colonies.

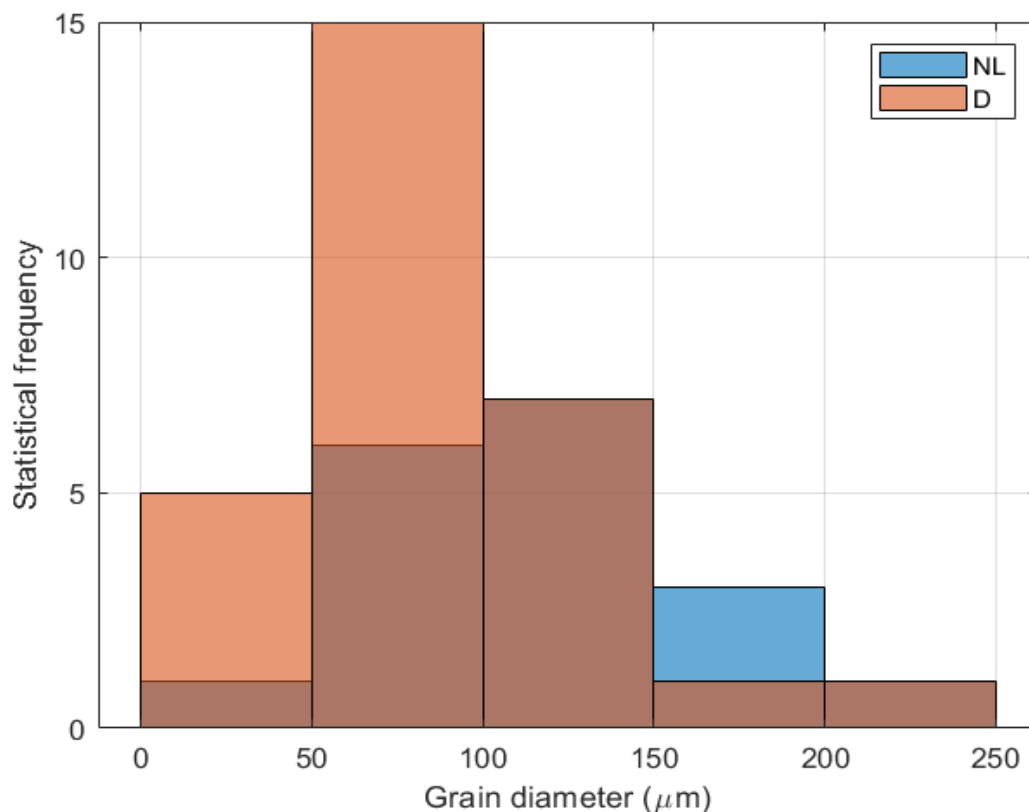


Figure 39 Grain diameter distribution of near lamellar and duplex microstructure between 0 – 250 μm

Because of the presence of the lamellar colonies in duplex microstructure along with α_2 and γ phases, a phase quantification was carried out and different phases were quantified. This quantification was done by classifying the gamma phase represented by the black colour. As gamma phase was of interest, rest of all the other phases were classified as $\alpha_2 + \gamma$ lamellar colonies. No distinction was made between lamellar colonies and free α_2 and γ . This γ phase quantification was later compared to theoretical phase composition. The quantification was carried out using the phase contrast LAS suite software provided with Leica optical microscope as presented in Figure 40. The software via image recognition identifies the phase of interest and delivers the amount of the phase present in micrograph. 5 – 6 micrographs were subjected to phase quantification and the mean values of the 6 micrographs were taken as the phase composition. 3 micrographs each were selected along and across

the axis. This procedure was repeated twice, thus a total of 12 micrographs of near lamellar and 12 micrographs of duplex were analysed.

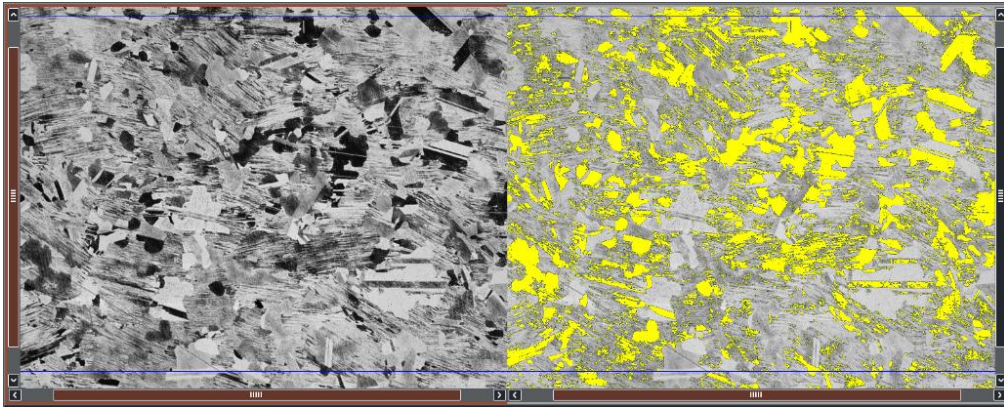


Figure 40 The phase quantification of the phases carried out via LAS suite software for Ti-48Al-2Cr-2Nb cast alloy

The results as shown in Table 13, indicated that the near lamellar microstructure consisted of 28.1 % of gamma phase with the rest amounting to lamellar colonies, while duplex showed higher composition of gamma phase – 54.1% and 45.9% lamellar colonies.

Table 13 Phase composition of cast and cast + HIP + HT microstructures

Microstructure	Heat treatment	Orientation	Amount (%) of gamma phase
Near lamellar	Cast	Longitudinal	28.1 ± 3.4
Duplex	Cast + HIP + HT	Longitudinal	54.1 ± 4.7

Importantly, the phase composition is in accordance phase compositions of microstructures of gamma titanium aluminide alloys. Gupta et al. [33] state that the gamma phase being the softer phase is known to improve room temperature ductility. This statement is validated by the observation of higher gamma composition in duplex microstructure in the present study.

3.3 THERMAL CHARACTERISATION AND MATERIAL HARDNESS

Following thermal properties of the cast bars with near lamellar microstructure (hereafter referred to as NL bars) and cast + HIP + HT bars (hereafter referred as Duplex bars) were characterized as a function of temperature till 1473 K.

- Density of both NL and Duplex bars was experimentally derived via dilatometry conducted on Linseis L75 Platinum Series Dilatometer from room temperature to 1573 K.
- Specific heat of NL and Duplex bars was experimentally derived via Differential Scanning Calorimetry (DSC) on Netzsch Jupiter STA 449 equipment from room temperature to 1473 K. Platinum cups with Y_2O_3 coated alumina inlays were used to hold the specimens.
- Thermal diffusivity of NL and Duplex bars was experimentally arrived via Laser flash method on Linseis LFA 1000 from room temperature to 1473 K.
- Thermal conductivity of NL and Duplex was calculated based on the values of foregoing properties from room temperature to 1473 K.

All the experiments were repeated twice, and readings were taken during heating cycles. The obtained results are presented in Figure 41. It could be ascertained from the results that both the NL bars and Duplex bars showed similar thermal properties. The density (ρ) of both the bars was found to decrease with the increase in temperature. The room temperature density was 3.96 g/cm^3 and 3.91 g/cm^3 for NL and Duplex bars as illustrated in Figure 41 (a). The densities of both the bars decreased linearly with increase in temperature with final values of 3.74 and 3.77 g/cm^3 for NL and Duplex bars.

The values from the experiments demonstrated that the density of the bars was stable even at elevated temperatures. During density measurements, the temperature crossed α -transus temperature estimated to be between 1360°C – 1380°C depending on the melt composition of the gamma –TiAl alloys as stated by Appel et al. [5]. Importantly, it was observed that upon increase in temperature the residual γ -grains dissolved leading to a coarse grain size. Thus, by heat treating the samples near the α -transus temperature, lamellar γ plates went into solution leading to a microstructure primarily with massive gamma which is in tune with the findings of McQuay et al. [139].

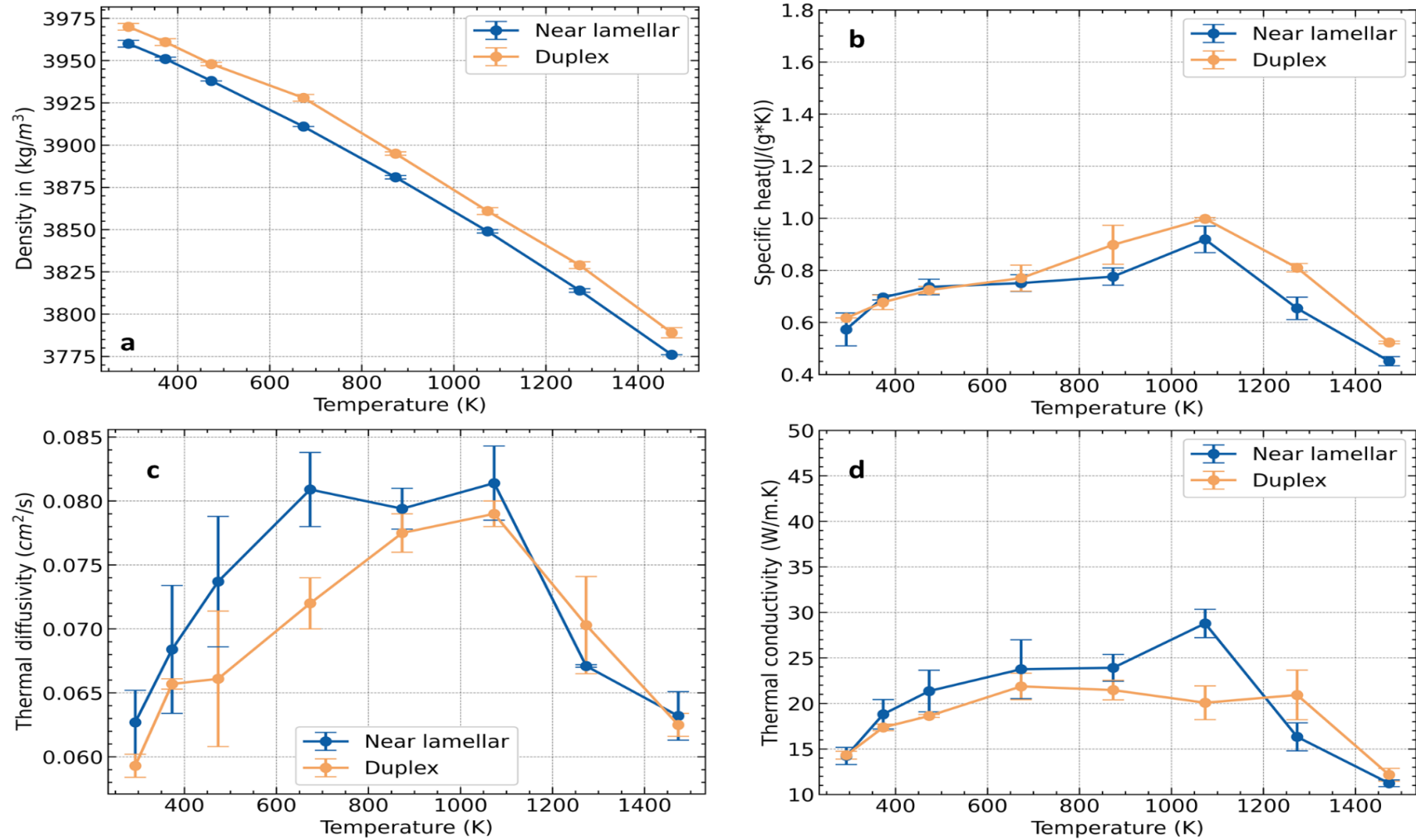


Figure 41 Thermal characterization of NL and Duplex bars represented by (a) density (b) specific heat (c) thermal diffusivity (d) thermal conductivity

The microstructural examination was conducted at room temperature before and after the density measurements to validate the changes. In the near lamellar microstructure as seen in Figure 38 (a and b), there was evidence of formation of stable α structure by the transformation of unstable γ . The lamellar colonies after heating cycles were pronounced even though residual γ existed in small proportions. In the case of duplex structure as seen in Figure 42 (c and d), the unstable γ transformed to α as seen in the case of near lamellar.

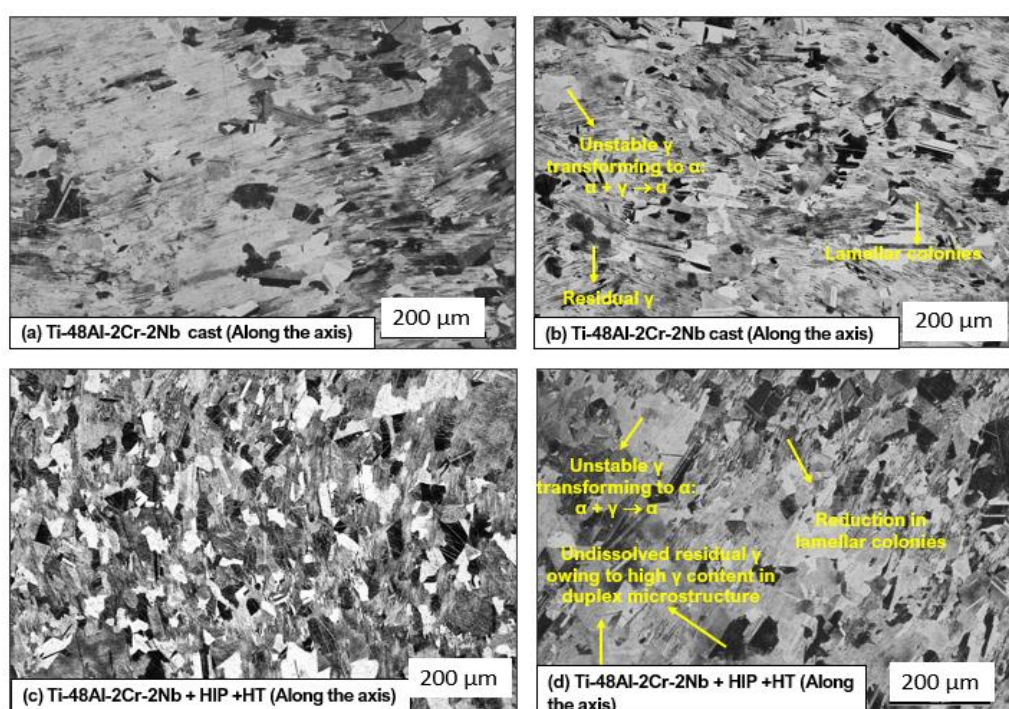


Figure 42 Optical metallographs of (a) near lamellar before heating (b) near lamellar after heating (c) duplex bars before heating (d) duplex bars after heating upto 1673.15 K

Naturally, because of the higher amount of residual γ in duplex structure, traces of γ grains were found indicating the absence of complete dissolution. However, the lamellar colonies after heating cycle were stunted indicating the solutioning of γ plates. Thus, from the microstructural assessment, post the density analysis, it was evident that when the samples were introduced to temperatures in the vicinity of α transus, the unstable γ began to dissolve forming a stable α phase. A complete dissolution of residual γ was not seen as the transformation warrants a repetitive heating and cooling cycles. The results are in tune with the findings of thermal analysis reported by McQuay [140]. The Figure 42 (b) shows results of specific heat (C_p) measurements. The specific heat determinations were conducted in Platinum cups with Y_2O_3 coated alumina inlays

as the combination is known to have the least reaction between the specimen and container. The trend emulates a rough bell shape curve where the specific heat of both the samples rose till 1080 K – 1100 K. Upon crossing the range, the specific heat values began declining with increase in temperature. The resulting curves display an endothermic rise at temperature near brittle – ductile regime. However, any further rise in specific heat values could only be confirmed at higher temperature ranges between 1468 K – 1674.15 K, corresponding to phase change of $\alpha_2 + \gamma \rightarrow \alpha + \gamma$. As the experiments were conducted only till 1400 K, this foregoing phase change could not be validated.

The thermal diffusivity (α) measurements as seen in Figure 42 (c) of both the bars follow a similar bell-shaped curve with peaks indicative of brittle-ductile regime transition.

The thermal conductivity (λ) calculated is a function of the three foregoing thermal properties and is presented in Figure 42 (d). The density measurements conducted at 1673 K are neglected in the current analysis as the rest of the measurements were carried out only upto 1473 K. The thermal conductivity was calculated using Equation 16 as:

$$\lambda_{therm} = a_{therm} * \rho * C_p \quad (16)$$

Though both bars show similar trends in thermal conductivity values, there is some difference observed particularly at elevated temperatures. The thermal conductivity is known to vary based on the stoichiometric composition or the volume fraction of gamma -TiAl and α_2 -Ti₃Al phases as reported by Franzén et al. [141]. Consequently, this translates to a variation of 13 – 16% in thermal conductivity values; confirming the variation observed in experiments.

3.4 CONCLUSION OF MATERIAL CHARACTERISATION

The Ti-48Al-2Cr-2Nb bars were cast through centrifugal casting and subsequently subjected to Hot Iso Static Pressing to eliminate internal defects. The optical microscopy was conducted along and across the axis of ingots. The results showed that the cast + HIP bars comprised of near lamellar microstructure. The grain size analysis of the bar showed that grain sizes within the range 0 – 25 μm and 50 – 75 μm had equal statistical frequencies, indicating the presence of α_2 and γ grains along with the lamellar colonies. The finding was in line with the standard composition of near lamellar microstructure.

Four cast + HIP bars were subjected to an additional heat treatment in the ($\alpha + \gamma$) region. The microstructure revealed that the bars contained α_2 and γ grains embedded between lamellar colonies. This microstructure was not in accordance with the four standard microstructures reported for the gamma -TiAl alloys. The microstructure was subsequently characterized as duplex – lamellar with interdendritic γ -grains. Importantly, the cast+ HIP +HT bars were characterised by the presence of small α_2 and γ grains aligned near the periphery of the bars.

The small grains were present in a band of 120 $\mu\text{m} \pm 7 \mu\text{m}$. The presence of smaller than usual grain sizes indicated inconsistencies in the heat treatment which impeded the regular grain growth. The grain size increased sequentially from the periphery to the centre of the bars. The grain size distribution of the ingot indicated that for the range 0 – 25 μm had the highest statistical frequency followed sequentially by 25 – 50 μm and 50 – 75 μm with equal frequencies. The grains size of 75 – 100 μm had low frequencies, indicating that the lamellar colonies though present were in low proportion.

Thermal analysis in the form of density, specific heat, thermal diffusivity, and thermal conductivity of both the microstructures was carried out. No substantial difference in thermal properties of the microstructures was noted. The microstructural analysis after density tests showed that, temperatures near α transus were reached and that the unstable γ phase was being transformed to α .

Chapter 4

**TRIBOLOGICAL
CHARACTERISATION**

4 TRIBOLOGICAL CHARACTERISATION

To ensure comprehensive understanding of the end bull milling performance of the tool with different lubricants, the tribological phenomena occurring at the tool – workpiece contact should be studied. In the case of gamma – TiAl alloys, three aspects are highlighted:

1. No studies have been found which provided a comprehensive assessment of all tribological phenomena of friction, adhesion of workpiece material on tool, coating wear / effectivity of coatings, and quantification and distribution of heat during the experiments.
2. A lack of machining context in the derivation of tribological properties was noted. The contact pressures were lower than those occurring during machining.
3. No studies exist which explain the effect of microstructures of gamma – TiAl alloys on tribological phenomena.

To address these gaps, the tribological properties of friction, adhesion of workpiece on tool, coating wear and heat partition between tool and workpiece were evaluated. To this end, the POC methodology with a customized tribometer was employed. This tribometer is sensitive to normal forces as small as 5 N. Special spherical pins with coated surfaces and small holes to hold thermocouples were manufactured.

Ti-48Al-2Cr-2Nb (Near lamellar), Ti-48Al-2Cr-2Nb (Duplex), and Ti-6Al-4V alloys were characterised using dry, flood (Emulsion, Vasco mill 7000), MQLSE1 and MQLVP 19004 lubricants. Ti-6Al-4V is the most used titanium alloy, accounting for 50 – 60% of total titanium alloy production (Hood et al. [34]). It is also considered as the benchmark to develop cutting tool development for all titanium alloys (Sandvik Coromant). Thus, a comparison of tribological properties could usefully contribute to the development of cutting tool for gamma – TiAl alloys.

4.1 EXPERIMENTAL SETUP AND METHODOLOGY

This section is divided into three. The first part describes the experimental setup and procedure for the POC tests and explains the composition of the tribometer and pins. The equipment used, evaluation procedure for adhesion of workpiece to the pins, and coating wear are detailed in the second section. Finally, the calculation of heat partition between tool and workpiece during the tests is presented. The alloys and the lubricants referenced in the chapter are set out in Table 14.

Table 14 Nomenclature of the alloys and lubricants in the chapter 4

Nomenclature	
Entity	Referred as
Alloy	
Ti-6Al-4V	Ti64
Ti-48Al-2Cr-2Nb (Near lamellar)	NL
Ti-48Al-2Cr-2Nb (Duplex)	D
Lubricants	
Dry	Dry
Flood (Emulsion, vasco 7000)	EML
MQLVP 19004	MQLVP
MQLSE1	MQLSE1

4.1.1 PIN-ON-CYLINDER (POC) TESTS

The characterisation study was carried out using a CNC Victor Taichung V-turn A26 machine with a traverse (X/Z) of 260/1300 mm (Figure 43). The tribometer (comprising Kistler 9129AA dynamometer and a fixture to hold the pin) is based on the design of Claudin et al. [131].

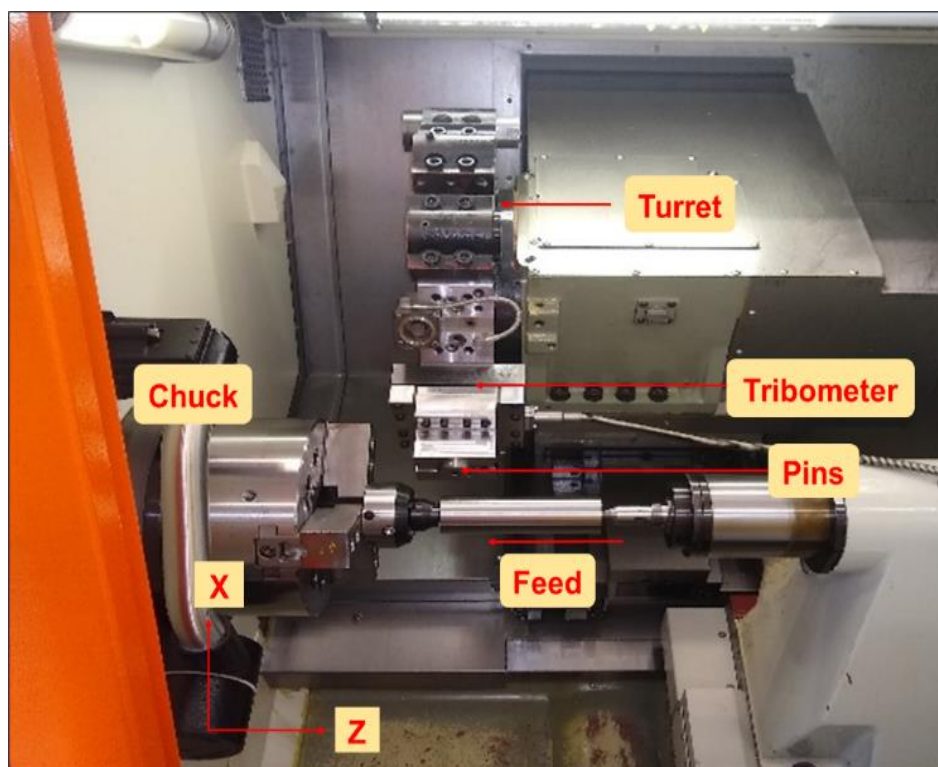


Figure 43 Pin-on-cylinder testing employing customized tribometer and pins

The spherical pins in the tribometer simulate the tool while the cylindrical bars (Ti64, NL & D bars) simulate the workpiece. The pin and the multi-layer coating is depicted in the Figure 44. The pins had an external diameter of 8 mm with a spherical head radius of 6mm. The heads were coated in two layers: (i) nano layered AlTiN inner part coating with modulation of aluminium content over total layer thickness (ii) a nano layered outer coating of AlSiTiN. The average coating thickness on the external surface was 2 – 5 μm . In order to expunge any inconsistencies during the experiments, the pins were polished to achieve a surface roughness of $R_a < 0.8 \mu\text{m}$.

At the commencement of each test, the pin slid from the tail stock to the end of chuck. Normal tests lasted for 24 s and the tests with temperature measurements lasted for 32 s. As the pin slid across the surface, the normal and the tangential forces were measured by the dynamometer. The ratio of the tangential force to the normal force gave the *Apparent friction coefficient*.

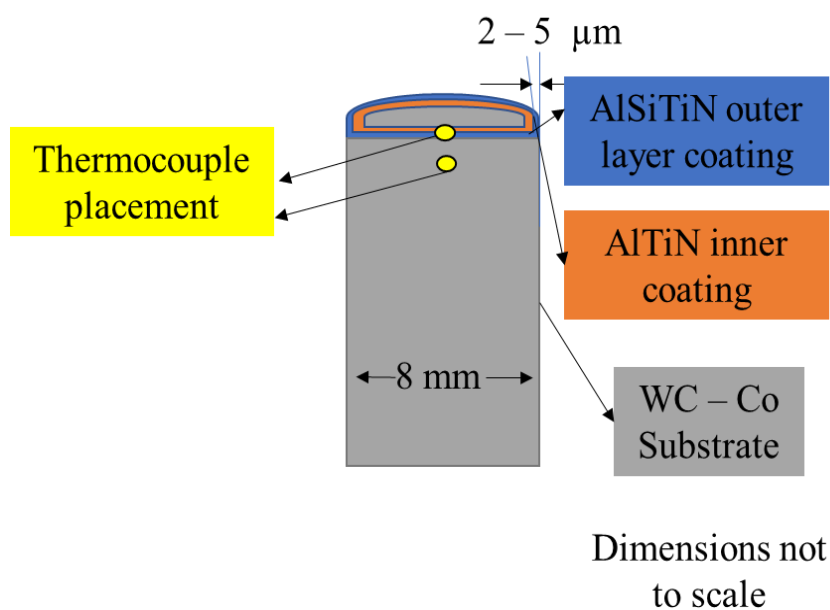


Figure 44 The composition of pins

After each test, a cutting tool refreshed the workpiece surface by removing the ploughed surface (by turning 0.2 mm of the workpiece surface). The subsequent test was commenced only if $Ra < 0.4 \mu\text{m}$. Else, the cutting tool removed 0.2 mm surface again. Based on the state of the art, the contact pressures from 1.31 – 3.27 GPa and sliding velocities between 37 – 120 m/min were chosen for the study. The requisite normal force was determined using Hertzian contact conditions as set out in equations 6 – 8.

The Hertzian contact conditions require the material properties of the alloys. The Poisson's ratios of the alloys were adopted from the literature (Budynas et al. [135]). The Young's moduli of each alloy were calculated with ultrasound analysis and the results are presented in Table 15. During the analysis, the ultrasound probe producing sonic waves was incident along and across the axis of the bars. The probes captured the longitudinal (V_l) and transversal (V_t) propagating velocities. With the density and the Poisson's ratios of the alloys known, the Young's modulus was calculated in accordance with the equation 7. Then, the normal forces for each of the alloy (Ti64, NL and D) were calculated chronologically, as described in section 2.3.

Table 15 Material properties obtained from ultrasound analysis and the literature

Material	Material properties		Source / Reference
	Poisson's ratio ν	Youngs Modulus, E (GPa)	
Ti64	0.34	100	ν : [32]; E: Empirically derived
NL	0.23	169	ν : [32]; E: Empirically derived
D	0.23	169	ν : [32]; E: Empirically derived
Pin	0.225	600	AB Sandvik Coromant

The physical-chemical properties of emulsion, MQLSE1 and MQLVP are reported in the Table 16. The emulsion was delivered via the turret and the MQL oils were delivered via a tube fixed at 30° to the workpieces. A special fixture was used to ensure the tube remained in the position during experiments (Figure 45). The optimum distance between the tube outlet and the spherical surface of the pins was determined to be 8.2 mm before the trials. The MQL flow rate of 70 ml/h was set based on the recommendation of the manufacturer (Blaser Swissslube) and from the published data. Special care was taken to ensure that the *K*-type thermo-couple wires did not become entangled with each other or any moving element to prevent inaccuracies during temperature measurements.

Table 16 Physical-Chemical data of all lubricants

Physical – Chemical data	Concentrate Vasco 7000	Emulsion (Mixed with water) Vasco 7000	MQL SE 1	MQLVP 19004
Density at 15°C, kg/m ³		Close to water	0.876	0.907
Density at 20°C, kg/m ³	0.98	Close to water	0.873	0.904
Viscosity at 40°C, mm ² /s	74 mm ² /s	Close to water	19.8	23.1
Flash point, °C	134	-	176	255
Specific heat (J/ kg. K) (Literature values)		Close to water	1.97	1.97
pH value		8.8 – 9.5	NA	NA
Nature	Ester based		Ester based oil with additives	Ester based oil with additives

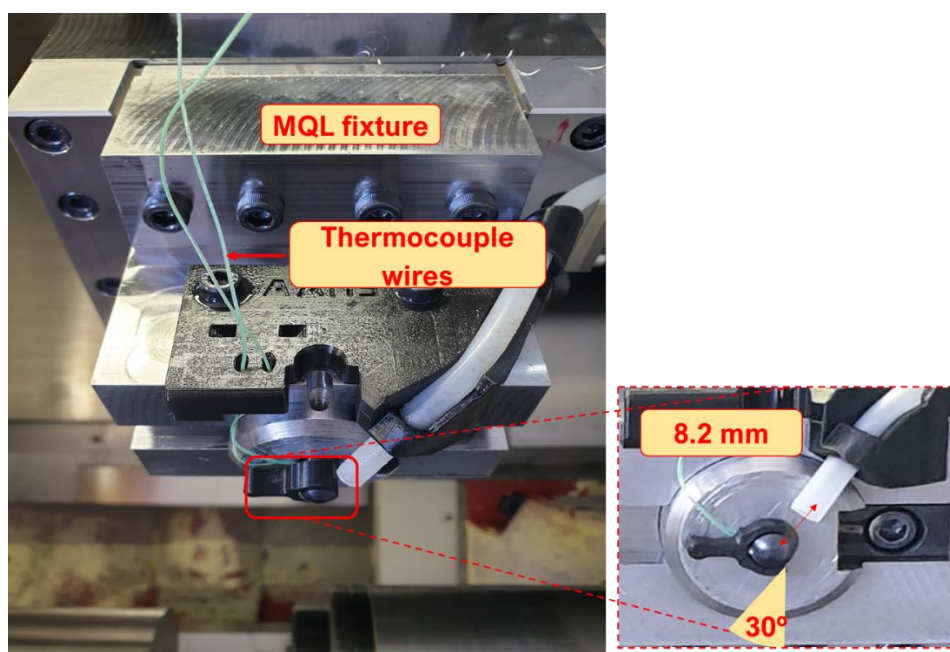


Figure 45 Special fixture to hold the MQL pipe in position

4.1.2 ADHESION AND WEAR ASSESSMENT

Adhesion of the workpiece to the pins and coating wear were studied using a Keyence Numerical Microscope VHX 5000 series with a tolerance of 50 μm each in the X and Z co-ordinate axes as shown in Figure 46. The wear debris on the pin surface was analysed with an 18 megapixels microscope with a 3CMOS 50 fps.



Figure 46 Representational image of Keyence VHX 5000 (McSwain Engineering Inc.)

After each POC test, microscopic analysis was carried on the raw pins to check for *accumulated particles* (comprising workpiece particles, micro-chips, dust, etc.) on the surface. Although *accumulated particles* are not experimentally or statistically significant, their presence indicates the degree of interaction between the coating and workpiece.

Any *accumulated particles* were then subsequently removed with a single swipe of a clean paper to reveal the true extent of the *sticking* work-material strongly bound on the pin coating (Figure 47 (a-b)). This area was quantified digitally.

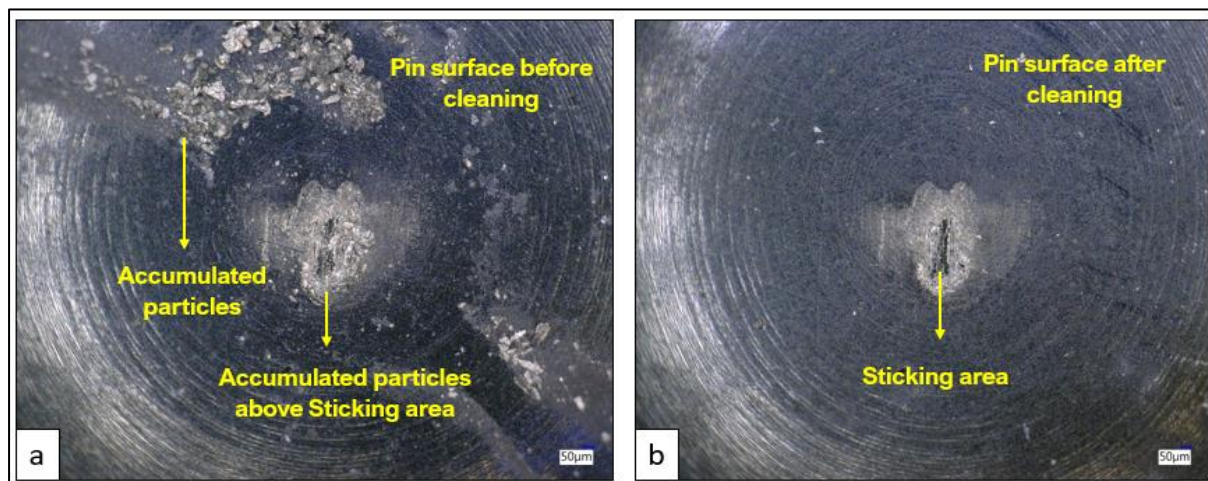


Figure 47 The quantification of adhesion (a) Accumulated particles above the sticking area (b) Sticking area after cleaning accumulated particles.

The pin *cross-sectioning* consisted of four steps:

1. **Step 1: Cutting**

- The pins were cut with EDM far away from the *sticking material* area.

2. **Step 2: Moulding**

- The samples were moulded into carbon dies.

3. **Step 3: Grinding**

- The samples were ground sequentially with grit size of 80, 240, 600, 800 and 1200 under water.

4. **Step 4: Polishing**

- Polishing lap cloths (coarse and fine) were used to obtain a mirror like finish for the samples. Monocrystalline diamond paste of 6 μm and 1 μm were used with ethyl alcohol. A final polishing was done with colloidal silica of 0.1 μm .

The coating wear (or wear) can be defined as the erosion of coating material which occurs as a result of extreme contact conditions. Microscopically, the coatings may limit the interactions between the tool and the workpiece and reduce all the three components of friction i.e., ploughing action of asperities, deformation of asperities and adhesion. The wear to the coating (if any) would be located underneath the *sticking area* of the workpiece on the pin. Therefore, a few selected pins (with highest and lowest contact pressure and sliding velocity combination) were cross-sectioned and examined microscopically to check for wear of the coating (Figure 48 a-d)

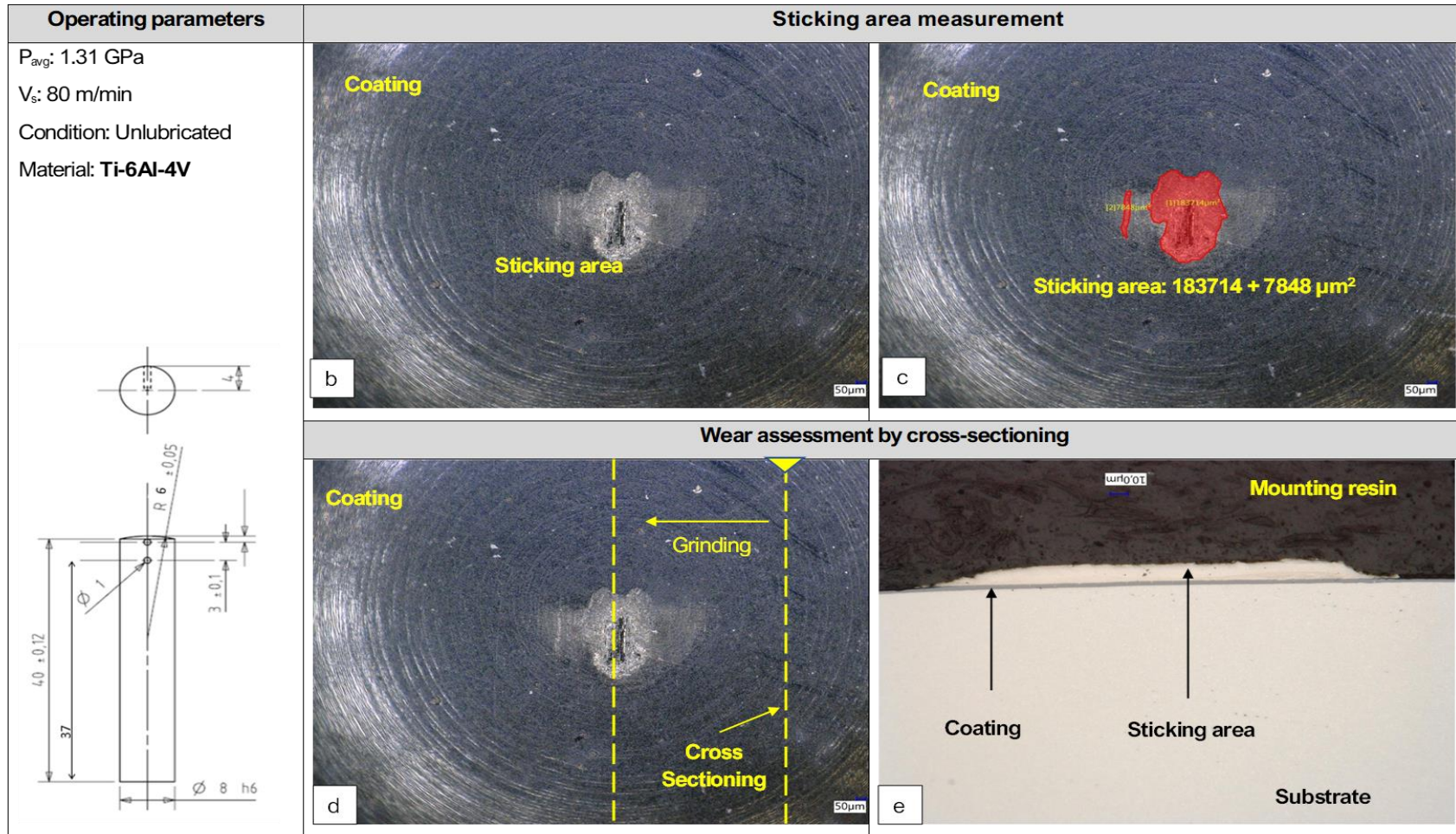


Figure 48 Cross-sectioning procedure for selected pins (a) pin dimensions (b) sticking area of the pins (c) optical measurement of sticking area (d) cross sectioning of the pins (e) measurement of coating wear

4.2 DESIGN OF EXPERIMENTS

The design of experimental plan had to accommodate the following the considerations:

- All the contact conditions existing during machining had to be experimented with i.e., the range of contact pressures from (1 – 3 GPa) combined with range of sliding velocities (35 – 120 m/min) are represented in the experimental plan. This was done to know the trends are low and high contact conditions.
- The combination of each contact condition had to be experimented with each lubricant (Dry, MQL, EML). For ex. 1.31 GPa + 37.50 m/min with each of dry, MQL, EML lubricants.
- Optimisation of time and resources (pin substrates and coating).

Thus to include all the foregoing aspects, a Central Composite Design (CCD) as described by Cavazzuti [143] was used to develop the test matrix for Ti64, NL and D alloys, each comprising eleven experiments. Thus, the central points of the CCD (2.30 GPa + 80 m/min) were repeated three times to calculate the uncertainty of the experiments. The validation of any experimental point in the test matrix was done by applying the uncertainty of central point repetitions.

Additionally, experiments were performed randomly without the set order to avoid any potential defects arising due to incremental order of contact pressure. For ex. if the first experiments were done with 2.30 GPa + 80 m/min, the next was done with 1.60 GPa + 110 m/min, and the next with 2.30 + 37.5 m/min and so on. A total of 132 tests were conducted with all lubricants.

The friction coefficient values obtained by the experiments were subjected to response surface modelling to assess the evolution of the friction coefficient as a function of sliding velocity and contact pressure. Sliding velocity and contact pressures were treated as input parameters, and the macroscopic friction coefficient was the output parameter. The Table 17 sets out the experimental plan for each lubricant, while the design of experiments is presented in Table 18.

A few tests with uncoated substrates were also carried out to know the effectivity of coatings. However, these tests were carried out at the central points of 2.30 GPa + 80 m/min. As the tribometer pins were customized and specially manufactured, the stock of these pins was limited. Thus, the effectivity of coatings could only be ascertained at

the central points. Thus, a total of 33 uncoated tests were conducted at 2.30 GPa + 80 m/min with all the lubricants. The uncoated tests were repeated three times and the difference was treated as uncertainty. The uncoated tests were further compared with the three repetitions of the coated pins to know the coating effectivity.

A few tests were conducted to assess the coating wear. The pins at 1.31 GPa + 80 m/min and 3.27 GPa + 80 min/min i.e., tests at the beginning and the end of the test matrix were selected for the assessment. The contact pressure ended up being the statistically significant property. This has been described in detail in Section 4.3. Therefore, pins at constant sliding velocity but different contact pressures were selected for coating wear analysis. The coating wear analysis was conducted after the friction assessment. No repetitions could be conducted as the contact conditions mentioned above were carried out only once during friction characterization.

The heat partition tests required temperature measurements. Thus, special pins were manufactured to place the thermocouples. No repetitions were carried out due to the limited stock of the pins. The measurements were taken at 2.30 GPa + 80m/min for each alloy with each lubricant.

The test matrix comprised of two Phases:

- **Phase 1:** Tests in dry conditions. A total of 33 tests were carried out with coated pins and 9 tests were conducted with uncoated pins.
- **Phase 2:** Tests with lubricants. A total of 99 tests were carried out with coated pins using EML, MQLVP and MQLSE1 lubricants. 27 tests were carried out with uncoated pins with the same lubricants.

All the experiments from friction measurement, adhesion assessment, coating wear analysis, and the measurement of temperature for the calculation of heat partition were done at CEROC, France. This entity later became Advanced Assisted Manufacturing Solutions (AAMS), Fondettes.

Tribological characterisation

Table 17 The total test carried out for Ti-6Al-4V, Ti-48Al-2Cr-2Nb NL and D alloys with different lubricants

Experimental plan for Pin on Cylinder tests with all lubricants							
Coated				Uncoated			
Phase	Material	Lubricants	DoE tests	Material	Lubricants	Normal	
Phase 1: Dry	NL	None	11	NL	None	3	
	D	None	11	D	None	3	
	Ti64	None	11	Ti64	None	3	
Phase 2: Lubricants	NL	EML	11	NL	EML	3	
	D	EML	11	D	EML	3	
	Ti64	EML	11	Ti64	EML	3	
	NL	MLSE1	11	NL	MLSE1	3	
	D	MLSE1	11	D	MLSE1	3	
	Ti64	MLSE1	11	Ti64	MLSE1	3	
	NL	MLVP	11	NL	MLVP	3	
	D	MLVP	11	D	MLVP	3	
	Ti64	MLVP	11	Ti64	MLVP	3	
	Total tests	132			36		

Table 18 Design of experiments for Ti-48Al-2Cr-2Nb (NL and D) and Ti-6Al-4V, phase 1 and phase 2

Central Composite Design for coated pins					
Test number and point	(NL & D)		Ti64		Sliding velocity, V_s , m/min
	Hertzian contact pressure, P_{avg} , GPa	Normal Force, F_n , N	Hertzian contact pressure, P_{avg} , GPa	Normal Force, F_n , N	
1	1.31	10	1.31	21	80
2	1.61	17	1.61	39	50
3	1.61	17	1.61	39	110
4	2.30	49	2.30	115	37.58
5	2.30	49	2.30	115	80
6	2.30	49	2.30	115	80
7	2.30	49	2.30	115	80
8	2.30	49	2.30	115	122.42
9	3.01	110	3.01	260	50
10	3.01	110	3.01	260	110
11	3.27	140	3.27	325	80
Design for uncoated pins					
13	2.30	49	2.30	115	80
14	2.30	49	2.30	115	80
15	2.30	49	2.30	115	80

4.3 RESULTS

The results are divided into three parts. The first part discusses friction characterisation and provides a compares friction evolution with dry, EML, MQLVP and MQLSE1 lubricants. The second section describes the adhesion and coating wear analysis of the pins with lubricants. The third section reports the heat partitioning between tool and workpiece during the experiments with all the lubricants.

4.3.1 FRICTION CHARACTERISATION

The CCD experimental plan for the POC experiments consists of three repetitions of 2.3 GPa and 80 m/min (centre points) for all the alloys. The differences observed during the repetitions at the central points are characterised as uncertainties of the experiments, set out in Table 19. According to the CCD design, these uncertainties are applicable to the other experimental points in the test matrix as well. The uncertainties change with the lubricants. This is because of the difference in tribological properties of lubricants. A lower uncertainty indicates better lubrication between tool – workpiece contact.

Table 19 Absolute uncertainty observed during the friction characterisation of NL, D and Ti64 alloys with dry, EML, MQLSE1 and MQLVP lubricants

Alloy	Absolute uncertainty in friction characterization			
	Dry	EML	MQLSE1	MQLVP
Coated				
NL	0.005	0.05	0.05	0.05
D	0.01	0.05	0.05	0.05
Ti64	0.01	0.05	0.01	0.01
Uncoated				
NL	0.005	0	0.05	0
D	0.005	0	0.05	0
Ti64	0	0.05	0.05	0.01

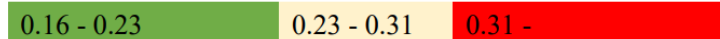
The main objective of analysing the results with Response Surface Modelling (RSM) was to assess which of the input parameter (sliding velocity, contact pressure, lubrication) have the maximum / or a statistically significant effect on the apparent friction coefficient. Thus, the p-values in the model analysed to determine if they were less than or equal to the significance level (α) of 0.05. An α value of 0.05 would indicate that there is a 5% risk of concluding that an association exist between parameters when there is no actual association. The result demonstrated that all parameters were

Tribological characterisation

statistically significant as their variance is less than the α value. The friction characteristics of each alloy are reported in Table 20.

Table 20 Apparent friction coefficients of Ti-6Al-4V and Ti-48Al-2Cr-2Nb (NL and D) with dry, EML, MQLSE1 and MQLVP lubricants

Sl. Nr	Contact pressure, (GPa)	Sliding Velocity, (m/min)	App. Friction coefficient (μ_{app}) of Ti-48Al-2Cr-2Nb (NL)				App. Friction coefficient (μ_{app}) of Ti-48Al-2Cr-2Nb (D)				App. Friction coefficient (μ_{app}) of Ti-6Al-4V			
			Dry	EML	MQLSE1	MQLVP	Dry	EML	MQLSE1	MQLVP	Dry	EML	MQLSE1	MQLVP
1	1.31	80	0.2	0.26	0.16	0.24	0.24	0.27	0.26	0.21	0.38	0.42	0.4	0.37
2	1.61	50	0.29	0.28	0.24	0.26	0.24	0.28	0.25	0.27	0.45	0.35	0.4	0.31
3	1.61	110	0.24	0.24	0.21	0.23	0.19	0.25	0.23	0.22	0.41	0.37	0.4	0.36
4	2.3	37.58	0.32	0.27	0.26	0.27	0.27	0.27	0.27	0.26	0.47	0.34	0.35	0.29
5	2.3	80	0.23	0.24	0.24	0.22	0.23	0.25	0.24	0.26	0.46	0.31	0.29	0.3
6	2.3	80	0.23	0.25	0.25	0.21	0.21	0.25	0.25	0.24	0.42	0.31	0.27	0.27
7	2.3	80	0.24	0.24	0.24	0.21	0.23	0.24	0.23	0.25	0.46	0.3	0.27	0.28
8	2.3	122.42	0.23	0.23	0.22	0.25	0.26	0.22	0.23	0.26	0.4	0.32	0.3	0.26
9	3.01	50	0.28	0.26	0.27	0.23	0.28	0.26	0.27	0.27	0.24	0.27	0.28	0.27
10	3.01	110	0.31	0.29	0.32	0.26	0.31	0.27	0.3	0.3	0.3	0.26	0.23	0.22
11	3.27	80	0.29	0.27	0.26	0.22	0.31	0.27	0.3	0.3	0.29	0.24	0.25	0.23
Uncoated pins														
1	2.3	80	0.24	0.25	0.26	0.23	0.24	0.25	0.25	0.25	0.27	0.31	0.29	0.29
2	2.3	80	0.24	0.25	0.25	0.23	0.23	0.25	0.26	0.25	0.27	0.3	0.28	0.27
3	2.3	80	0.25	0.25	0.26	0.23	0.24	0.25	0.26	0.25	0.27	0.31	0.27	0.27



Note: Sl. Nr 5,6, and 7 are repetitions. The difference in the values of repetitions is the uncertainty. The uncertainty is applicable to the other experimental points

- **Ti-6Al-4V**

The apparent friction coefficients for Ti64 were almost 50% higher than the NL and D alloys. For example, in dry conditions Ti64 presented a value of 0.44 ± 0.02 , whereas NL was 0.23 ± 0.01 and D 0.21 ± 0.01 . The results for the Ti64 alloy, showed that apparent friction coefficients were highest in dry conditions followed by EML and MQLSE1. MQLVP presented the lowest values.

For all the lubricants, an increase in contact pressure (P_{avg}) led to a decrease in μ_{app} indicating an inversely proportional relationship between contact pressure and μ_{app} . This trend is clearly depicted in Figure 49. Thus, the contact pressure was the statistically significant quantity/ property. This trend was similar to the findings of Grzesik et al [134], where the friction coefficient decreased with the increase in contact pressure. The authors report work hardening to be the reason for this trend. However, it is important to remark that the friction values could not be compared to the foregoing findings as normal forces from 10 – 30N were used. Additionally, the forces were not calculated by Hertzian contact theory. Yet, the trends could be compared on standalone basis.

The sliding velocity (v_c) presented conflicting trends (Table 21), depending on the lubricant. In dry conditions with $P_{avg} \leq 2.3$ GPa, any increase in v_c led to a fall in μ_{app} values. But as the P_{avg} passed the 2.3 GPa, any increase in sliding velocity led to an increase in the μ_{app} values. This can be seen at 3.01 GPa, where 50 m/min yielded a μ_{app} 0.24, that at 110 m/min had a value of 0.3.

Table 21 Dependency of sliding velocity on contact pressures in evolution of μ_{app} for all lubricants and Ti-6Al-4V alloy

Contact pressure, P_{avg} , (GPa)	Sliding velocity, v_c , (m/min)	Dry, Apparent friction coefficient, μ_{app}	EML, Apparent friction coefficient, μ_{app}	MQLSE1, Apparent friction coefficient, μ_{app}	MQLVP, Apparent friction coefficient, μ_{app}
1.61	50	0.45	0.35	0.4	0.31
1.61	110	0.41	0.37	0.4	0.36
2.3	37.58	0.47	0.34	0.35	0.29
2.3	122.42	0.4	0.32	0.3	0.26
3.01	50	0.24	0.27	0.28	0.27
3.01	110	0.3	0.26	0.23	0.22

Tribological characterisation

As the dry analysis had shown high μ_{app} than lubricants, track analysis was conducted to check the material surface quality. The chances of presence of material deformations are high with dry lubrication. However, the material was crack free and comprised of a smoother surface as shown in Figure 50.

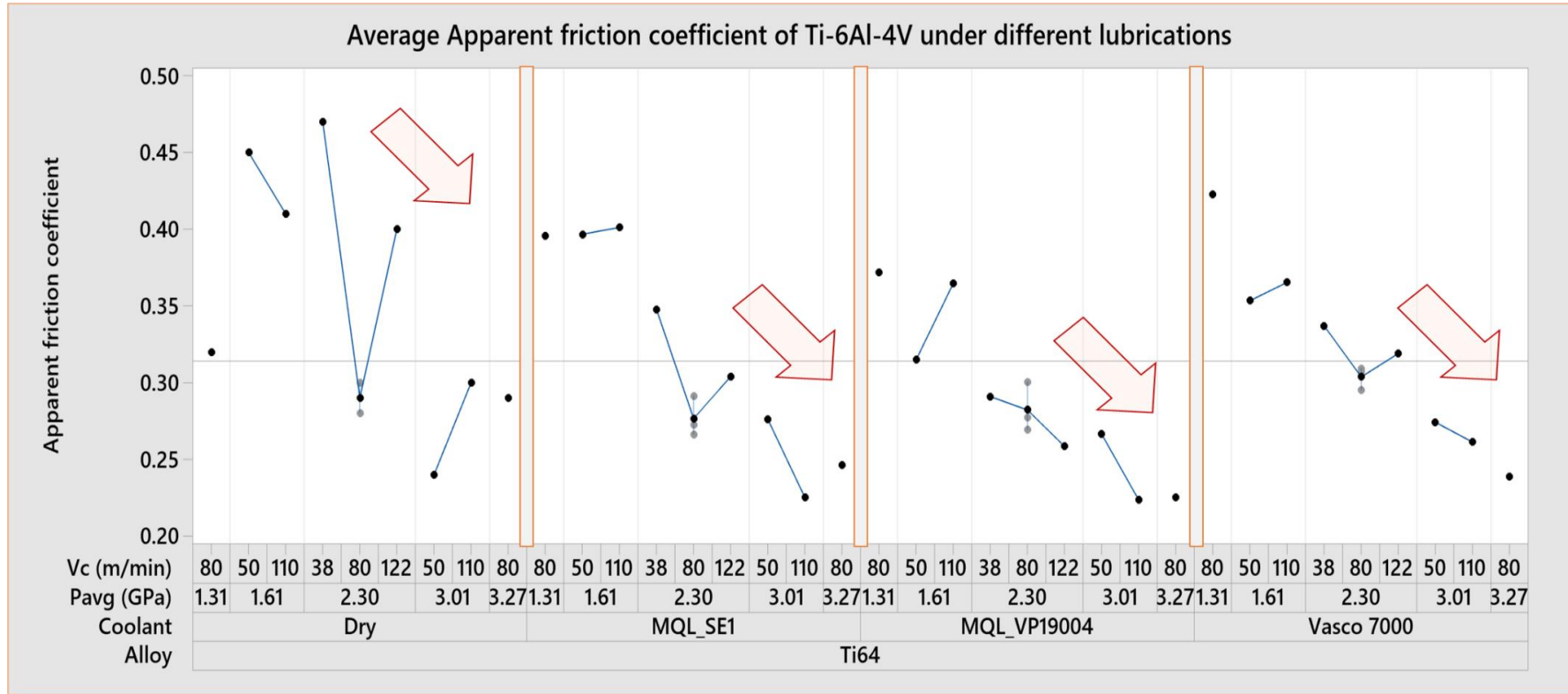


Figure 49 Variation of apparent friction coefficient of Ti-6Al-4V alloy with dry, EML, MQLSE1 and MQLVP

Thus, a parabolic trend for v_c was clearly seen in dry conditions. With EML and MQLSE1, no discernible trend was noted. While at low P_{avg} (1.31 GPa) with an increase in v_c led to only a marginal increase in μ_{app} , at high P_{avg} any increase in v_c led to a decrease in μ_{app} . Importantly, at 2.3 GPa, an increase in v_c resulted in increase of μ_{app} . Thus with both the lubricants, v_c is highly dependent on P_{avg} . In the case of MQLVP, except for one condition (1.61 GPa), an increase in v_c brought about a decrease in μ_{app} .

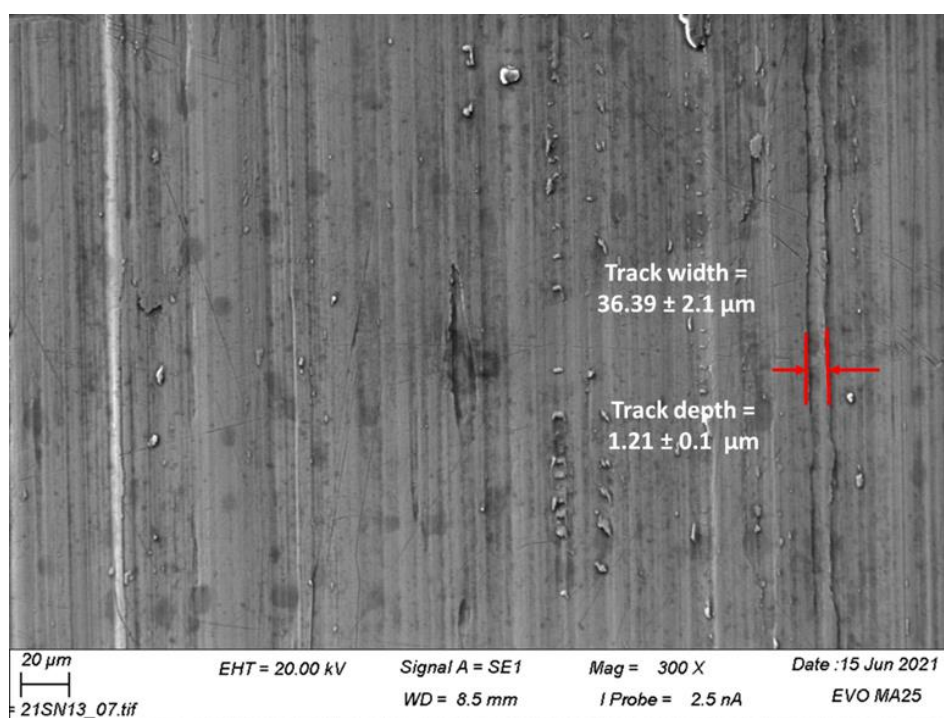


Figure 50 Track analysis of Ti-6Al-4V with dry lubrications showing a crack free surface

Importantly, the lubricants (EML, MQLSE1 and MQLVP) produced lower μ_{app} values than dry conditions. One possible explanation could be that the lubricants had a wetting effect on the asperities making them more susceptible to fracture as compared to the dry conditions leading to low μ_{app} values. This is in accordance with the findings of Suh et al. [102]. It would appear that when the contact pressures were lower, higher resistance needed to be overcome to satisfy shearing of asperities junctions leading to higher μ_{app} .

- **Ti-48Al-2Cr-2Nb (Near lamellar)**

The Ti-48Al-2Cr-2Nb alloys have a fundamentally different μ_{app} evolution pattern than Ti-6Al-4V alloy. No large deviation of μ_{app} were seen with all lubricants for all the contact conditions. The overall range of μ_{app} for all the lubricants fell between 0.2 – 0.30 except for MQLSE1 at 1.31 GPa ($\mu_{app} = 0.16$). At the outset, all the lubricants performed equally. However, statistically, the MQLVP oil yielded lower μ_{app} values than other lubricants.

The effect of contact conditions on μ_{app} is dependent on lubricants. With dry and MQLSE1, the μ_{app} increased with the increase in contact pressure. Only with EML and MQLVP 19004, the μ_{app} values were consistent with all the contact conditions and were not affected by the change in contact pressure. The μ_{app} trend of Ti-48Al-2Cr-2Nb (NL) alloy with all lubricants are set out in Figure 51.

The v_c showed conflicting outcomes based on the P_{avg} as seen in Table 22. The increase in sliding velocity led to a decrease in μ_{app} when the contact pressure was ≤ 2.3 GPa. Upon crossing this threshold, the μ_{app} increased increase in sliding velocity.

Table 22 Relationship between sliding velocity and contact pressures in terms of evolution of μ_{app} for all lubricants seen in Ti-48Al-2Cr-2Nb (NL) alloy

Contact pressure, P_{avg} , (GPa)	Sliding velocity, v_c , (m/min)	Dry, Apparent friction coefficient, μ_{app}	EML, Apparent friction coefficient, μ_{app}	MQLSE1, Apparent friction coefficient, μ_{app}	MQLVP, Apparent friction coefficient, μ_{app}
1.61	50	0.29	0.28	0.24	0.26
1.61	110	0.24	0.24	0.21	0.23
2.3	37.58	0.32	0.27	0.26	0.27
2.3	122.42	0.23	0.23	0.22	0.25
3.01	50	0.28	0.26	0.27	0.23
3.01	110	0.31	0.29	0.32	0.26

This trend was evident for all the lubricants. Thus, it can be seen that effect of sliding velocity on the apparent friction coefficient, is dependent on the contact pressure.

Nevertheless, it is important to analyse why the alloy shows similar μ_{app} across all contact pressures for EML and MQLVP. According to the work of Suh et al. [102], the initial

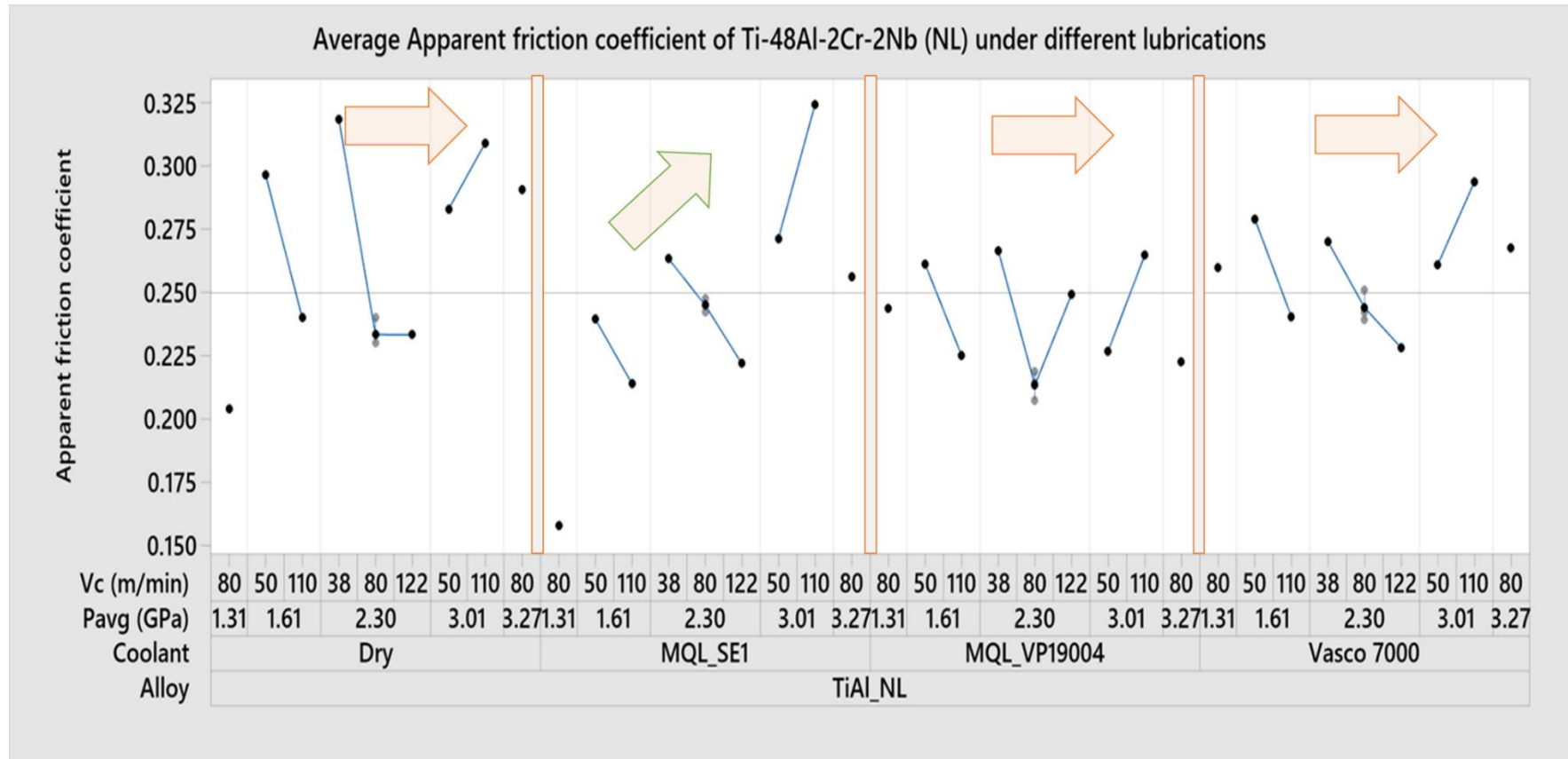


Figure 51 Variation of apparent friction coefficient of Ti-48Al-2Cr-2Nb (NL) alloy with dry, EML, MQLSE1 and MQLVP

values of friction coefficient are due to the ploughing action of surface by asperities and adhesion does not contribute to increasing μ_{app} at this stage due to contaminated nature of the surface. Beyond this stage the increase in friction values is dependent on the volume of entrapped workpiece debris.

Apparently, the consistency of μ_{app} under all contact pressures could be due to the high material integrity of Ti-48Al-2Cr-2Nb (NL) alloy when combined with EML and MQLVP19004 oil leading to low adhesion of workpiece to the pins. These lower μ_{app} values would suggest that friction evolution in the Ti-48Al-2Cr-2Nb (NL) alloy is unable to pass stage 1 (initial stage) of friction evolution. Thus, μ_{app} values represent the kinematic friction coefficient (μ_i) in all contact conditions. The wear track analysis conducted with dry condition showed crack free surfaces as seen in the Figure 52. Although, some damage to the material surface was evident, it was limited to pullouts.

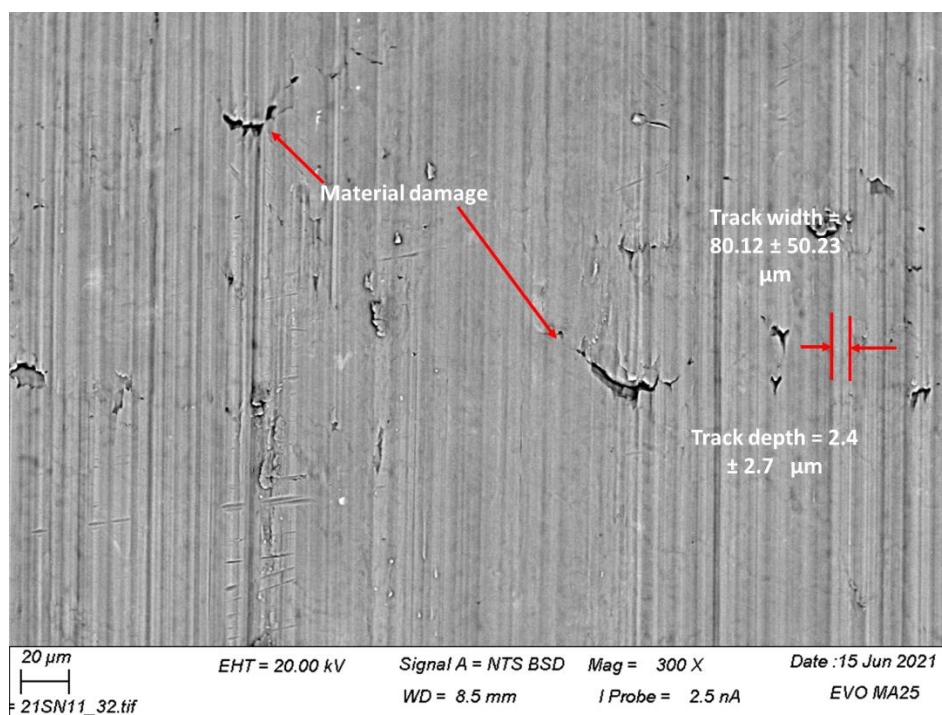


Figure 52 Track analysis of Ti-48Al-2Cr-2Nb (NL) with dry lubrications showing a crack free but damaged surface

- **Ti-48Al-2Cr-2Nb (Duplex)**

In the case of Ti-48Al-2Cr-2Nb (D), alloy it was seen that an increase in contact pressure led to the increase in μ_{app} with dry, MQLSE1 and MQLVP 19004 oils. The EML delivered consistent μ_{app} across all the contact conditions. No change in μ_{app} values was seen with change in contact pressures (0.27 at 1.31 GPa and 0.27 at 3.27 GPa). The trends are seen in Figure 53. The sliding velocity retraced the same pattern as seen with Ti-48Al-2Cr-2Nb (NL). The trend is highlighted in Table 23.

Table 23 Relationship between sliding velocity and contact pressures in terms of evolution of μ_{app} for all lubricants seen in Ti-48Al-2Cr-2Nb (D) alloy

Contact pressure, P_{avg}, (GPa)	Sliding velocity, v_c, (m/min)	Dry, Apparent friction coefficient, μ_{app}	EML, Apparent friction coefficient, μ_{app}	MQLSE1, Apparent friction coefficient, μ_{app}	MQLVP, Apparent friction coefficient, μ_{app}
1.61	50	0.24	0.28	0.25	0.24
1.61	110	0.19	0.25	0.23	0.22
2.3	37.58	0.27	0.27	0.27	0.26
2.3	122.42	0.26	0.22	0.23	0.26
3.01	50	0.28	0.26	0.27	0.27
3.01	110	0.31	0.27	0.3	0.3

The increase sliding velocity caused a decrease in μ_{app} until the contact pressure was ≤ 2.3 GPa. Once past this threshold value, the relationship became directly correlated. Therefore, it can be seen that sliding velocity is dependent on contact pressure. This leads to the conclusion that in the case of Ti-48Al-2Cr-2Nb (D) alloys the contact pressure is a statistically significant property for all lubricants except EML.

In the case of the latter, the trends indicate that μ_{app} is equivalent to the μ_p (friction due to ploughing action of asperities) and other components like friction like plastic deformation of asperities and friction component due to adhesion appear to have no influence on the μ_{app} . This could be attributed to high flowrate of EML preventing the build of adhesive material on the pins thereby delivering a consistent μ_{app} under all contact conditions. Interestingly, with MQLVP 19004, the Ti-48Al-2Cr-2Nb (D) did not show the same attributes as Ti-48Al-2Cr-2Nb (NL).

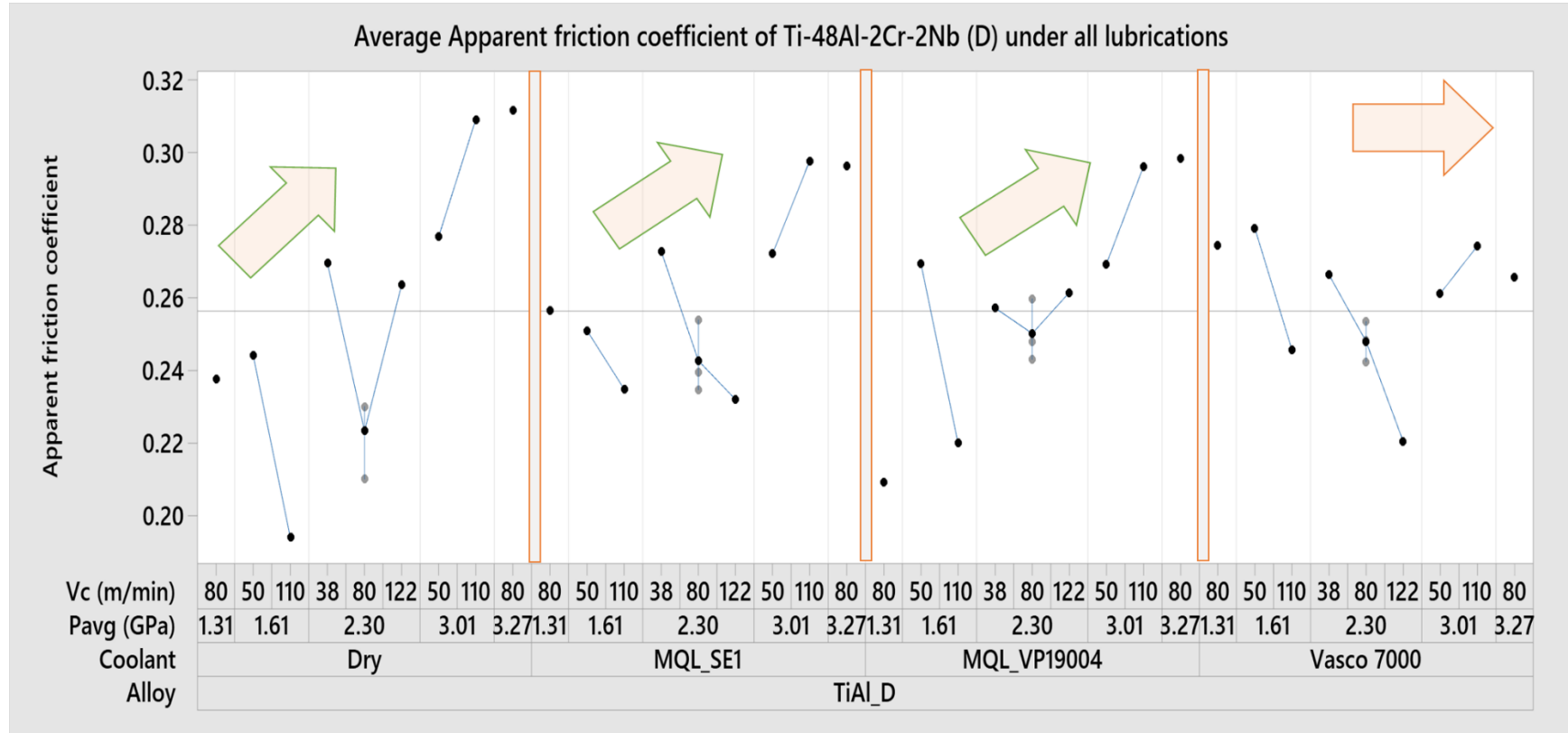


Figure 53 Variation of apparent friction coefficient of Ti-48Al-2Cr-2Nb (D) alloy with dry, EML, MQLSE1 and MQLVP19004

Interestingly, the wear track analysis of Ti-48Al-2Cr-2Nb (D) showed cracks as seen in Figure 54. The results are interesting as the Ti-48Al-2Cr-2Nb (NL) is the harder than Ti-48Al-2Cr-2Nb (D). The results also indicates that due to the friction, there is dragging of the cracks with high ploughing action/component.

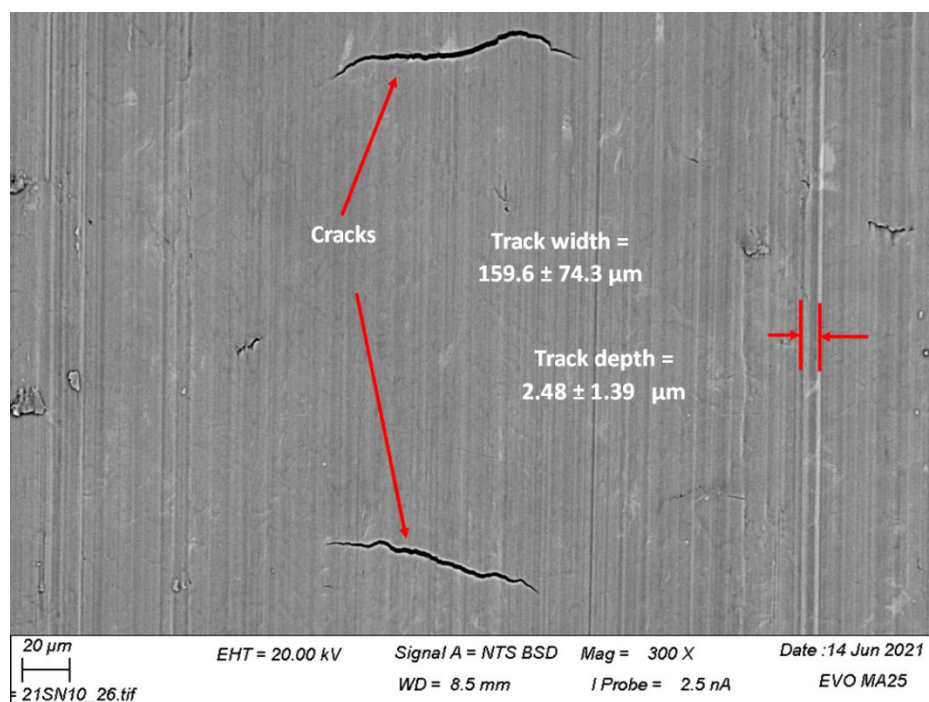


Figure 54 Track analysis of Ti-48Al-2Cr-2Nb (D) with dry lubrications showing wear track surface with cracks

4.3.2 ADHESION AND COATING WEAR ASSESSMENT

The experiments conducted to quantify the adhesion area were robust with low uncertainties, as shown in Table 24. As in the case of friction measurement, the uncertainties during adhesion measurement were carried out at the central points. Interestingly, the uncertainties during dry experiments are very low in comparison to the lubricants. Additionally, the difference the values of lubricants indicate the difference in tribological properties affecting the material adhesion on to the pin.

The Ti64 and NL & D alloys reported fundamentally different adhesion trends (Table 25). Since the trends and area for both NL and D are similar, the adhesion performance of these alloys is presented together to avoid repetition.

Table 24 Absolute uncertainty from adhesion measurements of the NL, D and Ti64 alloys with dry, EML, MQLSE1 and MQLVP lubricants

Alloy	Absolute uncertainty in adhesion measurement (mm ²)			
	Dry	EML	MQLSE1	MQLVP
Coated				
NL	0.005	0.05	0.01	0.025
D	0.02	0.02	0.005	0.02
Ti64	0.22	0.035	0.08	0.01
Uncoated				
NL	0.006	0.005	0.005	0.01
D	0.01	0.03	0.005	0
Ti64	0.03	0.02	0.03	0.005

The principal objective of the coating wear analysis was to identify any damage to the pin coating in any of the experiments. Therefore, a few selected pins (with lowest and highest $P_{avg} = 1.31$ and 3.27 GPa and constant $v_s = 80$ m/min) were chosen for cross section analysis. The cross section analysis was conducted after the friction assessment, wherein it was found that P_{avg} was the statistically significant property. Thus, pins with different P_{avg} but with same v_s were chosen for the analysis. A total of 18 tests were conducted during coating wear analysis. Every alloy was tested for minimum and maximum contact pressure at a given sliding velocity and lubricant. For example, Ti-6Al-4V at $P_{avg} = 1.31 + 80$ m/min and 3.27 GPa + 80 m/min in dry condition. This was repeated for EML and MQLSE1. Similarly for Ti-48Al-2Cr-2Nb alloys.

No repetitions were carried out of the analysis. It is important to note that the coating wear analysis was carried out after the friction experiments. As no repetitions were not carried out for $P_{avg} = 1.31$ and 3.27 GPa during friction characterisations, no pins were available for coating wear analysis. The coating wear analysis with MQLVP19004 could not be conducted due to budgetary constraints.

Tribological characterisation

Table 25 Quantification of adhesion area of Ti-48Al-2Cr-2Nb (NL) and Ti-48Al-2Cr-2Nb (D) with dry, EML, MQLSE1 and MQLVP 19004 lubricants

Sl. Nr	Contact pressure, (GPa)	Sliding Velocity, (m/min)	Adhesion area (mm ²) of Ti-48Al-2Cr-2Nb (NL)				Adhesion area (mm ²) of Ti-48Al-2Cr-2Nb (D)				Adhesion area (mm ²) of Ti-6Al-4V			
			Dry	EML	MQLSE1	MQLVP	Dry	EML	MQLSE1	MQLVP	Dry	EML	MQLSE1	MQLVP
1	1.31	80	0.05	0.05	0.02	0.05	0.06	0.04	0.02	0.02	0.29	0.06	0.10	0.09
2	1.61	50	0.04	0.04	0.01	0.01	0.09	0.03	0.01	0.01	0.14	0.06	0.19	0.07
3	1.61	110	0.00	0.03	0.02	0.06	0.15	0.04	0.02	0.06	0.18	0.07	0.21	0.12
4	2.3	37.58	0.02	0.07	0.03	0.02	0.06	0.03	0.03	0.04	0.17	0.10	0.12	0.11
5	2.3	80	0.03	0.02	0.03	0.13	0.08	0.04	0.02	0.03	0.63	0.26	0.17	0.19
6	2.3	80	0.02	0.03	0.03	0.08	0.06	0.06	0.02	0.06	0.23	0.19	0.12	0.17
7	2.3	80	0.02	0.03	0.05	0.08	0.09	0.08	0.03	0.07	0.66	0.20	0.33	0.19
8	2.3	122.42	0.05	0.05	0.06	0.10	0.11	0.06	0.02	0.05	1.10	0.26	0.25	0.24
9	3.01	50	0.06	0.07	0.08	0.08	0.1	0.10	0.06	0.05	0.23	0.21	0.24	0.28
10	3.01	110	0.16	0.15	0.08	0.14	0.21	0.15	0.11	0.08	0.67	0.49	0.39	0.28
11	3.27	80	0.13	0.11	0.07	0.10	0.15	0.13	0.12	0.08	0.62	0.51	0.52	0.34
Uncoated pins														
1	2.3	80	0.045	0.07	0.06	0.06	0.04	0.13	0.06	0.06	0.31	0.31	0.26	0.23
2	2.3	80	0.052	0.06	0.05	0.08	0.04	0.07	0.05	0.06	0.33	0.30	0.22	0.22
3	2.3	80	0.056	0.07	0.06	0.06	0.06	0.07	0.06	0.06	0.27	0.33	0.21	0.22
Scale							0.01 - 0.06			0.07 - 0.34		0.34 -		

Note: Sl. Nr 5,6, and 7 are repetitions. The difference in the values of repetitions is the uncertainty. The uncertainty is applicable to the other experimental points

- **Adhesion of Ti-6Al-4V**

Using dry lubricant, a clear trend existed in which the adhesion area increased with increase in contact pressure. Nevertheless, some differences were observed. The experimental uncertainty was high (0.22 mm²). While two repetitions yielded almost similar values of 0.63 mm² and 0.66 mm², the third repetition yielded a lower value of 0.23 mm².

Preliminary analysis of the results seemed to indicate that a higher sliding velocity led to the quick entrapment of wear debris and thus a higher sticking area. For example, a combination of contact pressure of 2.3 GPa and a high sliding velocity 122.42 m/min produced a very high adhesion area of 1.10 mm². This value was very high considering that all other experiments yielded values < 1.10 mm². When experimental values with other lubricants were examined, the value seemed more likely to be an aberration. Thus, if this value is considered as an outlier, then the trend in dry lubricant showed that as the contact pressure increased, more and more wear debris of workpiece got entrapped leading to a higher sticking material.

It also appeared less material was able to leave the contacting bodies due to high pressure, thus increasing the amount of entrapped material. However, this observation needs further confirmation via measurement of adhesion volume.

The results showed greater adhesion area for the uncoated material. As it can be seen from Figure 55, the adhesion area increases with increase in contact pressure. The adhesion in dry conditions is greater than with lubricants. The adhesion of all the lubricants was found to be in the same range indicating that all lubricants are equally effective and play similar roles.

Nevertheless, the results did not explain that fact that though uncoated pins had delivered low (dry conditions) or equal (emulsion and both MQL oils) μ_{app} values than the coated pins, the adhesion area was found to be higher. The adhesion profile of pins is presented in Table 26.

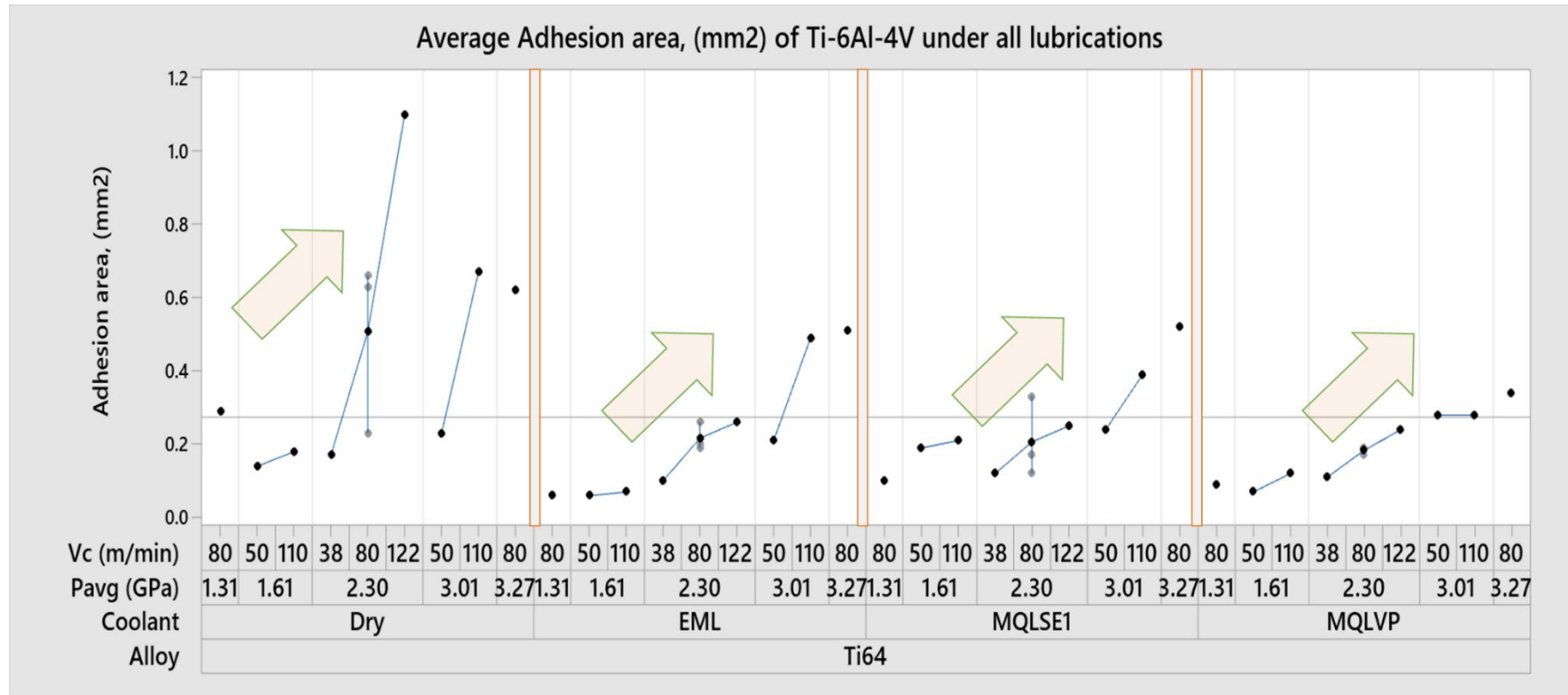


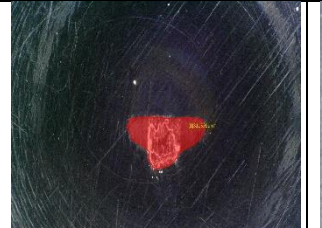






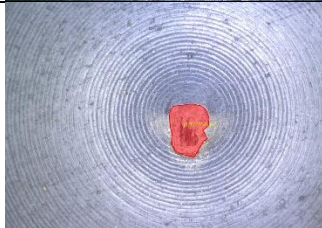

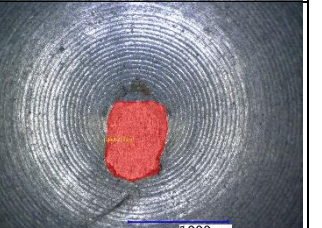






Figure 55 Increase in adhesion area with increase in contact pressure and sliding velocity for Ti-6Al-4V observed with dry, EML, MQLSE1 and MQLVP lubricants

Table 26 Adhesion profiles of Ti-6Al-4V at varying contact pressures with coated and uncoated pins under dry, emulsion, MQLSE1 and MQLVP oils

Ti-6Al-4V	1.31 GPa and 80 m/min (Coated)	2.30 GPa and 80 m/min (Coated)	2.30 GPa and 80 m/min (Uncoated)	3.27 GPa and 80 m/min (Coated)
Dry				
EML				
MQLSE1				
MQLVP				

The large adhesion area in dry condition compared to other lubricants suggested that the lubricants were able to penetrate the contacting bodies and wash away most of the wear debris. Claudin et al. [131] in their work corroborate that lubricants are able to enter the contact bodies even at high contact pressures > 2 GPa.

This trend was visible even for contact pressures up to 3.01 GPa and low sliding velocity 50 m/min in which the average adhesion area was 0.21 mm^2 . However, for the same contact pressure, as the sliding velocity increased to 110 m/min, a surge in adhesion area was observed up to 0.49 mm^2 .

The experiments with emulsion also revealed that sliding velocity played an important role in the increase of adhesion area, but only at high contact pressures. This trend was not observed at low contact pressures, however. When the sliding velocity was increased from 50 to 110 m/min at 1.61 GPa, no substantial increase in the adhesion area was recorded. This observation is in agreement with the findings of Claudin et al. [131] where the authors found that the duration of lubricant penetration is dependent on sliding velocity.

Thus, it would appear that increasing sliding velocity allows less time for the lubricant to wash the wear debris.

In the case of MQLSE1 the pure error / uncertainty arising from the repetitions was high. While two repetitions yielded 0.17 mm^2 and 0.12 mm^2 respectively, the third experiment yielded 0.33 mm^2 . The adhesion areas were quite similar to EML where adhesion area increased with increase in contact pressure. The uncoated pins had high adhesion compared to coated pins but interestingly the same μ_{app} values.

The MQLVP19004 delivered a better profile when compared to other lubricants. Though the adhesion area increased with the increase in contact pressure, the increase was not drastic as seen with other lubricants. For example, at the same and high contact pressure of 3.01 GPa, the adhesion area remained 0.28 mm^2 even after the sliding velocity increased from 50 to 110 m/min. This showed that MQLVP 19004 was able to better penetrate the contacting bodies. The adhesion areas of uncoated pins were higher than coated pins, yet the μ_{app} values remained same.

- **Coating wear of Ti-6Al4V**

At a contact pressure of 1.31 GPa as, the coating was uniform, and no erosion was observed as depicted in Figure 56 (a). However, small pockets of coating erosion were detected at 3.27 GPa as shown in Figure 56 (b). To accurately characterise and establish the type of wear, SEM analysis of the samples is necessary.

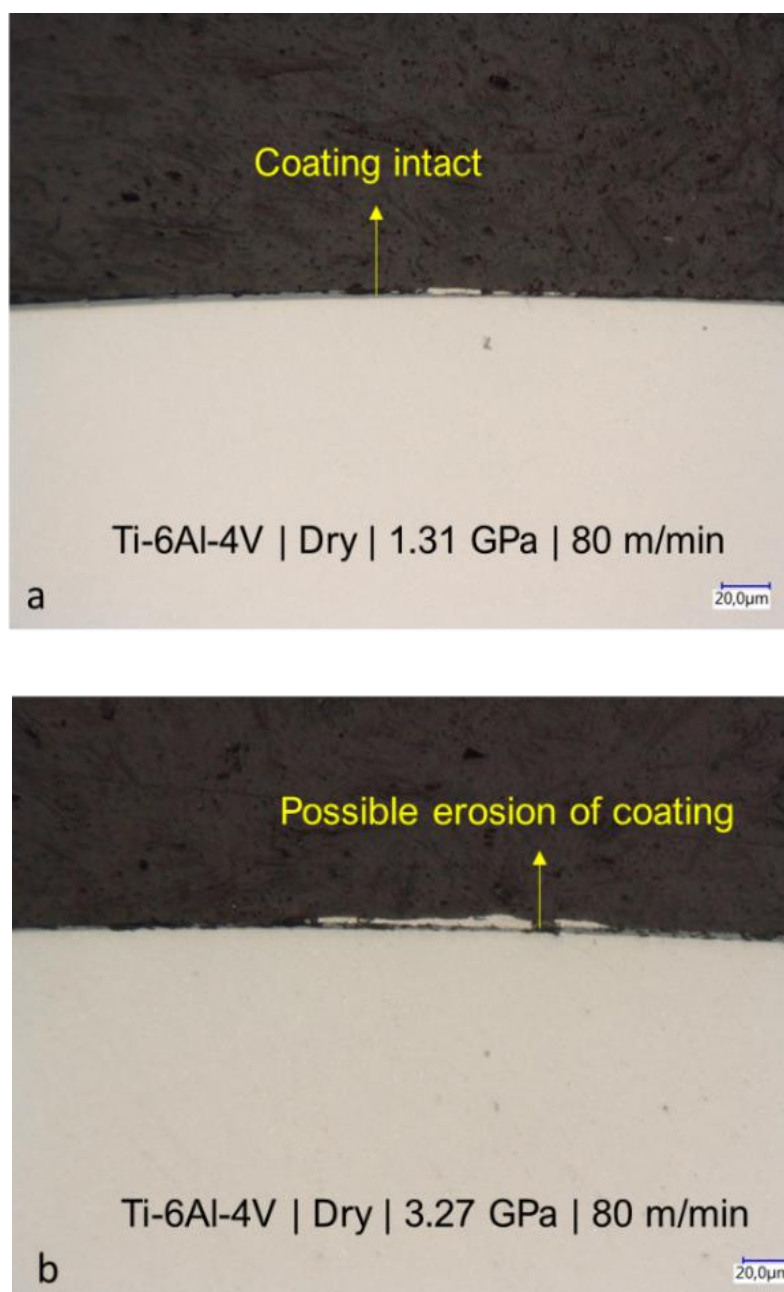


Figure 56 Coating intact at (a) 1.31 GPa and a possible coating erosion at (b) 3.27 GPa with EML for Ti-6Al-4V alloy

With emulsion, at 1.31 GPa, as depicted in Figure 57 (a), the coating was found to be intact. However, at 3.27 GPa as seen in Figure 57 (b), as observed in dry conditions, erosion of coating was found. The erosion in the form of cavities or craters was noticed in the present case. However, SEM analysis could confirm the exact nature of the wear.

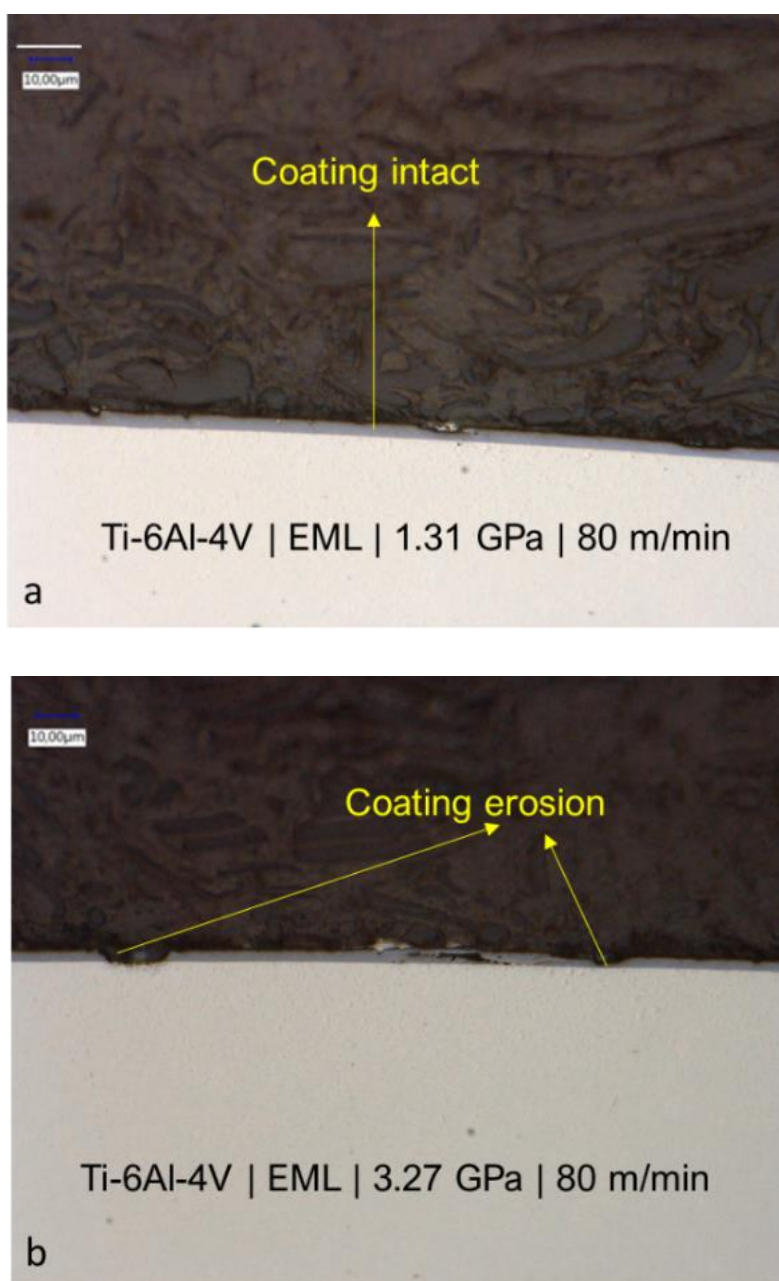


Figure 57 Coating intact at (a) 1.31 GPa and coating erosion at (b) 3.27 GPa with EML for Ti-6Al-4V alloy

In the case of MQLSE1, the coating was found to be intact in both the contact conditions. While at 1.31 GPa, as depicted in Figure 58 (a), the coating was nearly unaffected, at 3.27 GPa, seen in Figure 58 (b), some fissures in coating were detected

although they did not affect the integrity of the coatings. Like in previous cases, SEM analysis is necessary to accurately assess the nature of the fissures.

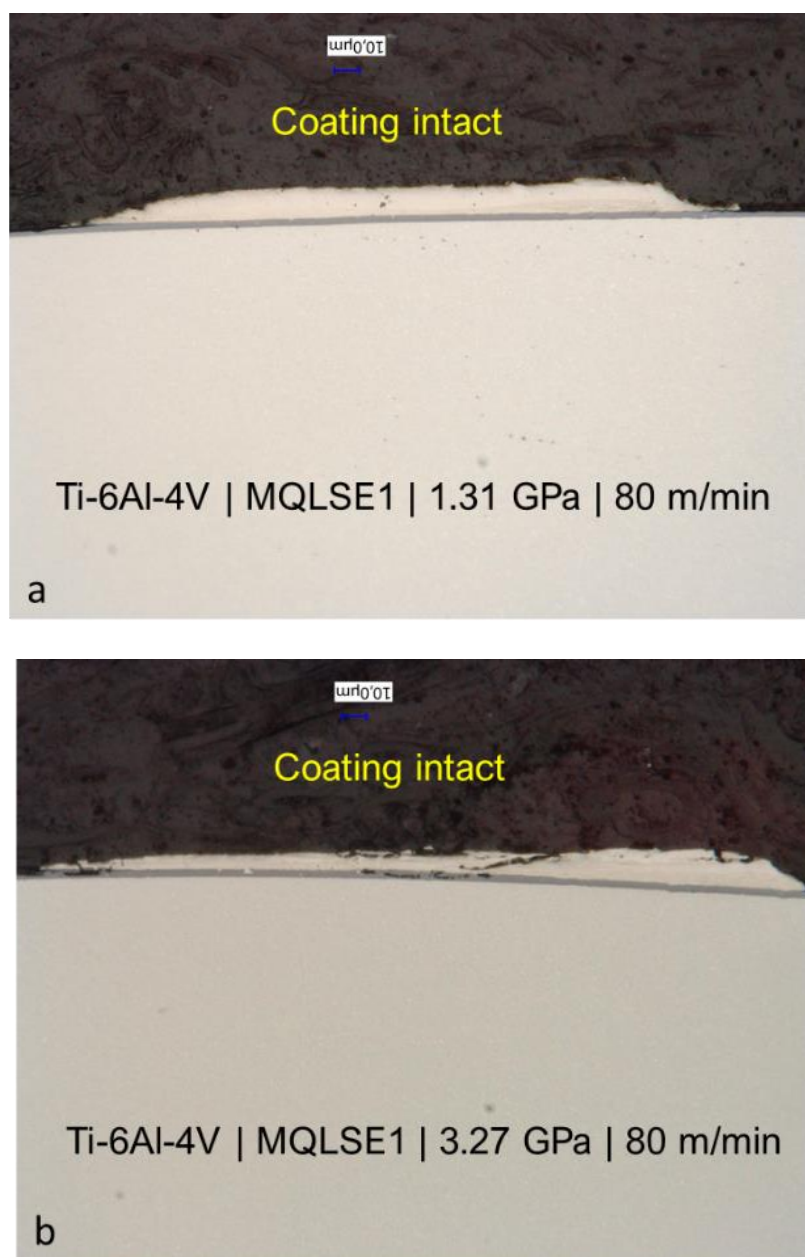


Figure 58 No damage to coating with MQLSE1 at (a) 1.31 GPa and (b) 3.27 for Ti-6Al-4V alloy

- **Adhesion of Ti48Al2Cr-2Nb (Near lamellar and Duplex)**

The adhesion area in dry conditions of Ti-48Al-2Cr-2Nb (NL) and Ti-48Al-2Cr-2Nb (D) trace the same pattern. However, area of adhesion area in Ti-48Al-2Cr-2Nb (D) microstructure was larger than Ti-48Al-2Cr-2Nb (NL). The adhesion area in both the alloys increased with increase in contact pressure.

When sliding velocity was increased from 50 m/min to 110 m/min for 1.61 GPa, a marginal increase in adhesion area was recorded (although NL showed no adhesion at 110 m/min, it could be considered to be an aberration). This meant that at lower contact pressures, adhesion area was quite consistent. This is similar to observation in Ti-6Al-4V, where no substantial increase in adhesion area was found by increasing sliding velocity at the low contact pressures.

At higher contact pressure (3.01 GPa) an increase in sliding velocity from 50 to 110 m/min led to 3-fold increase in the magnitude of adhesion area. Importantly, the μ_{app} values remained constant negating the effect of increase in the adhesion area. A significant outcome is that adhesion area did not contribute substantially to increasing μ_{app} with both the alloys. When the uncoated pins were compared, the adhesion area a little higher, 0.052 mm² against 0.03 mm². No substantial difference in μ_{app} values was registered. The trend is highlighted in Figure 59 and Figure 60.

With EML, the pure error was low (0.05 mm² and 0.02 mm²) for both the alloys indicating that experiments showed consistency. As seen with dry conditions, the low contact pressures did not lead to any substantial increase in adhesion or the sticking area. This could also be attributed to the fact that the adhesion area is very minute. With the increase in contact pressure, (3.01 GPa) an increase in the adhesion area was recorded when sliding velocity increased from 50 to 110 m/min. Importantly, this increase did not lead to any substantial increase in the values of μ_{app} . The uncoated tools showed higher adhesion area for both the alloys but as previously observed did not lead any change in μ_{app} values. An important outcome of EML assessment showed that microstructure played minimal role in the outcome as the trends for both the alloys are similar.

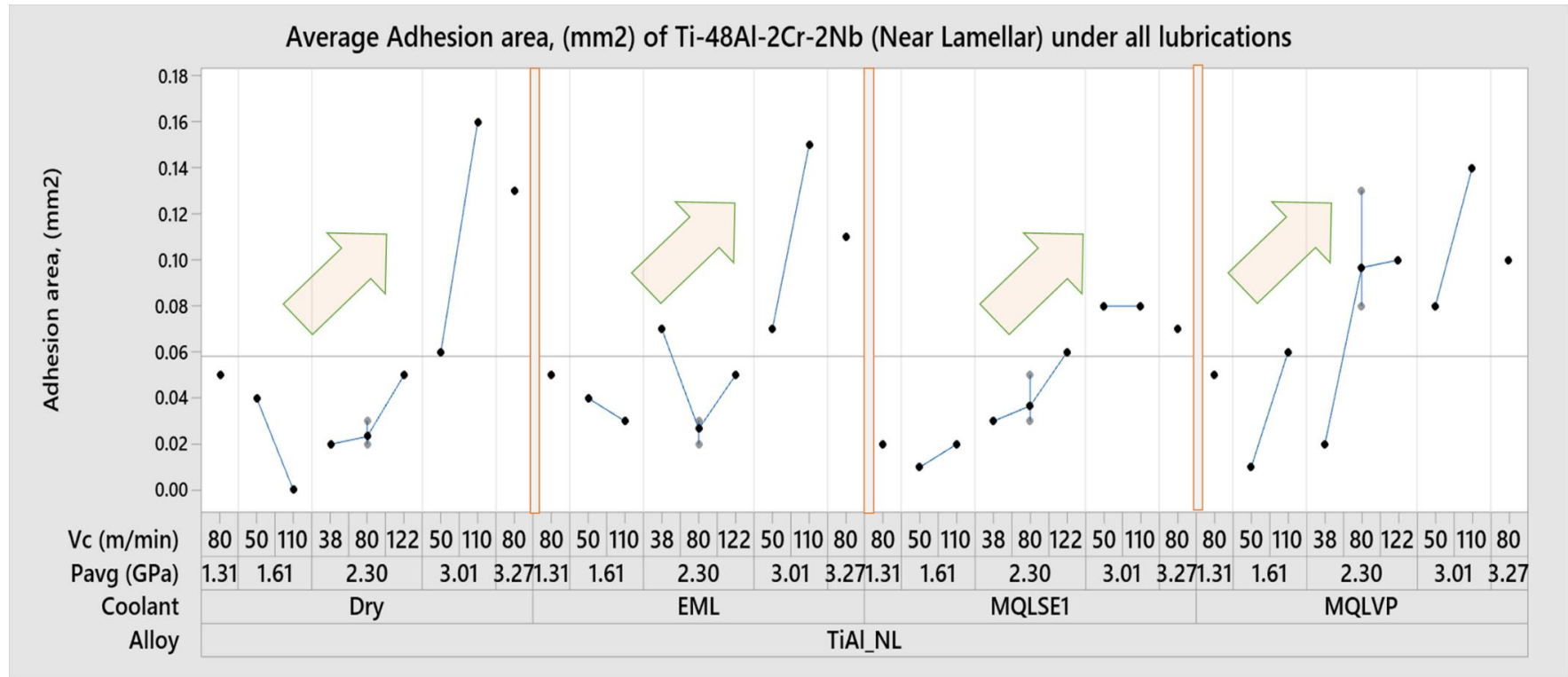


Figure 59 Marginal increase in adhesion area with increase in contact pressure and sliding velocity for Ti-48Al-2Cr-2Nb (NL) across all the contact conditions observed with dry, EML, MQLSE1 and MQLVP lubricants

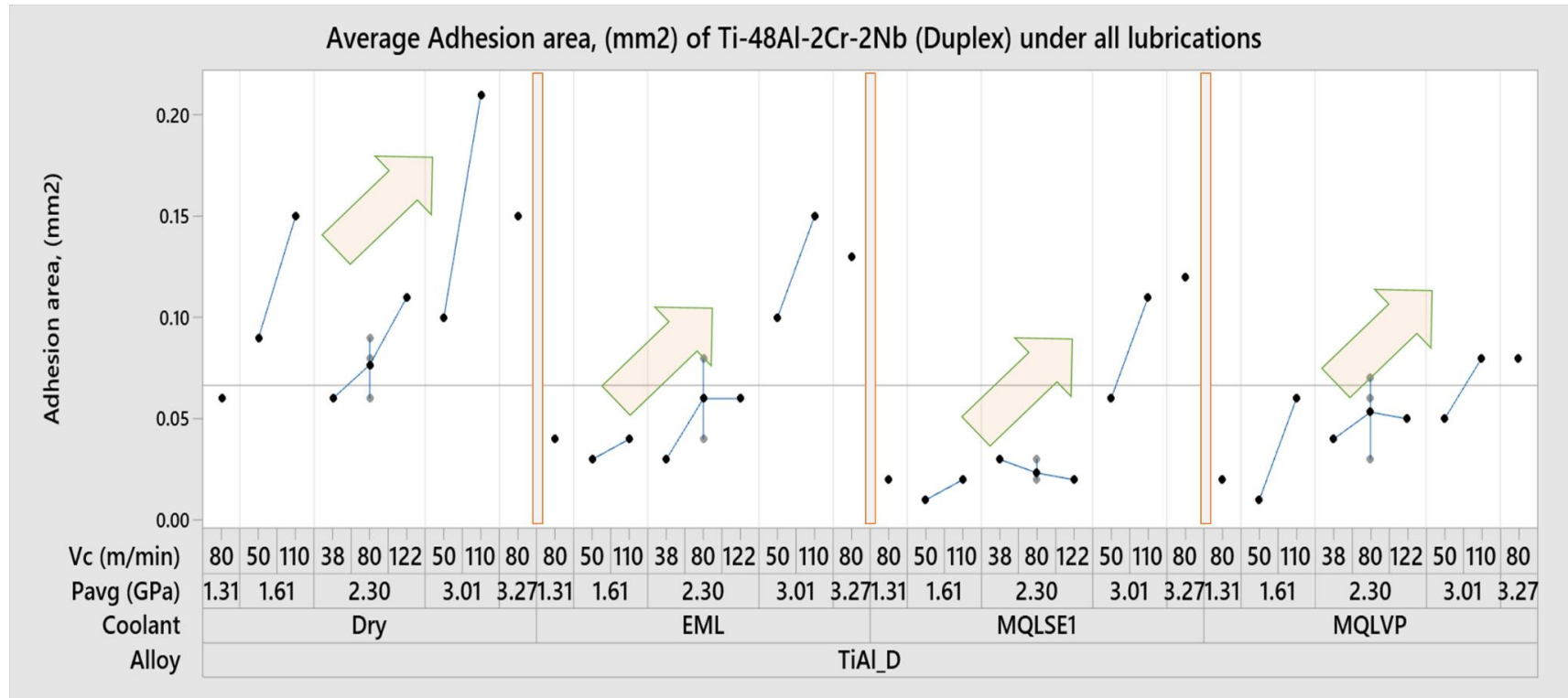






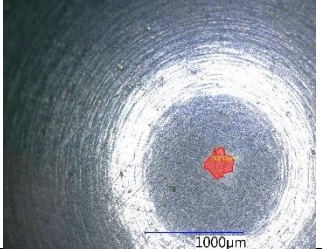


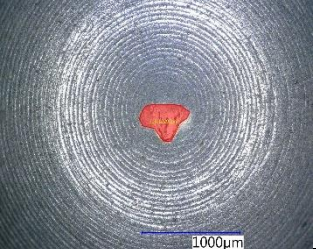
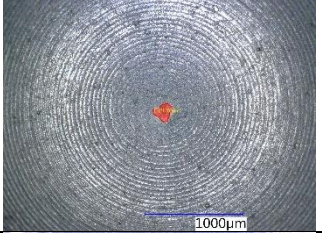
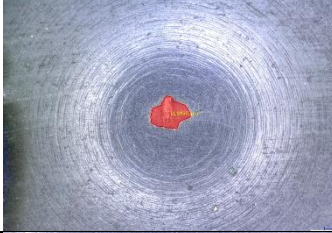

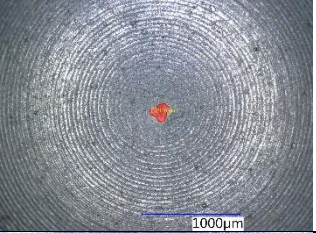




Figure 60 Marginal increase in adhesion area with increase in contact pressure and sliding velocity for Ti-48Al-2Cr-2Nb (D) across all the contact conditions observed with dry, EML, MQLSE1 and MQLVP lubricants

MQLSE1 alloy showed minimum adhesion of workpiece material on the pins. Very low and almost consistent adhesion at all contact conditions was noticed for the lubrications. An important observation was even at higher contact pressures, the increase in adhesion values was very minimal particularly for Ti-48Al-2Cr-2Nb (NL) alloy. As observed before the uncoated pins showed higher adhesion and the correspondingly no change in μ_{app} values were noticed. The adhesion area comparison of coated and uncoated pins in Ti-48Al-2Cr-2Nb (NL) and Ti-48Al-2Cr-2Nb (D) is set out in Table 27 and Table 28.

Not much change in the characteristics was noticed for the MQLVP 19004 lubricant. All the previously observed traits were fulfilled. At lower contact pressures, very low adhesion was observed even with the change in sliding velocities. Good integrity of tests results with a minimal change in the centre point values was seen. No substantial change in the adhesion values at higher contact pressures with the change in sliding velocities was recorded. A distinguishable aspect of MQLVP 19004 was the adhesion area of the uncoated pins was similar to that of coated pins, and μ_{app} values were also similar. Thus, the results showed that coating did not change the adhesion and friction profile with MQLVP 19004 lubricant.

















Tribological characterisation

Table 27 Adhesion profiles of Ti-48Al-2Cr-2Nb (NL) at varying contact pressures with coated and uncoated pins dry, emulsion, MQLSE1 and MQLVP oils

Ti-48Al-2Cr-2Nb (NL)	1.31 GPa and 80 m/min (Coated)	2.30 GPa and 80 m/min (Coated)	2.30 GPa and 80 m/min (Uncoated)	3.27 GPa and 80 m/min (Coated)
Dry				
EML				
MQLSE1				
MQLVP				

Tribological characterisation

Table 28 Adhesion profiles of Ti-48Al-2Cr-2Nb (D) at varying contact pressures with coated and uncoated pins dry, emulsion, MQLSE1 and MQLVP oils

Ti-48Al-2Cr-2Nb (D)	1.31 GPa and 80 m/min (Coated)	2.30 GPa and 80 m/min (Coated)	2.30 GPa and 80 m/min (Uncoated)	3.27 GPa and 80 m/min (Coated)
Dry				
EML				
MQLSE1				
MQLVP				

- **Coating wear analysis of Ti-48Al-2Cr-2Nb (Near lamellar and Duplex)**

The coating wear analysis showed that in the case of Ti-48Al-2Cr-2Nb (NL) alloy, no coating wear was observed. As seen in Figure 61 (a and b), the coating is intact under both the contact pressures with dry lubrications. Some fissures appear although, no damage to the integrity of the coating was seen.

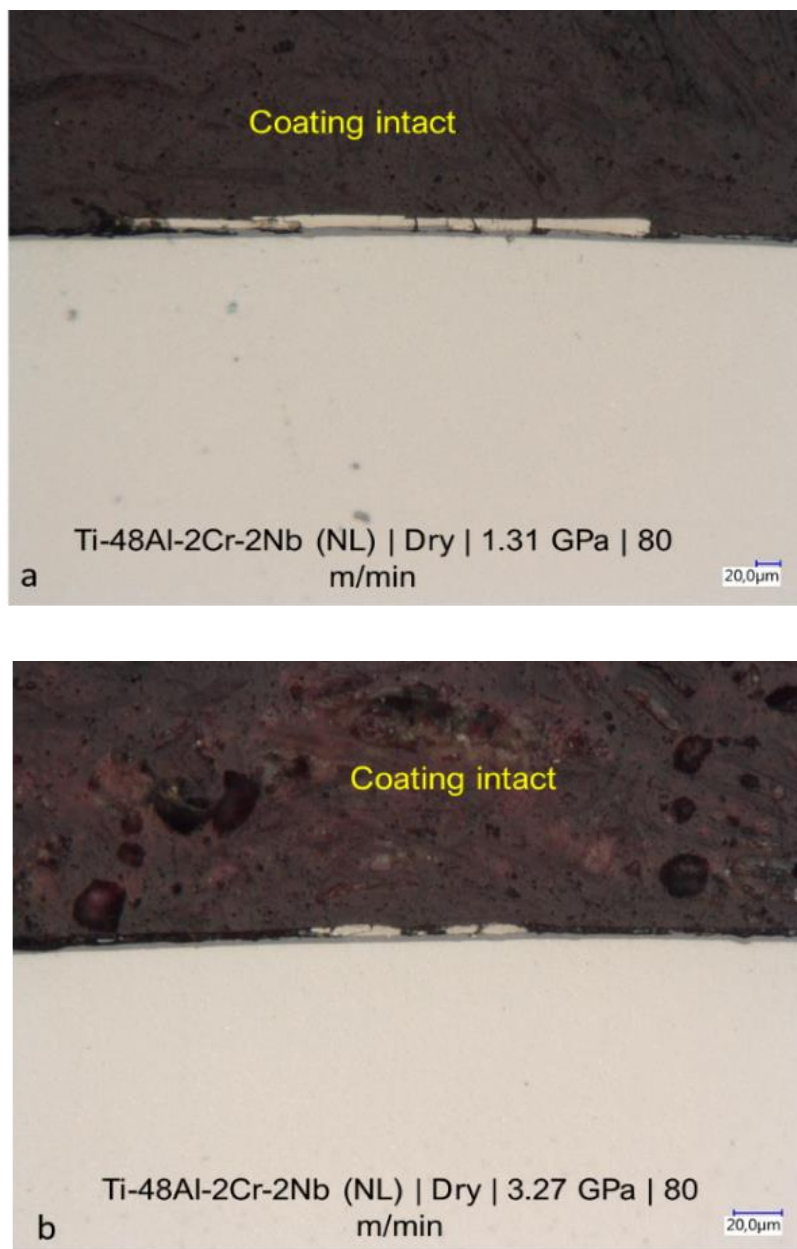


Figure 61 No damage to coating wear observed in dry conditions at (a) 1.31 GPa and (b) 3.27 GPa for Ti-48Al-2Cr-2Nb (NL) alloy

However, the nature of the coating fissures needs a deeper assessment via SEM. Even with EML, the coating was integral. No dissolution of coating or wear was noticed. As seen in Figure 62, the adhered material on the top of the pins is dissolved completely during mould making.

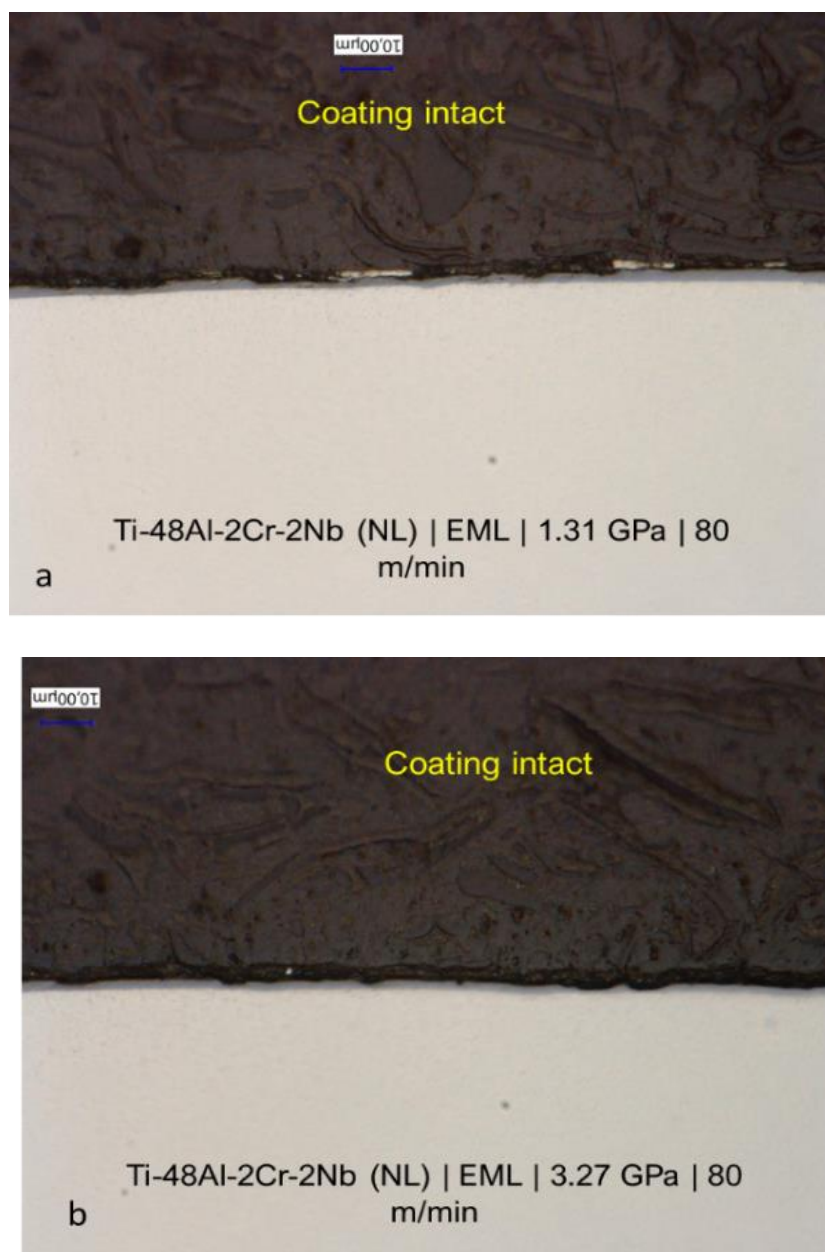


Figure 62 No damage to coating wear observed with EML at (a) 1.31 GPa and (b) 3.27 GPa for Ti-48Al-2Cr-2Nb (NL) alloy

With MQLSE1, the coating was in better shape than other lubricants. No cavities or any form of degradation was noticed. As seen in previous cases, no coating wear was seen (Figure 63)

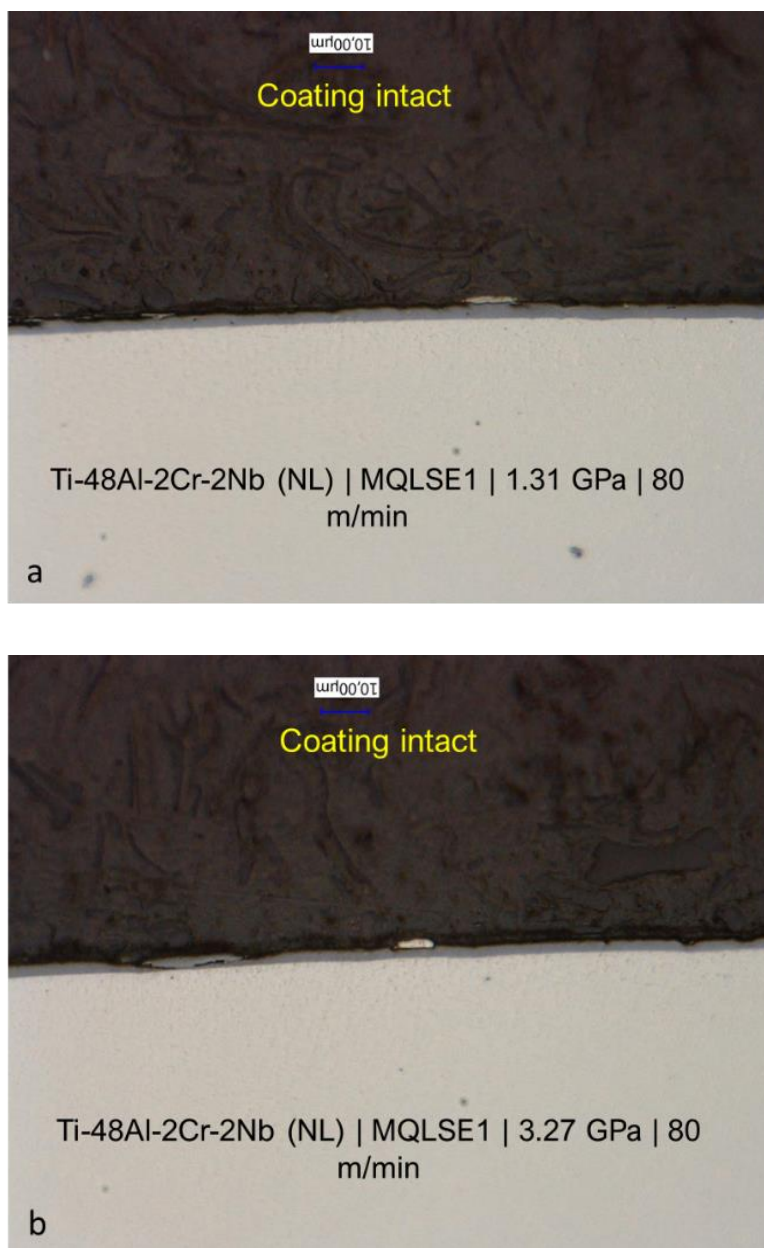


Figure 63 No damage to coating wear observed with MQLSE1 at (a) 1.31 GPa and (b) 3.27 GPa for Ti-48Al-2Cr-2Nb (NL) alloy

However, Ti-48Al-2Cr-2Nb (D) showed more damage to the coating than Ti-48Al-2Cr-2Nb (NL) alloys. In dry conditions, as seen in Figure 64, erosion to the coating was noticeable at high contact pressure at 3.27 GPa.

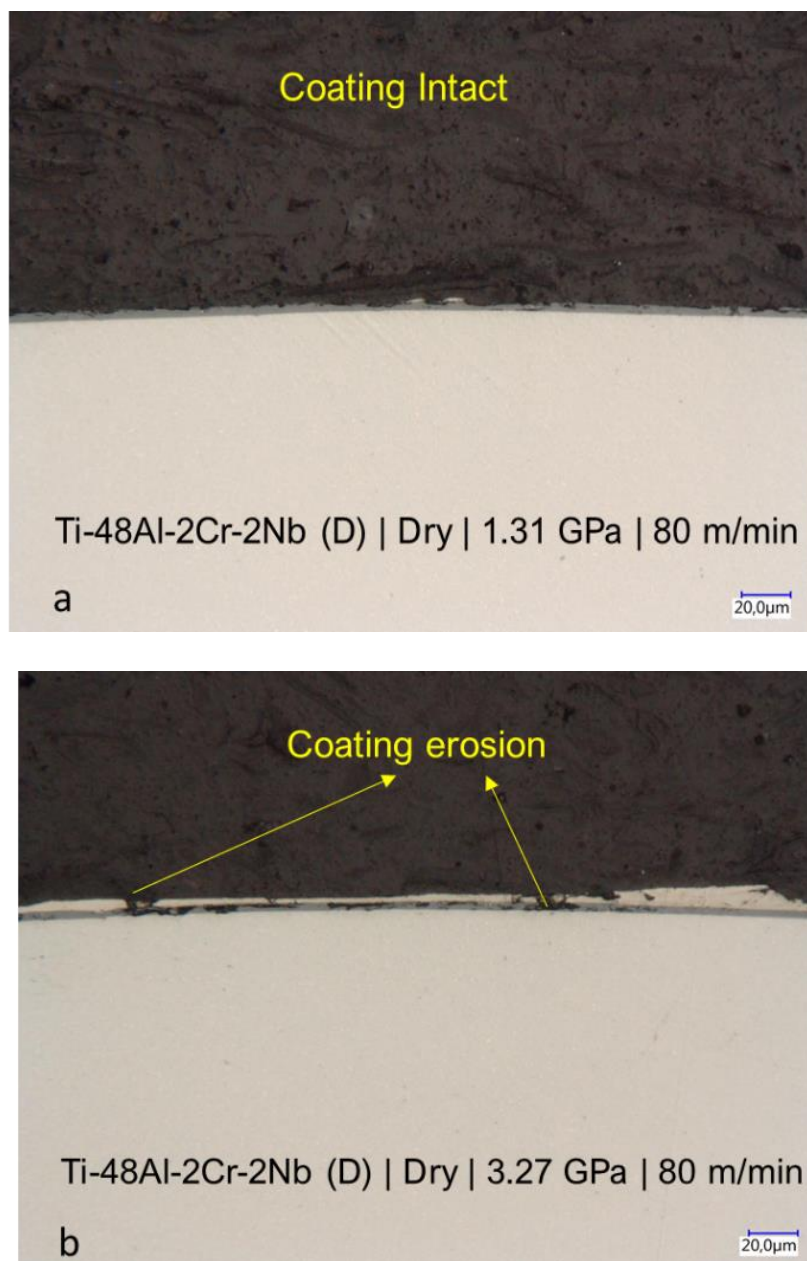


Figure 64 Coating intact at (a) 1.31 GPa and coating erosion at (b) 3.27 GPa in dry conditions for Ti-48Al-2Cr-2Nb (D) alloy

With EML, no damage was noticed. As could be seen from Figure 65 (a) and Figure 65 (b), no damage to coating was noticed. The coating was found to be in a good shape and with strong integrity. No fissures or degradation to coating surface was observed.

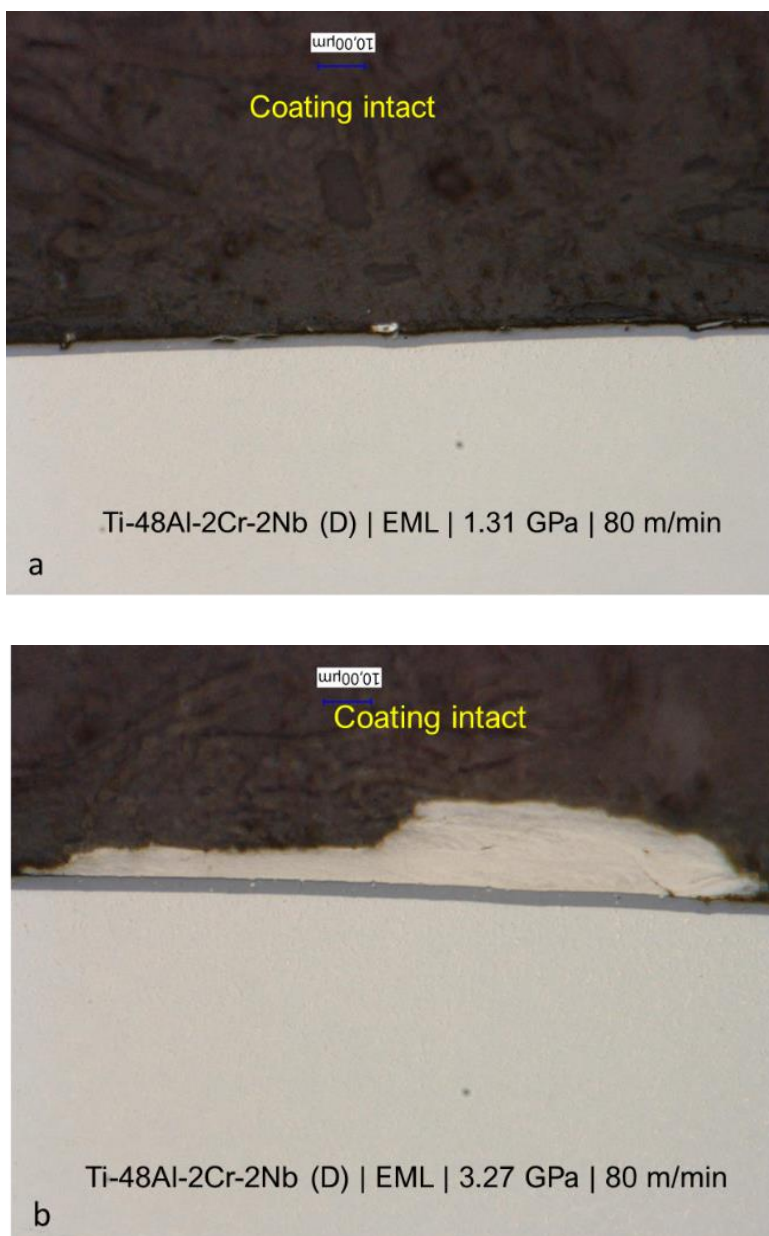


Figure 65 No damage to coating wear observed with EML at (a) 1.31 GPa and (b) 3.27 GPa for Ti-48Al-2Cr-2Nb (D) alloy

Interestingly, as seen in Figure 66, the coating was found to worn completely with MQLSE1 at 3.27 GPa. The outcome was interesting as no coating damage was observed with Ti-48Al-2Cr-2Nb (NL) in the corresponding contact conditions. The coating did not show any degradation at 1.31 GPa. However, the absence of coating was attributed to the loss of coating during the mould making process,

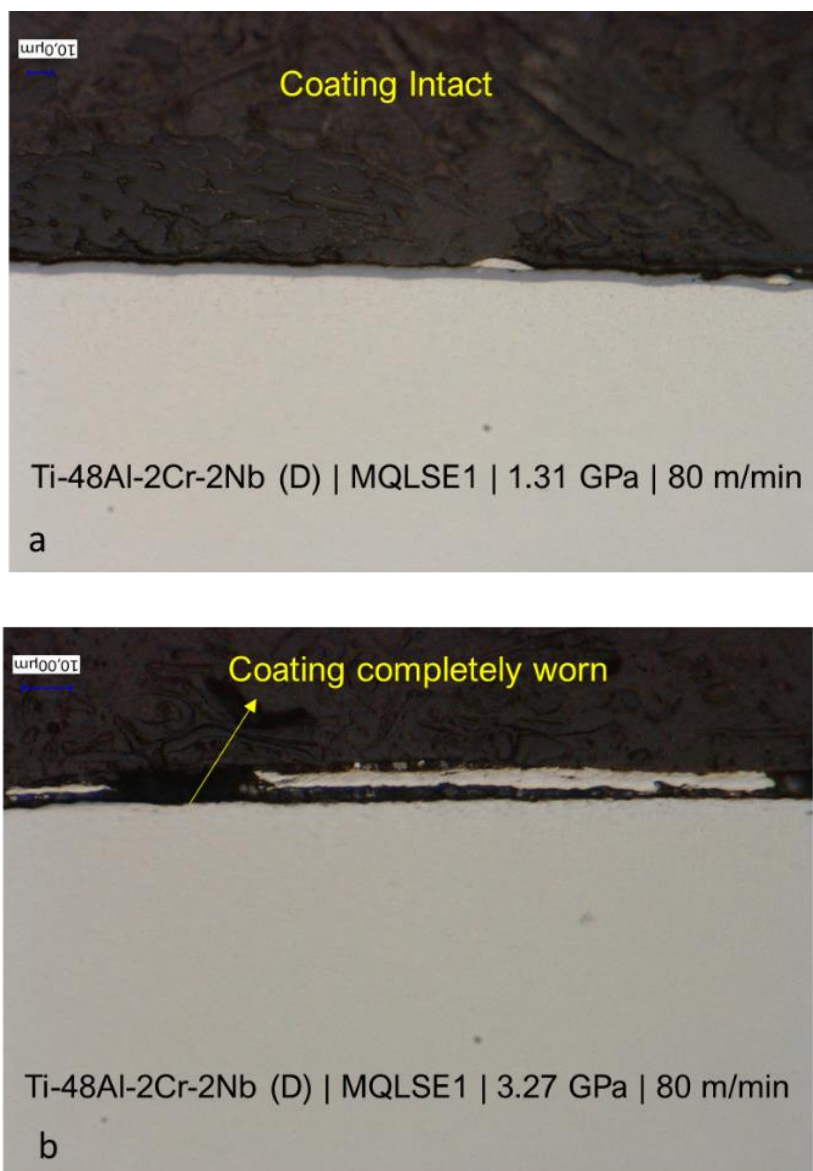


Figure 66 Coating intact at (a) 1.31 GPa and coating completely worn at (b) 3.27 GPa in MQLSE1 conditions for Ti-48Al-2Cr-2Nb (D) alloy

The compilation of coating wear analysis is done in Table 31. The results from both the alloys show that the except for one condition (Ti-48Al-2Cr-2Nb (D) alloy at 3.27 GPa) the evolution of friction coefficient with contact pressure and sliding velocities is without the wear to the coating. In other words, the wear to the coating could be neglected. Additionally, the experts at CEROC/AAMS also supported the theory that the loss of the coating could have occurred during the mould making process. To ensure the accuracy of the results, all the coating wear analysis were rechecked and discussed elaborately with all the industrial partners and with experts at CEROC/AAMS.

Tribological characterisation

Table 29 Coating wear analysis of Ti-6Al-4V, Ti-48Al-2Cr-2Nb (NL), and Ti-6Al-4V, Ti-48Al-2Cr-2Nb (D) in dry, EML and MQLSE1 lubricant at 1.31 and 3.27 GPa.

Material	Coolant	Pavg (GPa)	v_c (m/min)	Adhesion area (mm ²)	App. Fric. Coeff	Coating results
Ti-6Al-4V	Dry	1.31	80	0.29	0.38	Intact
Ti-6Al-4V	Dry	3.27	80	0.62	0.29	Erosion of coating
Ti-6Al-4V	EML	1.31	80	0.06	0.42	Intact
Ti-6Al-4V	EML	3.27	80	0.51	0.24	Erosion of coating
Ti-6Al-4V	MQLSE1	1.31	80	0.1	0.4	Intact
Ti-6Al-4V	MQLSE1	3.27	80	0.52	0.25	Intact
Ti-48Al-2Cr-2Nb (NL)	Dry	1.31	80	0.05	0.2	Intact
Ti-48Al-2Cr-2Nb (NL)	Dry	3.27	80	0.13	0.29	Intact
Ti-48Al-2Cr-2Nb (NL)	EML	1.31	80	0.05	0.26	Intact
Ti-48Al-2Cr-2Nb (NL)	EML	3.27	80	0.11	0.27	Intact
Ti-48Al-2Cr-2Nb (NL)	MQLSE1	1.31	80	0.02	0.16	Intact
Ti-48Al-2Cr-2Nb (NL)	MQLSE1	3.27	80	0.07	0.26	Intact
Ti-48Al-2Cr-2Nb (D)	Dry	1.31	80	0.06	0.24	Intact
Ti-48Al-2Cr-2Nb (D)	Dry	3.27	80	0.15	0.31	Erosion of coating
Ti-48Al-2Cr-2Nb (D)	EML	1.31	80	0.04	0.27	Intact
Ti-48Al-2Cr-2Nb (D)	EML	3.27	80	0.13	0.27	Intact
Ti-48Al-2Cr-2Nb (D)	MQLSE1	1.31	80	0.02	0.26	Intact
Ti-48Al-2Cr-2Nb (D)	MQLSE1	3.27	80	0.12	0.3	Completely worn

4.3.3 HEAT PARTITIONING BETWEEN TOOL AND WORKPIECE

The heat partition between the contacting solids was calculated in dynamic condition. As stated in section 2.3, the plastic deformation component during the calculation is neglected due to the lack of dedicated equipment for measurement.

With an assumption that entire power consumed during the POC experiments is converted to heat, the division of power into various components is explained via equations 9 – 13.

The Table 32 enlists the heat partition characteristics of all the alloys with different lubricants. While the $\phi_{fric-pin}$ is calculated in accordance with the equation 12, the ϕ_{fric} is calculated by the product of tangential force component and sliding velocity as depicted in equation 9.

The % β_{pin} (Heat incident on the pins) shows how much quantity of the total heat generated was directed towards the pins. The results obtained are reflective of thermal properties of lubricants and material properties of both the alloys. As presented in Figure 67, high temperature differences between thermocouples were noticed for Ti-6Al-4V with dry lubricant in comparison to other lubricants. The temperature difference recorded for Ti-48Al-2Cr-2Nb alloys also shows the same trend although temperature differences are not as high as Ti-6Al-4V.

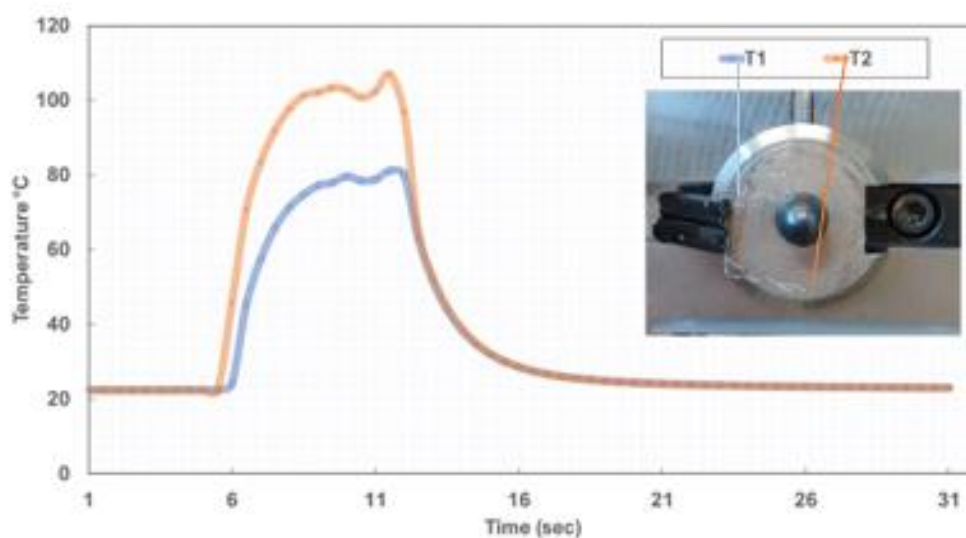


Figure 67 The difference in the temperature recorded by the thermocouples during the temperature measurements of Ti-6Al-4V alloy with dry lubricant

Table 30 The Heat partition coefficients of all alloys under all lubrications calculated at 2.3 GPa and 80 m/min

Alloys / Thermal properties	Ti-48Al-2Cr-2Nb (NL)				Ti-48Al-2Cr-2Nb (D)				Ti-6Al-4V			
	Dry	EML	MQ L SE1	MQLV P	Dry	EML	MQ L SE1	MQLV P	Dry	EML	MQ L SE1	MQL VP
Temperature difference recorded by the thermocouple, ΔT , (K)	8.9	1.8	4.5	3.5	8.2	2.66	4.56	6.33	24.33	11	12	13.33
Tangential force, F_t , (N)	12.23	12.19	12.72	10.64	11.28	12.19	11.65	12.33	38.72	37.56	36.04	35.42
Sliding velocity, v_s , (m/s)	1.33											
Total heat generated during tests, $\phi_{friction}$, (W)	16.27	16.21	16.91	14.15	15	16.21	15.5	20.47	51.5	49.95	47.93	47.11
Heat transmitted to pins, $\phi_{friction-pin}$, (W)	13.2	2.67	6.68	5.2	12.16	3.86	6.76	9.39	36.1	16.33	17.8	19.77
Percentage of total heat transmitted to the pin, % β_{pin}	81.13	16.47	39.5	36.74	81.06	23.81	43.61	45.87	70.1	32.69	37.14	41.96
Apparent friction coefficient, μ_{app}	0.23	0.25	0.25	0.21	0.21	0.25	0.25	0.24	0.42	0.31	0.27	0.27
Adhesion area, (mm ²)	0.02	0.03	0.03	0.08	0.06	0.06	0.02	0.06	0.23	0.19	0.12	0.17

Low	Medium	High
-----	--------	------

- **Ti-6Al-4V**

For the Ti-6Al-4V alloy, the results in the dry conditions indicated that 70.1% of the total heat generated was incident on the pins. Additionally, the heat generated was highest amongst all the experiments with 51.5 W. As a result of the high cooling properties of EML, less heat was generated and even less entered the pins. The heat incident on the pins was only 32.69%. The MQLSE1 also performed on similar lines as that of EML and subsequently let only 37.14 %. Though this heat is little high in magnitude, it highlights that the lubricating properties of oils are equally efficient in reducing the heat incidence as EML. The MQLVP 19004 performed better than the dry conditions but let in 42% of the heat generated to the pins.

An important aspect which determines the heat partition between pin and workpiece is the adhesion profile of the alloy on the pins. As the section 3.3.2 states, the adhesion profile of Ti-6Al-4V is higher than in the Ti-48Al-2Cr-2Nb alloy at a given contact condition. Milton et al. [144] report that the adhered material limits the heat entering to the pins. Though the adhered material is mainly the workpiece material, the added dust and foreign debris may contribute to preventing heat reaching the pins. Therefore, though high heat is generated during experiments with Ti-6Al-4V, and with low thermal conductivity as compared to Ti-48Al-2Cr-2Nb alloys, less heat is incident on the pins due to the higher adhesion of debris on the pin surface.

When the performances of MQLSE1 and MQLVP 19004 are considered, a difference of 5% was observed with MQLVP 19004 transferring more heat to the pins. Correspondingly, the adhesion profiles of the both the oils revealed similar results. The MQL oils yielded similar heat transfer profiles to pins in the Ti-48Al-2Cr-2Nb microstructures.

- **Ti-48Al-2Cr-2Nb (Near lamellar and Duplex)**

Since both the microstructures of Ti-48Al-2Cr-2Nb alloys have shown similar profiles, the results for both the alloys are presented together. The total heat generated with Ti-48Al-2Cr-2Nb (NL & D) alloys is less compared to Ti-6Al-4V alloy. This is based on the premise of the larger friction coefficient observed for Ti-6Al-4V alloy. No comments with regard to mechanical properties could be made as plastic deformation

is completely neglected while calculating the heat partition. In dry conditions, where the (NL & D) generated 16.27 W and 15.0 W respectively, the Ti-6Al-4V generated higher heat of 51.5 W. Importantly, comparing the thermal conductivities of Ti-6Al-4V (6.7 W/m.K) [133] and Ti-48Al-2Cr-2Nb (15 W/m.K, section 3.3), it is clear that more heat is reflected by the Ti-6Al-4V to the pin coating. This means that the probability of coating damage is higher for Ti-6Al-4V alloy.

Expectantly, the EML due to its superior heat extraction properties reduced the heat transmission to the pins. Though the quantum of the heat generated was similar for both the microstructures, only 16.47 % and 23.81 % heat were transmitted to pins by NL and D microstructures.

Both the (NL & D) microstructures performed similarly with the two MQL oils. The transmission of heat was in the range of 36 – 46% by both the microstructures for the two MQL oils. The adhesion profiles of both the microstructures with MQL oils was very limited as described in section 3.3.2.

Thus, the heat partition indicated that EML is best suited to extract maximum heat during the experiments. High heat is generated during experiments with dry lubricants. Therefore, this condition is not suitable for the tools as it would lead to more thermal shocks. MQL oils are also effective in heat extraction but not as effective as EML. This is due to the lubricating effect of MQL oils vis-à-vis cooling effect of EML. However, for sliding velocities up to 80 m/min, EML has 20% less heat incident on pins than MQL oils. Experiments with higher sliding velocities would help in knowing the boundaries of MQL oils. In order to assess the sensitivity of each input parameter with the outcome, a correlation matrix is developed as shown in Figure 68. A correlation matrix is a representation of relationship between the independent variables (contact pressure, sliding velocity) and dependent (apparent friction coefficient, adhesion, lubricants). The relationship is calculated in accordance with the equation 14. The results fall in between the values of 0 – 1. The values can also take negative values, indicating a negative correlation or inversely proportional relationship between the independent and dependent variables. For example, the correlation value of AFC_TiAl_NL_MQLSE1 with contact pressure is 0.80 indicating a positive correlation, while AFC_Ti64_MQLSE1 is -0.88 indicating a negative correlation.

Tribological characterisation

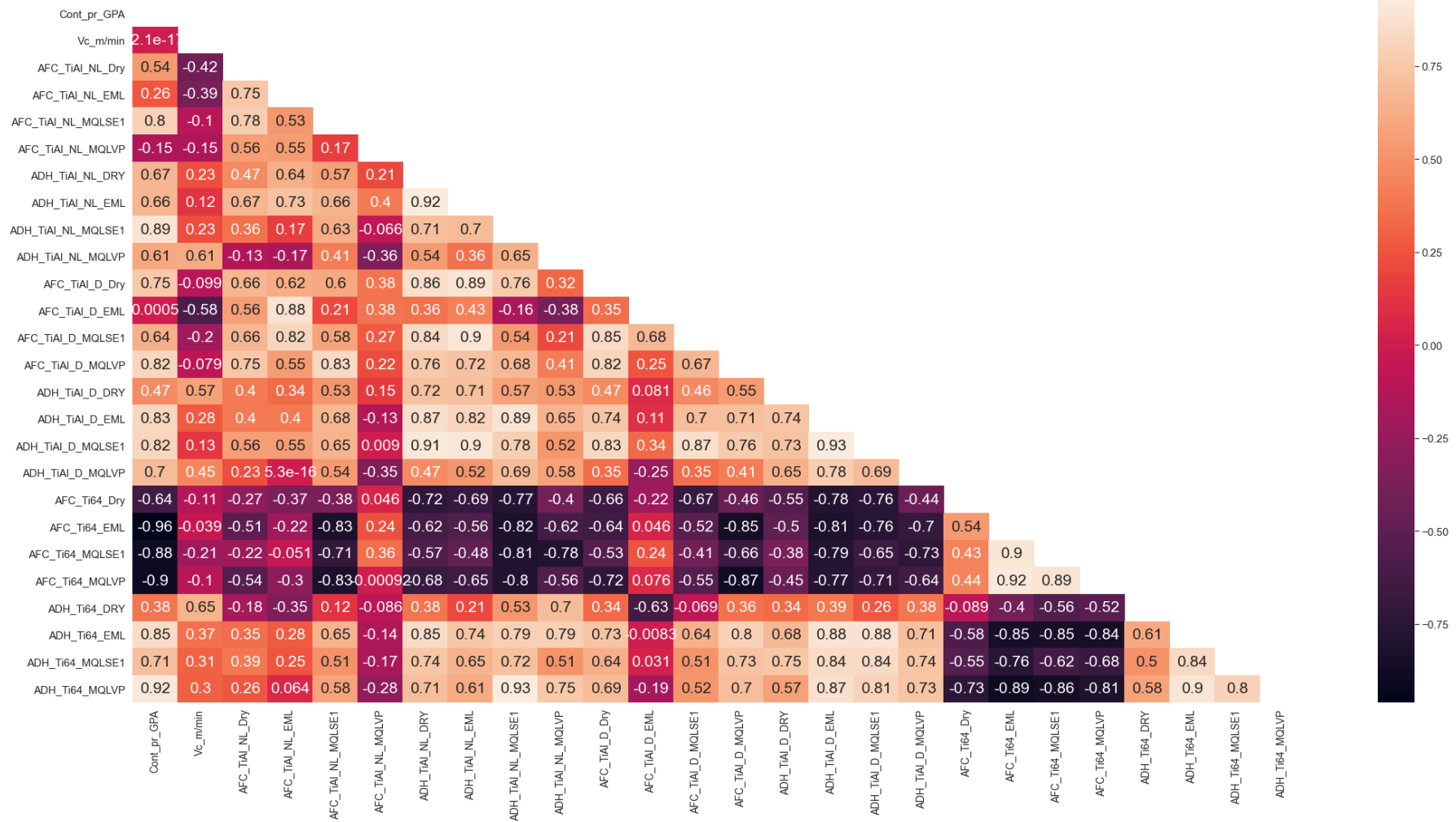


Figure 68 The statistical correlation of each alloy with input (sliding velocity, contact parameter) and output (apparent friction coefficient, adhesion area) based on Pearson correlationship

4.4 CONCLUSION OF TRIBOLOGICAL CHARACTERISATION

This chapter was dedicated to characterisation of the tribological aspects which occur during machining. The tribological properties of the Ti-48Al-2Cr-2Nb (Near lamellar) and Ti-48Al-2Cr-2Nb (Duplex) alloys were compared and benchmarked with Ti-6Al-4V alloy. Friction between the tool and workpiece. The Pin-on-Cylinder (POC) methodology with consisting of dynamometer and special pins were used to characterise:

- Friction between tool and workpiece
- Adhesion of workpiece on the pin and coating wear assessment.
- Evaluation of heat generated during machining and partitioning between workpiece and tool.

The design of experiments was based on CCD design with 11 experiments with three repetitions at the central points. Hertzian contact conditions were used to derive requisite normal forces.

The results showed that Ti-6Al-4V showed 50% high friction coefficients than the Ti-48Al-2Cr-2Nb (NL and D) alloys. Higher apparent friction coefficients were recorded with dry conditions. The contact pressure was statistically significant quantity, increasing which led to a decrease in friction coefficients. For the contact pressures between 1.31 – 3.27 GPa, a μ_{app} dropped by 30% in dry, 75% in EML, 60% each in MQLSE1 and MQLVP oils.

The sliding velocity was dependent on contact pressures to alter the friction coefficient. Increase in sliding velocity provided conflicting results in the trends of μ_{app} . Taking into account the machining context, where contact pressures exceed 2 GPa between contacting bodies, the results indicate that higher sliding velocities would aid in lowering friction between contacting bodies for Ti-6Al-4V. Among all the lubricants, MQLVP provided lower and more consistent results.

Quantification of adhesion area showed that adhesion area increased with increase in contact pressure. The increase in contact pressure also led to lower μ_{app} . This meant

that adhered material was lubricating the contact bodies lowering friction between them.

Notably, the coating of the pin was ineffective and detrimental in dry conditions as the uncoated pins provided lower μ_{app} than coated pins. However, with lubricants, no difference in the friction performance was noticed. The cross-section of the pins showed the possibility of the coating erosion with dry and EML lubricants at high contact pressure of 3.27 GPa. However, with the overall structure intact, it could be concluded that the coating wear did not affect the tribological outcomes. The results also revealed that, Ti-6Al-4V is more conducive to uncoated pins, particularly in dry conditions, than coated ones and the coating did not alter any tribological properties.

In the case of Ti-48Al-2Cr-2Nb alloys, change in microstructure did not offer any qualitative change in tribological properties. The contact pressure was found to be the statistically significant property and sliding velocity displayed a parabolic behaviour. The pattern of friction evolution was found to be similar in both the microstructures with all lubricants. In both the microstructures, the apparent friction coefficient was found to increase (not drastically) with increase in contact pressure. Higher friction coefficients were noticed at 3.01 and 3.27 GPa for both the microstructures.

All lubricants performed equally well but dry lubrication should be avoided as damage to coating was noticed and cracks were detected in the wear tracks with dry lubricant. A comparison with uncoated pins showed that the coating does not provide any qualitative improvement in tribological properties.

The adhesion profile was similar to the trend of friction evolution. The adhesion area increased with increasing in contact pressure for both the Ti-48Al-2Cr-2Nb (NL & D) alloys. However, the adhesion profile was found to be in a similar range for all lubricants.

The coating wear assessments showed that Ti-48Al-2Cr-2Nb (NL) did not show any damage to coatings under severe contact conditions. However, the Ti-48Al-2Cr-2Nb (D) alloy showed a pocket of coating delamination at 1.31 GPa in dry condition and complete wear damage at 3.27 GPa with MQLSE1. Therefore, these contact conditions and alloy – lubrication combination are not recommended for machining. The coating

wear assessment was not carried out under MQLVP 19004, therefore, no comments could be made about the lubricating or coating wear damage properties of the oil.

As a result of high heat extraction characteristic of EML, the heat transmitted to pins was low in comparison to other lubrications. This meant that damage to the coating due to thermal shocks was minimal. The MQL oils also showed good heat extraction but were not as effective as EML at higher sliding velocities (122.42 m/min). Thus, EML combined with Ti-48Al-2Cr-2Nb (NL) is a suitable combination to achieve the best tribological properties.

CHAPTER 5

BULL END MILLING TESTS

5 BULL END MILLING TESTS

The chapter is dedicated to the experimental sensitivity analysis between input parameters (alloys, lubricants, tools, cutting speed) and output parameters (cutting forces, tool wear and surface integrity) as presented in Table 1.

The chapter is divided into four sections. This first describes the equipment, test methodology and validation tests. This is followed by the input and output parameters assessed in the work. The second section details the experimental plan for the bull end milling tests, and the results and the discussion are presented in section three. The final section outlines the conclusion from the study.

5.1 EXPERIMENTAL SETUP: METHODOLOGY AND VALIDATION

The bull end milling tests were carried out in a 5 axes GF mill P 800 UD milling machine and experimental setup is illustrated in Figure 69. The climb milling methodology was adopted for the tests.

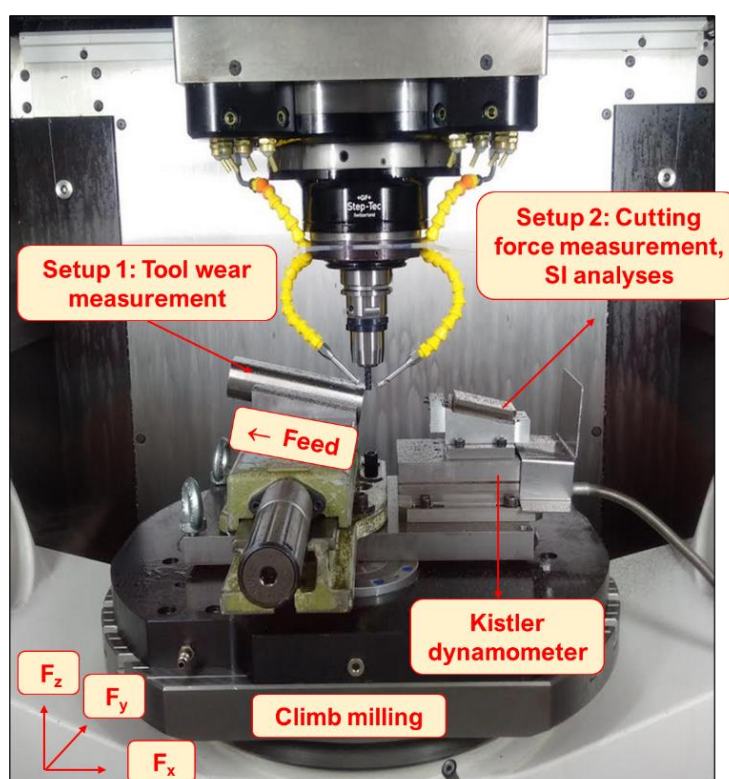


Figure 69 Milling machine used to carry out tests

Bull end milling tests

Two workpieces (*Setup 1* and *Setup 2*) of the same microstructure were used for a given test. The *Setup 1* was used exclusively for tool wear measurements, and *Setup 2* for measuring cutting forces and SI analyses. While the *Setup 1* is a cylinder ingot as shown in Figure 70 (a), the *Setup 2* is a semi-cylinder as depicted in Figure 70 (b).

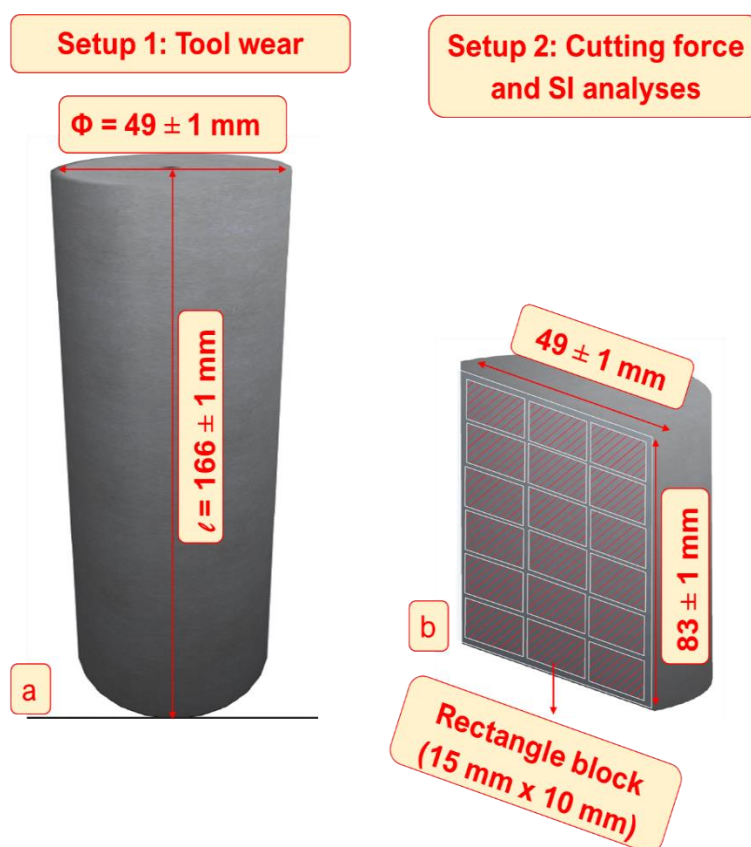


Figure 70 Dimensions of (a) *Setup 1* for tool wear measurement (b) *Setup 2* for cutting forces and SI analysis

Each test began with measuring the cutting forces on *Setup 2*. The machined area, as shown in Figure 70 (b), is referred to as a 'Rectangle block'. Each *Rectangle block* contained the SI information of the material at a given time. Both *Setup 1* and *Setup 2* were inclined at 12° . According to [83] climb milling reduces the load from the cutting edge, leaves a better surface finish, and improves the tool life. Thus, this method was adopted for the study. For the tests, the limit was set to 0.2 mm flank wear and time limit to 90 min. Both the limits were adopted from the work of Priarone et al. [87].

Figure 71 illustrates the step-wise procedure followed during the tests. First, the tool was checked for defects with optical microscopy. If dimensionally accurate, the tool was then used to measure the cutting forces in *Setup 2*. Based on the cutting speed, the

Bull end milling tests

As the sole objective of the validation tests was to confirm the accuracy of testing methodology, only tool wear results were compared against the previous tests. The assessment of cutting forces or the SI analyses was not within the purview of the tests. The tests were stopped after the tool wear crossed 0.2 mm and / or the cutting time reached 90 min. Table 31 sets out the experimental plan of the setup validation tests.

Table 31 The test matrix of setup validation tests

Setup Validation (SV) Tests		
Parameter	Variance	Value
Materials	1	Ti-48Al-2Cr-2Nb NL
Axial depth of cut (mm)	1	0.25
Radial depth of cut (mm)	1	0.80
Cutting speed (m/min)	1	100
Feed per tooth (mm/tooth)	1	0.03
Tools	3	1620, 1730, 1740
Lubrication	1	Flood (EML: Vasco 7000)
Coolant pressure (EML), bar		15 ± 2
Repetitions	2	
Total tests = 6		

The tool wear was measured in accordance with methodology described in section 5.1.2. The test results were consistent with the previous tests, indicating a good fit between testing methodology and best practises. The test results are presented in Figure 72. The validation tests led to the implementation of some corrective actions like the accurate orientation of coolant pipe on the tool tip and ensuring enough tool overhang to avoid being in the blind spot.

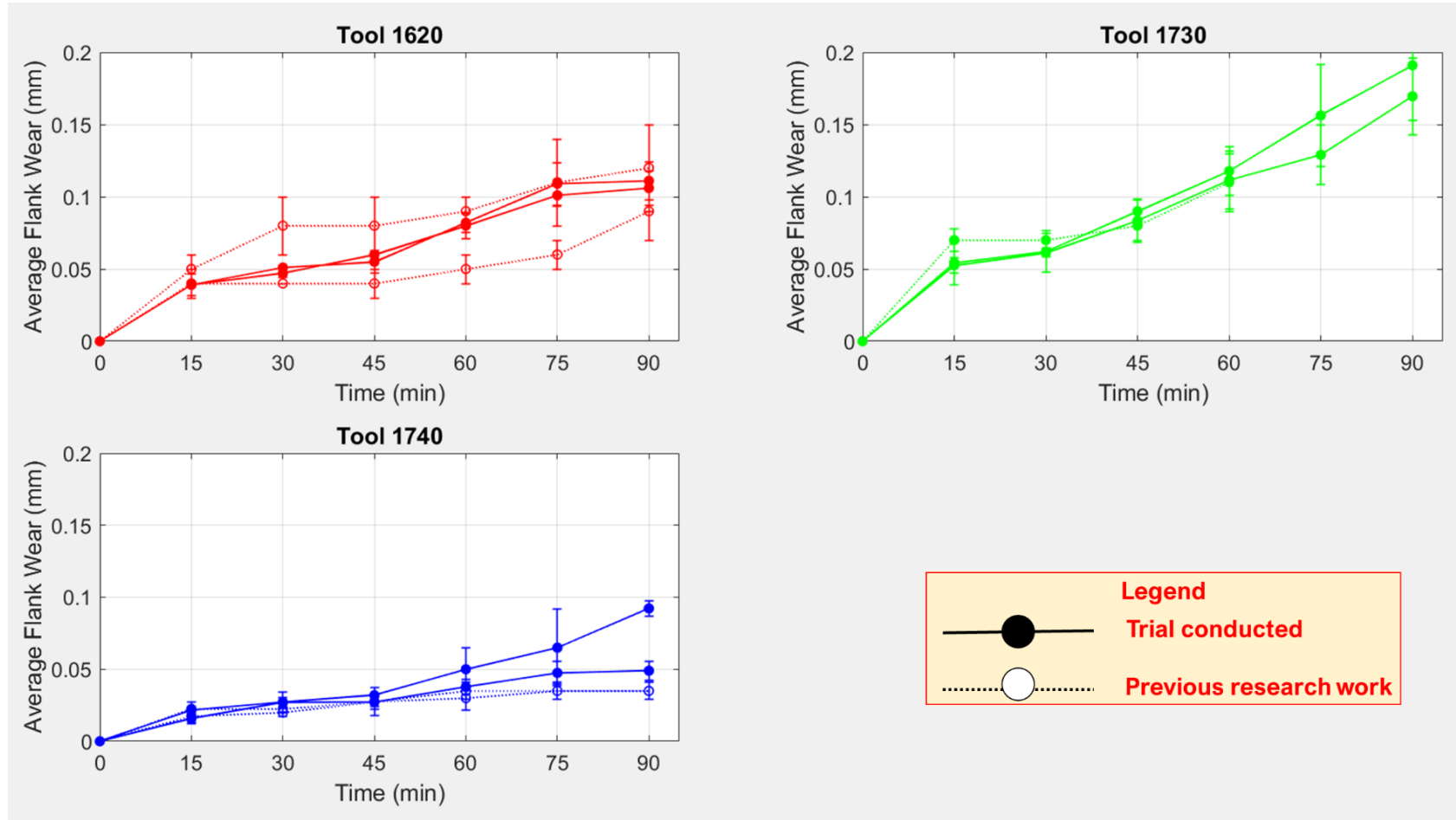


Figure 72 Setup validation of Ti-48Al-2Cr-2Nb (NL) with EML and $v_c = 100$ m/min compared to previous research

Bull end milling tests

The input parameters comprised two alloys (Ti-48Al-2Cr-2Nb (NL) and Ti-48Al-2Cr-2Nb (D)), one tool (T1745), three lubricants (EML, MQLSE1 and MQLVP 19004) and two cutting speeds (100 and 115 m/min). The feed, radial and axial depths of cut were kept constant. The input parameters are shown in Table 32.

Table 32 Input parameters used in the study

Input parameters			
Cutting tool	Tool reference		T1745, TSPL
	Geometry	Mill diameter (mm)	8
		Lead angle °	12
		Corner radius (mm)	0.5
		Cutting Edge Radius (µm)	5
		Number of teeth	5
	Material	Material	Plura Solid Carbide
Coating		PVD TiAlSiN (T1745), PVD Hardlox coating (TSPL)	
Coolant	Type	4 Lubricants: Dry, Emulsion (Vasco 7000), MQLSE1, MQLVP19004	
	Pressure MQL	15 ± 2 bar	
	Flow (MQL)	43 ± 3 ml/h	
	Concentration (%)	EML: 8.70	
	Distribution	External	
Material	Geometry	Cylindrical bar	
	Material	Gamma -TiAl	
	Composition and microstructure	Near lamellar and Duplex	
	Heat Treatment	HIP, HT	
	Dimensions	166 mm x 49 mm (dia)	
Working conditions	Operation	Bull nose end milling	
	Up milling/ Down milling	Down milling	
	Cutting speed (m/min)	100, 115, 125, 150	
	Feed per tooth (mm/tooth)	0.03	
	Radial Depth of cut (mm)	0.80	
	Axial Depth of cut (mm)	0.25	

Three output parameters studied were cutting forces, tool wear, and surface integrity.

The assessment methodology is detailed in the following sections.

Bull end milling tests

5.1.1 METHODOLOGY: CUTTING FORCES

The cutting force measurement was carried out with a Kistler 9129 AA dynamometer combined with 5070A signal amplifier. The dynamometer was placed horizontally parallel to the axis of tool path (Figure 73 (a)). The force signals generated by the movement of the tool were passed through a low pass filter to account for the noise.

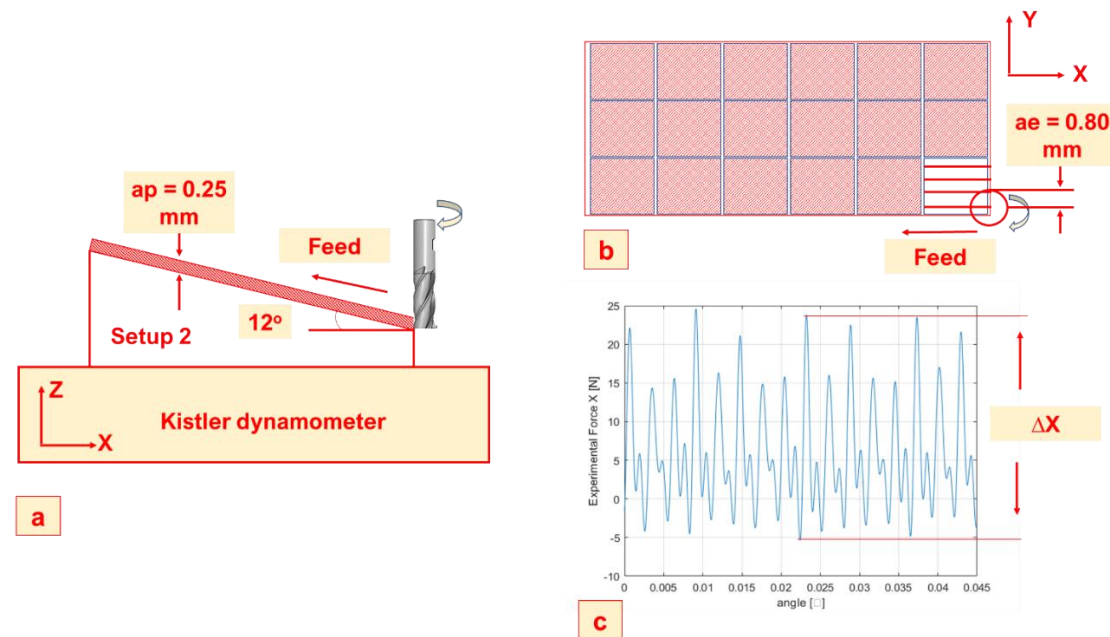


Figure 73 The methodology of measuring cutting forces

The natural frequency of the dynamometer was measured at 3500 kHz. When the fixture to hold the workpiece was added, the natural frequency dropped to 2000 kHz. For a $v_c = 100$ m/min and effective tool diameter of 8 mm, the spindle speed of 3980 RPM was arrived at. With 5 teeth, each tooth had a passing frequency of 379 Hz. Anything above this frequency was treated as noise and negated from the force signal. The forces collected are delta forces as:

1. Delta Fx (dF_x) = $F_{x \text{ Max}} - F_{x \text{ Min}}$
2. Delta Fy (dF_y) = $F_{y \text{ Max}} - F_{y \text{ Min}}$
3. Delta Fz (dF_z) = $F_{z \text{ Max}} - F_{z \text{ Min}}$

When measuring the forces, each force component drops to zero or negative values depending on the teeth rotation and when the tool loses contact with the workpiece at the end of each pass. To accommodate them, a difference between the maximum and minimum forces of each component (X, Y, and Z) is considered. This is shown in Figure 73 (c).

Bull end milling tests

5.1.2 METHODOLOGY: TOOL WEAR

The tool wear analysis was performed by orienting the tool at 45°. The tool holder was extracted after completing the tool wear tests (every 15 min) and placed in the fixture as shown in Figure 74. The fixture was made of machinable foam. This fixture was situated below Leica Optical microscope. The base plate was bolted to ensure that the fixture was immobile during wear measurements. The flank wear of each tooth was measured to make sure that all teeth had similar workpiece contact times and ensure that wear was uniform.

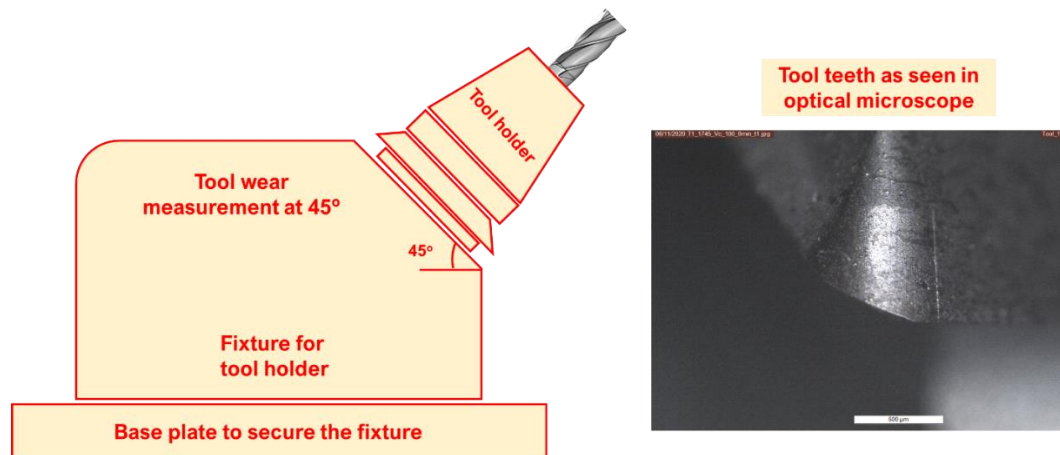


Figure 74 Methodology followed for tool wear measurement

The Table 33 presents the tool wear of each tooth at recorded at 15 min time intervals. The mean of all the five teeth was considered tool wear, and differences as standard deviations.

Table 33 Tool wear measurement data for T1745 with EML at 100 m/min

Test nr	Identification	Micro	Date	Time (min)	Rectangle block number	Vb teeth 1 (mm)	Vb teeth 2 (mm)	Vb teeth 3 (mm)	Vb teeth 4 (mm)	Vb teeth 5 (mm)	Avg. Vb(mm)	Std. dev (mm)
34	T34_T745_vc_100_MQLVP19004	NL	19/01/2021	0	Q14_B5	0	0	0	0	0	0	0
				15	Q15_B5	0.029	0.043	0.031	0.044	0.039	0.0372	0.01
				30	Q16_B5	0.037	0.037	0.04	0.036	0.042	0.0384	0
				45	Q17_B5	0.044	0.048	0.035	0.044	0.049	0.044	0.01
				60	Q18_B5	0.041	0.048	0.049	0.056	0.038	0.0464	0.01
				75	Q19_B5	0.151	0.142	0.139	0.125	0.12	0.1354	0.01
				90		100	100	100	100	100	100	0

While the cutting forces and tool wear were measured concurrently during the tests, the surface integrity of each *rectangle block* was conducted after the completion of all the bull end milling tests.

5.1.3 METHODOLOGY: SURFACE INTEGRITY

The surface integrity analysis of the *Rectangle blocks* in *Setup 2* was analysed to generate a minimum SI data sheet. The minimum SI data sheet comprises of study and control of surface texture and surface metallurgy as quoted by Hood et al. [34]. In the present study, the surface texture was studied by measuring the surface roughness, while the surface metallurgy was analysed by studying sub-surface microstructure alterations and conducting sub surface microhardness measurements. The methodology of studying both the components of surface integrity is presented as follows:

i. Surface roughness

The surface roughness comprised of measurement of three profiles as presented in Figure 75. The three profiles studied are as follows:

- R_a : Surface roughness average
- R_t : Maximum surface height of the profile
- R_z : Average maximum height of the profile

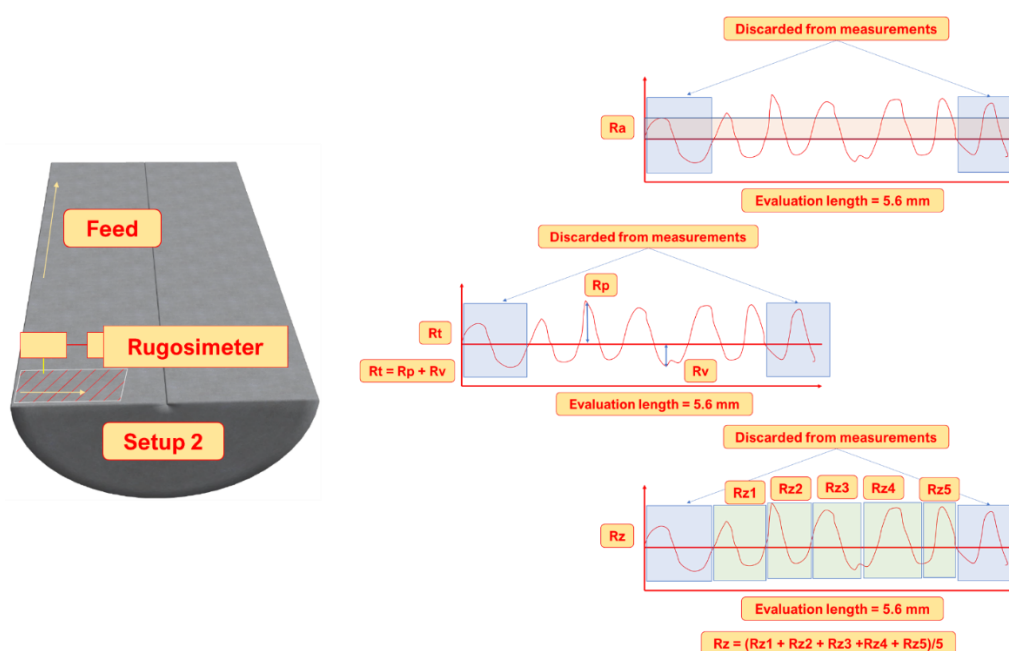


Figure 75 Surface roughness measurements of the Rectangle block to obtain R_a , R_t and R_z profiles

The total evaluation length was 5.6 mm, which corresponded to 7 profiles. The profiles at the beginning and at the end were discarded, and the central 5 profiles were used for evaluation. All the measurements were repeated four times and the mean was taken as the reading.

ii. Sub-surface microstructural alterations

Each *rectangle block* from *Setup 2* was extracted by means of WEDM. The sub surface plane representing the YZ plane of the workpiece was termed as longitudinal surface, and that representing XZ plane was labelled as transverse face (Figure 76).

- The longitudinal face: The vector defining the analysed surface perpendicular to the cutting speed movement and parallel to the feed movement.
- The transverse face: The vector defining the analysed surface parallel to the cutting speed movement and perpendicular to the feed movement.

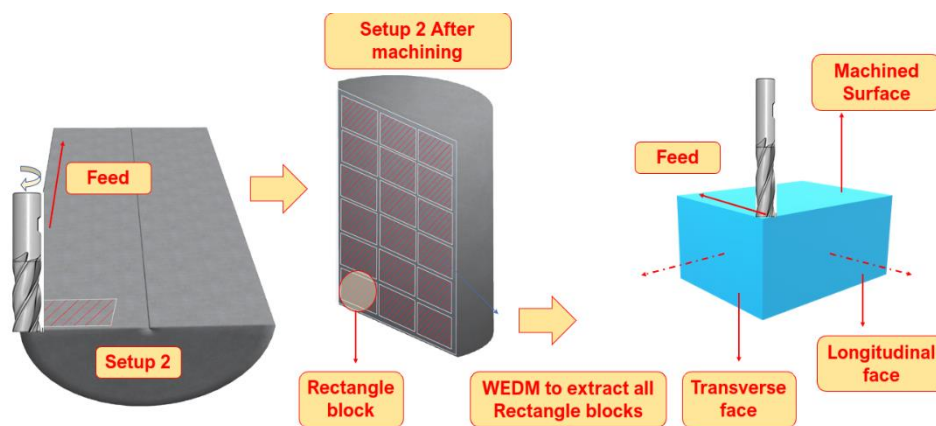


Figure 76 Assessment of sub-surface microstructure alteration of a Rectangle block

Only the longitudinal surface was used for subsurface assessment, as it would have more sub surface defects due to the tool contact at the start of each pass. The longitudinal face was subjected to moulding, grinding and polishing, and etching with Kroll's reagent (97 mL H₂O, 2 mL HNO₃, 1mL HF). Upto 7 optical micrographs were taken during the longitudinal face assessment to identify defects such as cracks, porosities, steps, surface drags/ bending of lamellae etc. In the case of Ti-48Al-2Cr-2Nb comprising of lamellar colonies and other phases like α_2 and γ , a surface drag can be referred to as length of the lamellar bending as shown in Figure 77.

In the case of surface drags, 2-3 readings were taken per optical micrograph. Up to 7 – 9 optical micrographs were studied resulting in a total of 20 – 21 measurement of surface drags for a given time interval. For example, Ti-48Al-2Cr-2Nb_NL (with EML, $vc = 100$ m/min, at 15 min) would have 20 – 21 measurements of surface drags and other sub surface defects. Similarly, other time intervals were studied.

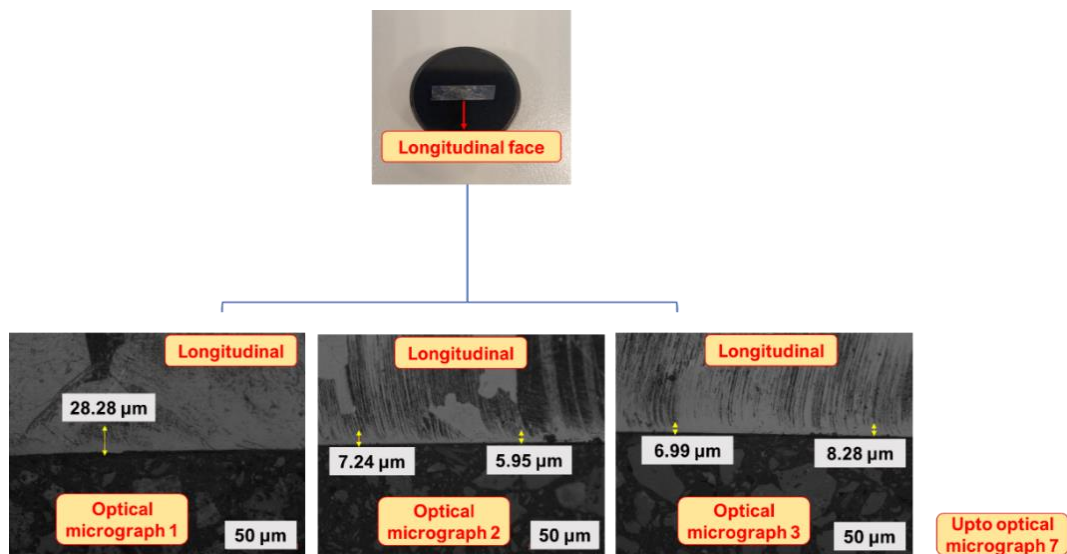


Figure 77 Analysis of surface drags

These readings were analysed statistically by studying the mean, mode and median of the values. The surface drags varied in length and thus the median and mode values would not have obtained an accurate representation, as the higher values would be discounted as outliers.

Therefore, the mean reading, together with the standard deviation of all the 21 – 22 values were used as the value of surface drag for a given *Rectangle block*. The mean, mode, and median values of the SD measurement are set out in Table 34. The surface drag was determined as the region where the bending of lamellar colonies occurred as shown in Figure 78.

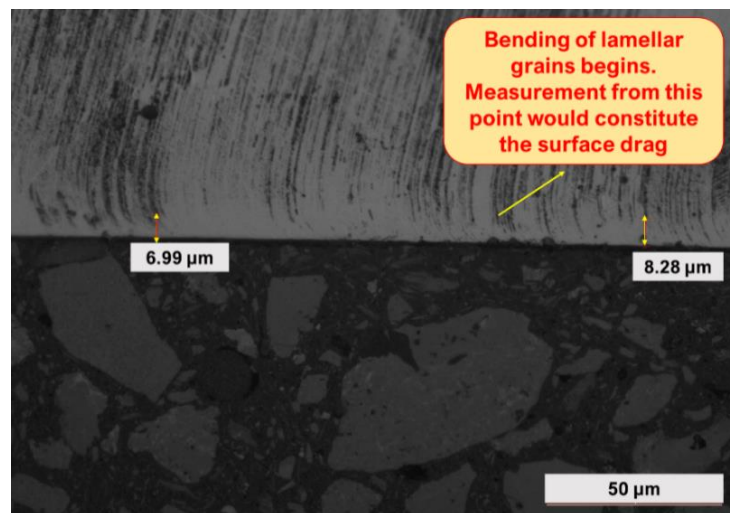


Figure 78 The bending length of surface drag

Bull end milling tests

Table 34 An example of SD measurements on specimen machined with MQLSE1 oil at $v_c = 115$ m/min

Material	v_c m/min	Test	Time (min)	Surface drag (μm)	Std dev (μm)	Median (μm)	Mode (μm)	Mean (μm)	Coolant
TiAl_NL	115	74	0	9.48	1.0241	9.48	9.48	9.589	MQLSE1
TiAl_NL	115	74	0	8.02					
TiAl_NL	115	74	0	10.21					
TiAl_NL	115	74	0	11.66					
TiAl_NL	115	74	0	10.93					
TiAl_NL	115	74	0	8.75					
TiAl_NL	115	74	0	9.48					
TiAl_NL	115	74	0	10.93					
TiAl_NL	115	74	0	10.21					
TiAl_NL	115	74	0	8.75					
TiAl_NL	115	74	0	8.02					
TiAl_NL	115	74	0	9.48					
TiAl_NL	115	74	0	8.75					
TiAl_NL	115	74	0	9.48					
TiAl_NL	115	74	0	9.27					
TiAl_NL	115	74	0	11.23					
TiAl_NL	115	74	0	9.11					
TiAl_NL	115	74	0	10.12					
TiAl_NL	115	74	0	9.13					
TiAl_NL	115	74	0	8.77					
MQLSE1									
TiAl_NL	115	74	2	28	3.0149	27.855	24.1	27.6365	MQLSE1
TiAl_NL	115	74	2	27.71					
TiAl_NL	115	74	2	28.03					
TiAl_NL	115	74	2	31.9					
TiAl_NL	115	74	2	29.3					
TiAl_NL	115	74	2	24.1					
TiAl_NL	115	74	2	28.65					
TiAl_NL	115	74	2	30.6					
TiAl_NL	115	74	2	31.25					
TiAl_NL	115	74	2	24.1					
TiAl_NL	115	74	2	31.25					
TiAl_NL	115	74	2	26.69					
TiAl_NL	115	74	2	26.7					
TiAl_NL	115	74	2	26.69					
TiAl_NL	115	74	2	21.44					
TiAl_NL	115	74	2	30.13					
TiAl_NL	115	74	2	24.23					
TiAl_NL	115	74	2	27.62					
TiAl_NL	115	74	2	23.22					
TiAl_NL	115	74	2	31.12					

iii. Sub-surface microhardness

The sub-surface micro-hardness was the third stage of the SI analyses. This test is important particularly for duplex microstructures which are composed of α_2 and γ grains with few lamellar colonies, and thus the surface drag is less prominent. In such cases, the difference in hardness between the machining affected zone and the bulk material reveals the true extent of alterations in the sub-surface.

The microhardness analysis was conducted on the longitudinal direction. Every measurement was repeated three times, and the mean value together with standard deviation were used for assessment. The analysis was conducted in accordance with the ISO 6507 – 1 standard, and thus measurements were taken at a depth of 0.02 mm and 0.05 mm, as illustrated in Figure 79.

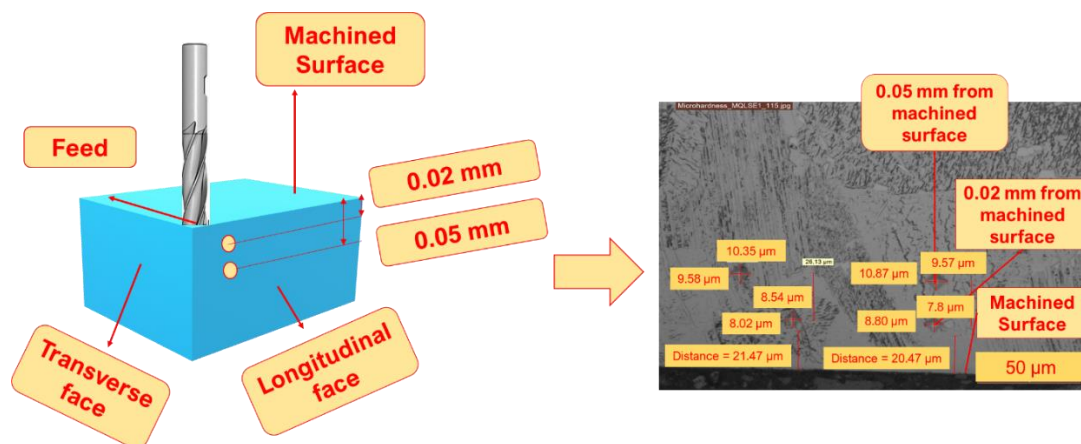


Figure 79 The microhardness profile of longitudinal surface at 115 m/min and MQLSE1

5.2 DESIGN OF EXPERIMENTS

Before establishing the test matrix, a set of preliminary bull end milling tests were conducted. The objective of this exercise was to select the tool with long tool life and eliminate those process parameters and lubricants that did not show sufficient tool life. The tests were limited only to assess the tool life and no SI analyses was conducted. The test matrix for comparative study is set out in Table 35. The tests were run upto 90 min or a tool wear reaching a limit of 0.2 mm.

Table 35 Experimental plan of preliminary tests

Preliminary tests		
Parameter	Variance	Value
Alloys	2	Ti-48Al-2Cr-2Nb (NL) Ti-48Al-2Cr-2Nb (D)
Axial depth of cut (mm)	1	0.25
Radial depth of cut (mm)	1	0.80
Cutting speed (m/min)	3	100, 125, 150
Feed per tooth (mm/tooth)	1	0.03
Tools	2	T1745, TSPL
Lubrication	4	Dry, EML, MQL VP19004, and MQL SE1
Coolant pressure, (EML), bar	1	15 ± 2
Flow rate of EML, l/min	1	25 ± 1
Coolant pressure, (MQL), bar	1	6 ± 1
Flow rate of MQL, ml/h	1	43 ± 3
Repetitions	2	
Total tests = 96		

The results of the tests are presented in Figure 80. The tests showed that T1745 tool performed better than SPL tool. The Ti-48Al-2Cr-2Nb (D) performed better with both the tools than Ti-48Al-2Cr-2Nb (NL). EML appeared to be delivering the highest tool life with tool completing 90 min test time and with tool wear < 0.2 mm with the T1745. With the TSPL, the highest tool life of Ti-48Al-2Cr-2Nb (D) was recorded with EML. The MQLVP 19004 oil performed comparatively better than MQLSE1, particular at

Bull end milling tests

low v_c (100 m/min). The MQLVP 19004 also reached a tool life of 90 min at $v_c = 100$ m/min with tool intact. However, with Hardlox coating, the performance was diminished with tool wearing off at 75 min. The tests conducted with EML at $v_c = 150$ m/min showed that the tool wear was instantaneous (2 min). At $v_c = 125$ m/min, a tool life of 60 min was recorded with T1745 tool. With both the tools, the MQL oils did not perform well when the cutting speed passed 100 m/min. Tests conducted in dry conditions with both the tools also led to instantaneous tool loss.

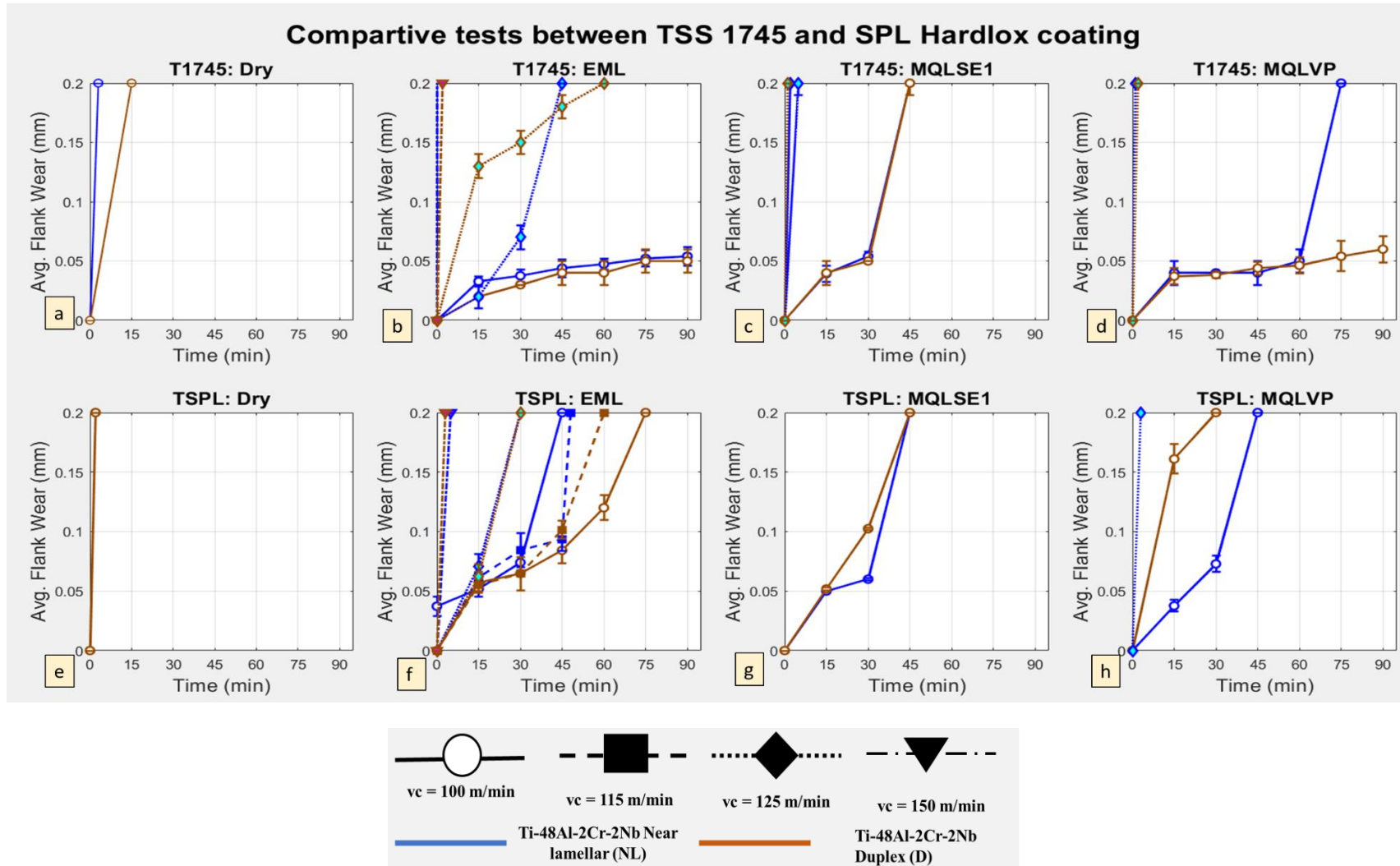


Figure 80 Comparative bull end mill tests between TSS and Hardlox coating at various contact conditions with (a) and (e) Dry, (b) and (f) EML, (c) and (g) MQLSE1 and (d) and (h) MQLVP lubricants

Bull end milling tests

The tests showed that T1745 with TIALSIN coating performed better than TSPL with Hardlox coating. Tests showed that EML is better when compared to MQL oils. The cutting speed of 150 m/min and dry lubrications are not suitable for bull end milling as they cause instantaneous tool loss.

Bull end milling tests

5.2.1 EXPERIMENTAL PLAN

The objective of the bull end milling tests was to provide a machinability comparison between Ti-48Al-2Cr-2Nb (NL) and Ti-48Al-2Cr-2Nb (D) alloys. Based on the results of preliminary tests, the test matrix comprised only of T1745 tool. Higher cutting speed of 150 m/min was also eliminated. Among the machining parameters, only the cutting speeds were varied between 100 m/min and 115 m/min for MQL oils. Only for EML, tests at 125 m/min were planned. The feed (0.03 mm/tooth) and the axial (0.25 mm) and radial (0.80 mm) depths of cut were kept constant. As for the lubricants, EML (flood), MQLSE1 and MQLVP 19004 were used. Tests in dry conditions were not included due to very poor tool life. Each test was repeated twice to confirm the test results. If major differences in the results of two trials were observed, the test was repeated a third time. The experimental plan of the test is as shown in Table 36.

Table 36 Experimental plan of milling tests

Experimental plan of bull end milling tests		
Parameter	Variance	Value
Alloys	2	Ti-48Al-2Cr-2Nb (NL); Ti-48Al-2Cr-2Nb (D)
Axial depth of cut (mm)	1	0.25
Radial depth of cut (mm)	1	0.80
Cutting speed (m/min)	3	100, 115, 125 (EML)
Feed per tooth (mm/tooth)	1	0.03
Tools	1	T1745
Lubrication	3	EML, MQL VP19004, and MQL SE1
Coolant pressure, (EML), bar	1	15 ± 2
Flow rate of EML, l/min		25 ± 1
Coolant pressure, (MQL), bar	1	6 ± 1
Flow rate of MQL, ml/h	1	43 ± 3
Repetitions	2	
Total tests = 36		

5.3 RESULTS

This section presents the bull end milling test results of Ti-48Al-2Cr-2Nb (NL) and Ti-48Al-2Cr-2Nb (D). The performance of both the alloys are compared using EML, MQLSE1 and MQLVP 19004 lubricants.

Flood (Emulsion)

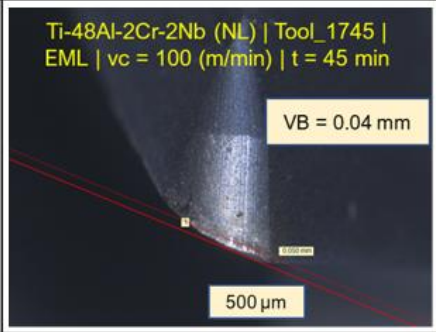
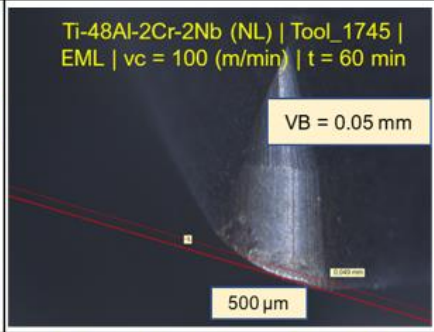
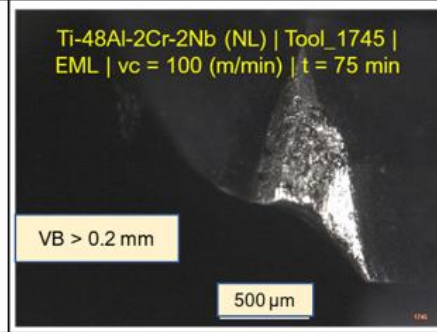
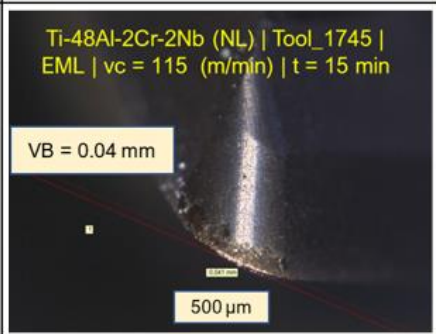
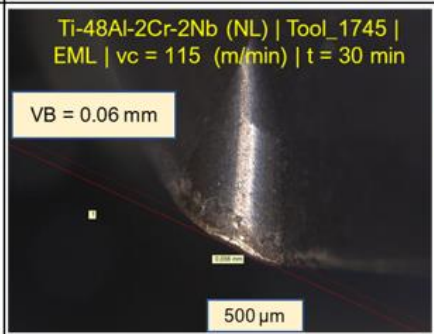
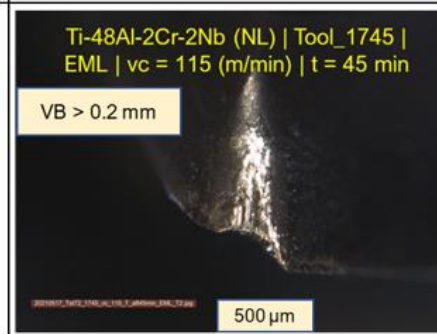
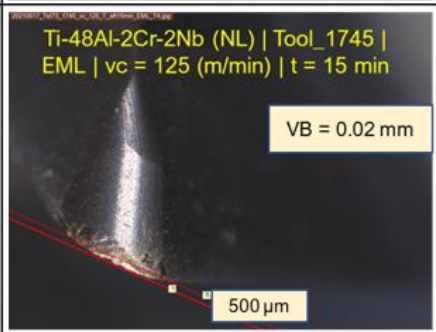
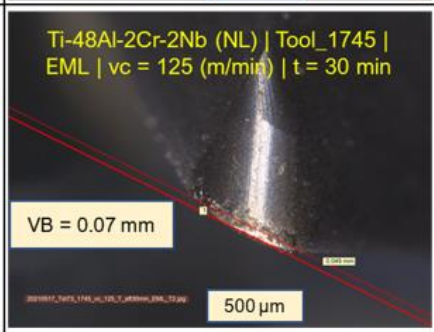
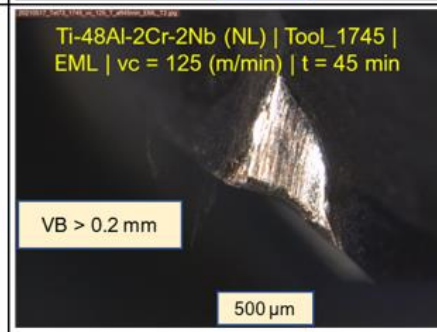
With emulsion, both the Ti-48Al-2Cr-2Nb (NL) and Ti-48Al-2Cr-2Nb (D) exhibited good tool life (≥ 75 min) at $vc = 100$ m/min. While the Ti-48Al-2Cr-2Nb (NL) completed 75 min before being completely worn out, Ti-48Al-2Cr-2Nb (D) delivered more robust performance with tool wear less than 0.2 mm even after 90 min.

When the cutting speed was increased, the tool life decreased. At 115 m/min, the Ti-48Al-2Cr-2Nb (NL) completed 45 min before reaching 0.2 mm, while the Ti-48Al-2Cr-2Nb (D) crossed the 0.2 mm threshold after 75 min.

As both Ti-48Al-2Cr-2Nb (NL) and Ti-48Al-2Cr-2Nb (D) exhibited long tool lives, particularly at lower cutting speeds, a few tests at $vc = 125$ m/min were carried out to assess the effect of a higher cutting speed on tool wear. Surprisingly, the Ti-48Al-2Cr-2Nb (D) completed 60 min before reaching 0.2 mm. The performance of Ti-48Al-2Cr-2Nb (NL) was considerably less, with the tool being completely worn at 45 min, as set out in Table 37 and 38.

Bull end milling tests

Table 37 The tool wear profiles of three time intervals before tool failure of Ti-48Al-2Cr-2Nb (NL) with EML at cutting speeds of 100, 115 and 125 m/min

<p>Ti-48Al-2Cr-2Nb (NL) Tool = 1745 Emulsion $v_c = 100$ m/min</p>	<p>Ti-48Al-2Cr-2Nb (NL) Tool_1745 EML $v_c = 100$ (m/min) $t = 45$ min VB = 0.04 mm 500 μm</p> 	<p>Ti-48Al-2Cr-2Nb (NL) Tool_1745 EML $v_c = 100$ (m/min) $t = 60$ min VB = 0.05 mm 500 μm</p> 	<p>Ti-48Al-2Cr-2Nb (NL) Tool_1745 EML $v_c = 100$ (m/min) $t = 75$ min VB > 0.2 mm 500 μm</p> 
<p>Ti-48Al-2Cr-2Nb (NL) Tool = 1745 Emulsion $v_c = 115$ m/min</p>	<p>Ti-48Al-2Cr-2Nb (NL) Tool_1745 EML $v_c = 115$ (m/min) $t = 15$ min VB = 0.04 mm 500 μm</p> 	<p>Ti-48Al-2Cr-2Nb (NL) Tool_1745 EML $v_c = 115$ (m/min) $t = 30$ min VB = 0.06 mm 500 μm</p> 	<p>Ti-48Al-2Cr-2Nb (NL) Tool_1745 EML $v_c = 115$ (m/min) $t = 45$ min VB > 0.2 mm 500 μm</p> 
<p>Ti-48Al-2Cr-2Nb (NL) Tool = 1745 Emulsion $v_c = 125$ m/min</p>	<p>Ti-48Al-2Cr-2Nb (NL) Tool_1745 EML $v_c = 125$ (m/min) $t = 15$ min VB = 0.02 mm 500 μm</p> 	<p>Ti-48Al-2Cr-2Nb (NL) Tool_1745 EML $v_c = 125$ (m/min) $t = 30$ min VB = 0.07 mm 500 μm</p> 	<p>Ti-48Al-2Cr-2Nb (NL) Tool_1745 EML $v_c = 125$ (m/min) $t = 45$ min VB > 0.2 mm 500 μm</p> 

Bull end milling tests

Table 38 The tool wear profiles of three time intervals before tool failure of Ti-48Al-2Cr-2Nb (D) with EML at cutting speeds of 100, 115 and 125 m/min

<p>Ti-48Al-2Cr-2Nb (D) Tool = 1745 Emulsion $v_c = 100$ m/min</p>	<p>Ti-48Al-2Cr-2Nb (D) Tool_1745 EML $v_c = 100$ (m/min) $t = 60$ min VB = 0.05 mm 500 μm</p>	<p>Ti-48Al-2Cr-2Nb (D) Tool_1745 EML $v_c = 100$ (m/min) $t = 75$ min VB = 0.04 mm 500 μm</p>	<p>Ti-48Al-2Cr-2Nb (D) Tool_1745 EML $v_c = 100$ (m/min) $t = 90$ min VB = 0.04 mm 500 μm</p>
<p>Ti-48Al-2Cr-2Nb (D) Tool = 1745 Emulsion $v_c = 115$ m/min</p>	<p>Ti-48Al-2Cr-2Nb (D) Tool_1745 EML $v_c = 115$ (m/min) $t = 45$ min VB = 0.02 mm 500 μm</p>	<p>Ti-48Al-2Cr-2Nb (D) Tool_1745 EML $v_c = 115$ (m/min) $t = 60$ min VB = 0.01 mm 500 μm</p>	<p>Ti-48Al-2Cr-2Nb (D) Tool_1745 EML $v_c = 115$ (m/min) $t = 75$ min VB > 0.2 mm 500 μm</p>
<p>Ti-48Al-2Cr-2Nb (D) Tool = 1745 Emulsion $v_c = 125$ m/min</p>	<p>Ti-48Al-2Cr-2Nb (D) Tool_1745 EML $v_c = 115$ (m/min) $t = 45$ min VB = 0.15 mm 500 μm</p>	<p>Ti-48Al-2Cr-2Nb (D) Tool_1745 EML $v_c = 115$ (m/min) $t = 60$ min VB = 0.18 mm 500 μm</p>	<p>Ti-48Al-2Cr-2Nb (D) Tool_1745 EML $v_c = 125$ (m/min) $t = 60$ min VB > 0.2 mm 500 μm</p>

Bull end milling tests

The results indicated that, apparently during the last 15 min the wear rate of the tool increased substantially (Figure 81). This trend is adequately evident for both the alloys, particularly at $v_c = 115$ and 125 m/min. The Ti-48Al-2Cr-2Nb (D) at $v_c = 100$ m/min was an exception as the wear rate was consistent for the entire tool life. Thus, it can be concluded that $v_c = 100$ m/min is the optimum speed to achieve good tool life with Emulsion, and in particular with the Ti-48Al-2Cr-2Nb (D) alloy.

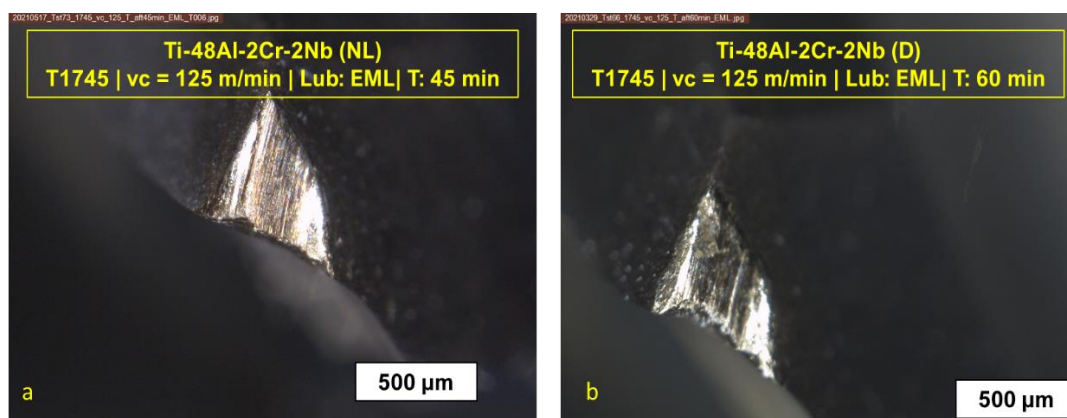


Figure 81 Higher tool lives observed for (a) Ti-48Al-2Cr-2Nb (NL) and (b) Ti-48Al-2Cr-2Nb (D) with EML at $v_c = 125$ m/min

Lower cutting speeds recorded low cutting forces. Importantly, the cutting forces for Ti-48Al-2Cr-2Nb (D) were lower than Ti-48Al-2Cr-2Nb (NL). This difference was particularly noticeable at $v_c = 100$ m/min. Increasing the cutting speed to $v_c = 115$ m/min, resulted in an increase in cutting forces. However, both the alloys recorded equal forces. This trend was also evident at $v_c = 125$ m/min. It should be noted that, although the Ti-48Al-2Cr-2Nb (D) presented longer tool life (60 min) than Ti-48Al-2Cr-2Nb (NL) (45 min), both alloys exhibited similar force profiles after tool failure. This evolution is shown in Figure 82.

The surface roughness measurements also varied with cutting speeds and alloys. This change was particularly evident in the Ti-48Al-2Cr-2Nb (D) alloy where R_a values decreased with the increase in v_c . The Ti-48Al-2Cr-2Nb (NL) showed more robust results with minimal differences in R_a profiles as seen in Figure 82.

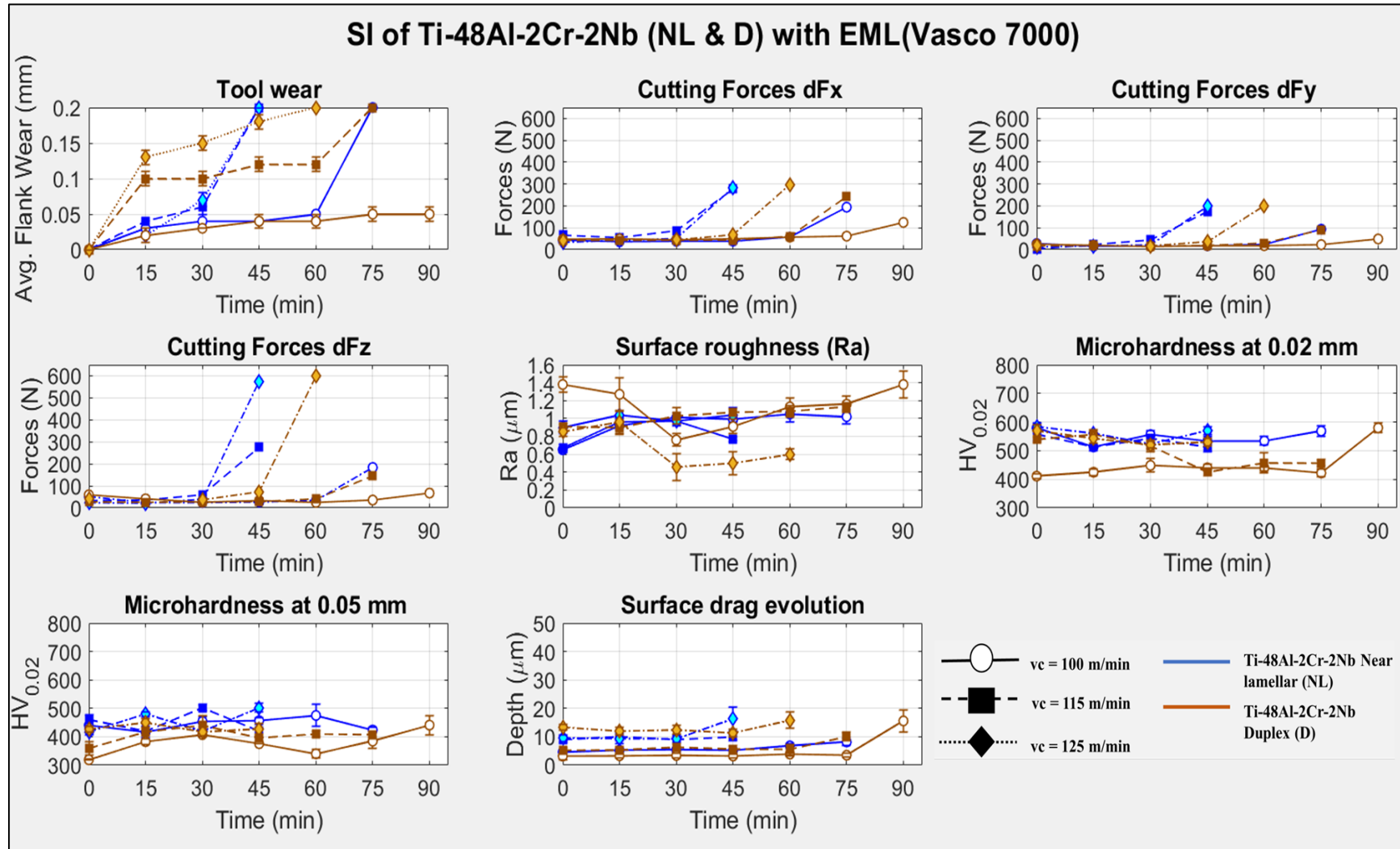


Figure 82 Output parameters of Ti-48Al-2Cr-2Nb (NL) and Ti-48Al-2Cr-2Nb (D) observed with EML at $v_c = 100, 115$ and 125 m/min

The microhardness ($HV_{0.02}$) measurements revealed a marked difference between the Ti-48Al-2Cr-2Nb (NL) and Ti-48Al-2Cr-2Nb (D) alloys. The Ti-48Al-2Cr-2Nb (D) alloy presented lower microhardness values than the Ti-48Al-2Cr-2Nb (NL), at all cutting speeds, with the exception of 0 and 15 min with $v_c = 115$ m/min. This observation is in agreement with the work of Gupta et al. [30] who reported the higher hardness of lamellar structures in comparison to finer duplex microstructures. With Ti-48Al-2Cr-2Nb (NL), the microhardness values were in a similar range for all the cutting speeds. On the other hand, Ti-48Al-2Cr-2Nb (D) indicated that microhardness values increased with the increase in cutting speed. Importantly, the microhardness for the both the alloys decreased with the increase in measurement depth (0.02 mm and 0.05 mm below the machined surface). This seems to indicate stress accumulation in the machining affected zone.

Both alloys presented the same trends for sub-surface microstructure alterations. Surface drag (SD) was the most prominent defect observed with lamellar bending occurring across the entire examined surface. While pits were only observed at $v_c = 125$ m/min with Ti-48Al-2Cr-2Nb (D) alloy (Figure 83), SD was obvious in both alloys at all cutting speeds.

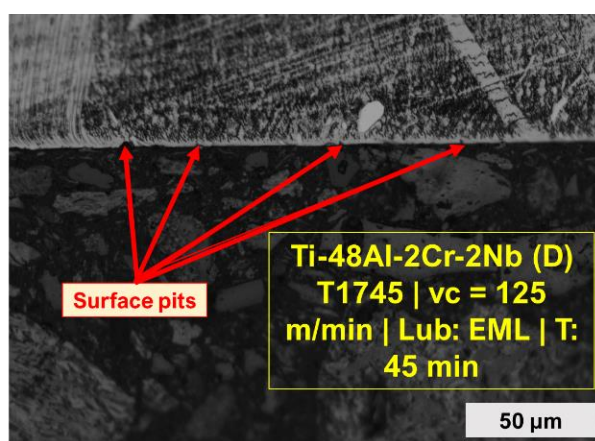


Figure 83 Surface pits observed for Ti-48Al-2Cr-2Nb (D) with EML at $v_c = 125$ m/min

The SD were seen continuously on the entire longitudinal face for Ti-48Al-2Cr-2Nb (NL) alloy. As seen in Figure 82, the depth of SD seemingly increased with the increase in cutting speed. However, this increase was not high as the SD were in the range of 5-8 μ m. Notably, the evolution profile of SD depth did not match the tool wear profile. At $v_c = 100$ m/min, $t = 75$ min when the tool was completely worn, the increase in depth

of SD was minimal. The drastic increase in tool wear rate during the final minutes of tool life did not translate to an increase in SD depth. Thus, no correlation could be established between the tool wear and SD depth. This outcome is consistent with the findings of Hood et al. [13] who noted that no relationship existed between flank wear and depth of damage for Ti-45Al-8Nb-0.2C and Ti-45Al-2Mn-2Nb +0.8% vol. TiB₂.

In the case of Ti-48Al-2Cr-2Nb (D), SD was not found to be continuous across the examined surface, but rather occurred intermittently. This could be attributed to the lower volume of lamellar colonies in Duplex microstructures. Additionally, the observed SD were diminished in depth when compared to Ti-48Al-2Cr-2Nb (NL) alloy. Nevertheless, an increase in SD depth was observed with increase in cutting speed. Although a slight increase in SD depth was noted at the end of tool life at all cutting speeds, the trend indicated no relationship between SD depth, cutting speed and flank wear. The minimum SI data sheet of the alloys is set out in Table 39.

Bull end milling tests

Table 39 The minimum SI data sheet of Ti-48Al-2Cr-2Nb (NL) and Ti-48Al-2Cr-2Nb (D) observed with EML at $v_c = 100, 115$ and 125 m/min

Material	v_c (m/min)	Time (min)	Avg_SD	HV 0.02 (N/mm ²)	HV 0.05 (N/mm ²)	Ra (μ m)	Rt (μ m)	Rz (μ m)	Vb (mm)	dFx (N)	dFy (N)	dFz (N)	
TiAl_NL	100	0	4.675	579.5	440	0.65	4.44	3.25	0	42.81	27.87	51.57	
TiAl_NL	100	15	5.3	513	416	0.92	5.16	4.06	0.03	36.49	15.86	23.62	
TiAl_NL	100	30	5.44	556	454	1.01	5.16	4.53	0.04	38.2	15.53	24.14	
TiAl_NL	100	45	5.23	533.5	456.5	0.99	4.69	4	0.04	38.5	17.15	26.45	
TiAl_NL	100	60	6.79	534	475	1.05	6.25	4.55	0.05	57.64	23.73	34.16	
TiAl_NL	100	75	8.18	568.5	423.5	1.02	5.1	4.2	0.2	194.28	93.27	183.56	
TiAl_NL	115	0	9.11	558	459.5	0.67	3.98	3.2	0	65.88	2.7	33.37	
TiAl_NL	115	15	10.05	513	419	0.96	5.25	4.13	0.04	54.94	23.08	35.76	
TiAl_NL	115	30	9.07	542	502	0.97	5.35	4.12	0.06	86.6	44.1	59.43	
TiAl_NL	115	45	9.85	512	423	0.77	4.47	3.64	0.2	277	174.1	275.2	
TiAl_NL	125	0	9.48	584	418	0.9	4.83	3.76	0	33.38	12.69	23.76	
TiAl_NL	125	15	9.42	561	480	1.04	5.63	4.57	0.02	42.23	16.83	21.42	
TiAl_NL	125	30	9.26	523	419	0.97	5.55	4.14	0.07	51.04	21.63	39.27	
TiAl_NL	125	45	16.26	571	502	1.04	5.21	4.48	0.2	284	198	574.86	
TiAl_D	100	0	3.2	411	319	Values missing			0	47.81	24.81	59.37	
TiAl_D	100	15	3.31	424.5	382.5	1.27	8.1	5.76	0.02	49.27	19.77	41.07	
TiAl_D	100	30	3.4	448.5	407.5	0.76	4.39	3.25	0.03	45.32	13.95	25.58	
TiAl_D	100	45	3.24	440	375.5	0.91	5.34	4.01	0.04	49.48	17.96	33.22	
TiAl_D	100	60	3.89	440	340	1.13	6.12	4.7	0.04	57.27	18.2	24.89	
TiAl_D	100	75	3.5	422	384.5	1.16	5.95	4.79	0.05	61.75	22.76	35.54	
TiAl_D	100	90	15.57	579.5	441	1.38	9.96	7.31	0.05	124.45	48.93	67.29	
TiAl_D	115	0	5.2	538.5	359	0.91	4.62	4.27	0	42.15	17.26	27.1	
TiAl_D	115	15	5.4	556.5	417.5	0.9	4.9	3.99	0.1	41.93	19.23	25.67	
TiAl_D	115	30	6.35	517	439.5	1.03	5.87	4.54	0.1	42.7	15.47	27.34	
TiAl_D	115	45	5.71	424.5	395.5	1.07	6.65	4.66	0.12	43.22	18.97	28.68	
TiAl_D	115	60	5.51	457.5	409.5	1.08	5.59	4.4	0.12	61.03	30.1	40.87	
TiAl_D	115	75	10.09	456.5	408	1.13	5.36	4.6	0.2	242.27	90.34	145.26	
TiAl_D	125	0	13.31	569	427	0.85	5.47	3.94	0	39.68	18	40.59	
TiAl_D	125	15	11.93	542	449	0.96	4.55	4	0.13	Values missing			
TiAl_D	125	30	12.46	521	418	0.46	2.95	1.77	0.15	44.54	17.4	36.8	
TiAl_D	125	45	11.33	531	428	0.5	3.18	2.45	0.18	68.17	36.28	73.23	
TiAl_D	125	60	15.87	Values missing			0.6	4.22	3.2	0.2	298	201	598

MQLSE1

Using MQLSE1, the tool lives of Ti-48Al-2Cr-2Nb (NL) and Ti-48Al-2Cr-2Nb (D) were shorter in comparison to EML. At $v_c = 100$ m/min, both Ti-48Al-2Cr-2Nb (NL) and Ti-48Al-2Cr-2Nb (D) delivered a tool life of 45 min before facing a catastrophic tool failure. The tool wear profiles are set out in Table 40 and Table 41 for Ti-48Al-2Cr-2Nb (NL) and Ti-48Al-2Cr-2Nb (D).

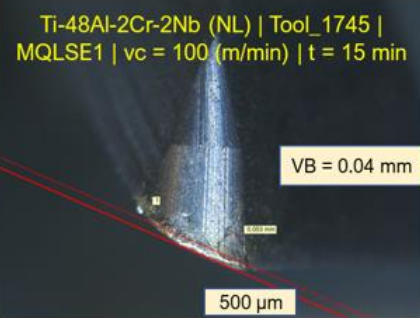
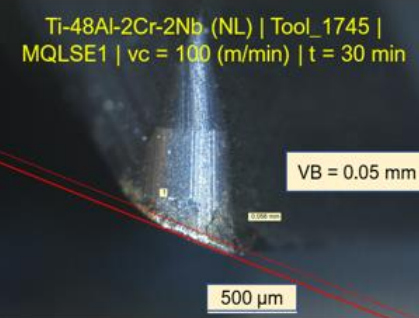
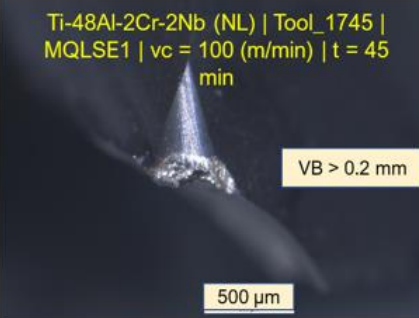
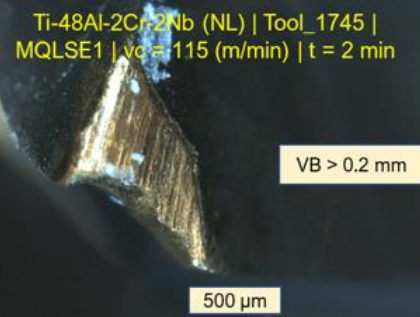
As seen previously with EML, the wear rate was severe in the final minutes before the tool exceeded the flank wear limit of 0.2 mm. With an increase in cutting speed to $v_c = 115$ m/min, the tool life decreased sharply (within 2 min for Ti-48Al-2Cr-2Nb (NL) and 5 min Ti-48Al-2Cr-2Nb (D)). The tool wear was so severe that the entire flank face was missing after the short tool life. Considering these results at $v_c = 115$ m/min, tests with $v_c = 125$ m/min were not conducted.

The lower cutting speeds reported lower cutting forces. The cutting forces increased proportionally with an increase in tool wear. At $v_c = 100$ m/min, Ti-48Al-2Cr-2Nb (NL) showed lower cutting forces than Ti-48Al-2Cr-2Nb (D), however at $v_c = 115$ m/min, a reciprocal trend was seen (Figure 84).

The surface roughness profiles showed that Ti-48Al-2Cr-2Nb (NL) exhibited lower R_a values than Ti-48Al-2Cr-2Nb (D) at both cutting speeds. Increased R_a values were noted with an increase in cutting speeds for both the alloys.

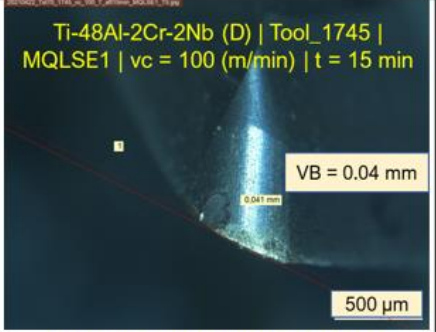
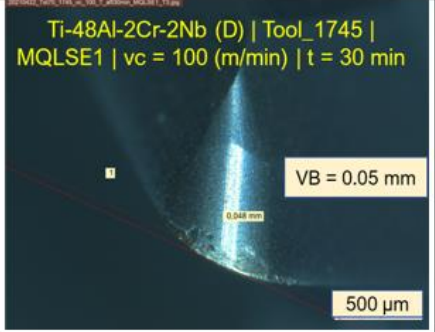
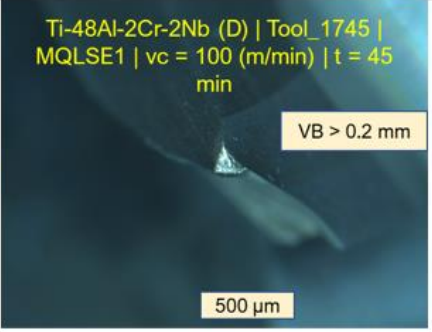
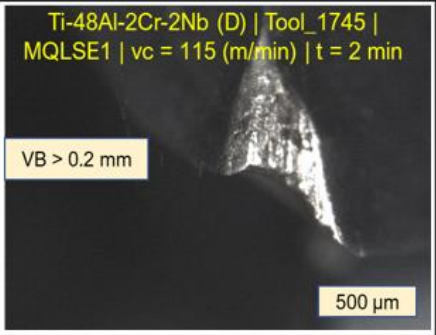
Bull end milling tests

Table 40 The tool wear profiles of three time intervals at 100 m/min and with last time interval at 115 m/min, before tool failure for Ti-48Al-2Cr-2Nb (NL) with MQLSE1

<p>Ti-48Al-2Cr-2Nb (NL) Tool = 1745 MQLSE1 $v_c = 100$ m/min</p>	<p>Ti-48Al-2Cr-2Nb (NL) Tool_1745 MQLSE1 $v_c = 100$ (m/min) $t = 15$ min</p>  <p>VB = 0.04 mm</p> <p>500 μm</p>	<p>Ti-48Al-2Cr-2Nb (NL) Tool_1745 MQLSE1 $v_c = 100$ (m/min) $t = 30$ min</p>  <p>VB = 0.05 mm</p> <p>500 μm</p>	<p>Ti-48Al-2Cr-2Nb (NL) Tool_1745 MQLSE1 $v_c = 100$ (m/min) $t = 45$ min</p>  <p>VB > 0.2 mm</p> <p>500 μm</p>
<p>Ti-48Al-2Cr-2Nb (NL) Tool = 1745 MQLSE1 $v_c = 115$ m/min</p>	<p>Ti-48Al-2Cr-2Nb (NL) Tool_1745 MQLSE1 $v_c = 115$ (m/min) $t = 2$ min</p>  <p>VB > 0.2 mm</p> <p>500 μm</p>		

Bull end milling tests

Table 41 The tool wear profiles of three time intervals at 100 m/min and with last time interval at 115 m/min, before tool failure for Ti-48Al-2Cr-2Nb (D) with MQLSE1

<p>Ti-48Al-2Cr-2Nb (D) Tool = 1745 MQLSE1 $v_c = 100$ m/min</p>	<p>Ti-48Al-2Cr-2Nb (D) Tool_1745 MQLSE1 $v_c = 100$ (m/min) t = 15 min</p>  <p>VB = 0.04 mm 500 μm</p>	<p>Ti-48Al-2Cr-2Nb (D) Tool_1745 MQLSE1 $v_c = 100$ (m/min) t = 30 min</p>  <p>VB = 0.05 mm 500 μm</p>	<p>Ti-48Al-2Cr-2Nb (D) Tool_1745 MQLSE1 $v_c = 100$ (m/min) t = 45 min</p>  <p>VB > 0.2 mm 500 μm</p>
<p>Ti-48Al-2Cr-2Nb (D) Tool = 1745 MQLSE1 $v_c = 115$ m/min</p>	<p>Ti-48Al-2Cr-2Nb (D) Tool_1745 MQLSE1 $v_c = 115$ (m/min) t = 2 min</p>  <p>VB > 0.2 mm 500 μm</p>		

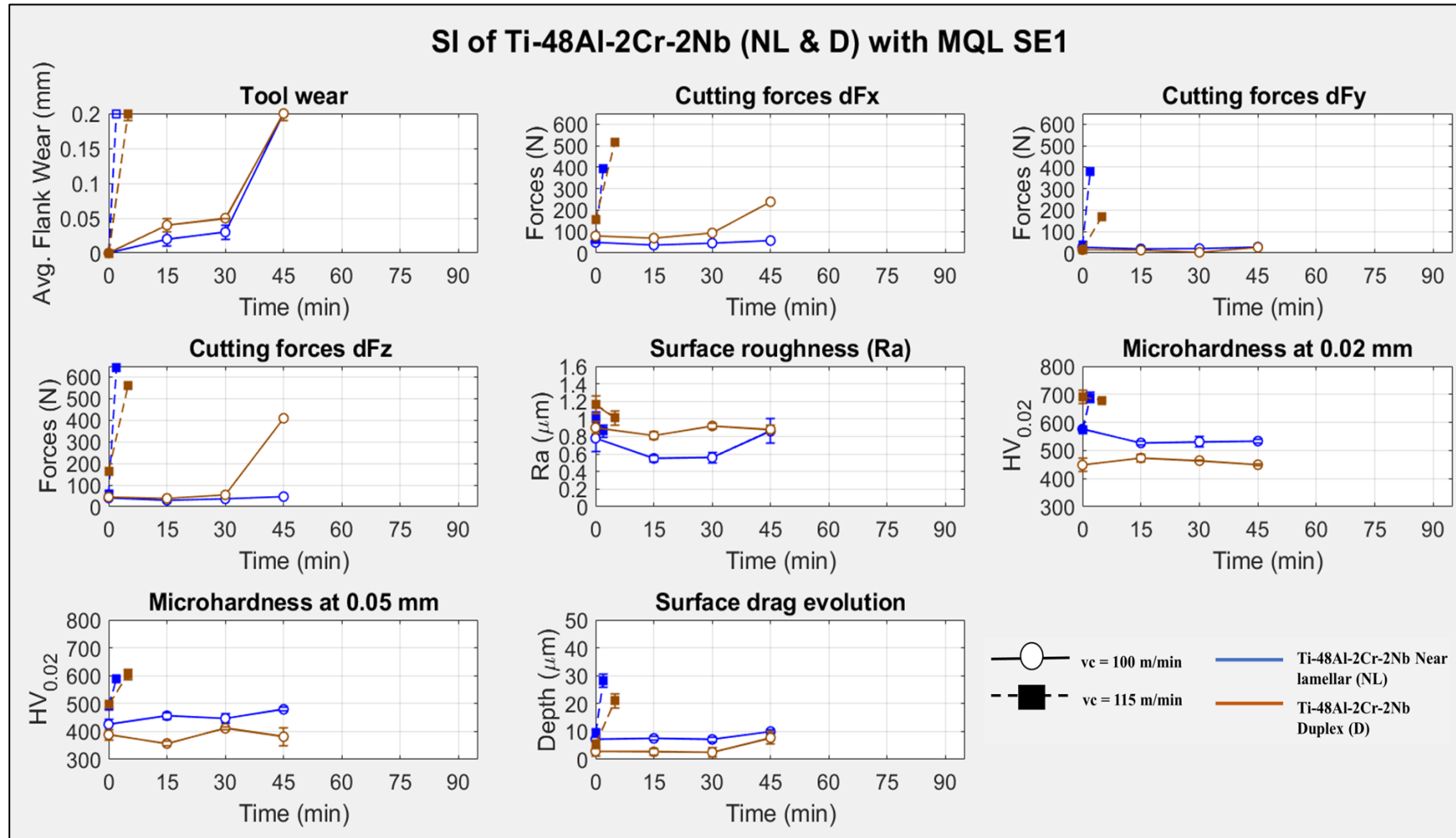


Figure 84 Output parameters of Ti-48Al-2Cr-2Nb (NL) and Ti-48Al-2Cr-2Nb (D) observed with MQLSE1 at $v_c = 100$ and 115 m/min

Bull end milling tests

As seen previously with emulsion, there was a marked difference between microhardness measurements of both the alloys. The Ti-48Al-2Cr-2Nb (D) showed lower HV_{0.02} than Ti-48Al-2Cr-2Nb (NL) alloy. The HV_{0.02} values rose with an increase in cutting speed for both the alloys. Notably, the at $vc = 115$ m/min for both the alloys, the increase in HV_{0.02} was substantial and matched the tool wear profile. The sub-surface alterations showed that both the alloys had distinct behaviours based on the cutting speed. SD was the most prominent sub-surface defect seen in both the alloys. Cracks were seen at $vc = 115$ m/min at $t = 2$ min for Ti-48Al-2Cr-2Nb (D) alloy, as seen in Figure 85.

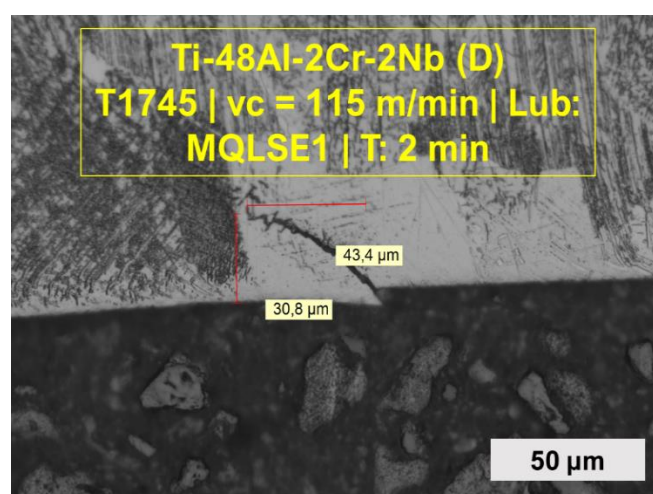


Figure 85 Cracks observed for Ti-48Al-2Cr-2Nb (D) at $vc = 115$ m/min with MQLSE1

While no correlation between tool wear and the depth of SD was observed at $vc = 100$ m/min, at $vc = 115$ m/min, a substantial increase in SD depth was noted at the end of tool life for both the alloys. This is evident in the profiles presented in Figure 84.

As seen previously, the occurrence of SD in Ti-48Al-2Cr-2Nb (D) was intermittent due to the low volume of lamellar colonies. With Ti-48Al-2Cr-2Nb (NL) SD was present continuously across the entire examined surface. Thus, with MQLSE1, at $vc = 100$ m/min, no correlation was found between the tool wear profile and SD depth. However, at a high cutting speed of $vc = 115$ m/min, the severe tool wear was matched by SD depth. The minimum SI data sheet of the alloys is presented in Table 42.

Bull end milling tests

Table 42 The minimum SI data sheet of Ti-48Al-2Cr-2Nb (NL) and Ti-48Al-2Cr-2Nb (D) observed with MQLSE1 at $v_c = 100$ and 115 m/min

Material	v_c (m/min)	Time (min)	Avg_SD (μm)	HV 0.02 (N/mm ²)	HV 0.05 (N/mm ²)	Ra (μm)	Rt (μm)	Rz (μm)	Vb (mm)	dFx (N)	dFy (N)	dFz (N)
TiAl_NL	100	0	7.22	576	425.5	0.78	4.63	3.73	0	49.88	27.05	40.55
TiAl_NL	100	15	7.54	527	456.5	0.55	3.72	2.74	0.02	37.24	19.64	29.69
TiAl_NL	100	30	7.17	531	447	0.56	3.43	2.93	0.03	46.31	20.85	36.59
TiAl_NL	100	45	9.99	533.5	479.5	0.86	4.17	3.49	0.2	58.06	28.06	46.77
TiAl_NL	115	0	9.58	575	492	1	4.89	4	0	65.28	35.33	56.92
TiAl_NL	115	2	28.21	688	587.5	0.86	5.06	4	0.2	394.6	379.5	643.1
TiAl_D	100	0	2.9	448.5	388.5	0.9	4.78	3.88	0	79.71	16.16	44.66
TiAl_D	100	15	2.73	473.5	357	0.81	4.7	3.63	0.04	69.46	13.59	38.59
TiAl_D	100	30	2.57	464	411.5	0.92	4.46	3.7	0.05	93.57	3.62	54.68
TiAl_D	100	45	7.76	449.5	381.5	0.88	5.33	3.81	0.2	238.8	26.62	409.2
TiAl_D	115	0	5.52	691	496	1.16	6.43	4.87	0	154	16.13	163.9
TiAl_D	115	5	20.96	679	605	1.01	5.13	4.56	0.2	518.2	170.4	560.2

MQLVP19004

Using MQLVP 19004, both Ti-48Al-2Cr-2Nb (NL) and Ti-48Al-2Cr-2Nb (D) had similar profiles with respect to cutting speeds. At $v_c = 100$ m/min, both Ti-48Al-2Cr-2Nb (NL) and Ti-48Al-2Cr-2Nb (D) exhibited reasonably good tool lives of 75 min and 90 min each. However, at $v_c = 115$ m/min, tool life decreased for both the alloys. This was particularly the case for Ti-48Al-2Cr-2Nb (NL), where the tool lasted for only 3 min before catastrophic tool failure. On the other hand, the Ti-48Al-2Cr-2Nb (D) lasted 30 min before suffering tool failure as depicted. The tool wear profiles are presented in Table 43 and Table 44.

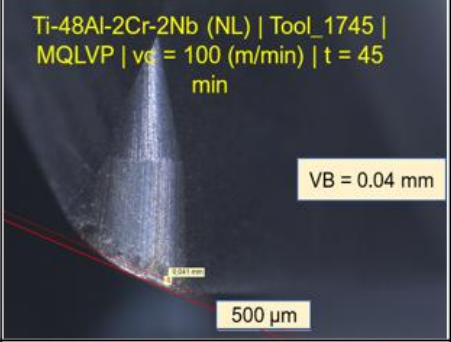
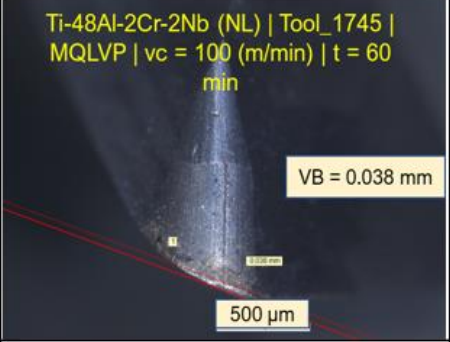
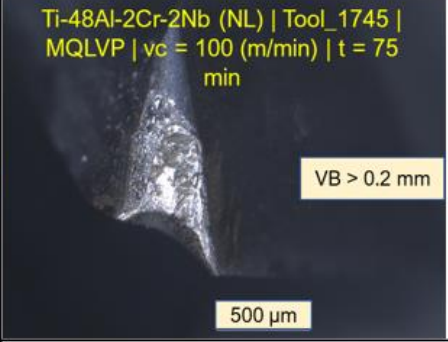
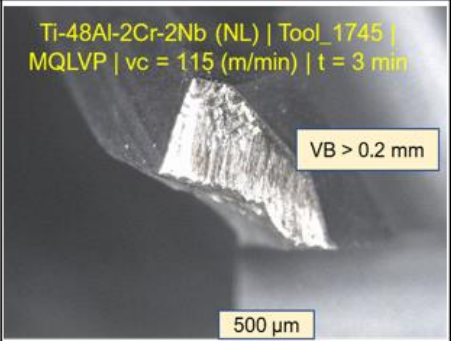
This indicated that cutting speeds greater than 100 m/min were not suitable for both alloys when using MQLVP 19004. The cutting forces increased with an increase in cutting speed. At $v_c = 100$ m/min, Ti-48Al-2Cr-2Nb (D) showed constant cutting forces till 90 min. This was in accordance with the tool wear profile of the alloy. At 115 m/min, both the alloys presented a marked increase in forces which corresponded to the tool wear.

The surface roughness profiles varied with the alloys and cutting speeds. The R_a values increased with increase in cutting speed for both alloys. At $v_c = 100$ m/min, both the alloys had similar R_a profiles as seen in Figure 86. However, Ti-48Al-2Cr-2Nb (NL) reported lower R_a values at 45 min and 60 min. At $v_c = 115$ m/min, Ti-48Al-2Cr-2Nb (NL) presented a substantial increase in R_a value, whereas the increase for Ti-48Al-2Cr-2Nb (D) was gradual. This difference could be attributed to very short tool life of Ti-48Al-2Cr-2Nb (NL), where the tool suffered catastrophic failure at 3 min.

The microhardness profiles of both alloys are similar to observations made in EML and MQLSE1 with Ti-48Al-2Cr-2Nb (NL) showing higher $HV_{0.02}$ values than Ti-48Al-2Cr-2Nb (D). The $HV_{0.02}$ were higher at $v_c = 100$ m/min vis-à-vis 115 m/min for both the alloys. The $HV_{0.02}$ values decreased with increase in the depth of microhardness.

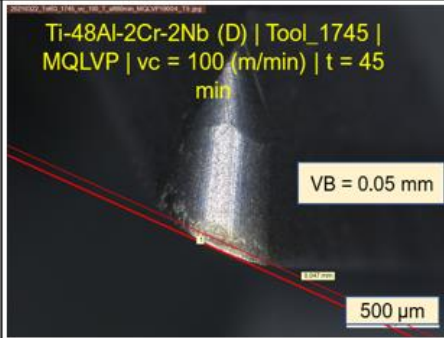
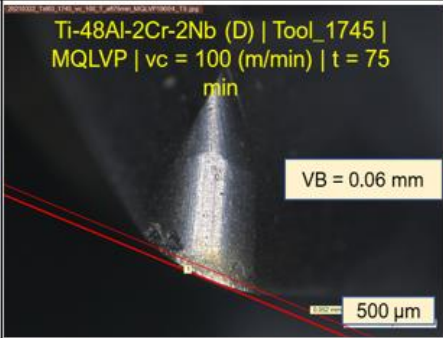
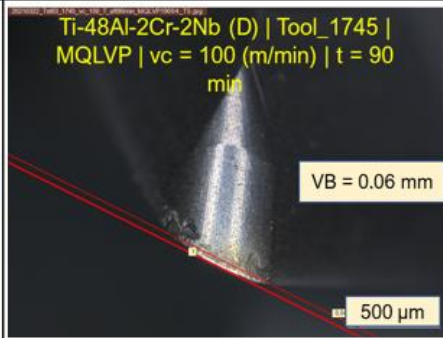
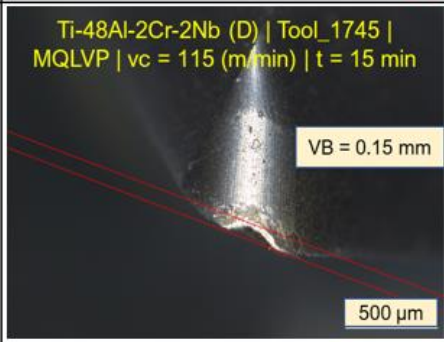
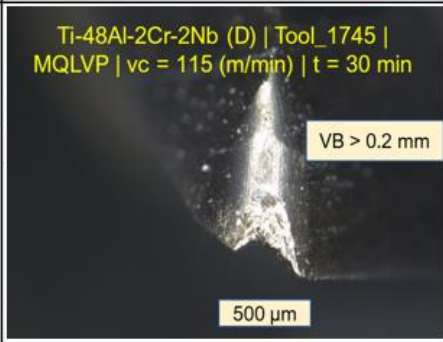
Bull end milling tests

Table 43 The tool wear profiles of last three time intervals at 100 m/min and with last time interval at 115 m/min, before tool failure for Ti-48Al-2Cr-2Nb (NL) with MQLVP

<p>Ti-48Al-2Cr-2Nb (NL) Tool = 1745 MQLVP v_c = 100 m/min</p>	<p>Ti-48Al-2Cr-2Nb (NL) Tool_1745 MQLVP v_c = 100 (m/min) t = 45 min</p>  <p>VB = 0.04 mm</p> <p>500 μm</p>	<p>Ti-48Al-2Cr-2Nb (NL) Tool_1745 MQLVP v_c = 100 (m/min) t = 60 min</p>  <p>VB = 0.038 mm</p> <p>500 μm</p>	<p>Ti-48Al-2Cr-2Nb (NL) Tool_1745 MQLVP v_c = 100 (m/min) t = 75 min</p>  <p>VB > 0.2 mm</p> <p>500 μm</p>
<p>Ti-48Al-2Cr-2Nb (NL) Tool = 1745 MQLVP v_c = 115 m/min</p>	<p>Ti-48Al-2Cr-2Nb (NL) Tool_1745 MQLVP v_c = 115 (m/min) t = 3 min</p>  <p>VB > 0.2 mm</p> <p>500 μm</p>		

Bull end milling tests

Table 44 The tool wear profiles of last three time intervals at 100 m/min and with last time interval at 115 m/min, before tool failure for Ti-48Al-2Cr-2Nb (D) with MQLVP

<p>Ti-48Al-2Cr-2Nb (D) Tool = 1745 MQLVP v_c = 100 m/min</p>	<p>Ti-48Al-2Cr-2Nb (D) Tool_1745 MQLVP v_c = 100 (m/min) t = 45 min VB = 0.05 mm 500 μm</p> 	<p>Ti-48Al-2Cr-2Nb (D) Tool_1745 MQLVP v_c = 100 (m/min) t = 75 min VB = 0.06 mm 500 μm</p> 	<p>Ti-48Al-2Cr-2Nb (D) Tool_1745 MQLVP v_c = 100 (m/min) t = 90 min VB = 0.06 mm 500 μm</p> 
<p>Ti-48Al-2Cr-2Nb (D) Tool = 1745 MQLVP v_c = 115 m/min</p>	<p>Ti-48Al-2Cr-2Nb (D) Tool_1745 MQLVP v_c = 115 (m/min) t = 15 min VB = 0.15 mm 500 μm</p> 	<p>Ti-48Al-2Cr-2Nb (D) Tool_1745 MQLVP v_c = 115 (m/min) t = 30 min VB > 0.2 mm 500 μm</p> 	

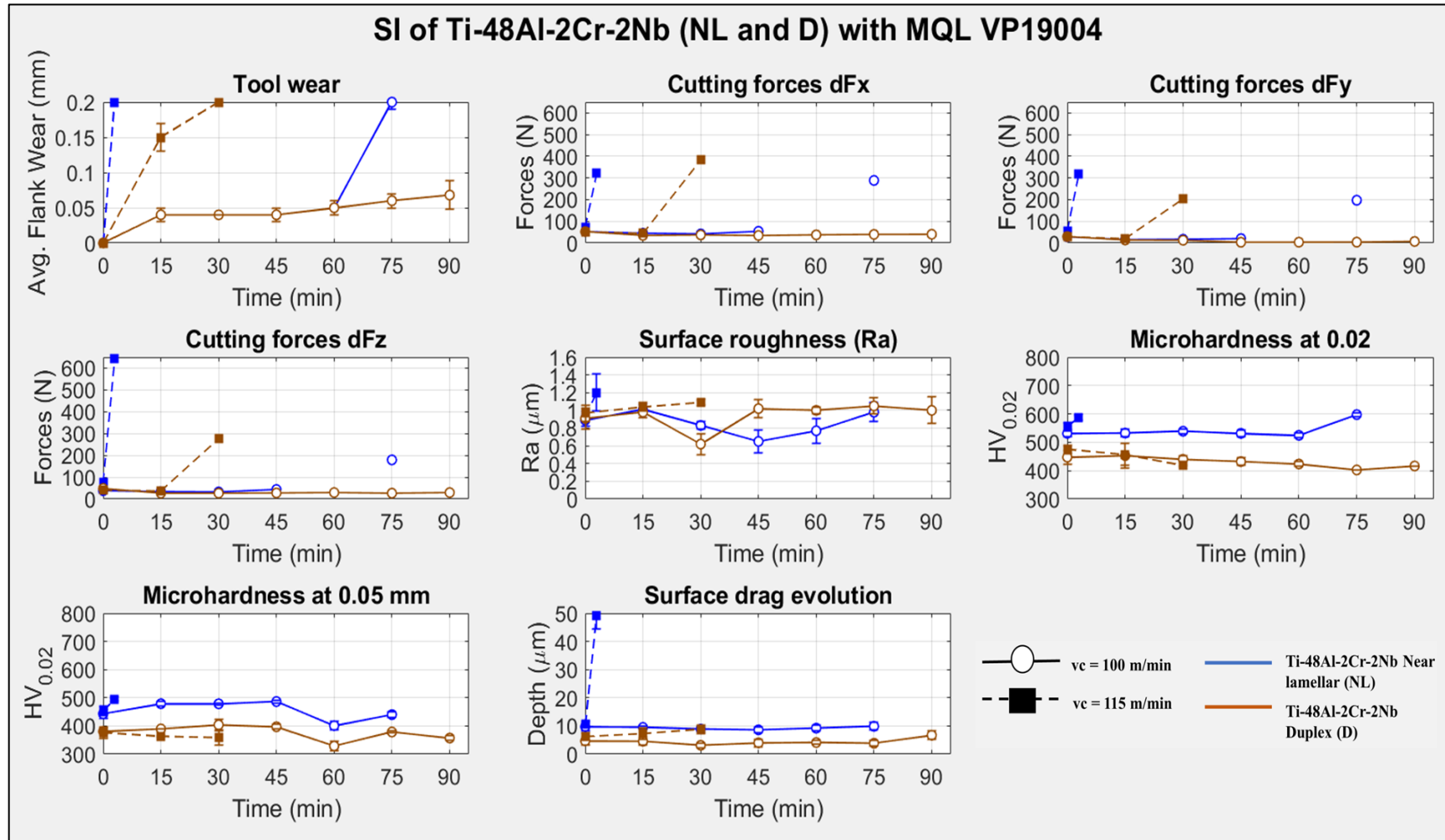


Figure 86 The output parameters of Ti-48Al-2Cr-2Nb (NL) and Ti-48Al-2Cr-2Nb (D) observed with MQLVP19004 at $v_c = 100$ and 115 m/min

Bull end milling tests

The sub-surface microstructure assessment revealed that the SD was the only defect. The profiles of both the alloys were distinct. At $v_c = 100$ m/min, the Ti-48Al-2Cr-2Nb (NL) alloy showed a constant SD depth of approx. 10 μm for all cutting times. Even with the tool worn at 75 min, no increase in SD depth was recorded (Figure 86). However, at $v_c = 115$ m/min, when the tool wore at 3 min, the depth of SD was recorded at 50 μm . Thus, the correlation between tool wear and the depth of SD exists only at $v_c = 115$ m/min.

The Ti-48Al-2Cr-2Nb (D), in contrast, presented intermittent SD as seen with other lubricants. However, this SD depth was not affected by the change in the cutting speed, and the depth of SD at $v_c = 115$ m/min was only marginally higher than at $v_c = 100$ m/min. This trend is depicted in Figure 86. The minimum SI data sheet of both the alloys is presented in Table 45.

Bull end milling tests

Table 45 The minimum SI data sheet of Ti-48Al-2Cr-2Nb (NL) and Ti-48Al-2Cr-2Nb (D) observed with MQLVP19004 at $v_c = 100$ and 115 m/min

Material	v_c (m/min)	Time (min)	Avg_SD	HV 0.02 (N/mm ²)	HV 0.05 (N/mm ²)	Ra (μ m)	Rt (μ m)	Rz (μ m)	Vb (mm)	dFx (N)	dFy (N)	dFz (N)
TiAl_NL	100	0	9.79	531.5	443	0.89	4.95	3.73	0	52.57	28.42	38.23
TiAl_NL	100	15	9.48	532.5	479	1.01	4.56	4.09	0.04	45.22	15.46	34.08
TiAl_NL	100	30	8.9	539	478.5	0.83	4.05	3.39	0.04	41.85	17.17	32.56
TiAl_NL	100	45	8.61	531.5	486.5	0.65	3.45	3.28	0.04	53.68	20.13	43.77
TiAl_NL	100	60	9.21	524.5	401	0.77	4.71	3.73	0.05	Missing		
TiAl_NL	100	75	9.88	597.5	440	0.98	6.03	4.5	0.2	288.73	197.22	179.26
TiAl_NL	115	0	10.6	556	454	0.93	4.9	3.98	0	73.43	55.47	76.73
TiAl_NL	115	3	49.24	586.5	495	1.2	6.23	4.9	0.2	321.1	317.9	642.3
TiAl_D	100	0	4.68	447.5	381	0.91	5.07	3.98	0	52.58	29.51	48.41
TiAl_D	100	15	4.57	453	389.5	0.98	4.84	3.95	0.04	35.04	13.91	26.69
TiAl_D	100	30	3.12	440	404	0.62	3.48	2.87	0.04	37.27	12.62	26.8
TiAl_D	100	45	4	432	397	1.02	5.78	4.38	0.04	34.64	13.55	27.89
TiAl_D	100	60	4.11	423.5	329	1	5.12	4.14	0.05	37.67	13.78	29.6
TiAl_D	100	75	3.85	402.5	378.5	1.05	5.37	4.41	0.06	39.61	14.03	26.82
TiAl_D	100	90	6.7	416.5	357	1	5.98	4.22	0.068	40.23	17.11	29.54
TiAl_D	115	0	6.2	474.5	376.5	0.97	5.2	4.31	0	52.34	29.13	40.28
TiAl_D	115	15	7.3	457	364	1.04	5.4	4.54	0.15	44.1	19.96	36.94
TiAl_D	115	30	8.8	417.5	358	1.09	5.16	4.53	0.2	382.27	203.27	276.27

From the SI analyses, the Ti-48Al-2Cr-2Nb (NL) alloy revealed consistent occurrence of surface drags with all lubricants and all cutting speeds. Although, the increase in depth of SD was not commensurate with the increase in tool wear, sharp increases in the depth were recorded for the MQLSE1 and MQLVP oils at $v_c = 115$ m/min. This was only true when the tool had very low tool life. Else, the SD did not present qualitative differences with increase in cutting speed. The near lamellar microstructure is composed of long lamellar colonies ($\alpha_2 + \gamma$) together with fine α_2 and γ grains. The longer lamellar laths could get embedded between the α_2 and γ grains as seen in Figure 87. In the present case, as seen from the grain size distribution of Ti-48Al-2Cr-2Nb (NL) in section 3.2, the grains from 10 μm (fine) to 75 μm (long) are almost equally distributed. When the lamellar colonies are surrounded by α_2 and γ grains of equal measure at the periphery, the drag may apparently become limited in size. This could explain the short depth of surface drag observed at high tool wear.

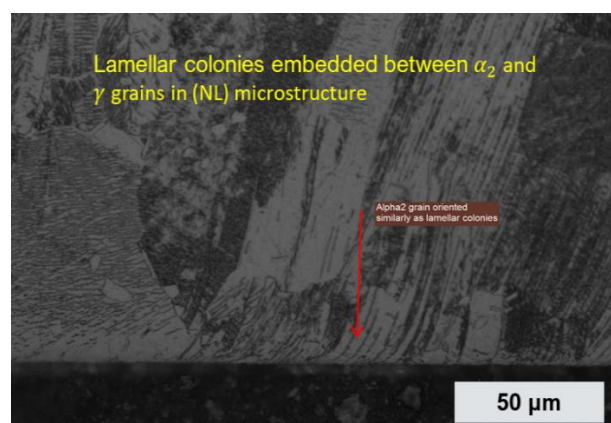


Figure 87 The lamellar colonies embedded between alpha 2 and gamma grains in Ti-48Al-2Cr-2Nb (NL) microstructure

Moreover, from the works of Klocke et al. [10] it could be understood that the bending of the lamellar colonies is specific to the orientation of the colonies with respect to the cutting tool. It was observed that surface drag in lamellar microstructures was prominent when the drag was parallel to the tool tip. Correspondingly, the surrounding lamellae with perpendicular orientation were not seen to be deformed. These criteria explain the existence of continuous but non-commensurate rise of surface drag with tool wear in (NL) microstructure. This is evident in the subsurface micrographs of Ti-48Al-2Cr-2Nb (NL) and Ti-48Al-2Cr-2Nb (D) with each lubricant and cutting speed as presented in Tables 46 - 51

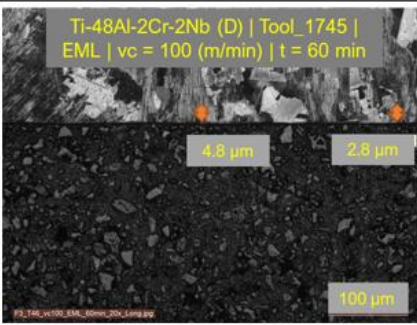
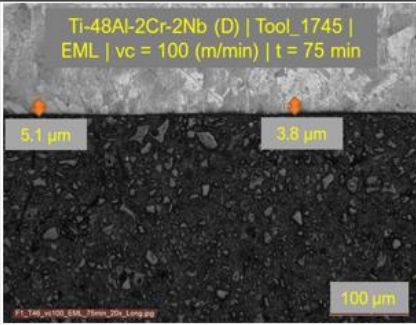
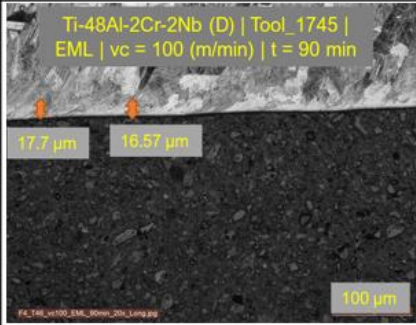
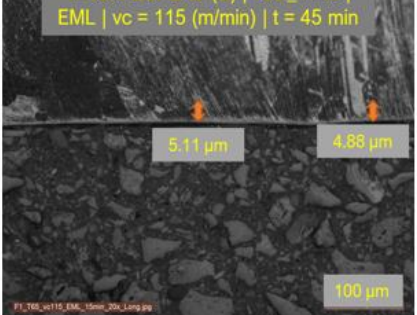
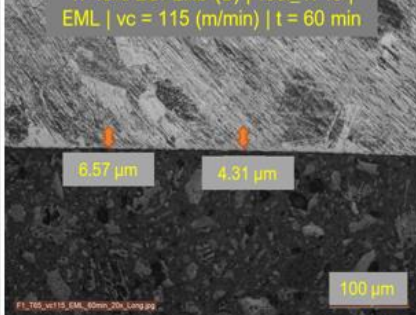
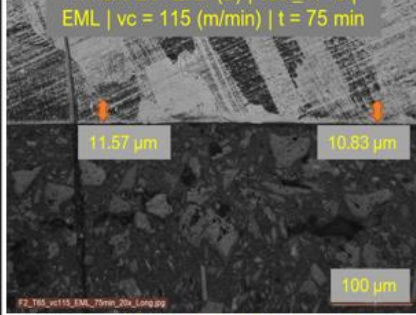
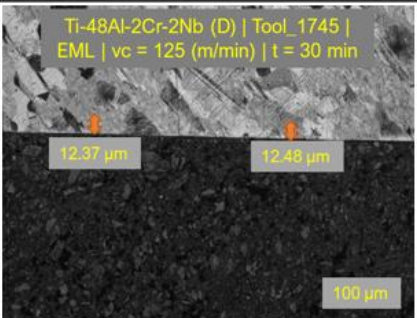
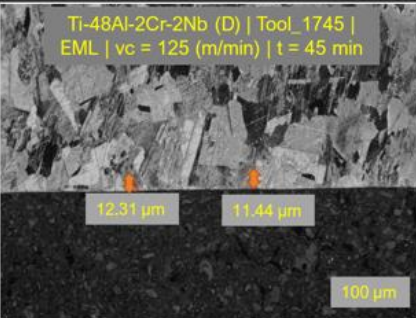
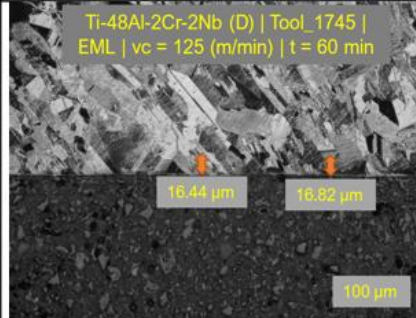
Bull end milling tests

Table 46 The longitudinal face subsurface micrographs of three time intervals before tool failure of Ti-48Al-2Cr-2Nb (NL) with EML at cutting speeds of 100, 115 and 125 m/min

<p>Ti-48Al-2Cr-2Nb (NL) Tool = 1745 Emulsion $v_c = 100$ m/min</p> <p>Note: The SD is constant throughout. Tool intact with VB = 0.04 mm.</p>	<p>Ti-48Al-2Cr-2Nb (NL) Tool_1745 EML $v_c = 100$ (m/min) t = 45 min</p> <p>5.59 μm 5.16 μm</p> <p>100 μm</p>	<p>Ti-48Al-2Cr-2Nb (NL) Tool_1745 EML $v_c = 100$ (m/min) t = 60 min</p> <p>6.04 μm 6.46 μm</p> <p>100 μm</p>	<p>Ti-48Al-2Cr-2Nb (NL) Tool_1745 EML $v_c = 100$ (m/min) t = 45 min</p> <p>5.59 μm 5.16 μm</p> <p>100 μm</p>
<p>Ti-48Al-2Cr-2Nb (NL) Tool = 1745 Emulsion $v_c = 115$ m/min</p> <p>Note: The SD is constant throughout. No rise in SD depth with tool wear.</p>	<p>Ti-48Al-2Cr-2Nb (NL) Tool_1745 EML $v_c = 115$ (m/min) t = 15 min</p> <p>9.48 μm 8.02 μm</p> <p>100 μm</p>	<p>Ti-48Al-2Cr-2Nb (NL) Tool_1745 EML $v_c = 115$ (m/min) t = 30 min</p> <p>9.02 μm 9.40 μm</p> <p>100 μm</p>	<p>Ti-48Al-2Cr-2Nb (NL) Tool_1745 EML $v_c = 115$ (m/min) t = 45 min</p> <p>9.02 μm 9.75 μm</p> <p>100 μm</p>
<p>Ti-48Al-2Cr-2Nb (NL) Tool = 1745 Emulsion $v_c = 125$ m/min</p> <p>Note: The SD is constant The SD rose only before the tool wear at 45 min</p>	<p>Ti-48Al-2Cr-2Nb (NL) Tool_1745 EML $v_c = 125$ (m/min) t = 15 min</p> <p>10.21 μm 9.48 μm</p> <p>100 μm</p>	<p>Ti-48Al-2Cr-2Nb (NL) Tool_1745 EML $v_c = 125$ (m/min) t = 30 min</p> <p>8.16 μm 9.07 μm</p> <p>100 μm</p>	<p>Ti-48Al-2Cr-2Nb (NL) Tool_1745 EML $v_c = 125$ (m/min) t = 45 min</p> <p>20.69 μm 18.27 μm</p> <p>100 μm</p>

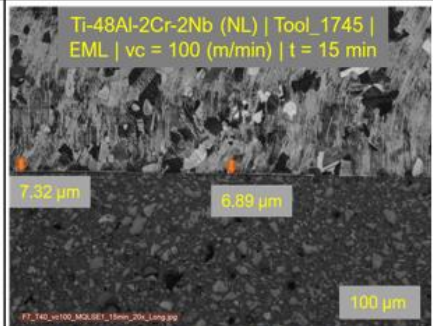
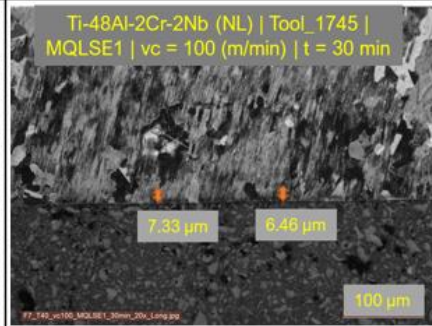
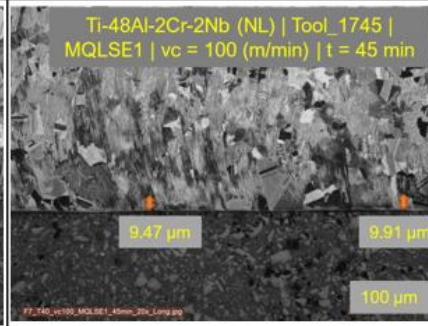
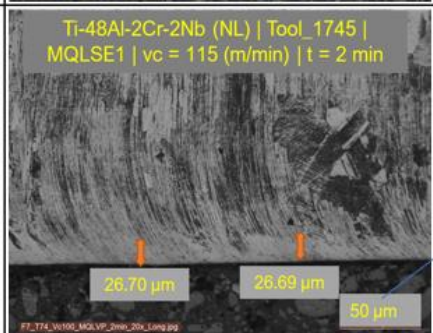
Bull end milling tests

Table 47 The longitudinal face subsurface micrographs of three time intervals before tool failure of Ti-48Al-2Cr-2Nb (D) with EML at cutting speeds of 100, 115 and 125 m/min

<p>Ti-48Al-2Cr-2Nb (D) Tool = 1745 Emulsion $v_c = 100$ m/min Note: The SD rose only at tool life of 90 min. However, the rise in SD is not commensurate with tool wear.</p>	<p>Ti-48Al-2Cr-2Nb (D) Tool_1745 EML $v_c = 100$ (m/min) t = 60 min</p>  <p>4.8 μm 2.8 μm</p> <p>100 μm</p>	<p>Ti-48Al-2Cr-2Nb (D) Tool_1745 EML $v_c = 100$ (m/min) t = 75 min</p>  <p>5.1 μm 3.8 μm</p> <p>100 μm</p>	<p>Ti-48Al-2Cr-2Nb (D) Tool_1745 EML $v_c = 100$ (m/min) t = 90 min</p>  <p>17.7 μm 16.57 μm</p> <p>100 μm</p>
<p>Ti-48Al-2Cr-2Nb (D) Tool = 1745 Emulsion $v_c = 115$ m/min Note: The SD depth is small. The SD rose only at the end of tool life at 75 min.</p>	<p>Ti-48Al-2Cr-2Nb (D) Tool_1745 EML $v_c = 115$ (m/min) t = 45 min</p>  <p>5.11 μm 4.88 μm</p> <p>100 μm</p>	<p>Ti-48Al-2Cr-2Nb (D) Tool_1745 EML $v_c = 115$ (m/min) t = 60 min</p>  <p>6.57 μm 4.31 μm</p> <p>100 μm</p>	<p>Ti-48Al-2Cr-2Nb (D) Tool_1745 EML $v_c = 115$ (m/min) t = 75 min</p>  <p>11.57 μm 10.83 μm</p> <p>100 μm</p>
<p>Ti-48Al-2Cr-2Nb (D) Tool = 1745 Emulsion $v_c = 125$ m/min Note: The SD rose at the end of tool life.</p>	<p>Ti-48Al-2Cr-2Nb (D) Tool_1745 EML $v_c = 125$ (m/min) t = 30 min</p>  <p>12.37 μm 12.48 μm</p> <p>100 μm</p>	<p>Ti-48Al-2Cr-2Nb (D) Tool_1745 EML $v_c = 125$ (m/min) t = 45 min</p>  <p>12.31 μm 11.44 μm</p> <p>100 μm</p>	<p>Ti-48Al-2Cr-2Nb (D) Tool_1745 EML $v_c = 125$ (m/min) t = 60 min</p>  <p>16.44 μm 16.82 μm</p> <p>100 μm</p>

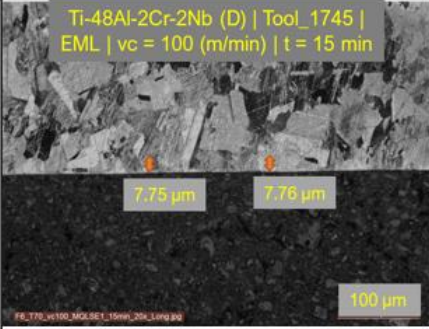
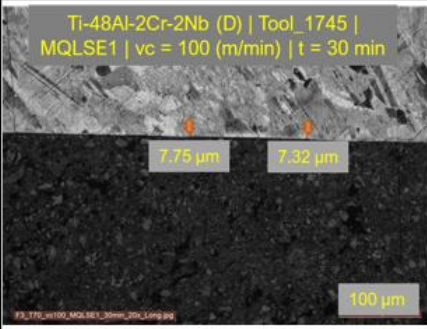
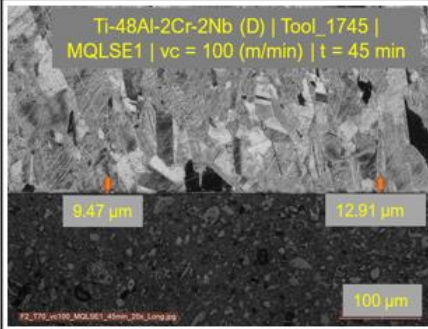
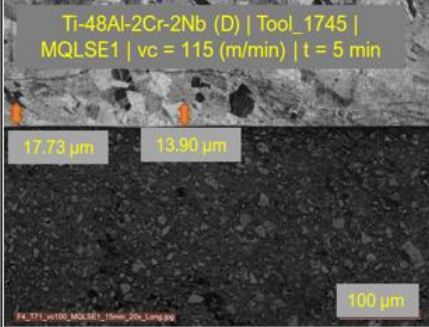
Bull end milling tests

Table 48 The longitudinal face subsurface micrographs of three time intervals before tool failure of Ti-48Al-2Cr-2Nb (NL) with MQLSE1 at cutting speeds of 100 m/min and last time interval at cutting speed 115 m/min

<p>Ti-48Al-2Cr-2Nb (NL) Tool = 1745 MQLSE1 $v_c = 100$ m/min Note: No correlation between tool wear and SD depth. Tool worn at 45 min but SD constant.</p>	 <p>Ti-48Al-2Cr-2Nb (NL) Tool_1745 EML $v_c = 100$ (m/min) t = 15 min 7.32 μm 6.89 μm 100 μm</p>	 <p>Ti-48Al-2Cr-2Nb (NL) Tool_1745 MQLSE1 $v_c = 100$ (m/min) t = 30 min 7.33 μm 6.46 μm 100 μm</p>	 <p>Ti-48Al-2Cr-2Nb (NL) Tool_1745 MQLSE1 $v_c = 100$ (m/min) t = 45 min 9.47 μm 9.91 μm 100 μm</p>
<p>Ti-48Al-2Cr-2Nb (NL) Tool = 1745 MQLSE1 $v_c = 115$ m/min Note: Increase in depth of SD is evident.</p>	 <p>Ti-48Al-2Cr-2Nb (NL) Tool_1745 MQLSE1 $v_c = 115$ (m/min) t = 2 min 26.70 μm 26.69 μm 50 μm</p>	<p>Micrograph with scale 50 microns. With 100 microns not present.</p>	

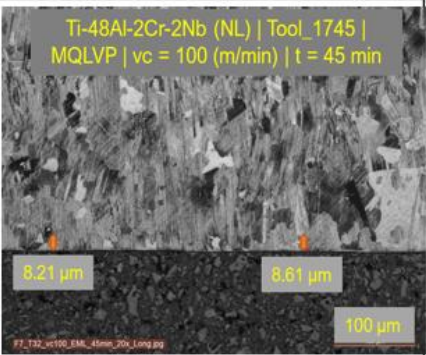
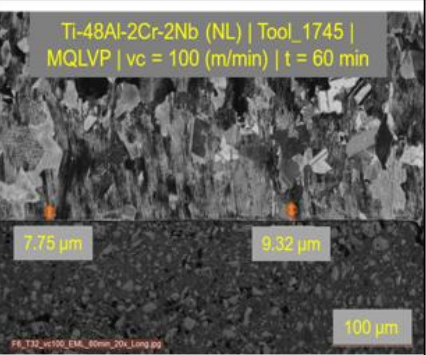
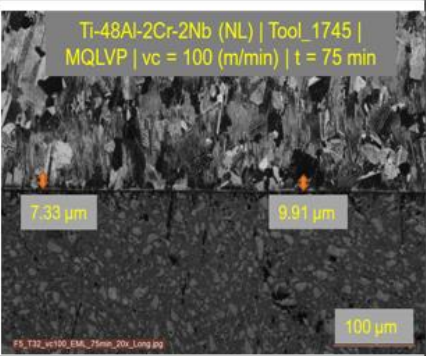
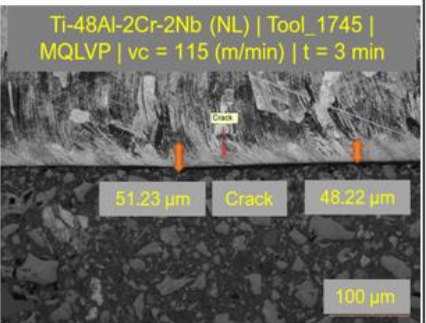
Bull end milling tests

Table 49 The longitudinal face subsurface micrographs of three time intervals before tool failure of Ti-48Al-2Cr-2Nb (D) with MQLSE1 at cutting speeds of 100 m/min and last time interval at cutting speed 115 m/min

<p>Ti-48Al-2Cr-2Nb (D) Tool = 1745 MQLSE1 $v_c = 100$ m/min Note: No correlation between tool wear and SD depth. Tool worn at 45 min but SD constant.</p>	 <p>Ti-48Al-2Cr-2Nb (D) Tool_1745 EML $v_c = 100$ (m/min) t = 15 min</p> <p>7.75 μm 7.76 μm</p> <p>100 μm</p>	 <p>Ti-48Al-2Cr-2Nb (D) Tool_1745 MQLSE1 $v_c = 100$ (m/min) t = 30 min</p> <p>7.75 μm 7.32 μm</p> <p>100 μm</p>	 <p>Ti-48Al-2Cr-2Nb (D) Tool_1745 MQLSE1 $v_c = 100$ (m/min) t = 45 min</p> <p>9.47 μm 12.91 μm</p> <p>100 μm</p>
<p>Ti-48Al-2Cr-2Nb (D) Tool = 1745 MQLSE1 $v_c = 115$ m/min Note: Increase in depth of SD is evident.</p>	 <p>Ti-48Al-2Cr-2Nb (D) Tool_1745 MQLSE1 $v_c = 115$ (m/min) t = 5 min</p> <p>17.73 μm 13.90 μm</p> <p>100 μm</p>		

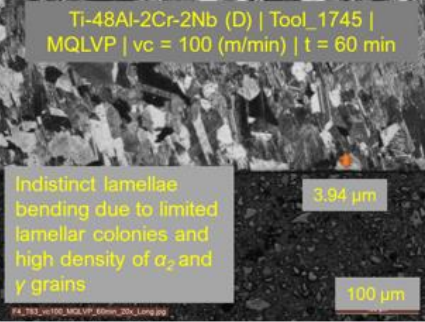
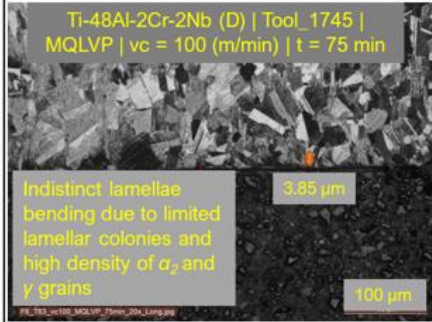
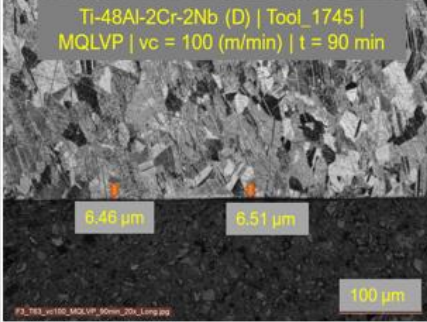
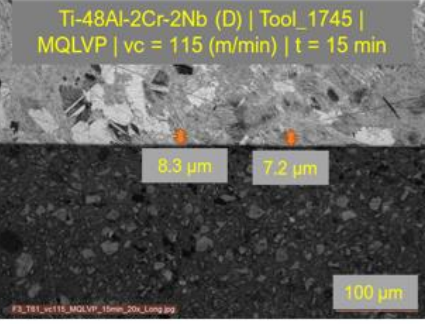
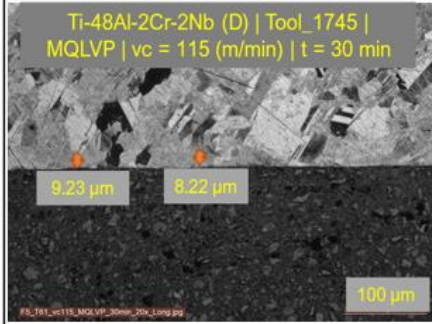
Bull end milling tests

Table 50 The longitudinal face subsurface micrographs of three time intervals before tool failure of Ti-48Al-2Cr-2Nb (NL) with MQLVP at cutting speeds of 100 m/min and last time interval at cutting speed 115 m/min

<p>Ti-48Al-2Cr-2Nb (NL) Tool = 1745 MQLVP $v_c = 100$ m/min Note: No correlation between tool wear and SD depth. Tool worn at 75 min but SD is constant</p>	 <p>Ti-48Al-2Cr-2Nb (NL) Tool_1745 MQLVP $v_c = 100$ (m/min) t = 45 min 8.21 μm 8.61 μm 100 μm</p>	 <p>Ti-48Al-2Cr-2Nb (NL) Tool_1745 MQLVP $v_c = 100$ (m/min) t = 60 min 7.75 μm 9.32 μm 100 μm</p>	 <p>Ti-48Al-2Cr-2Nb (NL) Tool_1745 MQLVP $v_c = 100$ (m/min) t = 75 min 7.33 μm 9.91 μm 100 μm</p>
<p>Ti-48Al-2Cr-2Nb (NL) Tool = 1745 MQLVP $v_c = 115$ m/min Note: Very high SD noted. The tool life was only 3 min</p>	 <p>Ti-48Al-2Cr-2Nb (NL) Tool_1745 MQLVP $v_c = 115$ (m/min) t = 3 min 51.23 μm Crack 48.22 μm 100 μm</p>		

Bull end milling tests

Table 51 The longitudinal face subsurface micrographs of three time intervals before tool failure of Ti-48Al-2Cr-2Nb (NL) with MQLVP at cutting speeds of 100 m/min and last time interval at cutting speed 115 m/min

<p>Ti-48Al-2Cr-2Nb (D) Tool = 1745 MQLVP $v_c = 100$ m/min Note: The SD is discontinuous. No correlationship between tool wear and SD depth</p>	 <p>Ti-48Al-2Cr-2Nb (D) Tool_1745 MQLVP $v_c = 100$ (m/min) t = 60 min Indistinct lamellae bending due to limited lamellar colonies and high density of α_2 and γ grains 3.94 μm 100 μm</p>	 <p>Ti-48Al-2Cr-2Nb (D) Tool_1745 MQLVP $v_c = 100$ (m/min) t = 75 min Indistinct lamellae bending due to limited lamellar colonies and high density of α_2 and γ grains 3.85 μm 100 μm</p>	 <p>Ti-48Al-2Cr-2Nb (D) Tool_1745 MQLVP $v_c = 100$ (m/min) t = 90 min 6.46 μm 6.51 μm 100 μm</p>
<p>Ti-48Al-2Cr-2Nb (D) Tool = 1745 MQLVP $v_c = 115$ m/min Note: The SD is discontinuous. No correlationship between tool wear and SD depth</p>	 <p>Ti-48Al-2Cr-2Nb (D) Tool_1745 MQLVP $v_c = 115$ (m/min) t = 15 min 8.3 μm 7.2 μm 100 μm</p>	 <p>Ti-48Al-2Cr-2Nb (D) Tool_1745 MQLVP $v_c = 115$ (m/min) t = 30 min 9.23 μm 8.22 μm 100 μm</p>	

Bull end milling tests

In case of Ti-48Al-2Cr-2Nb (D), the height of the SD was considerably less than Ti-48Al-2Cr-2Nb (NL). In fact, the Ti-48Al-2Cr-2Nb (D) alloy presented ideal duplex composition in some cases as seen in Figure 88.

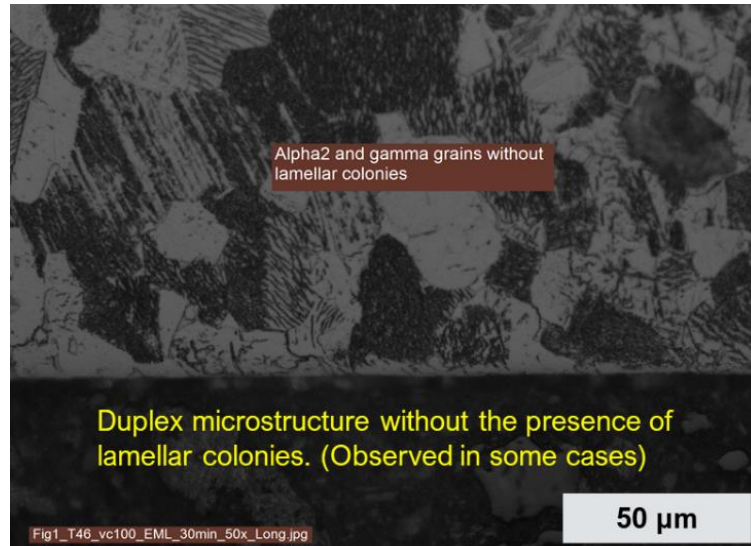


Figure 88 Duplex microstructure showing the absence of lamellar colonies in some cases

However, the composition was not completely ideal, and the presence of lamellar colonies and small α_2 and γ grains along the periphery of the ingots was found, as described in section 3.2. Thus, any residual lamellar colonies along the periphery showed SD when deformed. However, since they were present in minute quantities and were barely distributed, the height of the SD observed was shorter than Ti-48Al-2Cr-2Nb (NL). This may be the reason why Ti-48Al-2Cr-2Nb (D) reported inconsistent and shorter SD in comparison to Ti-48Al-2Cr-2Nb (NL).

5.4 CONCLUSION OF THE BULL END MILLING TESTS

In this chapter, a process milling window was developed to bull end mill Near lamellar and Duplex microstructures of Ti-48Al-2Cr-2Nb alloy using four lubricants, TiAlSiN coated bull end mills, at different cutting speeds. Along with the tool wear and cutting forces, a Surface Integrity analysis was carried out to assess the surface texture and surface metallurgy. The following conclusions were drawn:

1. TiAlSiN cutting tools reported a longer tool life than Hardlox coated SPL tools. The cutting speed had a significant influence on the tool wear of both alloys. Tool wear increased with an increase in cutting speed and the wear rate was found to be gradual for most of the tool life. However, a sudden rise in tool wear was noted immediately before tool failure.
2. Of the lubricants studied, EML delivered a long tool life at all cutting speeds for both the alloys. Even $v_c = 125$ m/min yielded a reasonable tool life of 60 min before tool failure. On the other hand, only the MQLVP 19004 oil delivered good tool life at $v_c = 100$ m/min, but when the cutting speed was increased to $v_c = 115$ m/min, the tool life decreased for both alloys. The performance of MQLSE1 was the lowest of all lubricants. With all lubricants, the Ti-48Al-2Cr-2Nb (Duplex) alloy showed better tool life than the Ti-48Al-2Cr-2Nb (Near lamellar) alloy.
3. The surface roughness assessment revealed that R_a was dependent on both lubricants and cutting speeds. MQLSE1 and MQLVP 19004 presented a better R_a profile than EML. With the MQL lubricants, the R_a increased when the cutting speed was increased. In contrast, EML indicated the opposite trend, with R_a values decreasing with increased cutting speed.
4. An increase in microhardness ($HV_{0.02}$) corresponding to an increase in depth (from 0.02 mm to 0.05 mm below the machined surface) was observed in both alloys. This showed that the sub-surface was prone to hardening. With EML, the $HV_{0.02}$ of Ti-48Al-2Cr-2Nb (Near lamellar) was found to be independent of cutting speeds. For the Ti-48Al-2Cr-2Nb (Duplex) alloy, however, the $HV_{0.02}$ increased with the increase in cutting speed from 100 to 115 m/min. Nevertheless, any further increase in cutting speed did not translate to higher

microhardness, as $HV_{0.02}$ values at $vc = 125$ m/min were found to be in the same range as $vc = 115$ m/min.

5. Interestingly, the microhardness results were different for the MQL lubricants. MQLSE1 yielded a drastic increase in $HV_{0.02}$ values with increased cutting speed, a trend which was evident for both alloys. However, with MQLVP 19004, the microhardness was found to be independent of cutting speed, for each alloy. Even with a short tool life of 5 min for the Ti-48Al-2Cr-2Nb (Near lamellar) alloy at $vc = 115$ m/min, no substantial change in hardness values was recorded.
6. Sub-surface alterations were also found to be directly related to lubricants, with both Ti-48Al-2Cr-2Nb (Near lamellar) and Ti-48Al-2Cr-2Nb (Duplex) showing distinguishable trends. Although cracks (MQLSE1 at $vc = 115$ m/min), and steps and pits (EML at $vc = 125$ m/min) were observed, Surface Drag (SD) was by far the most prominent surface defect. The SD profiles differed between the alloys.
7. SD was present across the entire longitudinal face of the Ti-48Al-2Cr-2Nb (Near lamellar). This phenomenon was found to be constant with EML at all cutting speeds and relatively unaffected by tool wear. Even when the tool was worn, the increase in the depth of SD was minimal. This could be attributed to the composition of the near lamellar microstructure where lamellar colonies were found to be embedded between the α_2 and γ grains.
8. Importantly, for Ti-48Al-2Cr-2Nb (Near lamellar) with MQL lubricants, SD increased with cutting speeds only when the tool life was very short. At $vc = 100$ m/min, both the MQL lubricants presented lower SD with the depth unchanged even when the tool was worn. However, when the cutting speed was increased to 115 m/min (very short tool life of 2 min and 3 min), a drastic rise in the depth of SD was recorded. Thus, SD was affected by the cutting speed only when the tool life was very short (< 5 min).
9. The Ti-48Al-2Cr-2Nb (Duplex) alloy showed intermittent occurrences of SD on the examined surface. This could be attributed to the higher density of α_2 and γ grains than lamellar colonies. Importantly, the depth of SD in the Ti-48Al-2Cr-2Nb (Duplex) alloy was less than in the Ti-48Al-2Cr-2Nb (Near lamellar) alloy. In the former, the depth of SD was almost constant in all conditions and

cutting speeds except with MQLSE1 at $v_c = 115$ m/min with tool life of 5 min, where the SD depth increased drastically.

Bull end milling with EML delivered good tool life. Even a reasonable tool life of 60 min was achieved with $v_c = 125$ m/min. Gamma – TiAl alloys are brittle at room temperature and have low thermal conductivity which generates high levels of heat at the tool workpiece contact (Klocke et al. [8]). Thus, it would appear that the high heat extraction properties of EML leads to longer tool life.

The MQLVP 19004 lubricant provided both lubrication and cooling and delivered low Ra, low microhardness, and a good tool life, particularly with the Ti-48Al-2Cr-2Nb (Duplex) alloy at $v_c = 100$ m/min. The sub-surface assessment also revealed an absence of major defects like cracks and pits and low depth of SD. However, any increase in cutting speed above 100 m/min led to reduced tool life and diminished surface integrity, which demonstrates the ineffectiveness of the lubricant at high cutting speeds.

In view of these results, the most optimum bull end milling conditions with TiAlSiN PVD coated tools to machine Ti-48Al-2Cr-2Nb alloys would be with Duplex microstructure at $v_c = 100$ m/min ($f_z = 0.03$ mm/tooth, $a_p = 0.25$ mm, and $a_e = 0.80$ mm) using EML or MQLVP 19004 lubricant. MQLVP 19004 was found to perform as effectively as EML only up to $v_c = 100$ m/min. However, any increase in cutting speed would lead to a reduced tool life and diminished SI.

Even at $v_c = 115$ m/min EML yielded a tool life of 75 m/min with good SI. At $v_c = 125$ m/min, a tool life of 60 m/min was achieved, however this is not recommended due to the presence of surface pits and steps in the sub-surface microstructure. The MQLSE1 lubricant is not recommended at all because of the short tool life achieved with this lubricant.

6 CONCLUSIONS AND FUTURE OUTLOOK

6.1 CONCLUSIONS

Gamma titanium aluminides (γ – TiAl) are intermetallic alloys suitable for high temperature applications. Characteristics such as low density, high specific strength and moduli, low diffusivity, and good structural stability even at high temperatures make them ideal candidates for use in aero-engine components such as Low-Pressure Turbine blades (LPT blades). However, the very abilities which provide this superior performance, limit their machining. High brittleness at room temperature, low thermal conductivity, poor ductility (< 2%), and chemical affinity at temperatures above 500 °C, has hindered their commercial production and increased the cost.

In particular, the machinability of γ – TiAl components is poor due factors such as accelerated tool wear, poor surface finish, and sub-surface alterations. Thus, this Ph.D. work identifies the impediments to machinability of a second generation γ – TiAl alloy and determines an optimised bull end milling window consisting of suitable alloy microstructure, tool coating, machining parameters, and lubricants so as to deliver components with acceptable Surface Integrity (SI).

To this end, the tribological properties of friction, adhesion, and heat partition were studied. Additionally, an experimental sensitivity analysis of input parameters (microstructure, lubrication, tool and cutting parameters) to output parameters (tool wear, cutting forces, and surface integrity) while bull end milling Ti-48Al-2Cr-2Nb (Near lamellar) and Ti-48Al-2Cr-2Nb (Duplex) alloys was carried out. The bull end milling tests were conducted at cutting speeds of 100, 115, 125 and 150 m/min using TiAlSiN and Hardlox coated tools. A feed per tooth of 0.03 mm, and the axial and radial depths of cut of 0.25 mm and 0.80 mm were determined. Dry, emulsion (EML), MQLSE1, and MQLVP 19004 lubricants were used in the study. The following conclusions were obtained:

1. The TiAlSiN coated T1745 tools were found to have a longer tool life than the Hardlox coated Special Tools (TSPL), with both alloys and all lubricants. Dry bull end milling with both the tools led to accelerated tool life with catastrophic tool failure even at low cutting speeds. Thus, these conditions are not recommended for machining.

2. The bull end milling evaluation with T1745 revealed that the Ti-48Al-2Cr-2Nb (Duplex) microstructure had better machinability than the Ti-48Al-2Cr-2Nb (Near lamellar) alloy, with EML providing a longer tool life over a broader range of cutting speeds 100 – 125 m/min. A higher cutting speed of $v_c = 150$ m/min led to accelerated tool wear and hence was found unsuitable for bull end milling.
3. MQLVP 19004 was found to be effective only upto $v_c = 100$ m/min, particularly with Ti-48Al-2Cr-2Nb (Duplex), where the lubricant delivered a tool life of 90 min with tool intact ($V_b < 0.2$ mm). However, any increase in cutting speed led to drastically reduced tool life and high sub-surface damage in comparison to EML.
4. Surface roughness of the MQL oils was found to be slightly better than EML. The sub-surface microhardness measurements revealed that hardening of sub-surface with alterations occurring in the microstructure. The sub-surface microhardness of Ti-48Al-2Cr-2Nb (Duplex) was less than Ti-48Al-2Cr-2Nb (Near lamellar).
5. The sub-surface microstructural assessment of the longitudinal sub face (subsurface with axis parallel to the feed) showed that Surface Drag (SD, bending of lamellar colonies) to be the most prominent defect. Although cracks ($v_c = 115$ m/min, MQLSE1), pits and steps (EML, $v_c = 125$ m/min) were observed, their occurrence was rare.
6. The Ti-48Al-2Cr-2Nb (Near lamellar) showed continuous occurrence of SD across the entire longitudinal face. The Ti-48Al-2Cr-2Nb (D) alloy displayed intermittent occurrence of SD due to the higher proportion of α_2 and γ grains. The microstructure plays an important role in evolving the nature of SD. For all the lubricants, the depth of SD is independent of tool wear. Importantly, only when the tool life was very short (2 min, 3 min at 115m/min with MQL oils), the SD profiles and the tool wear profiles were commensurate i.e., the tool wear evolution matched with SD depth evolution. Other cases showed no correlation between the flank wear, cutting speed and the size of drags.
7. The tribological characterisation with TiAlSiN coated pins showed that the apparent friction coefficient between the pin and Ti-48Al-2Cr-2Nb (Near lamellar) and Ti-48Al-2cr-2Nb (Duplex) alloys is 50% lower than the Ti-6Al-

4V alloy. The microstructure of Ti-48Al-2Cr-2Nb alloys did not present any difference in tribological properties.

8. Contact pressure was found to be the statistically significant parameter, with increase of which led to the increase in friction, adhesion, and coating wear. Minimal adhesion of workpiece material to pins was recorded. This adhesion was not affected by the lubricants as similar values were seen for all of them.
9. Coating wear is likely to occur in dry conditions or at contact pressures ≥ 3.0 GPa with MQLSE1. Thus, this combination should be avoided for increased tool life. Though, the performance of both the alloys was almost similar, statistically, the Ti-48Al-2Cr-2Nb (Duplex) with EML delivered the least friction, minimum adhesion, and no coating wear even at higher sliding velocities.
10. Hence the recommendations to ball end mill Ti-48Al-2Cr-2Nb alloys with TiAlSiN coated T1745 tools, with a criteria of tool life = 90 min and/or the tool wear ≤ 0.2 mm are:
 - a. At $v_c = 100$ m/min with tool wear less than 0.2 mm:
 - **Ti-48Al-2Cr-2Nb (Duplex):** EML is recommended. MQLVP19004 performs equally well. Expected tool life is ≥ 90 min.
 - **Ti-48Al-2Cr-2Nb (Near lamellar):** EML is recommended. MQLVP19004 performs equally well. Expected tool life is 75 min.
 - b. At $v_c = 115$ m/min with tool wear less than 0.2 mm:
 - **Ti-48Al-2Cr-2Nb (Duplex):** EML is recommended. MQL lubricants should be avoided as they are not effective in providing a good tool life and SI. Expected tool life is 75 min.
 - **Ti-48Al-2Cr-2Nb (Near lamellar):** EML is recommended. MQL lubricants should be avoided as they are not effective in providing a good tool life and SI. Expected tool life is 45 min.

6.2 FUTURE PROSPECTS

In the course of the research work many interesting outcomes were arrived at. The study would be more comprehensive and complete if some more aspects are studied.

1. The study has revealed that microstructure affects the tool life. As, fully lamellar, and duplex microstructures are preferred for high temperature applications, bull end milling of machining a fully lamellar would be an interesting addition. Additionally, tests with uncoated tools with varying feed and depths of cut would help in assessing the effectiveness of the tools.
2. A SEM analysis of smearing of workpiece material on the tool would help in understanding the tool workpiece interactions. This could help in understanding why the tool shows gradual tool wear rate for most of time before catastrophically destroyed.
3. Emulsion has showed to better tool life apparently because of its heat extraction properties. As seen in tribological characterization, heat is very important quantity in the study. To quantify heat, temperature measurements be made during bull end milling experiments.
4. The tribological characterisation established that friction performance of coated and uncoated pins is almost similar. As the comparison is carried out only at 2.3 GPa and 80 m/min, it would be interesting to expand the comparison to other contact conditions ($P_{avg} = 1.31 - 3.27$ GPa, $v_c = 30 - 120$ m/min) also.
5. The tribological characterisation also established that the heat plays a very important role in coating wear. Similarly, the temperature measurements at all the contact conditions could also yield more detailed information on heat transfer profiles and behaviour of lubricants at different contact conditions.
6. The machinability study would be more robust if other machining parameters like feed, depth of cut (radial and axial) are also varied and studied.
7. As the MQLVP 19004 lubricant emerged as the preferred lubricant to machine Ti-48Al-2Cr-2Nb alloy, coating wear analysis at 3.27 GP and 80 m/min be conducted to have a comparison with the readings of dry, emulsion and MQLSE1 in the study.
8. A comparative machining study with a third generation gamma – TiAl alloys of Ti-45Al-2Mn-2Nb-0.8% TiB₂ (XDTM) and / or Ti-43.5Al-4Nb-1Mo-0.1B

Conclusions and future outlook

(TNM) would help benchmark the machinability of Ti-48Al-2Cr-2Nb alloy against them.

9. Additionally, the experiments could be complemented with Finite Element Modelling (FEM) could be included to develop friction models and machinability models.
10. The SI could be expanded by conducting residual stress analysis.

References

- [1] F. Klocke, D. Lung, A. Krämer, T. Cayli, and H. Sangermann, “Potential of Modern Lubricoolant Strategies on Cutting Performance,” *Key Eng. Mater.*, vol. 554–557, pp. 2062–2071, 2013, doi: 10.4028/www.scientific.net/KEM.554-557.2062.
- [2] International Civil Aviation Organization, “Envisioning a Zero Climate Impact” international aviation pathway towards 2050: how governments and the aviation industry can step-up amidst the climate emergency for a sustainable aviation future,” A40-WP/561, 2019. [Online]. Available: https://www.icao.int/Meetings/a40/Documents/WP/wp_561_en.pdf.
- [3] Honeywell International Inc., “Sustainability and airlines.” <https://aerospace.honeywell.com/us/en/learn/connected-aircraft/airlines/sustainability-and-airlines>.
- [4] D. . Dimiduk, “Gamma titanium aluminide alloys—an assessment within the competition of aerospace structural materials,” *Mater. Sci. Eng. A*, vol. 263, no. 2, pp. 281–288, May 1999, doi: 10.1016/S0921-5093(98)01158-7.
- [5] F. Appel, J. D. H. Paul, and M. Oehring, *Gamma Titanium Aluminide Alloys: Science and Technology*. 2011.
- [6] B. P. Bewlay, S. Nag, A. Suzuki, and M. J. Weimer, “TiAl alloys in commercial aircraft engines,” *Mater. High Temp.*, vol. 33, no. 4–5, pp. 549–559, 2016, doi: 10.1080/09603409.2016.1183068.
- [7] E. E. Ibrahim *et al.*, “Process performance of low frequency vibratory grinding of Inconel 718,” 2019, doi: 10.1016/j.promfg.2019.02.075.
- [8] F. Klocke, L. Settineri, D. Lung, P. Claudio Priarone, and M. Arft, “High performance cutting of gamma titanium aluminides: Influence of lubricoolant strategy on tool wear and surface integrity,” *Wear*, vol. 302, no. 1–2, pp. 1136–1144, 2013, doi: 10.1016/j.wear.2012.12.035.
- [9] D. K. Aspinwall, R. C. Dewes, and A. L. Mantle, “The machining of γ -TiAl intermetallic alloys,” *CIRP Ann. - Manuf. Technol.*, 2005, doi: 10.1016/S0007-8506(07)60059-6.
- [10] F. Klocke, D. Lung, M. Arft, P. C. Priarone, and L. Settineri, “On high-speed turning of a third-generation gamma titanium aluminide,” *Int. J. Adv. Manuf. Technol.*, 2013, doi: 10.1007/s00170-012-4157-5.
- [11] S. A. Bentley, A. L. Mantle, and D. K. Aspinwall, “Effect of machining on the fatigue strength of a gamma titanium aluminide intermetallic alloy,” *Intermetallics*, vol. 7, no. 8, pp. 967–969, 1999, doi: 10.1016/S0966-9795(99)00008-4.
- [12] U. Habel *et al.*, “Forged intermetallic gamma-TiAl based alloy low pressure turbine blade in the geared turbofan,” *13th World Titan. Conf.*, 2015.
- [13] R. Hood, D. K. Aspinwall, C. Sage, and W. Voice, “High speed ball nose end milling of γ -TiAl alloys,” *Intermetallics*, vol. 32, pp. 284–291, Jan. 2013, doi:

References

- 10.1016/j.intermet.2012.09.011.
- [14] T. Tetsui, “Development of a TiAl turbocharger for passenger vehicles,” *Mater. Sci. Eng. A*, 2002, doi: 10.1016/S0921-5093(01)01584-2.
- [15] F. Appel and M. Oehring, “ γ -Titanium Aluminide Alloys: Alloy Design and Properties,” *Titan. Titan. Alloy.*, pp. 89–152, 2005, doi: 10.1002/3527602119.ch4.
- [16] H. Clemens and W. Smarsly, “Light-Weight Intermetallic Titanium Aluminides – Status of Research and Development,” *Adv. Mater. Res.*, vol. 278, pp. 551–556, 2011, doi: 10.4028/www.scientific.net/AMR.278.551.
- [17] B. H. Clemens, S. Mayer, E. Schwaighofer, R. Werner, and A. Gaitze-, “Design , Processing , Microstructure , Properties , and Applications of Advanced Intermetallic TiAl Alloys **,” no. 4, pp. 191–215, 2013, doi: 10.1002/adem.201200231.
- [18] B. Liu and Y. Liu, “Powder metallurgy titanium aluminide alloys,” in *Titanium Powder Metallurgy: Science, Technology and Applications*, 2015.
- [19] A. Couret, G. Molénat, J. Galy, and M. Thomas, “Microstructures and mechanical properties of TiAl alloys consolidated by spark plasma sintering,” *Intermetallics*, 2008, doi: 10.1016/j.intermet.2008.06.015.
- [20] G. Molénat, M. Thomas, J. Galy, and A. Couret, “Application of spark plasma sintering to titanium aluminide alloys,” *Adv. Eng. Mater.*, 2007, doi: 10.1002/adem.200700094.
- [21] T. Voisin, J. P. Monchoux, L. Durand, N. Karnatak, M. Thomas, and A. Couret, “An Innovative Way to Produce γ -TiAl Blades: Spark Plasma Sintering,” *Adv. Eng. Mater.*, 2015, doi: 10.1002/adem.201500019.
- [22] “Spark Plasma Sintering schematic.” https://www.substech.com/dokuwiki/doku.php?id=spark_plasma_sintering (accessed Jan. 19, 2022).
- [23] J. Aguilar, A. Schievenbusch, and O. Kättlitz, “Investment casting technology for production of TiAl low pressure turbine blades - Process engineering and parameter analysis,” *Intermetallics*, vol. 19, no. 6, pp. 757–761, 2011, doi: 10.1016/j.intermet.2010.11.014.
- [24] S. Jana, O. Kättlitz, F. Hediger, J. Jakumeit, and J. Aguilar, “Predictions of misruns using three-phase coupled mold-filling and solidification simulations in low pressure turbine (LPT) blades,” 2012, doi: 10.1088/1757-899X/33/1/012007.
- [25] Y. K. Kim, S. J. Youn, S. W. Kim, J. Hong, and K. A. Lee, “High-temperature creep behavior of gamma Ti-48Al-2Cr-2Nb alloy additively manufactured by electron beam melting,” *Mater. Sci. Eng. A*, 2019, doi: 10.1016/j.msea.2019.138138.
- [26] J. Schwerdtfeger and C. Körner, “Selective electron beam melting of Ti-48Al-2Nb-2Cr: Microstructure and aluminium loss,” *Intermetallics*, 2014, doi:

References

- 10.1016/j.intermet.2014.01.004.
- [27] K. Mizuta, Y. Hijikata, T. Fujii, K. Gokan, and K. Takechi, “Characterization of Ti-48Al-2Cr-2Nb built by selective laser melting,” *Scr. Mater.*, 2021, doi: 10.1016/j.scriptamat.2021.114107.
- [28] “GE additive manufacturing.” <https://www.ge.com/news/reports/future-manufacturing-take-look-inside-factory-3d-printing-jet-engine-parts>.
- [29] J. C. Schuster and M. Palm, “Reassessment of the binary aluminum-titanium phase diagram,” *J. Phase Equilibria Diffus.*, vol. 27, no. 3, pp. 255–277, 2006, doi: 10.1361/154770306X109809.
- [30] R. K. Gupta, B. Pant, and P. P. Sinha, “Theory and practice of $\gamma + \alpha_2$ Ti aluminide: A review,” *Trans. Indian Inst. Met.*, vol. 67, no. 2, pp. 143–165, 2014, doi: 10.1007/s12666-013-0334-y.
- [31] I. P. Polmear, “Light Alloys - From Traditional Alloys to Nanocrystals,” *Light Alloy.*, 2006.
- [32] S. Brookes, *Thermo-mechanical fatigue behaviour of the near- γ - titanium aluminide alloy TNB-V5 under uniaxial and multiaxial loading*. 2009.
- [33] R. K. Gupta and B. Pant, “Titanium aluminides,” *Intermet. Matrix Compos.*, pp. 71–93, 2018, doi: 10.1016/B978-0-85709-346-2.00004-2.
- [34] R. Hood, “The machinability of a gamma titanium aluminide intermetallic,” no. June, p. 318, 2010, [Online]. Available: <http://theses.bham.ac.uk/1380/>.
- [35] H. Saari, D. Y. Seo, J. Blumm, and J. Beddoes, “Thermophysical property determination of high temperature alloys by thermal analysis,” *J. Therm. Anal. Calorim.*, 2003, doi: 10.1023/A:1025130902174.
- [36] A. Brotzu, F. Felli, F. Marra, D. Pilone, and G. Pulci, “Mechanical properties of a TiAl-based alloy at room and high temperatures,” *Mater. Sci. Technol. (United Kingdom)*, 2018, doi: 10.1080/02670836.2018.1491931.
- [37] K. Kothari, “Manufacturing techniques for titanium aluminide based alloys and metal matrix composites,” *Univ. Maryland, Coll. Park. Park.*, no. Doctoral thesis, 2010, [Online]. Available: <https://apps.dtic.mil/dtic/tr/fulltext/u2/a631137.pdf>.
- [38] R. V. Ramanujan, “Phase transformations in γ based titanium aluminides,” *Int. Mater. Rev.*, vol. 45, no. 6, pp. 217–240, 2000, doi: 10.1179/095066000101528377.
- [39] Y. W. (Y W.). Kim, “Microstructural evolution and mechanical properties of a forged gamma titanium aluminide alloy,” *Acta Metall. Mater.*, vol. 40, no. 6, pp. 1121–1134, 1992, doi: 10.1016/0956-7151(92)90411-7.
- [40] F. Appel and R. Wagner, “Microstructure and deformation of two-phase γ -titanium aluminides,” *Materials Science and Engineering R: Reports*. 1998, doi: 10.1016/S0927-796X(97)00018-1.
- [41] D. S. Shih, S. C. Huang, G. K. Scarr, H. Jang, and J. C. Chestnut,

References

- “Microstructural dependence of mechanical properties of Ti-48Al-2Cr-2Nb,” 1991.
- [42] G. Hénaff and A. L. Gloanec, “Fatigue properties of TiAl alloys,” *Intermetallics*, 2005, doi: 10.1016/j.intermet.2004.09.007.
- [43] P. A. Bartolotta and D. L. Krause, “Titanium aluminide applications in the high speed civil transport,” *Gamma Titan. Alum.*, 1999.
- [44] B. Skrotzki, T. Rudolf, and G. Eggeler, “Creep behavior and microstructural evolution of a near- γ -TiAl alloy with duplex microstructure,” *Zeitschrift fuer Met. Res. Adv. Tech.*, 1999.
- [45] N. Bhibhansu, “Thermo-Mechanical Processing of Third Generation γ – Titanium Aluminides,” Indian Institute of Science, 2019.
- [46] F. Appel, M. Oehring, and R. Wagner, “Novel design concepts for gamma-base titanium aluminide alloys,” *Intermetallics*, 2000, doi: 10.1016/S0966-9795(00)00036-4.
- [47] M. Takeyama and S. Kobayashi, “Physical metallurgy for wrought gamma titanium aluminides: Microstructure control through phase transformations,” 2005, doi: 10.1016/j.intermet.2004.12.014.
- [48] T. Tetsui, K. Shindo, S. Kobayashi, and M. Takeyama, “A newly developed hot worked TiAl alloy for blades and structural components,” *Scr. Mater.*, vol. 47, no. 6, pp. 399–403, 2002, doi: 10.1016/S1359-6462(02)00158-6.
- [49] T. Tetsui, K. Shindo, S. Kaji, S. Kobayashi, and M. Takeyama, “Fabrication of TiAl components by means of hot forging and machining,” *Intermetallics*, vol. 13, no. 9, pp. 971–978, 2005, doi: 10.1016/j.intermet.2004.12.012.
- [50] N. A. Nochovnaya, P. V. Panin, A. S. Kochetkov, and K. A. Bokov, “Modern Refractory Alloys Based on Titanium Gamma-Aluminide: Prospects of Development and Application,” *Met. Sci. Heat Treat.*, 2014, doi: 10.1007/s11041-014-9763-4.
- [51] B. P. Bewlay, S. Nag, A. Suzuki, and M. J. Weimer, “TiAl alloys in commercial aircraft engines,” *Mater. High Temp.*, vol. 33, no. 4–5, pp. 549–559, Jun. 2016, doi: 10.1080/09603409.2016.1183068.
- [52] Flex mill, “Turbine blade finishing,” 2021, [Online]. Available: <https://www.flexmill.fi/applications/turbine-blade-finishing/>.
- [53] S. Castellanos and J. L. Alves, “A Review of Milling of Gamma Titanium Aluminides,” *U. Prto J. Eng.*, 2017, doi: 10.24840/2183-6493.
- [54] P. C. Priarone, F. Klocke, M. G. Faga, D. Lung, and L. Settineri, “Tool life and surface integrity when turning titanium aluminides with PCD tools under conventional wet cutting and cryogenic cooling,” *Int. J. Adv. Manuf. Technol.*, vol. 85, no. 1–4, pp. 807–816, 2016, doi: 10.1007/s00170-015-7958-5.
- [55] P. C. Priarone, M. Robiglio, L. Settineri, and V. Tebaldo, “Milling and Turning of Titanium Aluminides by Using Minimum Quantity Lubrication,” *Procedia CIRP*, vol. 24, pp. 62–67, 2014, doi: 10.1016/j.procir.2014.07.147.

References

- [56] D. K. Aspinwall, A. L. Mantle, W. K. Chan, R. Hood, S. L. Soo, "Cutting temperatures when ball nose end milling γ -TiAl intermetallic alloys," *CIRP Ann. - Manuf. Technol.*, vol. 62, no. 1, pp. 75–78, 2013, doi: 10.1016/j.cirp.2013.03.007.
- [57] S. Kolahdouz, M. Hadi, B. Arezoo, and S. Zamani, "Investigation of surface integrity in high speed milling of gamma titanium aluminide under dry and minimum quantity lubricant conditions," *Procedia CIRP*, vol. 26, pp. 367–372, 2015, doi: 10.1016/j.procir.2014.08.016.
- [58] F. Appel, U. Sparka, and R. Wagner, "Work hardening and recovery of gamma base titanium aluminides," *Intermetallics*, 1999, doi: 10.1016/S0966-9795(98)00109-5.
- [59] L. Settineri, P. C. Priarone, M. Arft, D. Lung, and T. Stoyanov, "An evaluative approach to correlate machinability, microstructures, and material properties of gamma titanium aluminides," *CIRP Ann.*, vol. 63, no. 1, pp. 57–60, 2014, doi: 10.1016/j.cirp.2014.03.068.
- [60] Y. F. Ge, Y. C. Fu, and J. H. Xu, "Experimental Study on High Speed Milling of γ -TiAl Alloy," *Key Eng. Mater.*, vol. 339, pp. 6–10, May 2007, doi: 10.4028/www.scientific.net/KEM.339.6.
- [61] P. C. Priarone, S. Rizzuti, G. Rotella, and L. Settineri, "Technological and Environmental Aspects in Milling of γ -TiAl," *Adv. Mater. Res.*, vol. 223, pp. 340–349, 2011, doi: 10.4028/www.scientific.net/AMR.223.340.
- [62] P. C. Priarone, M. Robiglio, L. Settineri, and V. Tebaldo, "Effectiveness of minimizing cutting fluid use when turning difficult-to-cut alloys," *Procedia CIRP*, vol. 29, pp. 341–346, 2015, doi: 10.1016/j.procir.2015.02.006.
- [63] N. T. Mathew, "Drilling of titanium aluminide at different aspect ratio under dry and wet conditions," *J. Manuf. Process.*, 2016, doi: 10.1016/j.jmapro.2016.09.009.
- [64] P. C. Priarone, S. Ruffa, J. S. Bedolla, and L. Settineri, "A DoE approach to hole quality evaluation in drilling of an electron beam melted titanium aluminide," *Procedia CIRP*, vol. 8, pp. 481–486, 2013, doi: 10.1016/j.procir.2013.06.137.
- [65] G. Gautier, P. C. Priarone, S. Rizzuti, L. Settineri, and V. Tebaldo, "A Contribution on the Modelling of Wire Electrical Discharge Machining of a γ -TiAl Alloy," *Procedia CIRP*, vol. 31, no. July, pp. 203–208, 2015, doi: 10.1016/j.procir.2015.03.019.
- [66] A. L. Mantle and D. K. Aspinwall, "Surface integrity of a high speed milled gamma titanium aluminide," *J. Mater. Process. Technol.*, vol. 118, no. 1–3, pp. 143–150, 2001, doi: 10.1016/S0924-0136(01)00914-1.
- [67] A. Beranoagirre, D. Olvera, and L. N. López De Lacalle, "Milling of gamma titanium-aluminum alloys," *Int. J. Adv. Manuf. Technol.*, 2012, doi: 10.1007/s00170-011-3812-6.
- [68] R. G. V. Pérez, "Wear mechanisms of WC inserts in face milling of gamma

References

- titanium aluminides,” *Wear*, vol. 259, no. 7–12, pp. 1160–1167, 2005, doi: 10.1016/j.wear.2005.02.062.
- [69] A. L. Mantle and D. K. Aspinwall, “Surface integrity and fatigue life of turned gamma titanium aluminide,” *J. Mater. Process. Technol.*, vol. 72, no. 3, pp. 413–420, 1997, doi: 10.1016/S0924-0136(97)00204-5.
- [70] A. R. C. Sharman, D. K. Aspinwall, R. C. Dewes, and P. Bowen, “Workpiece surface integrity considerations when finish turning gamma titanium aluminide,” *Wear*, vol. 249, no. 5–6, pp. 473–481, 2001, doi: 10.1016/S0043-1648(01)00575-0.
- [71] D. Bhaduri *et al.*, “Ultrasonic assisted creep feed grinding of gamma titanium aluminide using conventional and superabrasive wheels,” *CIRP Ann. - Manuf. Technol.*, vol. 66, no. 1, pp. 341–344, 2017, doi: 10.1016/j.cirp.2017.04.085.
- [72] R. Hood, D. K. Aspinwall, and W. Voice, “Creep feed grinding of a gamma titanium aluminide intermetallic alloy using SiC abrasives,” *J. Mater. Process. Technol.*, 2007, doi: 10.1016/j.jmatprotec.2007.03.081.
- [73] F. Klocke, T. Herrig, M. Zeis, and A. Klink, “Experimental Research on the Electrochemical Machinability of selected γ -TiAl alloys for the Manufacture of Future Aero Engine Components,” *Procedia CIRP*, vol. 35, pp. 50–54, 2015, doi: 10.1016/j.procir.2015.08.050.
- [74] A. Beranoagirre, G. Urbikain, A. Calleja, and L. López de Lacalle, “Hole Making by Electrical Discharge Machining (EDM) of γ -TiAl Intermetallic Alloys,” *Metals (Basel)*, vol. 8, no. 7, p. 543, Jul. 2018, doi: 10.3390/met8070543.
- [75] P. C. Priarone, S. Rizzuti, L. Settineri, and G. Vergnano, “Effects of cutting angle, edge preparation, and nano-structured coating on milling performance of a gamma titanium aluminide,” *J. Mater. Process. Technol.*, vol. 212, no. 12, pp. 2619–2628, Dec. 2012, doi: 10.1016/j.jmatprotec.2012.07.021.
- [76] D. Finkeldei and F. Bleicher, “Investigation of Coolants in Machining of Titanium Aluminides,” no. 2016, pp. 0825–0833, 2016, doi: 10.2507/26th.daaam.proceedings.115.
- [77] R. Hood, P. Cooper, D. K. Aspinwall, S. L. Soo, and D. S. Lee, “Creep feed grinding of γ -TiAl using single layer electroplated diamond superabrasive wheels,” *CIRP J. Manuf. Sci. Technol.*, vol. 11, pp. 36–44, 2015, doi: 10.1016/j.cirpj.2015.07.001.
- [78] N. T. Mathew, “Drilling of titanium aluminide at different aspect ratio under dry and wet conditions,” *J. Manuf. Process.*, vol. 24, pp. 256–269, 2016, doi: 10.1016/j.jmapro.2016.09.009.
- [79] D. Clifton, A. R. Mount, D. J. Jardine, and R. Roth, “Electrochemical machining of gamma titanium aluminide intermetallics,” *J. Mater. Process. Technol.*, 2001, doi: 10.1016/S0924-0136(00)00739-1.
- [80] R. M’Saoubi *et al.*, “High performance cutting of advanced aerospace alloys and composite materials,” *CIRP Ann. - Manuf. Technol.*, vol. 64, no. 2, pp.

References

- 557–580, 2015, doi: 10.1016/j.cirp.2015.05.002.
- [81] A. Al-Ahmari, M. Ashfaq, A. Alfaify, B. Abdo, A. Alomar, and A. Dawud, “Predicting surface quality of γ -TiAl produced by additive manufacturing process using response surface method,” *J. Mech. Sci. Technol.*, vol. 30, no. 1, pp. 345–352, Jan. 2016, doi: 10.1007/s12206-015-1239-y.
- [82] Kalpajian, *Manufacturing processes for engineering materials*. 1985.
- [83] A. S. Coromant, *Modern Metal Cutting - A Practical Handbook*. 1994.
- [84] ISO-8688-2, “Tool life testing in milling - Part 2: End Milling,” 1989.
- [85] E.-G. Ng, D. W. Lee, R. C. Dewes, and D. K. Aspinwall, “The Effect of Cutting Environments When High Speed Ball Nose End Milling Inconel 718,” in *Intermetallics and Superalloys*, 2006.
- [86] P. C. Priarone, S. Rizzuti, S. Ruffa, and L. Settineri, “Drilling experiments on a gamma titanium aluminide obtained via electron beam melting,” *Int. J. Adv. Manuf. Technol.*, vol. 69, no. 1–4, pp. 483–490, 2013, doi: 10.1007/s00170-013-5050-6.
- [87] P. C. Priarone, S. Rizzuti, G. Rotella, and L. Settineri, “Tool wear and surface quality in milling of a gamma-TiAl intermetallic,” *Int. J. Adv. Manuf. Technol.*, vol. 61, no. 1–4, pp. 25–33, 2012, doi: 10.1007/s00170-011-3691-x.
- [88] H. Zang, M. L. H. Wise, and D. K. Aspinwall, “The Surface Quality of Hipped Gamma Titanium Aluminide Bar after Turning,” in *Proceedings of the Thirty-First International Matador Conference*, 1995.
- [89] M. Field, “REVIEW OF SURFACE INTEGRITY OF MACHINED COMPONENTS.,” *Ann CIRP*, 1971.
- [90] X. Liang, Z. Liu, and B. Wang, “State-of-the-art of surface integrity induced by tool wear effects in machining process of titanium and nickel alloys: A review,” *Meas. J. Int. Meas. Confed.*, vol. 132, no. October, pp. 150–181, 2019, doi: 10.1016/j.measurement.2018.09.045.
- [91] X. Liang, Z. Liu, and B. Wang, “State-of-the-art of surface integrity induced by tool wear effects in machining process of titanium and nickel alloys: A review,” *Meas. J. Int. Meas. Confed.*, vol. 132, no. October, pp. 150–181, 2019, doi: 10.1016/j.measurement.2018.09.045.
- [92] KAHLES JF, BELLOWS G, and FIELD M, “SURFACE INTEGRITY GUIDELINES FOR MACHINING,” 1968.
- [93] Mitutoyo America Corporation, “Quick guide to surface roughness measurement,” 2016. [Online]. Available: https://www.mitutoyo.com/wp-content/uploads/2012/11/1984_Surf_Roughness_PG.pdf.
- [94] M. Dąbski, “Time-dependent surface deterioration of glacially abraded basaltic boulders by Fláajökull, SE Iceland,” *Jokull*, vol. 63, pp. 55–70, 2013.
- [95] A. L. Mantle and D. K. Aspinwall, “Cutting Force Evaluation when High Speed End Milling a Gamma Titanium Aluminide Intermetallic Alloy,” in

References

- Intermetallics and Superalloys*, 2000.
- [96] E. Brinksmeier, D. Meyer, A. G. Huesmann-Cordes, and C. Herrmann, "Metalworking fluids - Mechanisms and performance," *CIRP Ann. - Manuf. Technol.*, vol. 64, no. 2, pp. 605–628, 2015, doi: 10.1016/j.cirp.2015.05.003.
- [97] E. J. A. Armarego, *The machining of metals [by] E. J. A. Armarego [and] R. H. Brown*. Englewood Cliffs, N.J: Prentice-Hall, 1969.
- [98] V. P. Astakhov, "Tribology of Cutting Tools," 2012.
- [99] E. M. Trent, "The tribology of metal cutting," *Tribol. Ser.*, 1983, doi: 10.1016/S0167-8922(08)70710-7.
- [100] W. Grzesik, "Tribology of Metal Cutting," in *Advanced Machining Processes of Metallic Materials*, Elsevier, 2017, pp. 197–214.
- [101] M. C. Shaw, *Metal Cutting Principles*. 2005.
- [102] N. P. Suh and H.-C. Sin, "The genesis of friction," *Wear*, vol. 69, no. 1, pp. 91–114, Jun. 1981, doi: 10.1016/0043-1648(81)90315-X.
- [103] K. Holmberg, A. Matthews, and H. Ronkainen, "Coatings tribology - Contact mechanisms and surface design," 1998, doi: 10.1016/S0301-679X(98)00013-9.
- [104] GGB Bearings, "Different wear mechanisms on the surface of the material." <https://www.ggbearings.com/en/tribou/tribology-surrounds-you>.
- [105] S. N. Melkote *et al.*, "Advances in material and friction data for modelling of metal machining," *CIRP Ann.*, vol. 66, no. 2, pp. 731–754, 2017, doi: 10.1016/j.cirp.2017.05.002.
- [106] M. E. Merchant, "Mechanics of the metal cutting process. I. Orthogonal cutting and a type 2 chip," *J. Appl. Phys.*, 1945, doi: 10.1063/1.1707586.
- [107] P. Albrecht, "New developments in the theory of the metal-cutting process: Part I. the ploughing process in metal cutting," *J. Manuf. Sci. Eng. Trans. ASME*, 1960, doi: 10.1115/1.3664242.
- [108] T. H. C. Childs, "Friction modelling in metal cutting," *Wear*, vol. 260, no. 3, pp. 310–318, 2006, doi: 10.1016/j.wear.2005.01.052.
- [109] G. Ortiz-de-Zarate, A. Madariaga, P. J. Arrazola, and T. H. C. Childs, "A novel methodology to characterize tool-chip contact in metal cutting using partially restricted contact length tools," *CIRP Ann.*, vol. 70, no. 1, pp. 61–64, 2021, doi: 10.1016/j.cirp.2021.03.002.
- [110] P. Hedenqvist and M. Olsson, "Sliding wear testing of coated cutting tool materials," *Tribol. Int.*, 1991, doi: 10.1016/0301-679X(91)90020-A.
- [111] F. Zemzemi, W. Bensalem, J. Rech, A. Dogui, and P. Kapsa, "New tribometer designed for the characterisation of the friction properties at the tool/chip/workpiece interfaces in machining," *Tribotest*, vol. 14, no. 1, pp. 11–25, Jan. 2008, doi: 10.1002/tt.50.
- [112] H. Puls, F. Klocke, and D. Lung, "Experimental investigation on friction under

References

- metal cutting conditions,” *Wear*, 2014, doi: 10.1016/j.wear.2013.12.020.
- [113] N. N. Zorev, *Metal cutting mechanics*. Pergamon, 1966.
- [114] N. N. Zorev, “Interrelationship between shear processes occurring along tool face and on shear plane in metal cutting,” 1963.
- [115] T. Shirakashi and E. Usui, “Friction Characteristics on Tool Face in Metal Machining,” *J. Japan Soc. Precis. Eng.*, 1973, doi: 10.2493/jjspe1933.39.966.
- [116] P. J. Arrazola, D. Ugarte, and X. Domínguez, “A new approach for the friction identification during machining through the use of finite element modeling,” *Int. J. Mach. Tools Manuf.*, vol. 48, no. 2, pp. 173–183, 2008, doi: 10.1016/j.ijmachtools.2007.08.022.
- [117] C. Zhang, J. Lu, F. Zhang, and S. I. Butt, “Identification of a new friction model at tool-chip interface in dry orthogonal cutting,” *Int. J. Adv. Manuf. Technol.*, 2017, doi: 10.1007/s00170-016-9149-4.
- [118] J. Rech, C. Claudin, W. Grzesik, and Z. Zalisz, “Characterization of the friction properties of various coatings at the tool-chip-workpiece interfaces in dry machining of AISI 4140 steel,” *Proc. Inst. Mech. Eng. Part J J. Eng. Tribol.*, 2008, doi: 10.1243/13506501JET416.
- [119] P. J. Arrazola and T. Özel, “Investigations on the effects of friction modeling in finite element simulation of machining,” *Int. J. Mech. Sci.*, vol. 52, no. 1, pp. 31–42, 2010, doi: 10.1016/j.ijmecsci.2009.10.001.
- [120] T. Özel, “The influence of friction models on finite element simulations of machining,” *Int. J. Mach. Tools Manuf.*, 2006, doi: 10.1016/j.ijmachtools.2005.07.001.
- [121] M. San-Juan, Ó. Martín, and F. Santos, “Experimental study of friction from cutting forces in orthogonal milling,” *Int. J. Mach. Tools Manuf.*, 2010, doi: 10.1016/j.ijmachtools.2010.03.013.
- [122] A. R. Rastkar and T. Bell, “Characterization and tribological performance of oxide layers on a gamma based titanium aluminide,” *Wear*, 2005, doi: 10.1016/j.wear.2004.11.014.
- [123] C. X. Li, J. Xia, and H. Dong, “Sliding wear of TiAl intermetallics against steel and ceramics of Al₂O₃, Si₃N₄ and WC/Co,” *Wear*, 2006, doi: 10.1016/j.wear.2006.01.044.
- [124] C. L. Chu and S. K. Wu, “A study on the dry uni-directional sliding behaviour of titanium aluminides,” *Scr. Metall. Mater.*, vol. 33, no. 1, pp. 139–143, Jul. 1995, doi: 10.1016/0956-716X(95)00109-9.
- [125] J. Cheng *et al.*, “Friction and wear properties of a high Nb-containing TiAl alloy against WC-8Co, Si₃N₄, and GCr15 in an unlubricated contact,” *Intermetallics*, vol. 106, no. 2, pp. 7–12, 2019, doi: 10.1016/j.intermet.2018.11.019.
- [126] S. Gialanella and G. Straffelini, “Interplay between oxidation and wear behavior of the Ti-48Al-2Cr-2Nb-1B alloy,” *Metall. Mater. Trans. A Phys.*

References

- Metall. Mater. Sci.*, vol. 30, no. 8, pp. 2019–2026, 1999, doi: 10.1007/s11661-999-0012-1.
- [127] T. Özel, M. Sima, A. K. Srivastava, and B. Kaftanoglu, “Investigations on the effects of multi-layered coated inserts in machining Ti–6Al–4V alloy with experiments and finite element simulations,” *CIRP Ann.*, vol. 59, no. 1, pp. 77–82, 2010, doi: 10.1016/j.cirp.2010.03.055.
- [128] Z. G. Wang, Y. S. Wong, and M. Rahman, “High-speed milling of titanium alloys using binderless CBN tools,” *Int. J. Mach. Tools Manuf.*, 2005, doi: 10.1016/j.ijmachtools.2004.06.021.
- [129] C. F. Wyen and K. Wegener, “Influence of cutting edge radius on cutting forces in machining titanium,” *CIRP Ann. - Manuf. Technol.*, 2010, doi: 10.1016/j.cirp.2010.03.056.
- [130] M. Cotterell and G. Byrne, “Dynamics of chip formation during orthogonal cutting of titanium alloy Ti-6Al-4V,” *CIRP Ann. - Manuf. Technol.*, 2008, doi: 10.1016/j.cirp.2008.03.007.
- [131] C. Claudin, A. Mondelin, J. Rech, and G. Fromentin, “Effects of a straight oil on friction at the tool–workmaterial interface in machining,” *Int. J. Mach. Tools Manuf.*, vol. 50, no. 8, pp. 681–688, Aug. 2010, doi: 10.1016/j.ijmachtools.2010.04.013.
- [132] F. Zemzemi, J. Rech, W. Ben Salem, A. Dogui, and P. Kapsa, “Identification of friction and heat partition model at the tool-chip-workpiece interfaces in dry cutting of an inconel 718 alloy with cbn and coated carbide tools,” *Adv. Manuf. Sci. Technol.*, vol. 38, no. 1, 2014, doi: 10.2478/amst-2014-0001.
- [133] S. Milton, “Study on the machinability and surface integrity of Ti6Al4V produced by Selective Laser Melting (SLM) and Electron Beam Melting (EBM) processes,” 2018.
- [134] W. Grzesik, J. Małecka, Z. Zalisz, K. Zak, and P. Niesłony, “Investigation of Friction and Wear Mechanisms of TiAlV Coated Carbide Against Ti6Al4V Titanium Alloy Using Pin-On-Disc Tribometer,” *Arch. Mech. Eng.*, vol. 63, no. 1, pp. 113–127, 2016, doi: 10.1515/meceng-2016-0006.
- [135] R. Budynas and J. K. Nisbett, *Shigley’s Mechanical Engineering Design*. 2015.
- [136] C. Bonnet *et al.*, “Identification of a friction model—Application to the context of dry cutting of an AISI 316L austenitic stainless steel with a TiN coated carbide tool,” *Int. J. Mach. Tools Manuf.*, vol. 48, no. 11, pp. 1211–1223, Sep. 2008, doi: 10.1016/j.ijmachtools.2008.03.011.
- [137] A. Brotzu, F. Felli, and D. Pilone, “Effect of alloying elements on the behaviour of TiAl-based alloys,” *Intermetallics*, vol. 54, pp. 176–180, 2014, doi: 10.1016/j.intermet.2014.06.007.
- [138] Y. D. Ivakin, M. N. Danchevskaya, and G. P. Muravieva, “Induced formation of corundum crystals in supercritical water fluid,” *Russ. J. Phys. Chem. B*, 2015, doi: 10.1134/S1990793115070088.

References

- [139] P. A. McQuay, V. K. Sikka, Y. E. Khalfalla, and K. Y. Benyounis, “Casting of Intermetallics,” in *Reference Module in Materials Science and Materials Engineering*, Elsevier, 2016.
- [140] P. A. McQuay, “Thermal analysis of phase transformations in a γ -TiAl alloy,” *Mater. Sci. Eng. A*, 1994, doi: 10.1016/0921-5093(94)90927-X.
- [141] S. F. Franzén and J. Karlsson, “ γ -Titanium Aluminide Manufactured by Electron,” p. 89, 2010.
- [142] “McSwain Engineering Inc.” <https://www.mcswain-eng.com/#>.
- [143] M. Cavazzuti, *Optimization Methods: From Theory to Design*. 2003.
- [144] S. Milton, A. Duchosal, F. Chalon, R. Leroy, and A. Morandea, “Thermal study during milling of Ti6Al4V produced by Electron Beam Melting (EBM) process,” *J. Manuf. Process.*, vol. 38, no. August 2018, pp. 256–265, 2019, doi: 10.1016/j.jmapro.2018.12.027.

